CHEMICAL TOOLS FOR THE ELUCIDATION OF THE ROLE OF PARP7 IN THE INNATE IMMUNE SYSTEM

By

Kelsie Marie Rodriguez

A DISSERTATION

Presented to the Department of Chemical Physiology and Biochemistry

and the Oregon Health & Science University

School of Medicine

in partial fulfillment of the requirements for the degree of

Doctor of Philosophy

January 2021

School of Medicine

Oregon Health & Science University

CERTIFICATE OF APPROVAL

This is to certify that the PhD dissertation of

Kelsie M. Rodriguez

has been approved

Michael Cohen, Ph.D. (Mentor)

Beth Habecker, Ph.D. (Committee chair)

Thomas Scanlan, Ph.D. (Member)

Larry David, Ph.D.(Member)

Carsten Schultz, Ph.D.(Member)

Cheryl Maslen, Ph.D.(Member)

Daniel Streblow (Member)

TABLE OF CONTENTS

Chapter 1: Introduction- Chemical genetic methodologies for identifying Poly(ADP- ribose) Polymerase targets……………………………………….…..…… 1

Chapter 2: Chemical genetics and proteome-wide site mapping reveal cysteine MARylation by PARP-7 on immune-relevant protein targets………………….…26

LIST OF FIGURES

LIST OF TABLES

All table supplements can currently be found using this link to a box folder. They contain large data sets of proteomics data, therefore traditional table format is not practical.

https://ohsu.box.com/s/09spflrl3kpri6xgwkueci0rlpmtk534

AKNOWLEGEMENTS

I am grateful to many individuals who have supported me through the long and arduous journey through graduate school.

I would first like to acknowledge my mentor **Mike Cohen** and thank him for his guidance throughout numerous projects in the lab these past five years. Mike, I admire your scientific prowess and continual optimism when experiments weren't working. I have learned a lot under your mentorship and I will take a number of the skills I have obtained in your lab with me throughout my career.

I would also like to thank my **Dissertation Advisory Committee** for their guidance and for their deep understanding of the ins and outs of graduate school. In particular I would like to thank **Beth Habecker** for her support as my DAC chair, **Cheryl Maslen** for her support through the PERT program and for always providing opportunities to enhance my career in any way she can, and **Larry David** for all of his help with the mass spec studies presented in this thesis.

I have learned something from every individual person I have encountered during my time in the Cohen lab. I am thankful that I had the pleasure of interacting with a number of amazing coworkers. **Ian,** thank you for your mentorship and guidance with my various projects in the lab and for providing empathy at times when I needed it most. I learned many skills from you that have helped me stay on track and be a better scientist. **Rory,** thank you for your unwavering kindness and for teaching me most of my synthetic chemistry skills. It was always fun sharing laughs with you in the lab. **Ilsa**, thank you for your hard work and for getting the PARP7 inhibitor project off the ground. **Madison**, thank you teaching me to embrace my differences and overcome imposter syndrome. Having a best friend in the lab made challenges a lot less stressful. **Anke**, thank you for being a great role model to look up to as a skillful and talented woman in science. **Sunil**, thank you for always keeping it real and for providing your amazing chemistry skills to the lab. You never hesitate to help people when they need it and you are a continually kind and positive presence in the lab. **Moriah**, thank you for your friendship and for making the lab a fun place to work. Tuesday trivia with you and Joyce was always a highlight of my week and a nice break from the stress of grad school. **Justina**, thank you for your positivity and warmth. You are queen of the experimental controls and a great scientific role model. **Daniel**, thank you for all the laughter and for your selfless deed of taking on so many lab jobs during your first year. You are incredibly hard working and I look forward to seeing your graduate success unfold. **Ivan**, your smile is always a beautiful thing to see in the lab and I appreciate your positivity. Thank you for your hard work and countless protein preps. **Danny**, your attention to detail is admirable and I am excited to see that your project has taken off so quickly. I look forward to seeing the rest of your graduate career successes.

To my friends: I can’t name all of you but you know who you are. I am not exaggerating when I say that I do not think I would have made it through grad school without you. You have made Portland an amazing place to spend the greater part of my 20s and I will cherish all of our memories. In particular, I would like to thank: **Haley Licon**, for her friendship and for her time spent editing parts of my thesis as well as **Lauren Sachs** for her unwavering friendship and support.

To my family: Thank you for encouraging me and supporting me in whatever I choose and for always providing me with unconditional love. Thank you to my fiancé **Jeff Tucker** who has made my life so much better and easier in every way possible. You an amazing partner and there is no one I would have rather survived 2020 quarantine with. You have carried me through hard times and I don’t know what I would do without your kind and supportive shoulder to lean on.

Chapter 1.

Introduction

Chemical genetic methodologies for identifying Poly(ADP- ribose) Polymerase targets

Parts of this chapter are to be used in a review on chemical genetics of PARPs in the journal Trends in Biochemical Sciences (to be edited and published 2021)

Abstract

PARPs are a family of 17 proteins that regulate a diverse range of cellular processes through the transfer of ADP-ribose from NAD^+ to amino acids on protein targets, a process known as ADP-ribosylation. Identifying the protein substrates of an individual PARP family member is essential for understanding its cellular role; however, doing so remained an impracticable task until the development of chemical genetic strategies. Two chemical genetic approaches, the Cohen method and the Kraus method, have been used to determine the substrate specificity of several PARP family members. These strategies have revealed targets that show roles for PARP family members outside of well-studied PARP-1-associated DNA damage repair. The PARP family members that have thus far been amenable to chemical genetic studies include: PARPs-1, 2, 3, 7, 10, 11, and 14. While unique targets have been identified for each of the characterized PARPs, patterns in target specificity have also emerged that point to overlapping functions and perhaps shared roles amongst the different PARP family members.

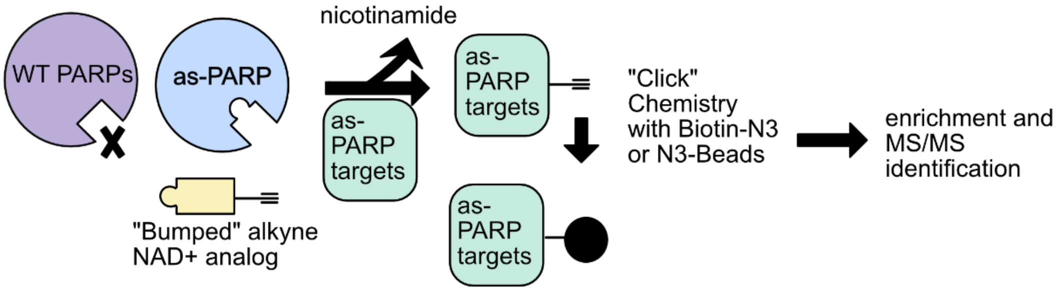

Figure 1.1 (Key figure). Schematic of chemical genetic methodologies developed to identify the substrates of individual PARP family members.

Mutations within the highly conserved active site of PARP enzymes create an analog sensitized pocket or “hole” (as-PARP) that allows the transfer of ADPr to target proteins from modified or “bumped” alkyne NAD$^+$ analogs. Importantly, these NAD$^+$ analogs are unable to be used by wildtype PARP enzymes, thus conferring specific labeling by single PARP. The ADPr protein targets of the as-PARP are then clicked to an amenable substrate, enriched and identified via mass spectrometry.

Introduction

The poly-ADP-ribose-polymerases (PARPs) are a family of enzymes that catalyze the post-translational transfer of ADP-ribose from nicotinamide adenine dinucleotide (NAD$^+$) to protein targets in a process known as ADP-ribosylation (ADPr)[1]. ADP-ribose can be transferred as either a single unit (mono-ADP-ribosylation, MARylation) or as multiple units (poly-ADP-ribosylation, PARylation).[2] There are 17 known PARP family members in humans and a large number of homologs in animals, plants, fungi, bacteria and viruses. Together, these enzymes control a range of essential cellular processes, including the DNA damage response, immune signaling in response to viral and bacterial infection, chromatin regulation, RNA biology, stress responses, metabolism, and cancer. Many of these functions were uncovered via genetic knockout or specific inhibition, and few distinct targets were described. PARPs are essential enzymes with diverse roles, many of which have yet to be uncovered. Chemical genetics (CG) offer a unique methodology for identifying these roles via target identification.

Historically, the task of assigning ADPr events to an individual PARP has proven technically challenging, due to both functional redundancy among the PARP family members and their highly conserved NAD$^+$ binding domain. Only with the advent of two

chemical genetic (CG) methodologies, referred to herein as the Cohen and Kraus methods, has the large-scale identification of specific PARP targets become feasible. In both strategies, a PARP of interest is mutated to create an analog-sensitized "hole" in its conserved active site **(Figure 1)**. This hole facilitates the transfer of ADPr to protein targets from a modified or "bumped" alkyne NAD$^+$ analog. ADP-ribosylated proteins are then enriched and subjected to tandem mass spectrometry to identify substrates specific to the analog-sensitized PARP (as-PARP). Using this "bump and hole" approach, the targets of PARP family members 1, 2, 3, 7, 10, 11 and 14 have been identified, exposing several previously unknown roles for this class of enzymes[3,4,5,6,7]. In addition, canonical roles for PARPs, such as the role of PARP-1 in DNA damage, have been elaborated upon by the discovery of novel targets within these pathways.
In this review, we consider the details of CG methodologies for identifying PARP family members and summarize the key results of these studies.

CG strategies and the substrate/ NAD$^+$ analog pairs that make them possible

The first CG strategy for PARPs, developed by the Cohen lab, showed the utility of bi-functional NAD$^+$ molecules with a "bump" positioned on the nicotinamide ring and a bioorthogonal alkyne handle positioned on the adenosine ring. The alkyne handle is amenable to "click" chemistry (CuAAC) and subsequent enrichment of protein targets[3,5,8]. This strategy established two gatekeeper residues within the nicotinamide pocket, annotated as "Hole 1" and "Hole 2" **(Figure 1.2).** Mutation of either position to a comparatively smaller residue (Ala or Gly) creates a hole, allowing bi-functional NAD$^+$ substrates to be utilized **(Figure 1.2A)**[3,5]. The Hole 1 gatekeeper mutations utilized to identify PARP-1 and PARP-2 targets include K903A and K469A, respectively **(Figure 1.2B)**. In subsequent studies by the Cohen lab, gatekeeper mutations were introduced into floor of the nicotinamide binding pocket (Hole 2, **Figure 1.2B**)[4,5]. In contrast to Hole 1, which accommodates a nicotinamide C5-ethyl substituent (5-et-6a-NAD^+), the pocket created by mutation of Hole 2 accommodates a larger “bump” in the form of a nicotinamide C5-benzyl modified NAD^+ analog (5bn-6a-NAD^+ or 5-bn-2e-NAD^+, **Figure 1.2B)**. Using NAD+ analogs with a biorthogonal handle at the N6 adenosine (5bn-6a-NAD^+), Hole 2 mutations I987G, I320G, and L1782G were deployed to identify targets of as-PARP-10, -11, and -14[4,7]. A similar approach was also taken in the study of as-PARP-7 (I631G). However, 5bn-6a-NAD^+ was found to serve as a poor substrate of this particular as-PARP, requiring the alkyne handle to be placed at the C2 adenosine position rather than the N6 (5-bn-2e-NAD^+, **Figure 1.2C)**.

The second CG strategy, developed by the Kraus lab, utilizes two separate gatekeeper residues (“Hole 3” and “Hole 4” in **Figure 1.2B**). Hole 3 was used to identify targets of as-PARP-1 (L877A), -2 (L443A), and -3 (L394A)[6]. The Hole 4 gatekeeper residue was used for the identification of as-PARP-7 targets (S563G). These holes both accommodate a bifunctional, bulky substituent placed off of the C8 position of the adenosine ring of NAD^+ (8-Bu(3-yne)T-NAD^+) to allow for transfer of ADPr to protein targets **(Figure 1.2C)**.

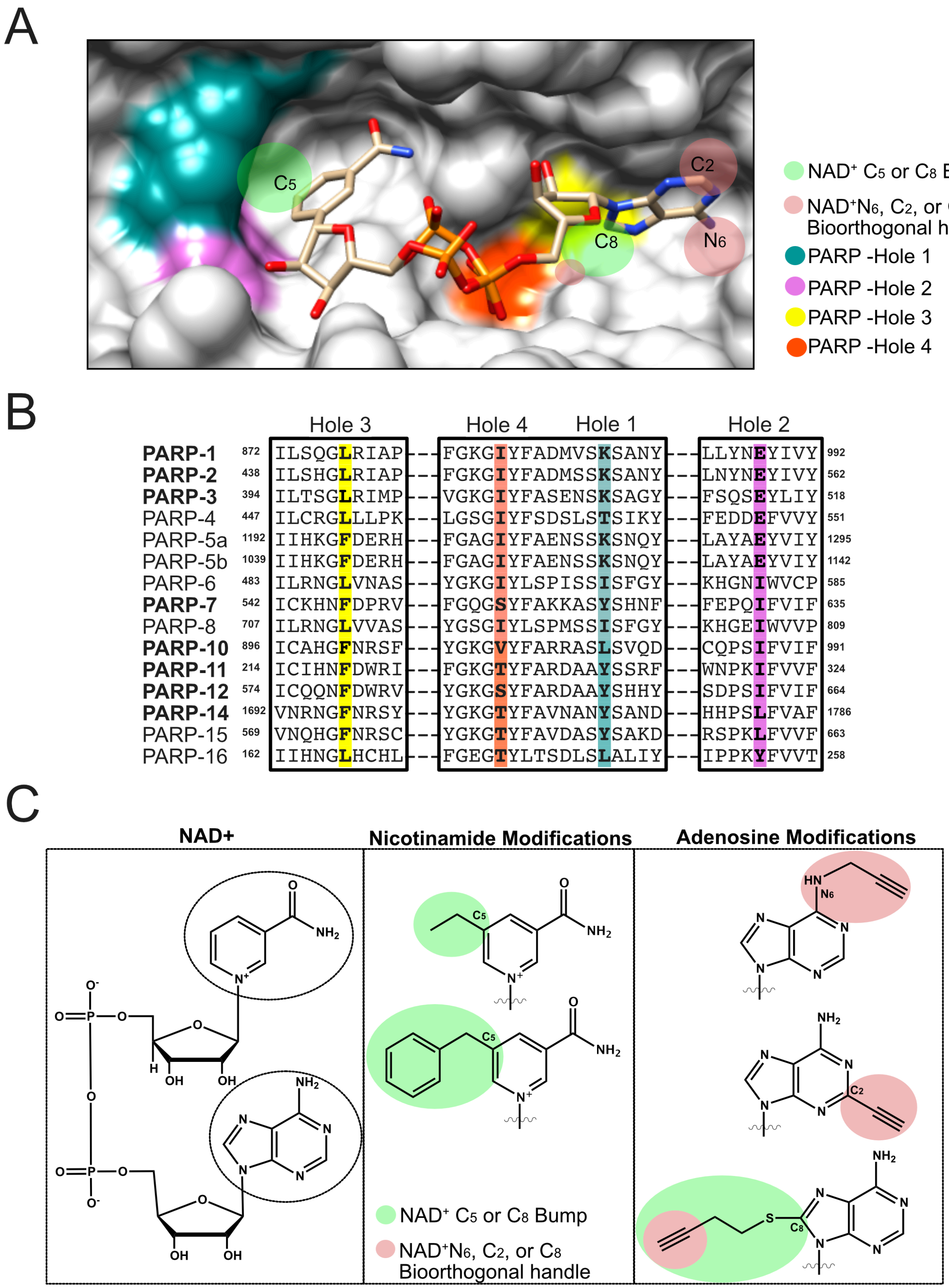

		Hole 3		Hole 4 / Hole 1		Hole 2	
PARP-1	872	ILSQGLRIAP	---	FGKGIYFADMVSKSANY	---	LLYNEYIVY	992
PARP-2	438	ILSHGLRIAP	---	FGKGIYFADMSSKSANY	---	LNYNEYIVY	562
PARP-3	394	ILTSGLRIMP	---	VGKGIYFASENSKSAGY	---	FSQSEYLIY	518
PARP-4	447	ILCRGLLLPK	---	LGSGIYFSDSLSTSIKY	---	FEDDEFVVY	551
PARP-5a	1192	IIHKGFDERH	---	FGAGIYFAENSSKSNQY	---	LAYAEYVIY	1295
PARP-5b	1039	IIHKGFDERH	---	FGAGIYFAENSSKSNQY	---	LAYAEYVIY	1142
PARP-6	483	ILRNGLVNAS	---	YGKGIYLSPISSISFGY	---	KHGNIWVCP	585
PARP-7	542	ICKHNFDPRV	---	FGQGSYFAKKASYSHNF	---	FEPQIFVIF	635
PARP-8	707	ILRNGLVVAS	---	YGSGIYLSPMSSISFGY	---	KHGEIWVVP	809
PARP-10	896	ICAHGFNRSF	---	YGKGVYFARRASLSVQD	---	CQPSIFVIF	991
PARP-11	214	ICIHNFDWRI	---	FGKGTYFARDAAYSSRF	---	WNPKIFVVF	324
PARP-12	574	ICQQNFDWRV	---	YGKGSYFARDAAYSHHY	---	SDPSIFVIF	664
PARP-14	1692	VNRNGFNRSY	---	YGKGTYFAVNANYSAND	---	HHPSLFVAF	1786
PARP-15	569	VNQHGFNRSC	---	YGKGTYFAVDASYSAKD	---	RSPKLFVVF	663
PARP-16	162	IIHNGLHCHL	---	FGEGTYLTSDLSLALIY	---	IPPKYFVVT	258

Figure 1.2. The bump and hole as-PARP/ NAD$^+$ pairs that make the chemical genetic methods possible.

(A) Crystal structure of human PARP-1 bound to the non-hydrolyzable NAD$^+$ analog benzamide adenine dinucleotide (BAD). PDB: 6bhv. The gatekeeper residues are colored to represent the “hole” that is created upon mutation to a smaller residue (Gly or Ala). The gatekeeper residues highlighted include: K903- Hole 1 (cyan) , E988- Hole 2 (magenta), Leu 877- Hole 3 (yellow), Ile 895- Hole 4 (orange). The representative location of NAD$^+$ modifications are indicated by colored circles: green to represent the “bump” and salmon to represent the bioorthogonal handle.

(B) Sequence alignment of catalytically active PARP family members. Chemical genetic strategies have been successfully designed, thus far, for each of the PARPs lists in bold lettering. The gatekeeper residues for all PARPs are highlighted as they align to PARP-1 and the coloring corresponds to figure 2a.

(C) NAD$^+$ analogs used in chemical genetic approaches. Modifications of the nicotinamide and adenosine portions of the molecule are indicated. The coloring of NAD+ modifications corresponds to figure 2a. The molecules shown here collectively represent the bifunctional NAD+ analogs discussed in this review, including: 1) 5-Et-6a-NAD$^+$, 2) 5bn-6a-NAD$^+$, 3) 5bn-2e-NAD$^+$, and 4) 8-Bu(3-yne)T-NAD$^+$

While both utilize a “bump and hole” approach, several key experimental details distinguish the Cohen and Kraus methodologies. First, the Cohen method relies on cellular expression of the as-PARP enzymes, facilitating capture of interactions formed in intact living cells. Cells are then lysed and targets labeled with using an NAD+ analog. This is in contrast to the Kraus strategy, wherein the recombinant as-PARP and NAD$^+$ analog are incubated with cell lysates to label targets. Another major difference between the methods is the placement of the bump and the clickable handle of the NAD$^+$ analog. In the Kraus method, the “bump” and the clickable handle are part of the same C8 substituent on the adenosine ring. This allows for ease of chemical synthesis and thus may perhaps be more broadly accessible to other laboratories choosing to apply the method. The NAD$^+$ molecules developed by the Cohen lab are more challenging to synthesize, given that they involve modification on two portions of the molecule; however, this also provides more chemical space to optimize the fit between the as-PARP and NAD$^+$ analog. Finally, it should be noted that both CG approaches have the potential to affect the activity of a given PARP, as illustrated by separate investigations of PARPs-1 and 2. Whereas the Kraus method of labeling PARPs-1-3 targets maintained PARylation activity, mutations to Hole 1 in the active sites of PARPs-1 and 2 disrupted PARylation activity and turned these PARPs into MARylators[6],[3].

PARP-specific cellular insights gained through chemical genetics

Novel and important discoveries have been made by identifying PARP family specific targets. In depth analysis of the targets identified by each of the as-PARPs thus far confirms prior published reports while also uncovering novel trends.

Using the Cohen method, several targets were identified which fit with the canonical role of PARP-1 in DNA damage repair. Among others; XRCC5 and XRCC6, both DNA damage repair agents, were identified as direct targets of PARP-1 **(Table S1)**[3]**.** One unexpected insight stemming from using the Kraus chemical genetics method on PARP-1, is the discovery of a novel role for PARP-1 in transcription elongation **(Figure 1.3)**[6]**.** PARP-1 was found to PARylate Negative Elongation factors (NELF) A and E of the larger NELF complex, which restricts transcriptional elongation by facilitating the pausing of RNA polymerase II. Mutation of the acidic amino acid sites (Glu/Asp) identified as ADPr sites showed a decreased ability of NELF to bind to RNA, a function critical to the pausing of RNA Pol II. Furthermore,Click-ChIP-seq (a method detailed later in this review) revealed enrichment of PARP-1 PARylation at the promoters of transcriptionally active genes. These results suggested that PARylation of NELF-E by PARP-1 reinforces Pol II pause release, thus facilitating elongation of NELF-regulated genes.

An unexpected result facilitated by chemical genetic studies is the finding that both PARP-7 and PARP-14 MARylate PARP-13[7]. PARP-14 MARylates PARP-13 on acidic amino acid sites (Glu/asp), whereas PARP-7 robustly MARylates PARP-13 on cysteine residues within the zinc finger domain of PARP-13. PARP-13 is a known antiviral protein that binds viral RNA through the zinc finger domains[9]. PARP-7, PARP-13, and PARP-14 have all been shown to play important roles in the viral process. PARP-14, PARP-13, and PARP-7 are all type-I interferon inducible genes, upregulated during the innate immune response to viral infection[10]. PARP-7 has been shown to play both pro-viral and anti-viral roles and regulate the type-I interferon response[11],[12],[13],[14]. PARP-14 has been shown to mitigate proinflammatory IFN- γ activation of human macrophages[15,16]. The observation that PARP-14 and PARP-7 both MARylate PARP-13 lays the groundwork for future studies to assess the role of ADPr in regulating PARP-13 during viral infection. Moreover, CG study of PARP-7 by the Kraus lab revealed a role for PARP-7 in microtubule control in ovarian cancer. Specifically, PARP-7 was found to MARylate α-tubulin and promote microtubule instability **(Figure 1.3).**

Through gene ontology analysis (GO analysis) of the targets identified by as-PARPs, several fascinating trends have been discovered for individual PARP family members. Through bioinformatical analysis of the CG datasets, we have begun to ucover unique roles for each PARP. PARP-11 targets are almost exclusively found at the nuclear membrane, which correlates well with the localization observed for PARP-11 **(Figure 1.3)**[17]. Through the discovery of a PARP-11 specific inhibitor, we know that this localization is dependent on catalytic activity and is highly specific to the nuclear pore[4]. Identification of high-confidence targets at this well-defined location provides insight into the biological role of PARP-11 at the nuclear pore. One validated target identified, NXF1, is a RNA export protein that has been shown to play a role in viral export form the nucleus[18],[19]. PARP-11 has been implicated in the antiviral response and it follows that the antiviral role of PARP-11 may in part be through ADPr of nuclear pore complexes[20].

Other trends that have been discovered for individual PARP family members through GO analysis include: the identification of targets associated with viral processes (PARPs-7, 14, and 2), autophagy (PARP-10), and nuclear and cytoplasmic stress response components identified in almost all PARP target lists **(Figure 1.3)**.

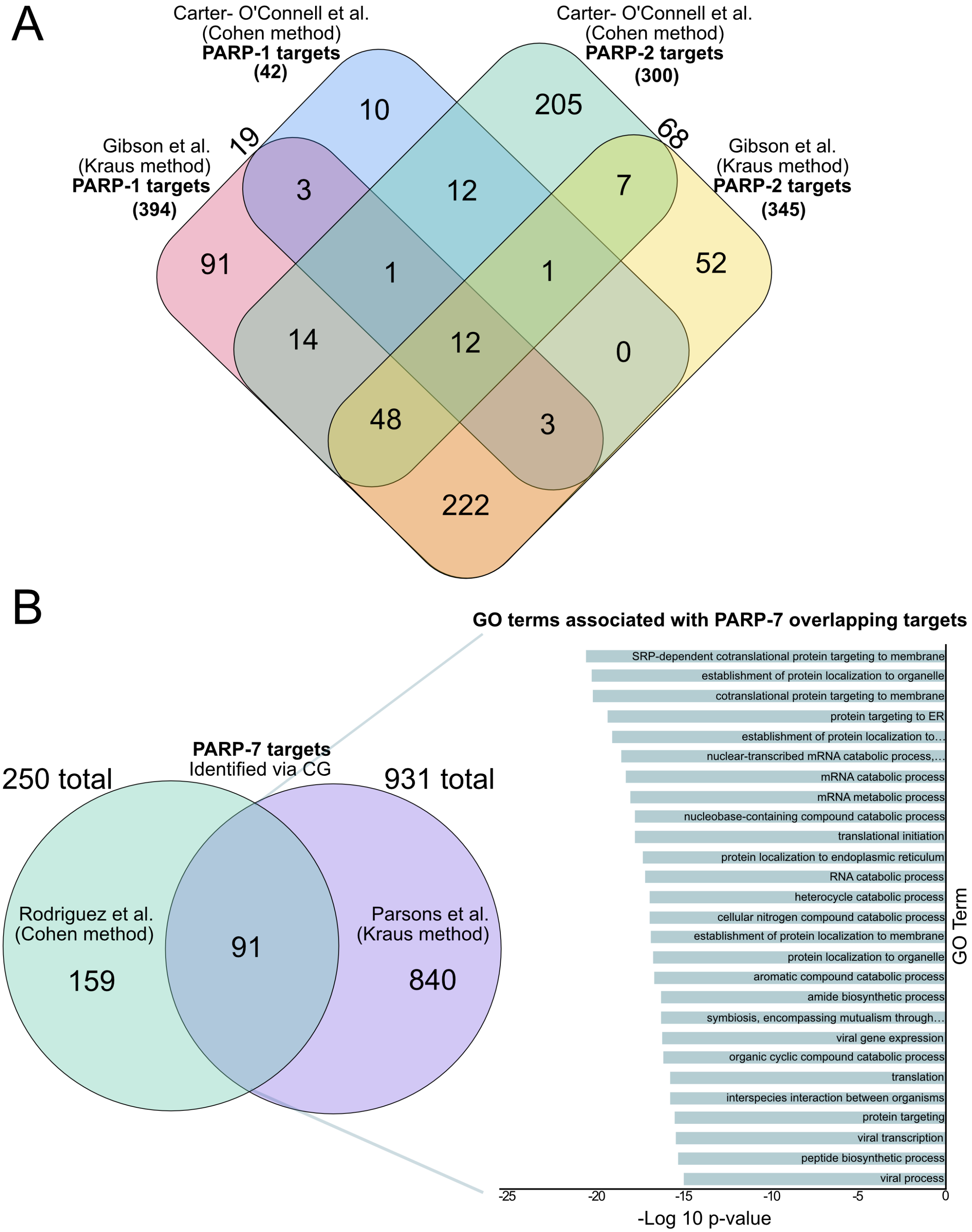
A
Carter- O'Connell et al.
(Cohen method)
PARP-1 targets
(42)
Carter- O'Connell et al.
(Cohen method)
PARP-2 targets
(300)
Gibson et al.
(Kraus method)
PARP-1 targets
(394)
Gibson et al.
(Kraus method)
PARP-2 targets
(345)
19
10
205
68
3
12
7
91
1
1
52
14
12
0
48
3
222
B
GO terms associated with PARP-7 overlapping targets
PARP-7 targets
Identified via CG
250 total
931 total
Rodriguez et al.
(Cohen method)
159
91
Parsons et al.
(Kraus method)
840
SRP-dependent cotranslational protein targeting to membrane
establishment of protein localization to organelle
cotranslational protein targeting to membrane
protein targeting to ER
establishment of protein localization to…
nuclear-transcribed mRNA catabolic process,…
mRNA catabolic process
mRNA metabolic process
nucleobase-containing compound catabolic process
translational initiation
protein localization to endoplasmic reticulum
RNA catabolic process
heterocycle catabolic process
cellular nitrogen compound catabolic process
establishment of protein localization to membrane
protein localization to organelle
aromatic compound catabolic process
amide biosynthetic process
symbiosis, encompassing mutualism through…
viral gene expression
organic cyclic compound catabolic process
translation
interspecies interaction between organisms
protein targeting
viral transcription
peptide biosynthetic process
viral process
GO Term
-25
-20
-15
-10
-5
0
-Log 10 p-value

Figure 1.3. Comparison of targets identified using two separate chemical genetic strategies.

(A) Overlap between PARP-1 and PARP-2 targets identified using as-PARPs engineered using two separate methodologies (Cohen and Kraus methods). There are 19 overlapping targets between the PARP-1 lists and 68 overlapping targets between the PARP-2 lists. Targets that are shared between PARP-1 and PARP-2 are indicated. **(B)** Overlap between PARP-7 targets identified using as-PARPs engineered by two separate methodologies (Cohen and Kraus methods). In this comparison, HEK293T cells were used for the Cohen method and Hela cells were used for the Kraus method. The top 30 corresponding GO analysis terms associated with the overlapping PARP-7 targets are indicated and organized by -Log 10 p-value.

Shared target trends amongst PARP family

There are numerous shared targets between PARP family members and some interesting trends that have emerged from the data. Between the two CG strategies used to identify as-PARP-1 targets (Cohen and Kraus methods), there are 19 overlapping targets, around half of the total targets Identified by the Cohen group **(Figure 1.4 A, Table S2 A)**. GO analysis of these terms shows the most prominent term defined as “gene expression”, which is consistent with the numerous roles of PARP-1 in gene expression found throughout the literature **(Table S2 B)**[21]**.** When the two lists of PARP-2 specific targets are compared, the 68 overlapping targets highlight significant enrichment of RNA metabolism related GO terms **(Figure 1.4 A, Table S3 A, and B)**. Although this term does not describe the bulk of literature on PARP-2, which is focalized around description of its role in the DNA damage response with PARP-1, it does correlate with the interactome described for PARP-2 which strongly enriched for proteins involved in RNA metabolism[22]. Furthermore, PARP-2 contains an SAF-A/B, Acinus, and PIAS (SAP) domain that has been shown to bind rRNA in vitro[23].

Between the two PARP-7 lists created by the separate CG strategies, some of the significant GO terms identified include: SRP dependent protein translocation into the ER, translational initiation, and viral process **(Figure 1.4 B, Table S4A and B).** These terms are supported well by the literature. PARP-7 has been shown to inhibit translation and affect viral replication[14],[12],[13],[11]. The strong overlap between cellular roles established in the literature and GO terms identified in CG studies, support the notion that the targets identified are substantive and relevant.

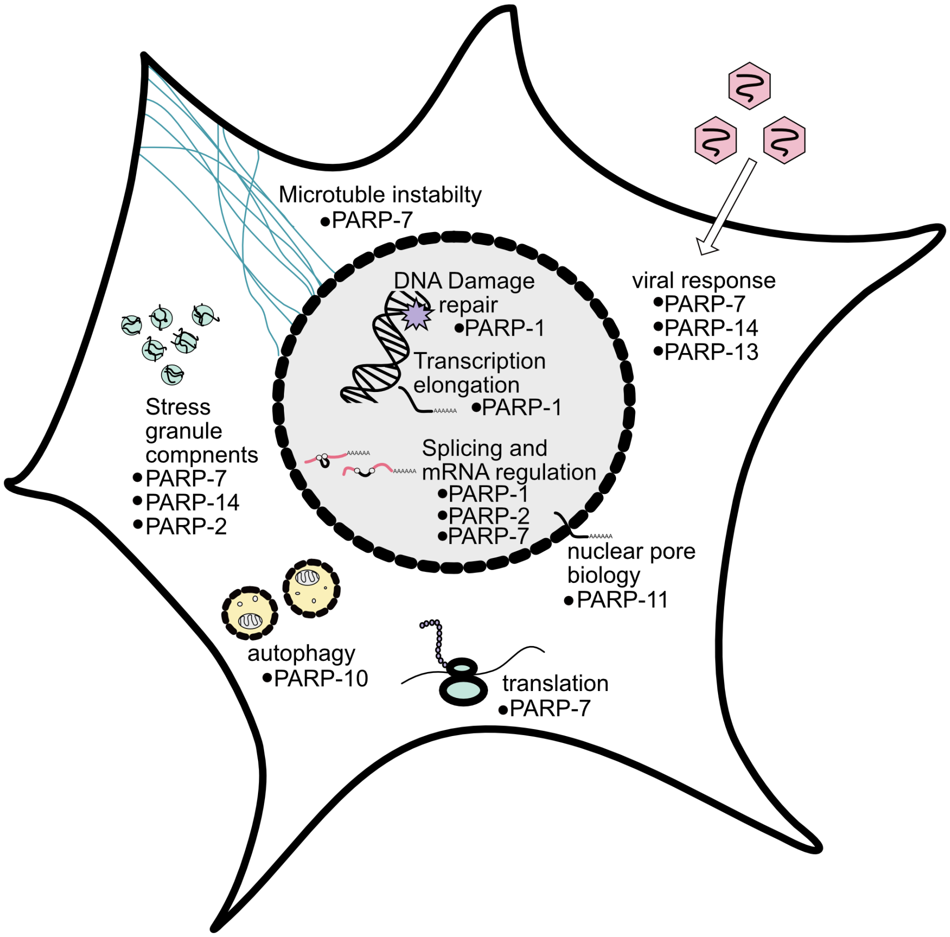

Figure 1.4. Cellular roles of individual PARP family members supported by chemical genetic studies.
Insights from chemical genetics studies and the targets identified, support a number of roles of individual PARP family members. These include but are not limited to: PARP-1- transcription elongation, DNA damage response and RNA regulation; PARP-2- RNA regulation and stress granule component; PARP-7- viral response, translation, microtubule instability, splicing and mRNA regulation and stress granule component; PARP-10- autophagy; PARP-11 nuclear pore biology; PARP-13- (a target of both PARP-7 and PARP-14) viral response; and PARP-14- viral response and stress granule components.

As a whole, one interesting observation is that all lists (except as-PARP-11 targets) include a number of ATP-dependent RNA helicases as targets **(Table S5)**. PARP-13 has been shown to interact with ATP dependent RNA helicase DEAD box-helicase 17 (DDX17) and DEXH-Box helicase 30 (DHX30) [24],[25]. The interaction between DDX17 and PARP-13 facilitates RNA degradation, an important anti-viral process[9],[26]. DDX17 and PARP-13 both show up as targets of PARP-7, PARP-14, and PARP-2. Interestingly these PARPs also have the most targets associates with the GO term “viral process”. Other ATP dependent RNA helicases in the DEAD/DEAH- box family were identified in both CG strategies, suggesting a possible interaction between PARPs and this large family of helicases. These findings have been independently observed by a separate proteomics study of PAR-associated proteins[27].

Another cluster shared between the target lists of PARP family members, is the ADPr of heterogeneous nuclear ribonucleoproteins (hnRNPs). **(Table S6)**. HnRNPs are RNA binding proteins shown to play diverse roles in the processing and regulation of mRNA and gene expression[26]. PARylation of hnRNPs has been shown to modulate the various activities of hnRNP proteins in splicing and RNA translation[28],[29]. PARylation of hnRNPs inhibits RNA-binding ability byhnRNPs, as determined by RNA electrophoretic mobility shift assay (EMSA)[29]. However, previous characterization of the interaction between hnRNPs and PARPs has been limited to studies on the effects of PARP-1 mediated PARylation. Results from CG studies indicate a broader role for the PARP family members in hnRNP-dependent RNA regulation.

Advanced methods used to accompany chemical genetic screens

Several methods have been used in conjunction with chemical genetics to substantiate CG targets and provide a more holistic view of the cellular roles of PARP family members **(Figure 1.5)**. One such method is the BioID approach, in which a protein of interest (a PARP) is fused to a promiscuous biotin ligase (BirA)[30],[31]. Upon cellular culture with biotin, BirA activates biotin to generate a lysine-reactive adenylate-biotin that reacts with proteins proximal to the fusion protein **(Figure 1.5 A)**. As CG methods are not yet able to be used in cell culture and rely on labelling that occurs post-lysis, the BioID approach provides a complimentary approach for identifying interacting proteins in an intracellular context. BioID has been used in partnership with CG methods to identify interactors[29] of PARP-14 and PARP-7[7]. In both studies, there was substantial overlap between PARP-BioID interactors and targets identified via CG methods.

Another approach used to compliment CG proteomics data is the development of a strategy mentioned earlier in this review, Click-ChIP-seq[7]. This method was developed by Gibson et. al to define regions of the genome marked by PARP-1 mediated ADPr.

This strategy relies on the CG method developed for as-PARP-1 utilizing Hole 3 (L877A) and 8-Bu(3-yne)T-NAD$^+$. Instead of enriching for proteins, Click-ChIP-seq enriches for DNA associated with PARP-1 mediated ADPr events **(Figure 1.5 B).** This method was used to correlate regions of the genome undergoing ADPr with classical markers of transcriptionally active genes, including histone H3 lysine 4 trimethylation (H3K4me3) and actively transcribing Pol II.

In addition to these methods, the sites of ADPr on protein targets of PARP-1, 2, 3, and 7 have been identified using the Kraus CG method **(Figure 1.5 C)**[7]. To identify acidic sites of modification (Glu/Asp), targets are first labeled by the as-PARP using 8-Bu(3-yne)T-NAD$^+$. Following enrichment of the ADPr targets, the proteins attached to the enrichment matrix then undergo tryptic digest to leave only the ADPr-peptide attached to the beads. This last peptide is then cleaved using hydroxylamine (NH_2OH) which leaves a +15.0109 marker on the ADPr site that can be recognized by mass spectrometry. A limitation with this method is that it can only identify sites of modification on acidic amino acids (glu/asp). Over the past few years, it has become evident that Glu/Asp sites are not the only sites modified by PARP family members[32],[33],[34]. This is particularly evident for PARPs-1 and 7 which have been shown to modify serine (PARP-1)[35],[36],[37],[38] and cysteine (PARP-7) residues[34].

In order to look at amino acid sites beyond acidic amino acids modified by PARP-7, a separate mass spectrometry approach was taken. This strategy, developed by Nielsen and colleagues, involves the enrichment of ADPr peptides using the macrodomain Af1521, which binds to ADPr-modified peptides[39],[38]. Enriched peptides are subjected to MS analysis using electron-transfer higher-energy collisional dissociation (EThcD) **(Figure 1.5 D)**. This fragmentation technique localizes ADPr to any amino acid acceptor with high confidence. Using this highly sensitive technique, sites of ADPr modification were identified on a proteome-wide scale in the presence and absence of PARP-7. The resulting data showed strong overlap in targets identified by CG and provided clear evidence that cysteine sites are the predominant sites of PARP-7 modification.

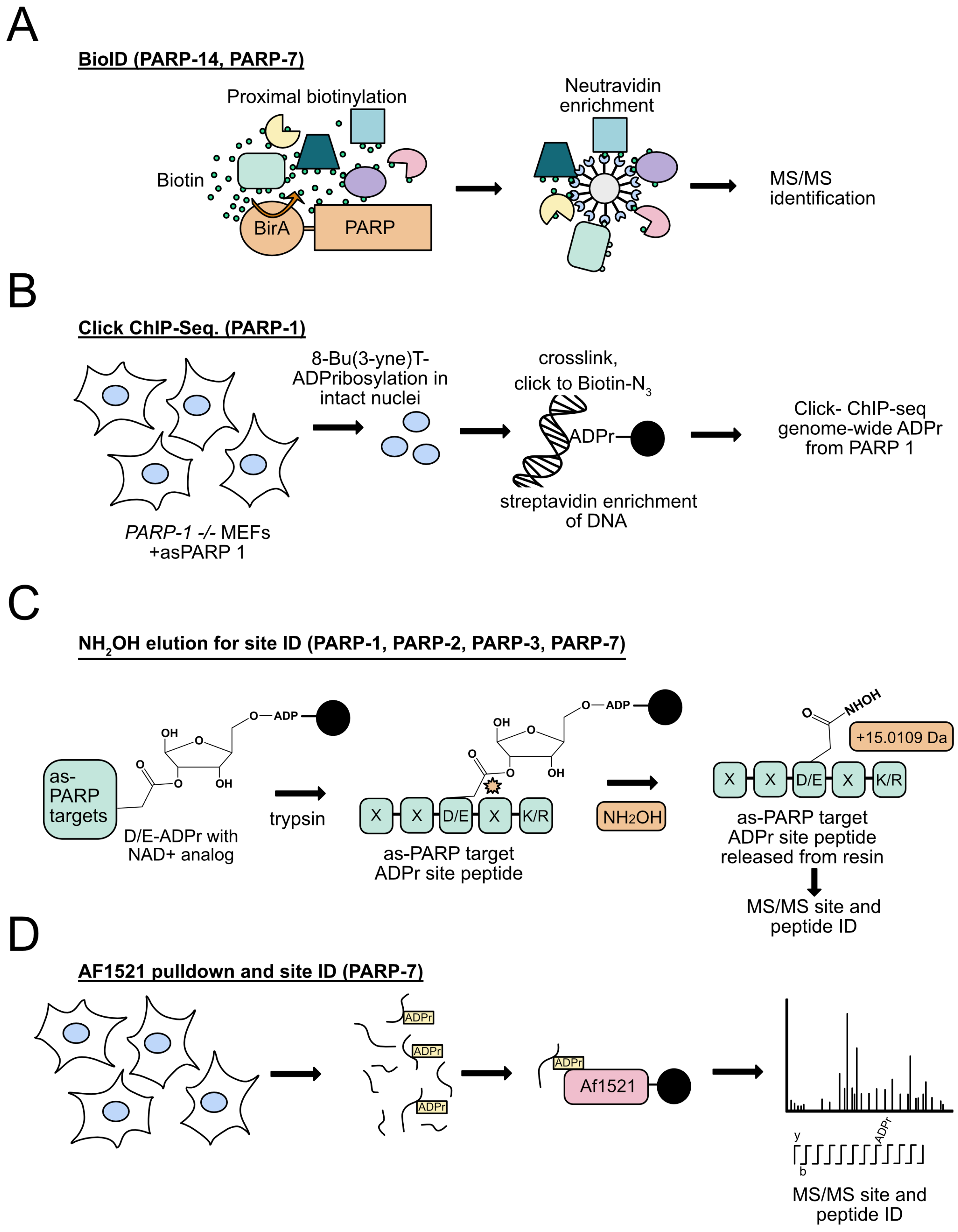

Figure1.5. Methods used to accompany chemical genetic methods

(A) Schematic of proximity labeling approach known as BioID

(B) Schematic of Click-ChIP-seq
(C) Schematic of Site ID using hydroxylamine
(D) Schematic of AF1521 pulldown and site ID using EThcD mass spectrometry

Concluding remarks and future perspectives

There are several improvements that can be made to the methodology to provide more detailed information about PARP specific roles. As new data emerges about the roles of individual PARP family members, future experiments should focus on identifying targets under specific contexts in relevant cellular conditions. The first step towards a deeper understanding of context specific roles of PARPs is to develop a CG strategy that can be used in living cells. Recent work from Bertozzi and colleagues points to a potential method for cellular identification through their efforts to identify glycosyl transferase targets in living cells[40]. This was made possible through the development of cell permeable precursors of “bumped” UDP-GalNAc, which upon entrance into cells is converted into a functional “bumped” UDP-GalNAc analog. This analog is capable of being used by an analog sensitized glycosyl transferase. Cell permeability of the “bumped” UDP-GalNAc precursor was accomplished by protecting the negatively charged phosphate groups with S-acetyl-2-thioethyl (SATE) groups to facilitate their delivery into cells. This methodology could in theory be applied to NAD^+ analogs to protect the phosphate groups and facilitate their delivery into cells. Cell permeable “bumped” NAD^+ analogs would facilitate temporal resolution of ADPr events mediated by an individual PARP family member in a context dependent manor. For example, cancer lines where PARPs are upregulated could be used, cells infected with virus, or cells under a particular type of stress.

CG strategies developed to identify PARP family specific targets have taught us that PARP family members appear to have both specific and shared cellular roles. However, the hypothesis generating information provided by CG studies is just the beginning. There is still plenty of work to be done to elucidate PARP specific mechanisms and the role of ADPr on the targets identified using these powerful proteomics methods.

All table supplements can be found using this link to a box folder under Chapter 1. The tables are not clear when the file is viewed in box, instead I suggest the full excel files be downloaded and viewed in excel. If you are unable to access these files please contact kelsiemrodriguez@gmail.com.

https://ohsu.box.com/s/09spflrl3kpri6xgwkueci0rlpmtk534

References

1. Gupte, R., Liu, Z. & Kraus, W. L. Parps and adp-ribosylation: Recent advances linking molecular functions to biological outcomes. *Genes Dev.* **31**, 101–126 (2017).
2. Vyas, S. *et al.* Family-wide analysis of poly(ADP-ribose) polymerase activity. *Nat. Commun.* **5**, (2014).
3. Carter-O'Connell, I., Jin, H., Morgan, R. K., David, L. L. & Cohen, M. S.

Engineering the substrate specificity of ADP-ribosyltransferases for identifying direct protein targets. *J. Am. Chem. Soc.* **136**, 5201–5204 (2014).

4. Carter-O’Connell, I. *et al.* Identifying Family-Member-Specific Targets of Mono-ARTDs by Using a Chemical Genetics Approach. *Cell Rep.* 1–11 (2015). doi:10.1016/j.celrep.2015.12.045
5. Carter-O’Connell, I. & Cohen, M. S. Identifying Direct Protein Targets of Poly-ADP-Ribose Polymerases (PARPs) Using Engineered PARP Variants-Orthogonal Nicotinamide Adenine Dinucleotide (NAD+) Analog Pairs. *Curr. Protoc. Chem. Biol.* **7**, 121–139 (2015).
6. Gibson, B. A. *et al.* Chemical genetic discovery of PARP targets reveals a role for PARP-1 in transcription elongation. *Science (80-.).* **353**, 45–50 (2016).
7. Carter-O’Connell, I. *et al.* Combining Chemical Genetics with Proximity-Dependent Labeling Reveals Cellular Targets of Poly(ADP-ribose) Polymerase 14 (PARP14). *ACS Chem. Biol.* **13**, 2841–2848 (2018).
8. Liang, L. & Astruc, D. The copper(I)-catalyzed alkyne-azide cycloaddition (CuAAC) “click” reaction and its applications. An overview. *Coord. Chem. Rev.* **255**, 2933–2945 (2011).
9. Todorova, T., Bock, F. J. & Chang, P. Poly(ADP-ribose) polymerase-13 and RNA regulation in immunity and cancer. *Trends Mol. Med.* **21**, 373–384 (2015).
10. Fehr, A. R. *et al.* The impact of PARPs and ADP-ribosylation on inflammation and host-pathogen interactions. *Genes Dev.* **34**, 341–359 (2020).
11. Atasheva, S., Frolova, E. I. & Frolov, I. Inhibitors of Cellular Translation and Virus Replication. **88**, 2116–2130 (2014).

12. Grunewald, M. E., Shaban, M. G., Mackin, S. R., Fehr, A. R. & Perlman, S. crossm Murine Coronavirus Infection Activates the Aryl Hydrocarbon TCDD-Inducible-PARP Expression. **94**, 1–17 (2020).

13. Kozaki, T. *et al.* Mitochondrial damage elicits a TCDD-inducible poly(ADP-ribose) polymerase-mediated antiviral response. *Proc. Natl. Acad. Sci.* **114**, 2681–2686 (2017).

14. Yamada, T. *et al.* Constitutive aryl hydrocarbon receptor signaling constrains type I interferon–mediated antiviral innate defense. *Nat. Immunol.* **17**, 687 (2016).

15. Iwata, H. *et al.* PARP9 and PARP14 cross-regulate macrophage activation via STAT1 ADP-ribosylation. *Nat. Commun.* **7**, 12849 (2016).

16. Caprara, G. *et al.* PARP14 Controls the Nuclear Accumulation of a Subset of Type I IFN–Inducible Proteins. *J. Immunol.* **200**, 2439 LP – 2454 (2018).

17. Meyer-Ficca, M. L. *et al.* Spermatid head elongation with normal nuclear shaping requires ADP-ribosyltransferase PARP11 (ARTD11) in mice. *Biol. Reprod.* **92**, 80 (2015).

18. Griffis, E. R., Xu, S. & Powers, M. A. Nup98 localizes to both nuclear and cytoplasmic sides of the nuclear pore and binds to two distinct nucleoporin subcomplexes. *Mol. Biol. Cell* **14**, 600–610 (2003).

19. Ramsinghani, S. *et al.* Syntheses of photoactive analogues of adenosine diphosphate (hydroxymethyl)pyrrolidinediol and photoaffinity labeling of poly(ADP-ribose) glycohydrolase. *Biochemistry* **37**, 7801–7812 (1998).

20. Guo, T. *et al.* ADP-ribosyltransferase PARP11 modulates the interferon antiviral response by mono-ADP-ribosylating the ubiquitin E3 ligase β-TrCP. *Nat.*

Microbiol. **4**, 1872–1884 (2019).

21. Kraus, W. L. & Hottiger, M. O. PARP-1 and gene regulation: progress and puzzles. *Mol. Aspects Med.* **34**, 1109–1123 (2013).

22. Isabelle, M. *et al.* Investigation of PARP-1, PARP-2, and PARG interactomes by affinity-purification mass spectrometry. *Proteome Sci.* **8**, 22 (2010).

23. Léger, K., Bär, D., Savić, N., Santoro, R. & Hottiger, M. O. ARTD2 activity is stimulated by RNA. *Nucleic Acids Res.* **42**, 5072–5082 (2014).

24. Chen, G., Guo, X., Lv, F., Xu, Y. & Gao, G. p72 DEAD box RNA helicase is required for optimal function of the zinc-finger antiviral protein. *Proc. Natl. Acad. Sci. U. S. A.* **105**, 4352–4357 (2008).

25. Ye, P., Liu, S., Zhu, Y., Chen, G. & Gao, G. DEXH-Box protein DHX30 is required for optimal function of the zinc-finger antiviral protein. *Protein Cell* **1**, 956–964 (2010).

26. Zhu, Y. *et al.* Zinc-finger antiviral protein inhibits HIV-1 infection by selectively targeting multiply spliced viral mRNAs for degradation. *Proc. Natl. Acad. Sci.* **108**, 15834 LP – 15839 (2011).

27. Gagné, J.-P. *et al.* Proteome-wide identification of poly(ADP-ribose) binding proteins and poly(ADP-ribose)-associated protein complexes. *Nucleic Acids Res.* **36**, 6959–6976 (2008).

28. Ji, Y. & Tulin, A. V. Post-transcriptional regulation by poly(ADP-ribosyl)ation of the RNA-binding proteins. *Int. J. Mol. Sci.* **14**, 16168–16183 (2013).

29. Ji, Y. & Tulin, A. V. Poly(ADP-ribosyl)ation of heterogeneous nuclear ribonucleoproteins modulates splicing. *Nucleic Acids Res.* **37**, 3501–3513 (2009).

30. Roux, K. J., Kim, D. I. & Burke, B. BioID: A screen for protein-protein interactions. *Curr. Protoc. Protein Sci.* **2013**, 19.23.1-19.23.14 (2013).

31. Roux, K. J., Kim, D. I., Raida, M. & Burke, B. A promiscuous biotin ligase fusion protein identifies proximal and interacting proteins in mammalian cells. *J. Cell Biol.* **196**, 801–810 (2012).

32. Cohen, M. S. & Chang, P. Insights into the biogenesis, function, and regulation of ADP-ribosylation. *Nat. Chem. Biol.* **14**, 236–243 (2018).

33. Daniels, C. M., Ong, S. E. & Leung, A. K. L. Phosphoproteomic approach to characterize protein mono- and poly(ADP-ribosyl)ation sites from cells. *J. Proteome Res.* **13**, 3510–3522 (2014).

34. Gomez, A. *et al.* Characterization of TCDD-inducible poly-ADP-ribose polymerase (TIPARP/ARTD14) catalytic activity. *Biochem. J.* **475**, 3827–3846 (2018).

35. Palazzo, L. *et al.* Serine is the major residue for ADP-ribosylation upon DNA damage. *Elife* **7**, 1–12 (2018).

36. Leidecker, O. *et al.* Serine is a new target residue for endogenous ADP-ribosylation on histones. *Nat. Chem. Biol.* **12**, 998–1000 (2016).

37. Fontana, P. *et al.* Serine ADP-ribosylation reversal by the hydrolase ARH3. *Elife* **6**, 1–20 (2017).

38. Larsen, S. C., Hendriks, I. A., Lyon, D., Jensen, L. J. & Nielsen, M. L. Systems-wide Analysis of Serine ADP-Ribosylation Reveals Widespread Occurrence and Site-Specific Overlap with Phosphorylation. *Cell Rep.* **24**, 2493-2505.e4 (2018).

39. Hendriks, I. A., Larsen, S. C. & Nielsen, M. L. An advanced strategy for comprehensive profiling of ADP-ribosylation sites using mass spectrometry-based

proteomics. *Mol. Cell. Proteomics* **18**, 1010–1024 (2019).

40. Schumann, B. *et al.* Bump-and-Hole Engineering Identifies Specific Substrates of Glycosyltransferases in Living Cells. *Mol. Cell* **78**, 824-834.e15 (2020).

Chapter 2.

Chemical genetics and proteome-wide site mapping reveal cysteine MARylation by PARP-7 on immune-relevant protein targets

Kelsie M. Rodriguez, Sara C. Buch-Larsen, Ilsa T. Kirby, Ivan Rodriguez Siordia, David Hutin, Marit Rasmussen, Denis M. Grant, Larry L. David, Jason Matthews, Michael L. Nielsen, and Michael S. Cohen

Portions of this chapter were originally published as part of: Rodriguez, K. M. *et al.* Chemical genetics and proteome-wide site mapping reveal cysteine MARylation by PARP-7 on immune-relevant protein targets. *Elife* **10**, e60480 (2021).

The manuscript has been adapted for this dissertation.

Author contributions

K.M.R. and M.S.C. designed the experiments. Most of the experiments presented were conducted by K.M.R. EThcD fragmentation MS and subsequent analysis for site identification was performed by S.C.B.L under the supervision of M.L.N. LC-MS/MS setup for CG and BioID experiments was performed by L.L.D in the OHSU proteomics core. Recombinant proteins were prepared by I.R.S and subsequent experiments using these proteins were also carried out by I.R.S. Creation and Characterization of novel PARP-7 antibody was performed by D.H., M.R., and D.M.G., under the supervision of J.M. Synthesis of Phthal01 and generation of *in vitro* IC_{50} data against the PARP family was performed and collected by I.T.K. The manuscript was written by K.M.R. and M.S.C. with contributions from all other authors.

Acknowledgments

We thank John Klimek and Philip Wilmarth for assistance with the CG and BioID MS analysis at the OHSU proteomics core. Mass spectrometry analysis performed by the OHSU Proteomics Shared Resource was partially supported by NIH grants P30EY010572, P30CA069533, and S10OD012246. We thank current and past members of the Cohen lab for many fruitful discussions regarding the experimental design, data analysis, and the preparation of the manuscript. We thank Jonas Damgaard Elsborg for writing the python script used for generation of background sequences for motif analyses, and Ivo Alexander Hendriks for fruitful discussions and help with data analysis of EThcD MS data. We thank Prof. W. Lee Kraus for sharing their PARP-7 chemical genetic studies prior to publication. We thank Prof. Michael O.

Hottiger for the PARG plasmid. We thank Prof. Ian Carter-O’Connell for the SUMO-PARP-13.2 plasmid. This work was funded by the NIH (NIH 2R01NS088629) and the Pew Foundation to M.S.C.

Abstract

Poly(ADP-ribose) polymerase 7 (PARP-7) has emerged as a critically important member of a large enzyme family that catalyzes ADP-ribosylation in mammalian cells. PARP-7 is a critical regulator of the innate immune response. What remains unclear is the mechanism by which PARP-7 regulates this process, namely because the protein targets of PARP-7 mono-ADP-ribosylation (MARylation) are largely unknown. Here, we combine chemical genetics, proximity labeling, and proteome-wide amino acid ADP-ribosylation site profiling for identifying the direct targets and sites of PARP-7-mediated MARylation in a cellular context. We found that the inactive PARP family member, PARP-13—a critical regulator of the antiviral innate immune response—is a major target of PARP-7. PARP-13 is preferentially MARylated on cysteine residues in its RNA binding zinc finger domain. Proteome-wide ADP-ribosylation analysis reveals cysteine as a major MARylation acceptor of PARP-7. This study provides insight into PARP-7 targeting and MARylation site preference.

Introduction

Poly-ADP-ribose-polymerases (PARPs) are a family of 17 proteins, many of which have emerged as critical regulators of cytokine signaling and innate immunity[1].

Most PARP family members catalyze the transfer of a single unit of ADP-ribose from nicotinamide adenine dinucleotide (NAD^+) to amino acids on protein targets, a reversible post-translational modification (PTM) known as mono-ADP-ribosylation (MARylation)[2]. Unlike other well-studied PTMs, such as phosphorylation or ubiquitylation, how PARP-mediated MARylation regulates protein function is still poorly understood.

Multiple independent lines of evidence point to PARP-7 playing a critical role in the innate immune signaling pathway, particularly as a negative regulator of the type I interferon antiviral response. Knockout of PARP-7 enhances nucleic acid sensor agonist- or virus-induced interferon-beta (IFN-β) expression in various cell types[3,4]. Given the antiviral functions of IFN-β, increases in IFN-β are expected to suppress viral replication. Consistent with this notion, viral titers after infection with several single-strand RNA viruses, including influenza, vesicular stomatitis virus, encephalomyocarditis virus, and mouse hepatitis virus (a murine coronavirus), are lower in PARP-7 knockout or knockdown cells compared to wild-type cells[3,5]. These results show that PARP-7 facilitates viral replication, in part, by shutting down IFN-β production. How PARP-7-mediated MARylation regulates IFN-β production, and perhaps other aspects of innate immune signaling, is unknown. This is largely because few direct MARylation targets of PARP-7 are known.

A unique feature of MARylation compared to other PTMs is that chemically diverse amino acids can act as ADP-ribose (ADPr) acceptors[6]. Historically, the chemical nature of the amino acid-MAR bonds in proteins was examined by chemical stability studies[7,8,9,10,11]. This led to the notion that the major ADPr acceptor residues are the acidic amino acids, glutamate (Glu) and aspartate (Asp), as well as the basic amino acid arginine (Arg). More recently, however, mass spectrometry-based proteomics has revealed that in addition to Glu/Asp and Arg, serine (Ser), tyrosine (Tyr), histidine (His), and cysteine (Cys) can also act as ADPr acceptors[12,13,14,15,16]. While many residues can act as ADPr acceptors, a major outstanding question in the field is whether or not individual PARP family members demonstrate selectivity toward ADP-ribosylation of specific residues in protein targets. Identifying the MARylated residues in protein targets is essential for understanding how ADPr modifications regulate protein function.

In this study, we combine chemical genetics, proximity labeling, and proteome-wide amino acid ADPr site profiling for identifying the direct targets and sites of PARP-7-mediated MARylation. Our study reveals that PARP-7 MARylates proteins in innate immune signaling and viral regulation. Additionally, we show that Cys MARylation in cells is more stable than Glu/Asp MARylation, suggesting that the site of MARylation in protein targets governs signal duration.

Results

Optimization of a chemical genetic strategy for identifying the direct targets of PARP-7

Identifying the protein targets of PARP-7 is a critical first step toward unraveling its function in cells. In previous work we have developed an engineered enzyme—

modified substrate strategy for identifying relevant targets of individual PARP family members[17,18,19,20]. This chemical genetic (CG) method uses engineered PARPs and an orthogonal NAD$^+$ analogue that contains a clickable handle (e.g. an alkyne) that is located at the N-6 position of the adenine ring (5-Bn-6-a-NAD$^+$). We showed that 5-Bn-6-a-NAD$^+$ is an excellent substrate for engineered PARPs in which a hydrophobic amino acid (isoleucine or leucine) at the floor position (so named because it sits at the floor of the nicotinamide subsite in the NAD$^+$ binding pocket) is mutated to a glycine. Importantly, 5-Bn-6-a-NAD$^+$ is not used by wild-type (WT) PARPs and in this way is orthogonal to native NAD$^+$. While 5-Bn-6-a-NAD$^+$ is a very good substrate for many floor position engineered PARPs (e.g. L1782G, LG-PARP-14), we found that it is a poor substrate for several other floor position PARP mutants, including PARP-7. We therefore sought a new orthogonal NAD$^+$ analogue that would serve as an efficient substrate for floor position engineered PARP-7, I631G PARP-7 (IG-PARP-7) **(Figure 2.1a).**

We focused our efforts on changing the position of the clickable handle. Recently, Pascal and colleagues reported a crystal structure of a non-hydrolyzable analogue of NAD$^+$, benzamide adenine dinucleotide (BAD), bound to PARP-1[21]. This is the first crystal structure of a PARP bound to an NAD$^+$ biomimetic and it shows how the adenine ring of NAD$^+$ binds in the NAD$^+$-binding pocket. Based on this structure, it is evident that the C-2 position of the adenine ring of BAD is more solvent exposed than the N-6 position of the adenine ring **(Figure 2.1b).** Indeed, work from Marx and colleagues showed that C-2 modified NAD$^+$ analogues were better PARP1 substrates than N-6 modified NAD^+ analogues [22]. Given the high degree of conservation in the NAD^+-binding pocket between PARP family members, we hypothesized that placing the clickable handle at the C-2 rather the N-6 position of 5-Bn-NAD^+ would yield a better substrate for IG-PARP-7. We therefore designed and synthesized 5-Bn-2-e-NAD^+, which has an ethynyl group at the C-2 position for Cu(I)-catalyzed Huisgen chemistry with an azide reporter **(Figure 2.1c and Scheme 2.1)**

Compared to 5-Bn-6-a-NAD^+, we found that 5-Bn-2-e-NAD^+ is a much better substrate for GFP-IG-PARP-7 as evidenced by the greater labeling (biotin signal following click conjugation to biotin-azide) of GFP-tagged IG-PARP-7 (GFP-IG-PARP-7) (auto-MARylation) as well as the labeling of many other discrete bands (trans-MARylation) in HEK 293T cell lysates **(Figure 2.1d).** Importantly, we did not detect labeling of GFP-WT-PARP-7, indicating that 5-Bn-2-e-NAD^+ is not a substrate for GFP-WT-PARP-7 **(Figure 2.1d).**

We next sought to identify the targets of PARP-7 using GFP-IG-PARP-7 and its optimized substrate, 5-Bn-2-e-NAD^+. Following incubation of HEK 293T lysates with 5-Bn-2-e-NAD^+ and subsequent conjugation with biotin-azide, we enriched biotinylated proteins (e.g. MARylation targets) using NeutrAvidin agarose **(Figure Supplement 2.1a).** We then proteolyzed enriched proteins and eluted peptides were subjected to tandem mass spectrometry (LC-MS/MS). We identified a total of 250 direct targets of PARP-7, many of which are RNA binding and RNA regulatory proteins **(Table Supplement 1).**

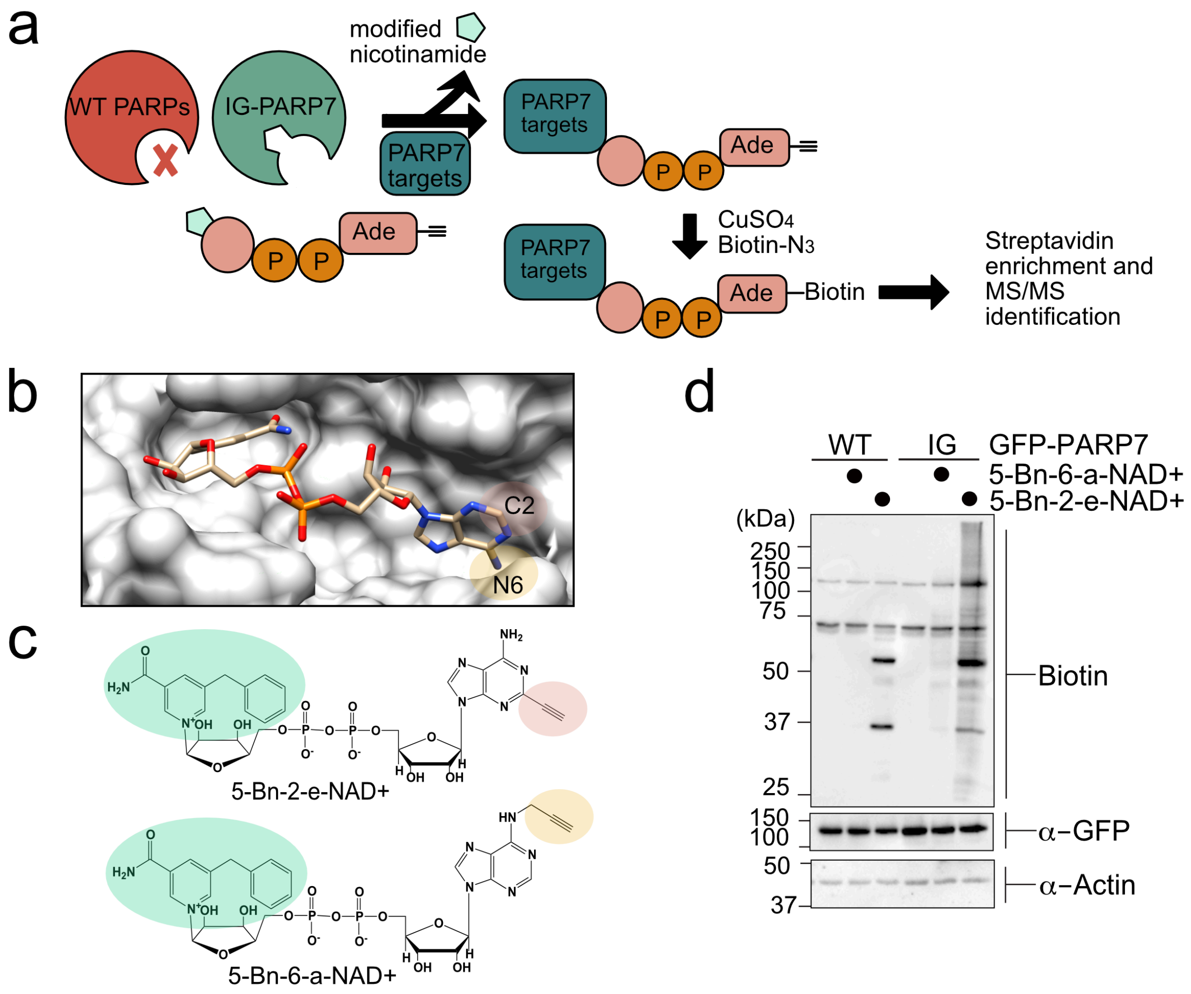

Figure 2.1. A chemical genetic strategy for identifying the direct MARylation targets of PARP-7.

(a) Schematic of chemical genetic approach for identifying direct targets of PARP-7.

(b) Crystal structure of human PARP1 bound to the non-hydrolyzable NAD$^+$ analog benzamide adenine dinucleotide (BAD). PDB: 6bhv. The structure shows that the C-2 position of BAD is pointed out of the ADP-ribose pocket.

(c) Chemical structure of the clickable, orthogonal NAD$^+$ analogs. 5-Bn-2-e-NAD$^+$ is the optimized substrate for the floor position engineered PARP-7, IG-PARP-7. 5-Bn-6-a-NAD$^+$ was used in our previous studies by other floor position engineered PARPs (e.g. PARP14).

(d) 5-Bn-2-e-NAD$^+$ is an efficient substrate for IG-PARP-7. HEK293T cells were transfected with either GFP-WT-PARP-7 (control) or GFP-IG-PARP-7. Cell lysates were prepared and incubated with either 5-Bn-2-e-NAD$^+$ or 5-Bn-6-a-NAD$^+$ (100µM). Following copper-catalyzed click chemistry with biotin-azide, proteins were resolved by SDS-PAGE and biotinylated proteins were detected by Western blot detection using Streptavidin-HRP. Biotinylated proteins represent direct MARylation targets of PARP-7.

Identification of the PARP-7 interactome using BioID proximity labeling

To obtain a more holistic view of PARP-7 function in cells we used a proximity labeling approach—commonly referred to as BioID—for identifying intracellular PARP-7 interactors **(Figure Supplement 2.2).** In the BioID approach, a protein of interest is fused to a promiscuous biotin ligase (BirA*)[23,24]. Upon addition of biotin to cultured cells, BirA* uses biotin as a substrate to generate a lysine-reactive adenylate-biotin that reacts with proteins proximal to the fusion protein. In this way, intracellular interactors can be identified. We generated a WT PARP-7 chimeric construct in which a Myc-tagged promiscuous biotin ligase (BirA*) was fused to the N-terminus of PARP-7 (Myc-BirA*-WT-PARP-7). We observed robust biotinylation of proteins across the full molecular weight range in HEK 293T cells expressing Myc-BirA*-WT-PARP-7, but not GFP-WT-PARP-7 **(Figure Supplement 2.2).** Biotinylated proteins were enriched using NeutrAvidin agarose **(Figure Supplement 2.2).** In the Myc-BirA*-PARP-7 NeutrAvidin pulldown sample we found an enrichment of auto-MARylated Myc-BirA*-PARP-7 as well as trans-MARylated proteins, demonstrating that Myc-BirA*-PARP-7 is catalytically active and that MARylated targets are enriched **(Figure Supplement 2.2).** Enriched proteins were proteolyzed, and eluted peptides were subjected to LC-MS/MS. We identified a total of 189 interacting proteins of PARP-7 **(Table Supplement 2).** We found that a subset of these PARP-7 interactors overlapped with targets identified using our CG approach **(Figure 2.2a),** suggesting that these interactors could be intracellular MARylation targets of PARP-7.

Gene ontology enrichment analysis of PARP-7 targets

To gain insight into the cellular functions of PARP-7, we performed gene ontology (GO) analysis using both the direct MARylation targets (CG approach) and the intracellular PARP-7 interactors (BioID approach). We performed GO biological process term enrichment using PANTHER and visualized terms using ReviGO **(Figure 2.2b).** We found a significant enrichment of terms related to viral processes, RNA regulation, and the innate immune response **(Figure 2.2b and Table Supplement 3).** The enrichment of these terms is consistent with the known role of PARP-7 in the regulation of the innate immune response during viral infection[3,4,5].

We also performed protein-protein interaction (PPI) analysis using the list of MARylation targets and intracellular interactors of PARP-7 using the Metascape tool [25]. To identify densely connected PPI network components, the Molecular Complex Detection (MCODE) algorithm was applied to the Uniprot IDs of all the proteins within our CG and BioID lists. These protein networks show clusters of interactions most abundantly related to mRNA translational silencing, mRNA splicing and metabolism, protein folding and localization to Cajal bodies **(Figure 2.2c and Table Supplement 4).** Taken together, these analyses support the notion that PARP-7 regulates various aspects of RNA regulation, including regulation of RNA localization, RNA splicing, and mRNA translation.

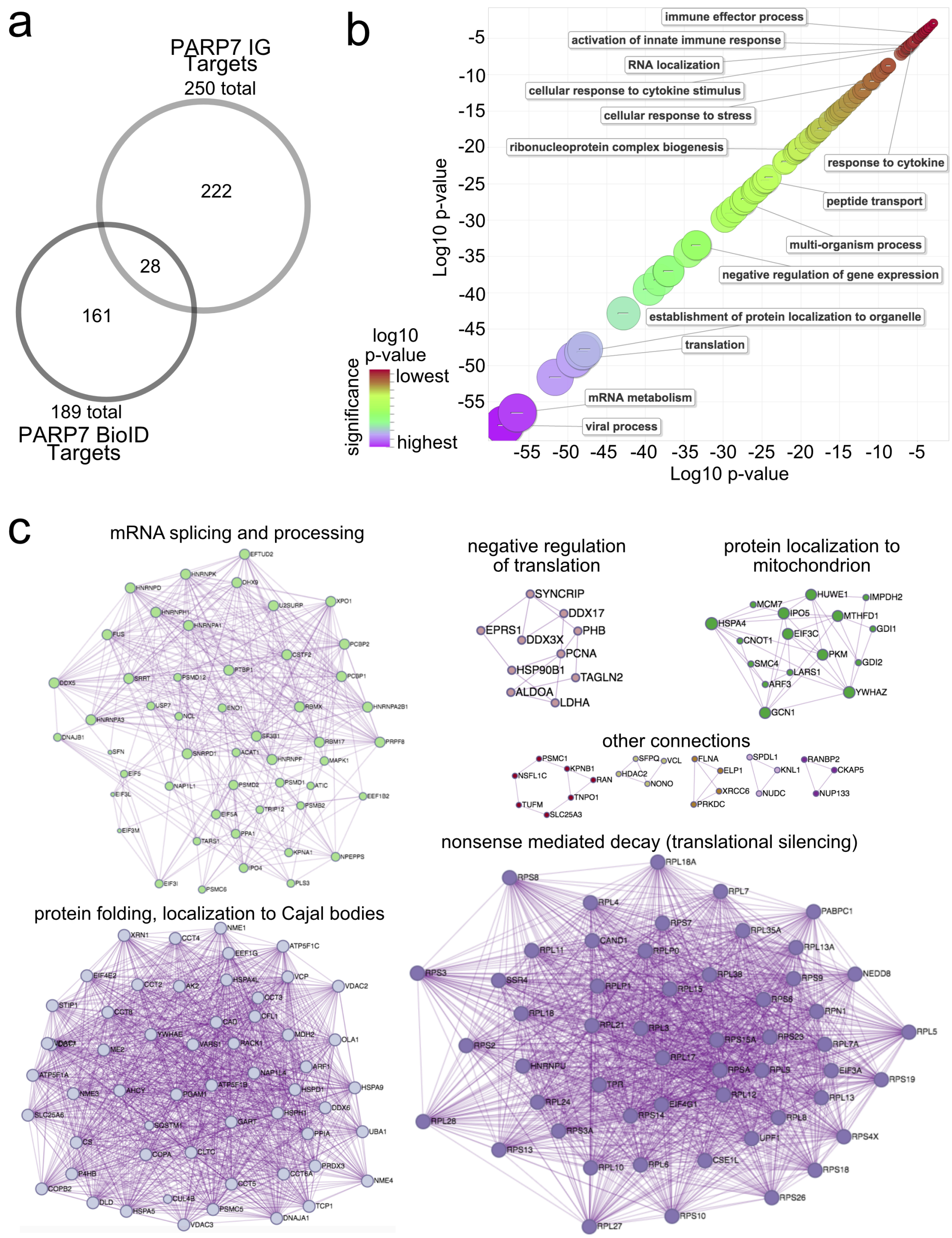

Figure 2.2. **Gene ontology analysis of PARP-7 MARylation targets and interactors reveals roles in innate immune signaling and RNA regulation.**
(a) Venn diagram comparing the 252 total PARP-7 targets identified by LC-MS/MS runs in comparison to the 181 PARP-7 interacting proteins identified using Myc-BirA–PARP-7. Data shown are the additive combined targets of two biological replicates for each type of strategy.
(b) Scatterplot depicting enriched gene ontology (GO) terms attached to the 439 total PARP-7 MARylation targets (chemical genetics) and PARP-7 interactors (BioID proximity labeling). GO term enrichment was performed using the PANTHER toolkit. Significantly enriched GO terms ($p < 0.05$) were condensed using ReviGO and similar terms were nested based on similarity. Terms are organized by $-\log10$(p-value). Significance ranges from -58.2 (most significant) to -2.8 (least significant). Selected terms are indicated.
(c) "Protein-protein Interaction Enrichment Analysis" of the 439 total PARP-7 MARylation targets and PARP-7 interactors. Images were created using Metascape.org. The Molecular Complex Detection (MCODE) algorithm has been applied to identify densely connected network components. The MCODE networks identified for individual gene lists have been gathered and are shown here.

Validation of PARP-13 as a target of PARP-7 in cells

We next sought to validate candidate proteins as MARylation targets of PARP-7 in intact cells. We focused our attention on PARP-13 (also known as ZAP and ZC3HAV1) as it was a top candidate in both proteomics datasets **(Table Supplement 1,2)** and because it is a well-known RNA binding protein[26,27]. PARP-13 is unique among PARP family members for two main reasons: i. it exists as two major isoforms, the full-length protein known as PARP-13.1 (ZAPL) and truncated variant known as PARP-13.2 (ZAPS) that is devoid of the catalytic domain, and ii. despite having the catalytic domain, PARP-13.1 is catalytically inactive. PARP-13.1 is constitutively expressed in most cells and PARP-13.2 is induced by interferons (e.g. IFN-β) as well as viral infection[28]. In HEK 293T cells, PARP-13.1 and PARP-13.2 are expressed, but PARP-13.1 is the major isoform[29]. Indeed, we confirmed that PARP-13.1 is the major endogenous isoform that interacts with Myc-BirA*-PARP-7 in HEK 293T cells **(Figure 2.3a).** Similar to PARP-7, both isoforms of PARP-13 are important regulators of innate immunity and the response to viral infection. This functional connection motivated us to determine if both PARP-13.1 and PARP-13.2 are intracellular targets of PARP-7.

To determine if PARP-13.1 and PARP-13.2 are MARylated by PARP-7 in cells, we co-expressed GFP-PARP-7 with MycX2- or HA-tagged PARP-13.1 or PARP-13.2. We found that both PARP-13.1 and PARP-13.2 are MARylated by GFP-PARP-7 **(Figure 2.3b and Figure Supplement 2.3**). Myc-BirA*-PARP-7 MARylated both PARP-13.1 and PARP-13.2 to a similar extent as GFP-PARP-7, indicating that the tag on PARP-7 does not impact PARP-13 MARylation **(Figure Supplement 2.3).** In the absence of PARP-7, we do not detect MARylation of PARP-13.1 or PARP-13.2 **(Figure 2.3b and Figure Supplement 2.3a).** Because the similar molecular weights of GFP-PARP-7 and PARP-13.1 made it challenging to distinguish trans-MARylation of PARP-13.1 from auto-MARylation of PARP-7, we focused all of our subsequent studies on PARP-13.2.

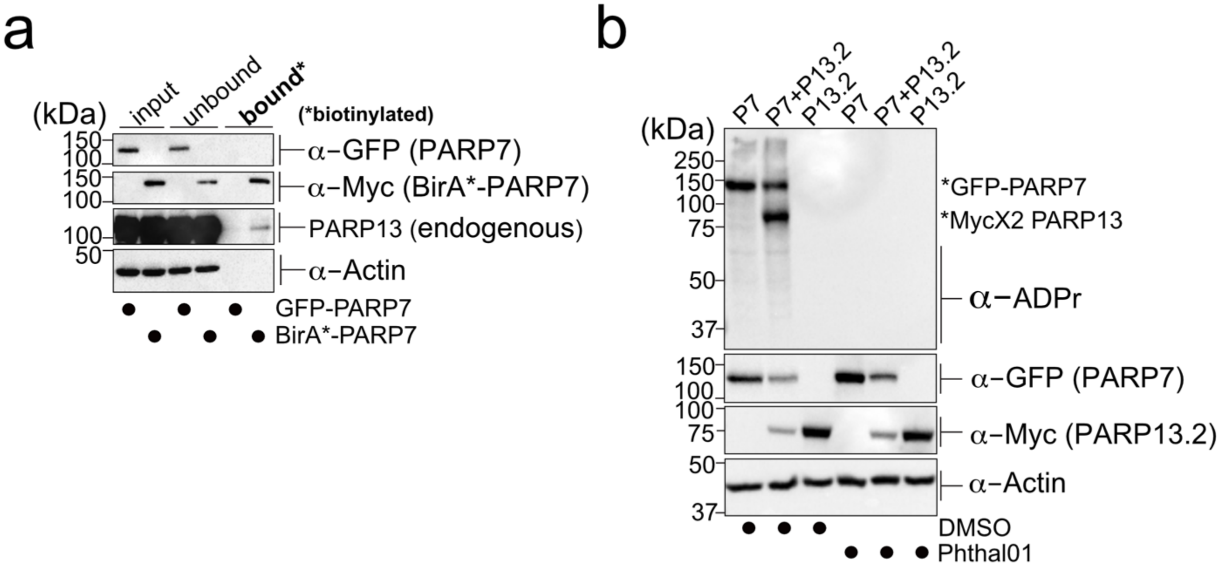

Figure 2.3. PARP-13 interacts with and is MARylated by PARP-7 in cells.
(a) PARP-7 interacts with endogenous PARP-13 (constitutive isoform PARP-13.1) in cells as shown by proximity labeling. HEK 293T cells were transfected with Myc-BirA*-PARP-7. Biotin (50 uM) was added to induce biotinylation of Myc-BirA*-PARP-7 interactors. Biotinylated proteins were enriched using Neutravidin agarose. Proteins were resolved by SDS-PAGE and were detected by Western blot using antibodies against GFP, Myc, PARP-13, and actin. Representative figure of data collected over three biological replicates.
(b) PARP-7 MARylates PARP-13.2 in cells. GFP-PARP-7 and MycX2-PARP-13.2 were co-expressed in HEK293T cells. Cells were treated overnight either with DMSO or with Phthal01 (1 uM). Proteins were resolved by SDS-PAGE and were detected by Western blot using antibodies against ADP-ribose (ADPr), GFP, Myc, and actin. Representative figure of data collected over three biological replicates.

We next asked if the catalytic activity of PARP-7 is required for the MARylation of PARP-13.2. For these experiments, we took a pharmacological approach. Recently a phthalazinone-based piperazine compound, AZ12629495, was reported in the patent literature [30]. AZ12629495 was shown to inhibit PARP-7 as well as PARP-1 and PARP-2 with nanomolar potency [30]. This was confirmed in another study, but family-wide analysis was not investigated [31]. We synthesized a close analog of AZ12629495, referred to here as Phthal01, and profiled it across the PARP family using an *in vitro* plate assay for screening PARP inhibitors developed in our lab[32]. We found that Phthal01 is most potent against PARP-7 (IC_{50} = 14 nM), followed closely by PARP1 (IC_{50} = 21 nM), and PARP2 (IC_{50} = 28 nM) **(Figure Supplement 2.4).** Phthal01 is at least 13-fold selective for PARP-7 versus the other PARP family members **(Figure Supplement 2.4).** We then evaluated the effects of Phthal01 against PARP-7 in HEK 293T cells by Western blot analysis using an ADPr-specific antibody. We found that Phthal01 dose dependently inhibits auto-MARylation of PARP-7 in GFP-PARP-7 expressing HEK 293T cells (EC_{50} ~60 nM) **(Figure Supplement 2.5).** At much higher concentrations, Phthal01 inhibits auto-MARylation of PARP-10 (EC_{50} ~3 uM) **(Figure Supplement 2.5).** Phthal01 (1 uM), but not the PARP1/2-selective inhibitor veliparib (1 uM), completely inhibits both auto-MARylation of PARP-7 and PARP-7-mediated trans-MARylation of PARP-13.2 **(Figure 2.3b and Figure Supplement 2.6).** Taken together, these results show that the that catalytic activity of PARP-7 is required for PARP-13.2 MARylation in cells.

We sought to further validate PARP-13.2 as a direct MARylation target of PARP-7 by performing in vitro MARylation assays with recombinantly expressed PARP-7 and PARP-13.2. In the presence of a physiological concentration of NAD^+ (100 uM), GST-PARP-7 trans-MARylated His_6-SUMO-PARP-13.2 in addition to itself (auto-MARylation) in a time-dependent manner **(Figure supplement 2.3b).** Despite strong auto-MARylation, His_6-SUMO-PARP-10 poorly trans-MARylated His_6-SUMO-PARP-13.2 under similar conditions **(Figure supplement 2.3b).** These data further demonstrate that PARP-13.2 is a *bona fide* MARylation target of PARP-7.

Having demonstrated that PARP-13.2 is a MARylation target of PARP-7 we next asked if PARP-7 catalytic activity is required for its interaction with PARP-13.2. Using recombinantly expressed GST-PARP-7 and His_6-SUMO-PARP-13.2 we performed co-immunoprecipitation experiments under the following conditions: No NAD^+, 100 uM NAD^+, or 100 uM NAD^+ + Phthal01 **(Figure supplement 2.3c).** GST-PARP-7 co-immunoprecipitated with His_6-SUMO-PARP-13.2 under all conditions, demonstrating that the interaction between PARP-7 and PARP-13.2 is independent of PARP-7 catalytic activity.

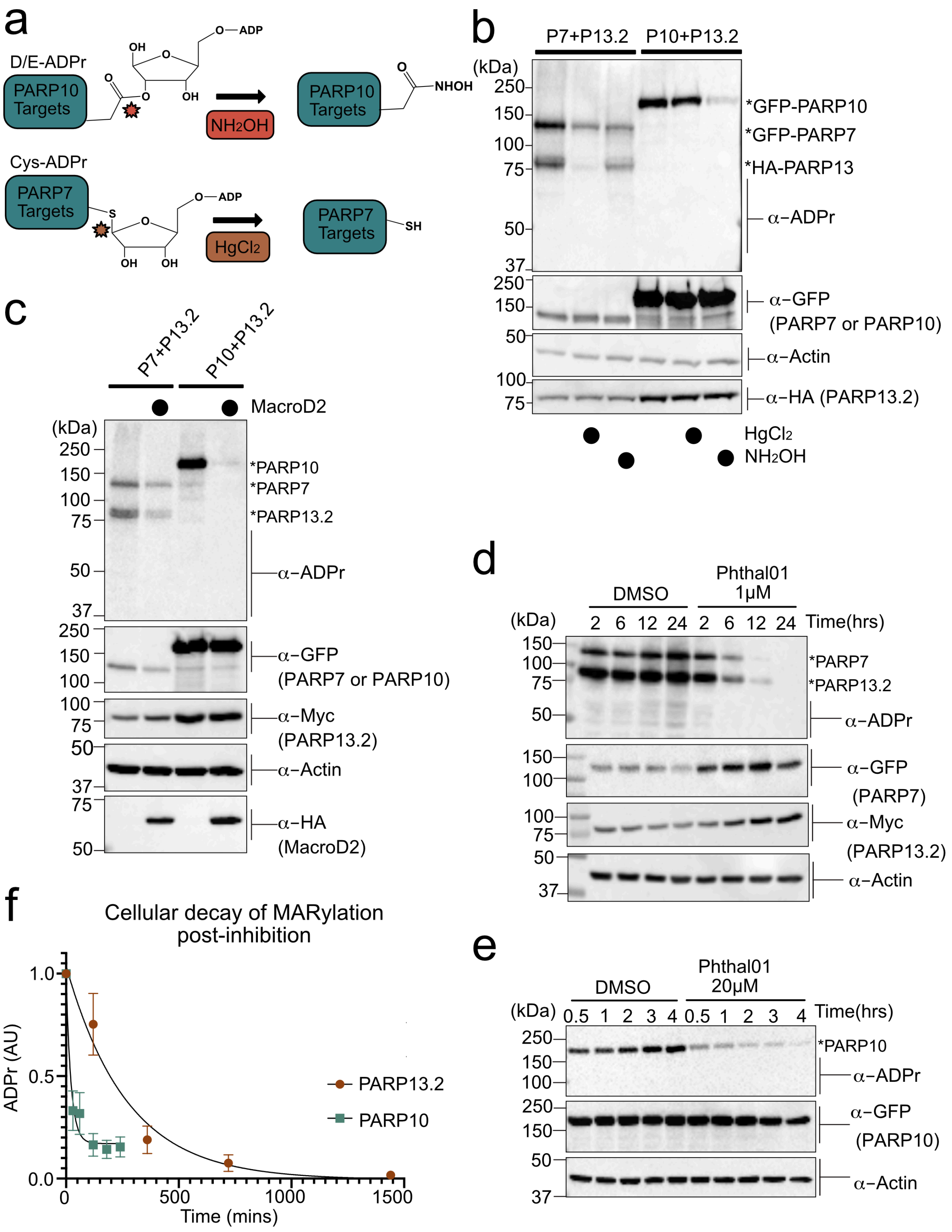
a
D/E-ADPr
PARP10 Targets
OH
O
O—ADP
OH
NH2OH
PARP10 Targets
NHOH
Cys-ADPr
PARP7 Targets
S
O—ADP
OH
OH
HgCl2
PARP7 Targets
SH
b
P7+P13.2
P10+P13.2
(kDa)
250
150
100
75
50
37
*GFP-PARP10
*GFP-PARP7
*HA-PARP13
α–ADPr
α–GFP
(PARP7 or PARP10)
α–Actin
α–HA (PARP13.2)
HgCl2
NH2OH
c
P7+P13.2
P10+P13.2
MacroD2
*PARP10
*PARP7
*PARP13.2
α–ADPr
α–GFP
(PARP7 or PARP10)
α–Myc
(PARP13.2)
α–Actin
α–HA
(MacroD2)
d
DMSO
Phthal01
1μM
Time(hrs)
2 6 12 24 2 6 12 24
*PARP7
*PARP13.2
α–ADPr
α–GFP
(PARP7)
α–Myc
(PARP13.2)
α–Actin
e
DMSO
Phthal01
20μM
Time(hrs)
0.5 1 2 3 4 0.5 1 2 3 4
*PARP10
α–ADPr
α–GFP
(PARP10)
α–Actin
f
Cellular decay of MARylation post-inhibition
ADPr (AU)
1.0
0.5
0.0
0
500
1000
1500
Time (mins)
PARP13.2
PARP10

Figure 2.4. PARP-13 is MARylated by PARP-7 predominately on Cys residues and Cys MARylation is more stable than Asp/Glu MARylation in cells.

(a) Schematic of chemical stability studies for analyzing the amino acid-ADPr linkage. Neutral hydroxylamine (NH_2OH) removes ADPr from acid residues to generate a hydroxamic acid, while mercuric chloride ($HgCl_2$) removes ADPr from Cys residues.

(b) PARP-7 MARylates predominately on Cys residues whereas PARP-10 MARylates predominately on Glu/Asp residues. GFP-PARP-7/HA-PARP-13.2 or GFP-PARP-10 alone were expressed in HEK 293T cells. Lysates were prepared and treated with either water control, $HgCl_2$ (2 mM), or NH_2OH (0.4 M). Following treatment, proteins were precipitated with ice cold methanol, and resolved by SDS-PAGE and were detected by Western blot using antibodies against ADPr, GFP, HA, and actin. Representative figure of data collected over three biological replicates.

(c) The Glu/Asp selective ADPr hydrolase MacroD2 efficiently removes ADPr from PARP-10, but only partially removes ADPr from PARP-7 and PARP-13. GFP-PARP-7/MycX2-PARP-13.2 or GFP-PARP-10 was co-expressed with either HA-MacroD2 or mCherry (negative control) in HEK 293T cells. Proteins were resolved by SDS-PAGE and were detected by Western blot using antibodies against ADPr, GFP, Myc, and actin. Representative figure of data collected over three biological replicates.

(d) Time course of Cys MARylation in cells. GFP-PARP-7 and MycX2-PARP-13.2 were co-expressed in HEK 293T cells. Cells were treated with either DMSO or Phthal01 (1µM) to stop PARP-7 MARylation. Cells were harvested at indicated time points and proteins were resolved by SDS-PAGE and were detected by Western blot using antibodies against ADPr, GFP, Myc, and actin. Representative figure of data collected over three biological replicates.

(e) Time course of Glu/Asp MARylation in cells. GFP-PARP-10 was expressed in HEK 293T cells. Cells were treated with either DMSO or Phthal01 (20 µM) to stop PARP-10 MARylation. Cells were harvested at indicated time points and proteins were resolved by SDS-PAGE and were detected by Western blot using antibodies against ADPr, GFP, and actin. Representative figure of data collected over five biological replicates.

(f) Quantification of replicate data from (d) and (e). ADPr signal is normalized to either GFP-PARP-10 or MycX2-PARP-13.2. Data are ± SEM.

Cys residues are the major sites of PARP-7-mediated MARylation in PARP-13

We next sought to identify the amino acid ADPr acceptors in PARP-13 that are MARylated by PARP-7 using chemical stability studies. NH_2OH cleaves the ester bond between Glu/Asp and ADPr whereas $HgCl_2$ cleaves the thioether bond between Cys and ADPr **(Figure 2.4a)**[9]. We co-expressed HA-PARP-13.2 with either GFP-PARP-7 or GFP-PARP-10 in HEK 293T cells and evaluated MARylation by Western blot analysis using an ADPr-specific antibody. In lysates from HEK 293T cells expressing GFP-PARP-7 and HA-tagged PARP-13.2, we found that $HgCl_2$ (2 mM) reduces substantially (~90%) the ADPr signal on HA-PARP-13.2, whereas neutral NH_2OH (0.4 M) only partially reduces (~30%) this signal **(Figure 2.4b).** In contrast, in lysates from HEK 293T cells expressing GFP-PARP-10 and HA-tagged PARP-13.2, we found that neutral NH_2OH reduces substantially (~90%) the ADPr-signal on PARP-10 whereas $HgCl_2$ has no effect **(Figure 2.4b).** The latter result is consistent with previous studies from our lab and others showing that PARP-10 is auto-MARylated predominately on Glu/Asp[33],[34]. Despite the strong auto-MARylation activity of PARP-10 in cells, we did not detect trans-MARylation of PARP-13.2 when these two constructs were co-expressed **(Figure 2.4b).** Treatment with either neutral NH_2OH or $HgCl_2$ equally reduces PARP-7 auto-MARylation suggesting it may be modified on both cysteine and acidic residues **(Figure 2.4b).** Although it is formally possible that another PARP modifies PARP-7 on acidic amino acids, the observation that PARP-7 MARylation is completely inhibited by Phthal01 (1 uM), but not veliparib (1 uM), suggests that these acid amino acids ADPr acceptor residues are auto-MARylation sites **(Figure 2.3b and Figure Supplement**

2.6). Taken together, these results show PARP-13.2 is a selective target of PARP-7 that it is MARylated predominately on Cys residues.

To further evaluate the ADPr acceptor residues in PARP-13, we took an enzymatic approach. Previous studies demonstrate that the macrodomain containing enzyme macroD2 removes ADPr attached to Glu/Asp, thereby reversing Glu/Asp-directed MARylation[35,36,37]. While it is not known if macroD2 removes ADPr attached to Cys, it does not remove ADPr attached to Ser[38]. We co-expressed HA-macroD2 with either GFP-PARP-7 and MycX2-PARP-13.2 or GFP-PARP-10 and MycX2-PARP-13.2 in HEK 293T cells and evaluated MARylation by Western blot analysis using an ADPr-specific antibody. We found that while macroD2 efficiently reverses auto-MARylation of PARP-10, macroD2 only partially reverses both auto-MARylation of PARP-7 and trans-MARylation of PARP-13.2 **(Figure 2.4c).** These results are consistent with the chemical stability studies and further support the notion that PARP-7 predominately MARylates Cys residues in PARP-13.2.

Intracellular MARylation stability is dependent on the chemical nature of the amino acid-ADPr bond

For many PTMs involved in cell signaling (e.g. phosphorylation), the rate of reversal is the major determinant of signal duration. It is unknown if disparate amino acid-ADPr bonds exhibit different cellular stabilities, which could impact the signal duration of MARylation. We measured the decay of PARP-7-mediated PARP-13 MARylation, which occurs predominately on Cys, and PARP-10 auto-MARylation, which occurs predominately on Glu/Asp. We used Phthal01 to stop the forward MARylation reaction: 1 uM for PARP-7, and 20 uM for PARP-10. We then harvested cells at different time points to measure the decay of PARP-7-mediated MARylation of PARP-13.2 and auto-MARylation of PARP-10 by Western blot using an ADPr-specific antibody. We found that the half-life ($t_{1/2}$) of ADPr in PARP-10 is 15 min whereas the $t_{1/2}$ of ADPr in PARP-13.2 is 189 min **(Figure 2.4d-f and Figure Supplement 2.6).** Importantly, the PARP-1/2 inhibitor veliparib does not lead to the decay of PARP-7-mediated MARylation of PARP-13.2 **(Figure Supplement 2.6).** The longer $t_{1/2}$ of MARylated PARP-13.2 versus MARylated PARP-10 suggests that the Cys-ADPr bond is more stable in HEK 293T cells than the Glu/Asp-ADPr bond.

We next determined if the longer $t_{1/2}$ for Cys-ADPr compared to Glu/Asp-ADPr was due to increased chemical or enzymatic stability. Lysates from HEK293T cells expressing PARP-10 or PARP-7 together with PARP-13.2 were treated with 2% SDS and heated to 95˚C to completely denature proteins; in this way, the inherent chemical stability of the Cys- versus Glu/Asp-ADPr bind could be assessed. We observed no change in the Cys- or Glu/Asp-ADPr signal over time (up to 24 h) **(Figure Supplement 2.7a)**. This result suggests that Cys-ADPr is more enzymatically stable than Glu/Asp-ADPr in HEK 293T cells.

Inhibition of PARP-7 catalytic activity increases its protein levels

The HEK 293T cell time course experiments revealed that Phthal01 increased the protein levels of ectopically expressed GFP-PARP-7 and MycX2-PARP-13.2

(Figure 2.4 and Figure Supplement 2.6). To test if endogenous PARP-7 and PARP-13 protein levels are similarly affected by inhibition of PARP-7 catalytic activity, we treated A549 cells, which express endogenously both PARP-7 and PARP-13, with Phthal01. PARP-13 was detected using two commercially available PARP-13 antibodies whereas PARP-7 was detected using a recently developed PARP-7 antibody (manuscript in preparation, J. Matthews). The specificity of the PARP-7 antibody was validated using *PARP-7*$^{+/+}$ and *PARP-7*$^{-/-}$ mouse embryonic fibroblasts **(Figure Supplement 2.7b)**[39].We found that endogenous PARP-7 protein levels increase substantially upon treatment with Phthal01; however, the levels of endogenous PARP-13.1 did not change **(Figure Supplement 2.7b,c).** PARP-13.1 is the major endogenously expressed isoform under basal conditions. These results suggest that while endogenous PARP-7 levels are regulated by its catalytic activity, endogenous PARP-13.1 levels are not regulated b PARP-7 catalytic activity under these conditions.

PARP-7 predominately MARylates Cys residues in the CCCH zinc finger domains of PARP-13

The chemical stability and enzymatic removal studies point to Cys residues as the predominate amino acids in PARP-13 that are MARylated by PARP-7. However, we sought direct evidence for PARP-7-mediated Cys MARylation in PARP-13, and perhaps other targets. Recently, Nielsen and colleagues established an unbiased MS platform for confidently identifying and localizing the amino acid ADPr acceptors in proteins on a proteome-wide scale[40,13]. This strategy involves the enrichment of ADP-ribosylated peptides (generated post trypsin digest) using the macrodomain Af1521, which binds with high affinity to ADPr-modified peptides. Enriched peptides containing ADPr are subjected to MS-based analysis using electron-transfer higher-energy collisional dissociation (EThcD), a fragmentation technique that can localize the ADPr moiety to any nucleophilic amino acid acceptor with high confidence[40,13]. We used this MS platform to search for amino acid-ADPr sites across the proteome in HEK 293T cells under three experimental conditions: i. GFP-PARP-7 overexpressing cells, ii. MycX2-PARP-13.2 overexpressing cells, or iii. GFP-PARP-7 and MycX2-PARP-13.2 overexpressing cells. We identified a total of 1,712 ADPr sites with a localization probability of >90% in all three conditions **(Table Supplement 5).** There is a low degree of variance between biological replicates, especially for the GFP-PARP-7 alone and the MycX2-PARP-13.2 alone conditions **(Figure Supplement 2.8).** As expected, there was a greater degree of overlap between the GFP-PARP-7 alone condition and the GFP-PARP-7/ MycX2-PARP-13.2 condition compared to the MycX2-PARP-13.2 condition **(Figure Supplement 2.9).** We identified amino acid-ADPr sites on all known ADPr acceptor residues, including Cys, Glu, Asp, His, Lys, Arg, Ser, Thr, and Tyr **(Table Supplement 5).**

Initially, we focused on analyzing the amino acid-ADPr sites in PARP-13. In the GFP-PARP-7 alone condition, endogenous PARP-13 (likely representing the two major isoforms PARP-13.1 and PARP-13.2) is MARylated exclusively on Cys residues **(Figure 2.5a, Figure Supplement 2.10, 2.11 and Table Supplement 5).** Intriguingly, all but one of the seven identified Cys-ADPr sites in endogenous PARP-13 are located in the four N-terminal zinc-finger (ZnF 1-4) domains; one Cys-ADPr (Cys721) is located in the inactive, catalytic domain of PARP-13.1 **(Figure 2.5b,c, Figure Supplement 2.10, Table Supplement 5).** Five out of the six ZnF Cys-ADPr sites are Zn-coordinating Cys residues **(Figure 2.5c).** Despite the relatively low conservation of PARP-13 across species, all of the endogenous PARP-13 Cys-ADPr sites in the ZnF domains are conserved between human, mouse and rat **(Figure Supplement 2.12).**

When PARP-13.2 was co-expressed with PARP-7, we identified additional Cys-ADPr sites in the ZnF in PARP-13. In this condition, other amino acid-ADPr sites are identified, most prominently on Arg and Tyr; however, the intensities for Arg-ADPr and Tyr-ADPr are at least an order of magnitude lower than the intensities found for Cys-ADPr **(Figure 2.5a and Figure Supplement 2.10).** Cys MARylation in PARP-13.2 is dependent on the co-expression of PARP-7 since we only detect Ser-ADPr (3 sites) and Arg-ADPr (1 site) in the PARP-13.2 alone condition **(Figure 2.5a and Figure Supplement 2.10)**. The intensity for Ser-ADPr is substantially higher than Arg-ADPr **(Figure 2.5a and Figure Supplement 2.10).**

In addition to identifying Cys-ADPr sites in PARP-13, we also found that GFP-PARP-7 is auto-MARylated predominately on Cys residues **(Figure Supplement 2.13 and Table Supplement 5).** One Cys, Cys39, was identified in a previous MS method using standard HCD fragmentation[41]. Two Cys-ADPr sites (Cys543 and Cys552) reside in the catalytic domain of PARP-7. At much lower intensities, we found several Tyr-ADPr, His-ADPr, and Arg-ADPr sites in PARP-7 **(Figure Supplement 2.13 and Table Supplement 5).** These lower intensity ADPr-sites could be sites of auto-MARylation or could be sites of trans-MARylation by other PARP family members. Regardless, it is clear that the major auto-MARylation sites in PARP-7 are Cys residues.

Using EThcD fragmentation, we confidently identified Cys residues as major PARP-7-mediated MARylation sites in PARP-13. Nevertheless, we sought to confirm the MS results using mutagenesis studies. We focused on the Cys residues in the ZnF domains since we found that they are the major sites of Cys MARylation in PARP-13. In HEK 293T cells expressing both GFP-PARP-7 and MycX2-PARP-13.2, we found that mutation of all of the Cys residues to alanine (Ala) residues in the ZnF domains of PARP-13.2 (CtoA ZnF all) substantially reduces PARP-13.2 MARylation compared to WT PARP-13.2 **(Figure 2.5d and Figure Supplement 2.14).** Mutation of the Cys residues to Ala residues in either ZnF domains 1-2 (CtoA ZnF 1-2) or 3-4 (CtoA ZnF 3-4) modestly reduces PARP-13.2 MARylation **(Figure 2.5d and Figure Supplement 2.14)**. The reduction in PARP-7-mediated MARylation of PARP-13.2 in the Cys mutants is not due to a loss in the interaction between PARP-13 and PARP-7 as shown by co-immunoprecipitation experiments **(Figure Supplement 2.15)**. Together these data support that the primary sites of MARylation by PARP-7 on PARP-13.2 are the ZnF cysteine residues.

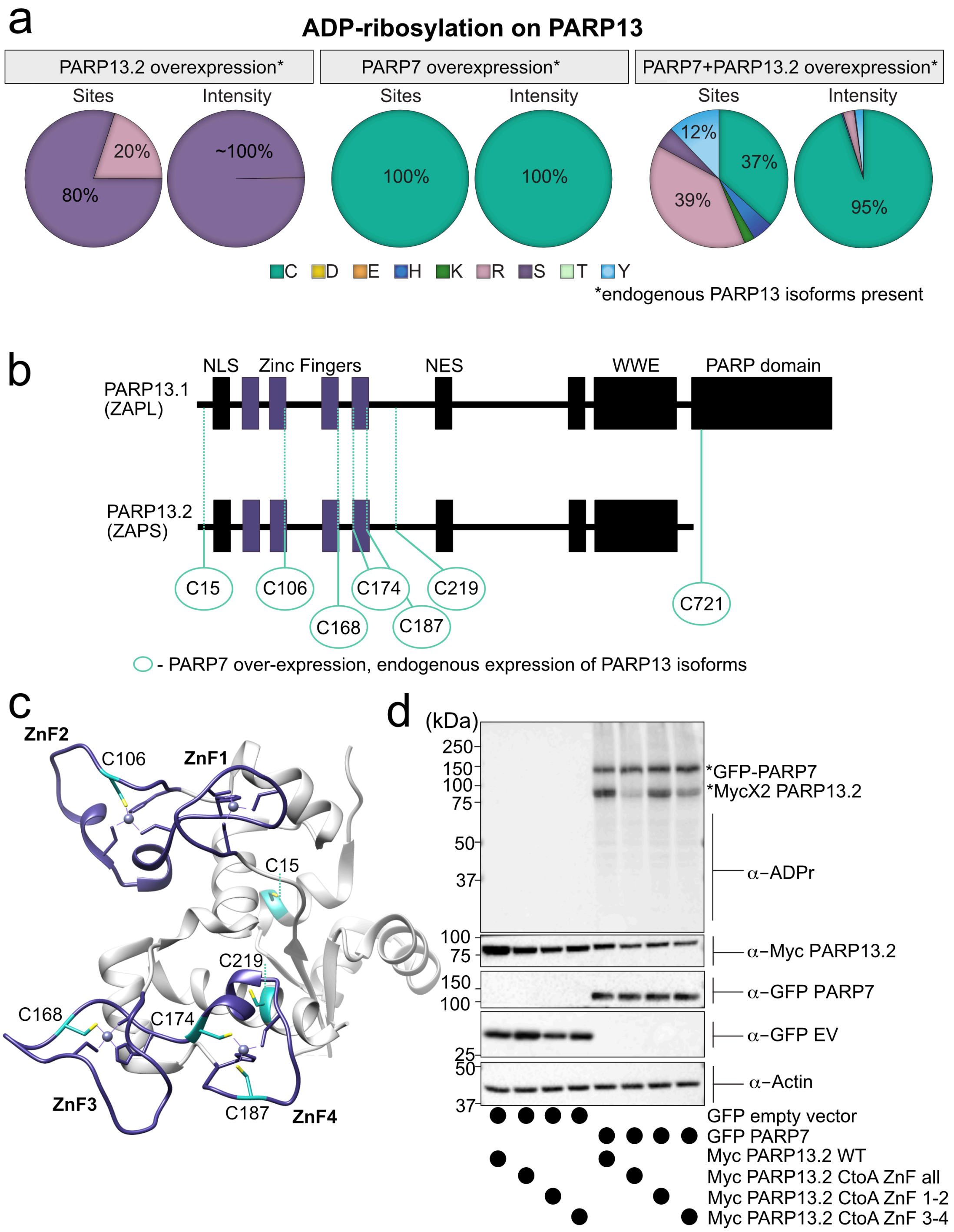
a
ADP-ribosylation on PARP13
PARP13.2 overexpression*
Sites
Intensity
20%
80%
~100%
PARP7 overexpression*
Sites
Intensity
100%
100%
PARP7+PARP13.2 overexpression*
Sites
Intensity
12%
37%
39%
95%
C D E H K R S T Y
*endogenous PARP13 isoforms present
b
NLS
Zinc Fingers
NES
WWE
PARP domain
PARP13.1 (ZAPL)
PARP13.2 (ZAPS)
C15
C106
C168
C174
C187
C219
C721
- PARP7 over-expression, endogenous expression of PARP13 isoforms
c
ZnF2
C106
ZnF1
C15
C219
C168
C174
ZnF3
C187
ZnF4
d
(kDa)
250
150
100
75
50
37
*GFP-PARP7
*MycX2 PARP13.2
α−ADPr
100
75
α−Myc PARP13.2
150
100
α−GFP PARP7
25
α−GFP EV
50
37
α−Actin
GFP empty vector
GFP PARP7
Myc PARP13.2 WT
Myc PARP13.2 CtoA ZnF all
Myc PARP13.2 CtoA ZnF 1-2
Myc PARP13.2 CtoA ZnF 3-4

Figure 2.5. MS-based ADPr site identification and mutagenesis studies demonstrate that PARP-7-mediated MARylation of PARP-13 occurs predominately on Cys residues in the ZnF domains.

(a) Pie-charts showing of the amino acid residue distribution of all ADP-ribosylation sites identified on PARP-13 using EThcD fragmentation. Experiments were performed under three conditions: MycX2-PARP-13.2 overexpressing cells, GFP-PARP-7 overexpressing cells, GFP-PARP-7 and MycX2-PARP-13.2 overexpressing cells. One letter code used for amino acids.

(b) Domain architecture of PARP-13.1 and PARP-13.2 showing positions of Cys ADPr sites.

(c) Crystal structure of the N-terminal ZnF domains of PARP-13highlighting Cys ADPr sites (cyan). ZnF domains are highlighted (purple). PDB: 6UEI.

(d) Mutation of the Cys to Ala in the ZnF domains of PARP-13 decreased PARP-7-mediated PARP-13 MARylation. GFP-PARP-7 was co-expressed with either WT- or CtoA ZnF all, CtoA ZnF1-2, or CtoA ZnF3-4 in HEK 293T cells.

GFP-PARP-7 or GFP-empty vector control co-expressed in HEK293T cells with MycX2-PARP-13.2 WT and mutants. Proteins were resolved by SDS-PAGE and were detected by Western blot using antibodies against ADPr, GFP, Myc, and actin. Representative figure of data collected over three biological replicates.

rminant for MARylation targeting by PARP-7.

Proteome-wide analysis reveals Cys residues as major ADPr acceptors in PARP-7 targets

Having validated Cys as the major PARP-7-mediated MARylation site in PARP-13, we broadened our analysis across the proteome in HEK 293T cells and focused on amino acid-ADPr sites that were either unique or enriched (at least 5-fold) in the GFP-PARP-7 alone condition compared to the MycX2-PARP-13.2 alone condition. We reasoned that these amino acid-ADPr sites are likely targets of PARP-7. Using the above criteria, we identified a total of 939 unique amino acid-ADPr sites on a total of 490 proteins **(Figure 2.6a)** as putative PARP-7 targets. Of these sites, the majority (471 Cys-ADPr sites on 374 proteins) were on Cys residues **(Figure 2.6a)**. When we compared the PARP-7-targeted, Cys-ADPr modified proteins to the direct PARP-7 targets identified using our CG strategy, we found 48 overlapping protein targets **(Figure 2.6b).** Among these 48 overlapping proteins, PARP-13 was a top target. We next asked how many Cys-ADPr sites there are per protein target. We found that the vast majority of proteins are MARylated on a single Cys **(Figure 2.6c and Table Supplement 6)**. Intriguingly, PARP-13, with 11 sites identified, stands out as the only target with >4 Cys-ADPr sites **(Figure 2.6c).**

In some cases, enzymes that catalyze PTMs are directed to the target amino acid site by proximal consensus sequence motifs. Previous proteome-wide studies analyzing Ser-ADPr sites revealed a strong preference for a Lys residue preceding the Ser (-1 position relative to Ser-ADPr) that is ADP-ribosylated[42].We wondered if a similar preference might exist for Cys-ADPr. For this analysis we used Icelogo, which can identify and visualize conserved patterns in proteins[43]. While we did not observe a strong preference for a particular amino acid at the -1 position, we did find a preference for a proline (Pro), followed by an Arg, in the +2 position **(Figure 2.6 d)**. This analysis suggests that the proximal sequence surrounding the Cys-ADPr site is not a strong determinant for MARylation targeting by PARP-7.

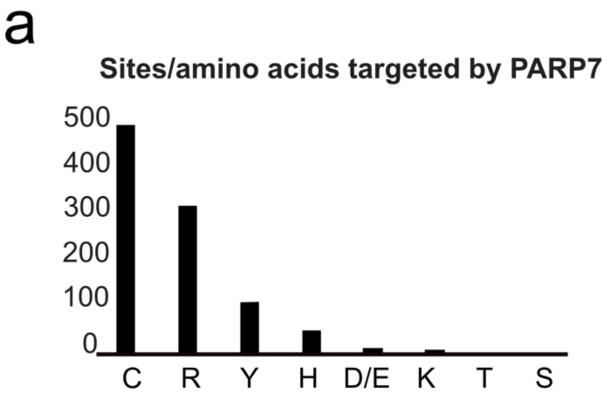

Sites/amino acids targeted by PARP7

Amino acid	Sites	Proteins
C	471	374
R	305	105
Y	105	66
H	45	37
D/E	8	7
K	5	4
T	0	0
S	0	0
Total sites		939
Total proteins		490

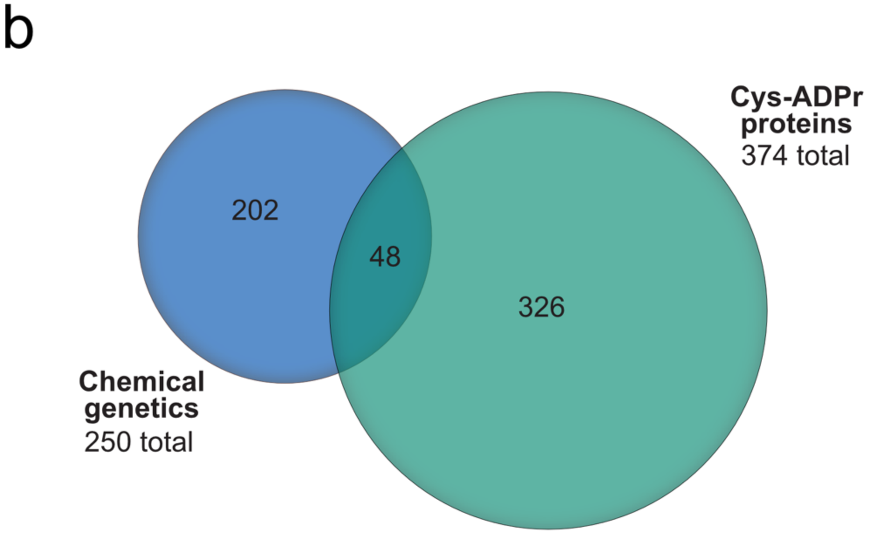

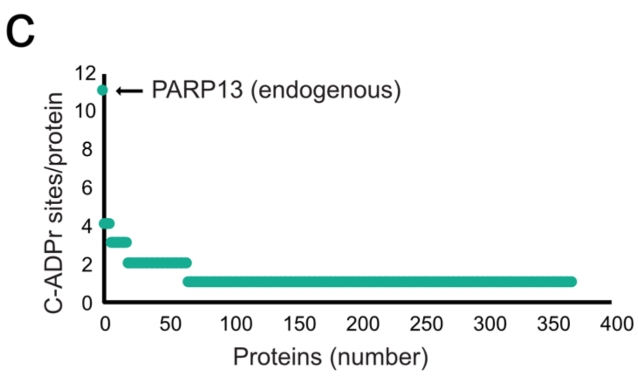

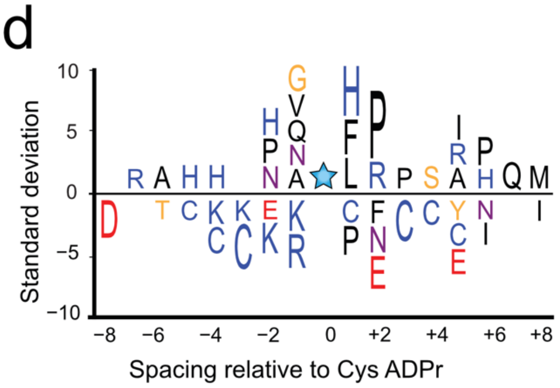

Figure 2.6. Proteome-wide analysis reveals Cys ADPr as a major MARylation site catalyzed by PARP-7.

(a) Graph and corresponding table showing unique ADPr sites (and proteins) enriched in the PARP-7 overexpression condition (compared to MycX2-PARP-13.2 overexpression condition).

(b) Venn diagram depicting the overlap of total proteins identified in our CG strategy compared to total Cys ADPr modified proteins enriched in the PARP-7 condition.

(c) Graph representing the number of endogenous Cys ADPr sites per protein in the PARP-7 overexpression sample. PARP-13, by far has the highest number of cysteine sites, with 11 sites identified.

(d) IceLogo representation of the sequence context surrounding Cys ADPr sites identified in GFP-PARP-7 overexpressing cells. Amino acids displayed above the line are enriched, and those displayed below are depleted, compared to the sequence context of all cysteine residues derived from the same proteins. *p*=0.05.

Discussion

We have successfully adapted our chemical genetic strategy for identifying the direct targets of PARP-7. This involved changing the position of the alkyne clickable handle from the N-6-position (5-Bn-6-a-NAD$^+$) to the 2-positon (5-Bn-2-e-NAD$^+$) of the adenosine ring in our modified NAD$^+$ analogs. 5-Bn-2-e-NAD$^+$ is a much better substrate for IG-PARP-7 compared to 5-Bn-6-a-NAD$^+$. Similarly, we found that 5-Bn-2-e-NAD$^+$ is a better substrate for floor position engineered PARP12, I660G PARP12 (IG-PARP12) compared to 5-Bn-6-a-NAD$^+$ **(Figure Supplement 2.1 b)**. The 5-Bn-2-e-NAD$^+$—IG-PARP12 pair will enable us, in future studies, to identify the direct targets of PARP12.

Combining our chemical genetics approach with a proximity labeling approach (BioID), we generated a list of PARP-7 MARylation targets and interactors with known roles in innate immune signaling. These results align with previous literature that demonstrate a critical role for PARP-7 as a negative regulator of interferon signaling during viral infection [3],[4],[5]. Particularly interesting is the enrichment of RNA binding and RNA regulatory proteins with known roles in viral regulation. Indeed, we found that the antiviral RNA-binding protein PARP-13 is a major MARylation target of PARP-7 in cells. In a co-submitted study, Kraus and colleagues also identified PARP-13 as PARP-7 target using a distinct, but complementary chemical genetic approach (Parsons et al., 2021). Chemical sensitivity studies using $HgCl_2$ and MS-based site identification studies show that PARP-7 predominately MARylates PARP-13 on several Cys residues, most prominently in the ZnF domains of both PARP-13 isoforms, PARP-13.1 and PARP-13.2.

How might Cys MARylation regulate PARP-13 function? The most well-characterized function for PARP-13 is as an antiviral restriction factor. PARP-13 inhibits the replication of many types of RNA viruses[1,2,26,44,45,46,47,48,49,50]. Recent studies show that PARP-13.1 and PARP-13.2 have distinct roles in innate antiviral immune response: PARP-13.2 binds and degrades host mRNAs (e.g. *IFN-β*), thereby negatively regulating the interferon response whereas PARP-13.1 targets viral RNA and is the major antiviral effector[28].The ZnF domains of PARP-13.1 and PARP-13.2 are required for binding to both host and viral mRNAs. Since the Cys residues in the ZnF domains of PARP-13 are important for Zn^{2+} coordination, it is possible that MARylation of these Cys residues alters or disrupts RNA binding. The ZnF domains of PARP-13.2 are also involved in protein-protein interactions relevant to innate immune signaling. PARP-13.2 stimulates the interferon response in response to influenza A viral infection via direct activation of the cytosolic nucleic acid sensor RNA helicase RIG-I[45]. PARP-13.2 interacts with RIG-I and stimulates its oligomerization and ATPase activity, leading to interferon induction. This interaction is dependent on the ZnF domains of PARP-13.2, hence Cys MARylation of PARP-13.2 by PARP-7 could potentially disrupt the interaction between PARP-13.2 and RIG-I. Future studies will be focused on understanding how PARP-7-mediated Cys MARylation of PARP-13.1 and/or PARP-13.2 regulate their antiviral and immune regulatory roles.

Beyond PARP-7-mediated Cys MARylation of PARP-13, PARP-13 is also modified by other PARP family members at different amino acid acceptors. In a previous chemical genetic study we found that PARP14 MARylates PARP-13 on several Glu/Asp residues in the C-terminus of the protein[20]. Another study showed that PARP-13.1 and PARP-13.2 can be poly-ADP-ribosylated (PARylated) in response to cell stress, although the PARP that mediates PARylation of PARP-13.1/2 was not identified[51]. Interestingly, in this study we find that in the absence of PARP-7, PARP-13.2 is ADP-ribosylated on several serines. Serines are known sites of PARylation by PARP1 and PARP2[49]; therefore PARylation of PARP-13 could be catalyzed by PARP1/2. Trans-M/PARylation of PARP-13 by other PARP family members suggests that PARP-13 is an important integrator of active PARP signaling. An intriguing idea is that M/PARylation at distinct amino acid acceptors elicits different downstream effects.

Proteome-wide ADPr site profiling suggests that many targets of PARP-7 are MARylated predominately on Cys residues. Cys MARylation was originally described for the bacterial ADP-ribosyltransferase Pertussis toxin (PTX)[50]. PTX MARylates a Cys in the carboxyl terminus of the alpha submit of the G proteins, G_i and G_o[50]. Studies dating back 30 years ago described endogenous Cys MARylation, similar to PTX-dependent MARylation[51,52], but the enzyme(s) that catalyzes Cys MARylation were not identified. In this study we provide strong evidence that PARP-7 catalyzes Cys MARylation. Our results are consistent with previous studies showing that PARP-7 auto-MARylates predominately on a Cys residue (Cys39)[41]. How PARP-7 preferentially targets Cys versus other potential amino acid acceptors is currently unknown. Recent studies on the amino acid selectivity of PARP1/2-mediated PARylation provides some clues: for example, a recent crystal structure of the histone PARylation factor (HPF1)[53]—PARP2 complex shows that HPF1 interacts directly with the NAD^+ binding site of PARP2[54], and demonstrates that HPF1 can act as an auxiliary factor to influence amino acid target preference. In the absence of HPF1, PARP1 predominately PARylates on Glu/Asp residues, however in the presence of HPF1, PARP1 predominately PARylates on Ser residues[49,55]. Perhaps this is similarly the case for PARP-7, and future studies may focus on identifying potential auxiliary factors for PARP-7.

Curiously, inhibition of PARP-7 catalytic activity by Phthal01 increased endogenous PARP-7 protein levels. This is consistent with previous studies showing that a catalytically inactive PARP-7 mutant is expressed at higher levels than WT-

PARP-7 [41]. Although endogenous PARP-13.1 levels were not impacted by Phthal01, it's possible that PARP-7 regulates the stability of PARP-13.2 in a context specific manner, for example, during viral infection. Future studies will focus on determining the mechanism by which inhibition of PARP-7 catalytic activity regulates PARP-7 protein levels, and if PARP-13.2 protein levels (or other PARP-7 targets) are regulated by PARP-7 trans-MARylation.

Until recently, PARP drug discovery efforts over the past 20 years have focused exclusively on PARP1/2 and its role in the DNA damage response. The role of PARP-7 in the innate immune response has stimulated interests in PARP-7 as an immunomodulatory agent for cancer treatment. Currently, there is the first PARP-7 inhibitor (RBN-2397) in Phase I clinical trials for solid tumor cancers (NCT04053673). This is the first clinical trial for an inhibitor of a MARylating PARP and represents and exciting new direction in the PARP field. The PARP-7 targets and ADPr sites identified in this study as well as the Parsons et al. study will guide future studies examining the mechanism by which PARP-7 regulates antitumor immunity.

References

1. Fehr, A. R. *et al.* The impact of PARPs and ADP-ribosylation on inflammation and host-pathogen interactions. *Genes Dev.* **3**, 1–19 (2020).
2. Daugherty, M. D., Young, J. M., Kerns, J. A. & Malik, H. S. Rapid Evolution of PARP Genes Suggests a Broad Role for ADP-Ribosylation in Host-Virus

Conflicts. *PLoS Genet.* **10**, (2014).

3. Yamada, T. *et al.* Constitutive aryl hydrocarbon receptor signaling constrains type I interferon–mediated antiviral innate defense. *Nat. Immunol.* **17**, 687 (2016).
4. Kozaki, T. *et al.* Mitochondrial damage elicits a TCDD-inducible poly(ADP-ribose) polymerase-mediated antiviral response. *Proc. Natl. Acad. Sci.* **114**, 2681–2686 (2017).
5. Grunewald, M. E., Shaban, M. G., Mackin, S. R., Fehr, A. R. & Perlman, S. crossm Murine Coronavirus Infection Activates the Aryl Hydrocarbon TCDD-Inducible-PARP Expression. **94**, 1–17 (2020).
6. Cohen, M. S. & Chang, P. Insights into the biogenesis, function, and regulation of ADP-ribosylation. *Nat. Chem. Biol.* **14**, 236–243 (2018).
7. Payne, D. M., Jacobson, E. L., Moss, J. & Jacobson, M. K. Modification of Proteins by Mono(ADP-ribosylation) in Vivo. *Biochemistry* **24**, 7540–7549 (1985).
8. Cervantes-Laurean, D., Jacobson, E. L., Jacobson, M. K. & Minter, D. E. Protein Glycation by ADP-Ribose: Studies of Model Conjugates. *Biochemistry* **32**, 1528–1534 (1993).
9. Hsia, J. A. *et al.* Amino acid-specific ADP-ribosylation. Sensitivity to hydroxylamine of [cysteine(ADP-ribose)]protein and [arginine(ADP-ribose)]protein linkages. *J. Biol. Chem.* **260**, 16187–16191 (1985).
10. Krantz, M. J. & Lee, Y. C. Quantitative Hydrolysis of Thioglycosides. *Anal. Biochem.* **71**, 318–321 (1976).
11. McDonald, L. J. & Moss, J. Enzymatic and nonenzymatic ADP-ribosylation of cysteine. *Mol. Cell. Biochem.* **138**, 221–226 (1994).

12. Buch-larsen, S. C. *et al.* Mapping physiological ADP-ribosylation using Activated Ion Electron Transfer Dissociation (AI-ETD). *bioRxiv* 2020.01.27.921650 (2020). doi:10.1101/2020.01.27.921650
13. Larsen, S. C., Hendriks, I. A., Lyon, D., Jensen, L. J. & Nielsen, M. L. Systems-wide Analysis of Serine ADP-Ribosylation Reveals Widespread Occurrence and Site-Specific Overlap with Phosphorylation. *Cell Rep.* **24**, 2493-2505.e4 (2018).
14. Leslie Pedrioli, D. M. *et al.* Comprehensive ADP-ribosylome analysis identifies tyrosine as an ADP-ribose acceptor site. *EMBO Rep.* **19**, 1–11 (2018).
15. Palazzo, L. *et al.* Serine is the major residue for ADP-ribosylation upon DNA damage. *Elife* **7**, 1–12 (2018).
16. Leidecker, O. *et al.* Serine is a new target residue for endogenous ADP-ribosylation on histones. *Nat. Chem. Biol.* **12**, 998–1000 (2016).
17. Carter-O'Connell, I., Jin, H., Morgan, R. K., David, L. L. & Cohen, M. S. Engineering the substrate specificity of ADP-ribosyltransferases for identifying direct protein targets. *J. Am. Chem. Soc.* **136**, 5201–5204 (2014).
18. Carter-O'Connell, I. *et al.* Identifying Family-Member-Specific Targets of Mono-ARTDs by Using a Chemical Genetics Approach. *Cell Rep.* **14**, 621–631 (2016).
19. Carter-O'Connell, I. & Cohen, M. S. Identifying Direct Protein Targets of Poly-ADP-Ribose Polymerases (PARPs) Using Engineered PARP Variants-Orthogonal Nicotinamide Adenine Dinucleotide (NAD+) Analog Pairs. *Curr. Protoc. Chem. Biol.* **7**, 121–139 (2015).
20. Carter-O'Connell, I. *et al.* Combining Chemical Genetics with Proximity-Dependent Labeling Reveals Cellular Targets of Poly(ADP-ribose) Polymerase 14

(PARP14). *ACS Chem. Biol.* **13**, 2841–2848 (2018).

21. Langelier, M. F., Zandarashvili, L., Aguiar, P. M., Black, B. E. & Pascal, J. M. NAD+ analog reveals PARP-1 substrate-blocking mechanism and allosteric communication from catalytic center to DNA-binding domains. *Nat. Commun.* **9**, (2018).
22. Wallrodt, S., Simpson, E. L. & Marx, A. Investigation of the action of poly(ADP-ribose)-synthesising enzymes on NAD+ analogues. *Beilstein J. Org. Chem.* **13**, 495–501 (2017).
23. Roux, K. J., Kim, D. I., Raida, M. & Burke, B. A promiscuous biotin ligase fusion protein identifies proximal and interacting proteins in mammalian cells. *J. Cell Biol.* **196**, 801–810 (2012).
24. Roux, K. J., Kim, D. I. & Burke, B. BioID: A screen for protein-protein interactions. *Curr. Protoc. Protein Sci.* **2013**, 19.23.1-19.23.14 (2013).
25. Zhou, Y. *et al.* Metascape provides a biologist-oriented resource for the analysis of systems-level datasets. *Nat. Commun.* **10**, (2019).
26. Todorova, T., Bock, F. J. & Chang, P. Poly(ADP-ribose) polymerase-13 and RNA regulation in immunity and cancer. *Trends Mol. Med.* **21**, 373–384 (2015).
27. Guo, X., Carroll, J.-W. N., MacDonald, M. R., Goff, S. P. & Gao, G. The Zinc Finger Antiviral Protein Directly Binds to Specific Viral mRNAs through the CCCH Zinc Finger Motifs. *J. Virol.* **78**, 12781–12787 (2004).
28. Schwerk, J. *et al.* RNA-binding protein isoforms ZAP-S and ZAP-L have distinct antiviral and immune resolution functions. *Nat. Immunol.* **20**, 1610–1620 (2019).
29. Li, M. M. H. *et al.* Characterization of Novel Splice Variants of Zinc Finger Antiviral

Protein (ZAP). *J. Virol.* **93**, (2019).

30. Limited, P. & Park, C. S. WO 2009/093032 Al. **2009**, (2009).

31. Lu, A. Z. *et al.* Enabling drug discovery for the PARP protein family through the detection of mono-ADP-ribosylation. *Biochem. Pharmacol.* **167**, 97–106 (2019).

32. Kirby, I. T. *et al.* A Potent and Selective PARP11 Inhibitor Suggests Coupling between Cellular Localization and Catalytic Activity. *Cell Chem. Biol.* **25**, 1547-1553.e12 (2018).

33. Morgan, R. K. & Cohen, M. S. A Clickable Aminooxy Probe for Monitoring Cellular ADP-Ribosylation. *ACS Chem. Biol.* **10**, 1778–1784 (2015).

34. Kleine, H. *et al.* Substrate-Assisted Catalysis by PARP-10 Limits Its Activity to Mono-ADP-Ribosylation. *Mol. Cell* **32**, 57–69 (2008).

35. Glowacki, G. *et al.* The family of toxin-related ecto-ADP-ribosyltransferases in humans and the mouse. *Protein Sci.* **11**, 1657–1670 (2009).

36. Jankevicius, G. *et al.* A family of macrodomain proteins reverses cellular mono-ADP-ribosylation. *Nat. Struct. Mol. Biol.* **20**, 508–514 (2013).

37. Rosenthal, F. *et al.* Macrodomain-containing proteins are new mono-ADP-ribosylhydrolases. *Nat. Struct. Mol. Biol.* **20**, 502–507 (2013).

38. Fontana, P. *et al.* Serine ADP-ribosylation reversal by the hydrolase ARH3. *Elife* **6**, 1–20 (2017).

39. MacPherson, L. *et al.* 2,3,7,8-Tetrachlorodibenzo-p-dioxin poly(ADP-ribose) polymerase (TiPARP, ARTD14) is a mono-ADP-ribosyltransferase and repressor of aryl hydrocarbon receptor transactivation. *Nucleic Acids Res.* **41**, 1604–1621 (2013).

40. Hendriks, I. A., Larsen, S. C. & Nielsen, M. L. An advanced strategy for comprehensive profiling of ADP-ribosylation sites using mass spectrometry-based proteomics. *Mol. Cell. Proteomics* **18**, 1010–1024 (2019).

41. Gomez, A. *et al.* Characterization of TCDD-inducible poly-ADP-ribose polymerase (TIPARP/ARTD14) catalytic activity. *Biochem. J.* **475**, 3827–3846 (2018).

42. Leidecker, O. *et al.* Serine is a new target residue for endogenous ADP-ribosylation on histones. *Nat. Chem. Biol.* **12**, 998–1000 (2016).

43. Colaert, N., Helsens, K., Martens, L., Vandekerckhove, J. & Gevaert, K. Improved visualization of protein consensus sequences by iceLogo. *Nat. Methods* **6**, 786–787 (2009).

44. Gao, G., Guo, X. & Goff, S. P. Inhibition of Retroviral RNA Production by ZAP, a CCCH-Type Zinc Finger Protein. *Science (80-.).* **297**, 1703 LP – 1706 (2002).

45. Hayakawa, S. *et al.* ZAPS is a potent stimulator of signaling mediated by the RNA helicase RIG-I during antiviral responses. *Nat. Immunol.* **12**, 37–44 (2011).

46. Karki, S. *et al.* Multiple interferon stimulated genes synergize with the zinc finger antiviral protein to mediate anti-alphavirus activity. *PLoS One* **7**, (2012).

47. MacDonald, M. R., Machlin, E. S., Albin, O. R. & Levy, D. E. The Zinc Finger Antiviral Protein Acts Synergistically with an Interferon-Induced Factor for Maximal Activity against Alphaviruses. *J. Virol.* **81**, 13509–13518 (2007).

48. Lee, H. *et al.* Zinc-finger antiviral protein mediates retinoic acid inducible gene I-like receptor-independent antiviral response to murine leukemia virus. *Proc. Natl. Acad. Sci.* **110**, 12379–12384 (2013).

49. Mao, R. *et al.* Inhibition of Hepatitis B Virus Replication by the Host Zinc Finger

Antiviral Protein. *PLoS Pathog.* **9**, (2013).

50. Müller, S. *et al.* Inhibition of filovirus replication by the zinc finger antiviral protein. *J. Virol.* **81**, 2391–2400 (2007).

51. Leung, A. K. L. *et al.* Poly(ADP-Ribose) Regulates Stress Responses and MicroRNA Activity in the Cytoplasm. *Mol. Cell* **42**, 489–499 (2011).

52. Rappsilber, J., Ishihama, Y. & Mann, M. Stop and go extraction tips for matrix-assisted laser desorption/ionization, nanoelectrospray, and LC/MS sample pretreatment in proteomics. *Anal. Chem.* **75**, 663–670 (2003).

53. Cox, J. & Mann, M. MaxQuant enables high peptide identification rates, individualized p.p.b.-range mass accuracies and proteome-wide protein quantification. *Nat. Biotechnol.* **26**, 1367–1372 (2008).

54. Tyanova, S. *et al.* The Perseus computational platform for comprehensive analysis of (prote)omics data. *Nat. Methods* **13**, 731–740 (2016).

Material and Methods

Key resources table: See excel file.

Cell culture

HEK293T and A549 (ATCC CCL-185) cells were grown in DMEM (Gibco) supplemented with 10% fetal bovine serum (FBS, Millipore Sigma), and glutamax (Gibco) at 37˚C and 5% CO2. Mouse embryonic fibroblasts (MEFs) derived from WT or KO PARP-7 mice were cultured as previously described[3]. Transient transfections of HEK293T cells with 15 ug of expression vectors per 10-cm dish (70% confluency) were performed using the CalPhos system (Clontech) according to manufacturer's instructions. Cells were lysed in HEPES buffer supplemented with 1% Triton X-100, 100 µM fresh TCEP-HCl (Thermo Scientific), cOmplete EDTA-free protease inhibitor (Roche), phosphatase inhibitor cocktail 2 (Sigma-Aldrich), and phosphatase inhibitor cocktail 2 (Sigma-Aldrich). Cell debris was cleared by centrifugation at 10,000 X g for 5 min at 4C.

PARP-7 MARylation target labeling and Neutravidin enrichment for LC-MS/MS analysis

Lysates from HEK 293T cells expressing WT- or IG-PARP-7 (1.169 mg) were diluted to a volume of 336 µl in lysis buffer (25 mM HEPES pH 7.4, 50 mM NaCl, 5 mM $MgCl_2$, 1% NP-40, 1X cOmplete EDTA-free protease inhibitor (Roche), 0.5mM TCEP). The lysates were then split into 6 tubes of 48µl. To each tube, 12 µl of 5X concentration (0.5 mM) 5-Bn-2e-NAD^+ was added for a final concentration of 100 µM in each tube. The samples were then incubated for 2 h shaking at 30˚C. Following incubation, the samples were precipitated with 1 ml 4:1 cold MeOH: CHCl3 for 1hour at -20˚C to remove excess 5-Bn-2e-NAD^+. This step was essential before proceeding to the click reaction. The protein was then pelleted at 6,000g at 4˚C for 30 min. Methanol supernatant was completely removed and the pellet was allowed to dry for approximately 15 min. The pellet was resuspended in 30 µl of 2% SDS and 30 µl of PBS was added. To this 30 µl of 3X concentration click buffer was added (15.8 mM THPTA in PBS, 3.15 mM CuSO4 made fresh in 1X PBS, 0.75 mM Biotin-peg3-azide (Click Chemistry Tools) in DMSO, 15.8 mM sodium ascorbate in PBS, diluted to respective concentrations with 1X PBS). Click conjugation to biotin−peg3-azide was performed for 1 hr at RT. Following click conjugation, WT-PARP-7 samples were pooled and IG-PARP-7 samples were pooled and precipitated overnight with 8 mL cold MeOH at 20˚C. The next day, samples were pelleted at 6,000g 4˚C. Importantly, the samples were pelleted, sonicated for 5 s, resuspended in cold methanol and pelleted again. This process was repeated 3 times with cold methanol and once with cold acetone. This step was essential to remove excess biotin-Peg3-azide before enrichment. The protein was then re-dissolved in 2% SDS and subjected to enrichment using NeutrAvidin agarose (Pierce) and proteolysis as previously described[17],[18],[19],[20].

CG and BioID proteomics methods

All MS methods and data analysis were followed as previously reported [17],[18],[19],[20]. {taken directly from Carter O'connell, 2016 [18]:MS/MS Acquisition and Processing. Digests were loaded onto an Acclaim PepMap 0.1 x 20 mm NanoViper C18 peptide trap (Thermo Scientific) for 5 min at a 5 µl/min flow rate in a 2% acetonitrile, 0.1% formic acid mobile phase and peptides separated using a PepMap RSLC C18, 2 µm particle, 75 µm x 25 cm EasySpray column (Thermo Scientific) using a 7.5–30% acetonitrile gradient over 60 min in mobile phase containing 0.1% formic acid and a 300 nl/min flow rate using a Dionex NCS-3500RS UltiMate RSLCnano UPLC system. Tandem mass spectrometry data was collected using an Orbitrap Fusion Tribrid mass spectrometer configured with an EasySpray NanoSource (Thermo Scientific). Survey scans were performed in the Orbitrap mass analyzer at 120,000 resolution, and data-dependent MS2 scans in the linear ion trap using HCD following isolation with the instrument's quadrupole. Full instrument details can be found at www.peptideatlas.org (ID:

PASS00764). Raw MS/MS scans were interpreted by SEQUEST using a UniProtKB/Swiss-Prot human database amended with sequences for the GFP-tagged PARP variants and common contaminants as previously described (Yan et al., 2010). False discovery rate (FDR) for both peptides and proteins was determined through the addition of a complement of sequence-reversed entries from the full search database and discovery of false identifications as previously described (Wilmarth et al., 2009).} For both the CG method or BioID method, a protein was considered a “valid” target (CG) or interactor (BioID) if the unique peptide count of the identified protein was at least twice as abundant in the IG-PARP-7 or Myc-BirA*-PARP-7 sample in comparison to the control sample (GFP-PARP-7).

In cell MARylation of MycX2-PARP-13.2 by GFP-PARP-7

HEK293T cells were seeded and grown overnight to ~60% confluency on a 6-well plate. The next morning the cells were transfected using CalPhos Mammalian Transfection kit. 1.5 µg of each plasmid (for co-transfection) were used in each well of the 6 well plate and transfection protocol according to manufacturer was followed. After 4-6 h transfection, the media was swapped with fresh warm media. The cells were allowed to grow overnight and typically reached ~90% confluency. The following morning, media was aspirated and cells were washed with 2 ml cold PBS/ well. All PBS was aspirated and the cell plate was frozen in the -80˚C until ready to lyse. Cell plates from -80˚C were taken out onto ice and 75 µl of LysB (50 mM HEPES pH7.4, 150 mM NaCl, 1 mM $MgCl_2$, 1% tritonX-100, 1X protease inhibitor, 1X phosphatase inhibitors, 1µM veliparib, 100 µM TCEP) added to the frozen wells of the plate. The plates were allowed to thaw for about 10 min on ice and the cells were removed from the plate by pipetting up and down in the wells to collect cell lysates. Lysates were transferred to Eppendorf tubes and centrifuged 10,000g for 5 min at 4˚C. The supernatant was transferred to a fresh tube and the protein concentration was determined by the Bradford assay (Biorad). The lysates were brought to 200 µg/60 µl and then 20 µl of 4X sample buffer was added for a final concentration of 2.5 µg/ul. The samples were boiled and 15µl (37.5 µg) of total proteins were separated by 10% SDS-PAGE. Proteins were then transferred to nitrocellulose, blocked with milk and probed for ADPr (CST) 1:1000, GFP (Chromotek, 1:1000), actin (Santa Cruz Biotechnology, 1:1000), and Myc (CST, 1:1000).

***In vitro* MARylation with bacterially expressed PARPs**

GST-PARP-7, His_6-SUMO-PARP-13.2, and His_6-SUMO-PARP-10 were expressed (*E. coli*) and purified as previously described[32]. MARylation reaction conditions: 10 nM PARP-10 or PARP-7, 30 nM PARP-13.2, and 100 uM NAD^+ in HEPES reaction buffer (HRB: 50 mM HEPES, 100 mM NaCl, 10 mM $MgCl_2$, and 0.5 mM TCEP). The MARylation reactions were allowed to proceed at 30˚C and stopped at various time intervals by the addition of sample buffer. The samples were boiled and proteins were separated by 10% SDS-PAGE. Proteins were transferred to nitrocellulose, blocked with milk and probed for ADPr (CST, 1:1000). Coomassie stain was used as a protein loading control.

GST pulldown of recombinant PARP-13.2 by recombinant PARP-7

His_6-SUMO-PARP-13.2 (100 nM) and GST-PARP-7 (100 nM) were incubated in HRB for 1 h at 4˚C. The above mixture was then incubated with either vehicle control, NAD^+ (100 uM), Phthal01 (1uM), or NAD^+ together with Phthal01 (100 ul/sample). After 2 h at 30˚C, protein complexes were enriched using GSH-Sepharose (Cytiva) (50 ul 50% slurry, rotation, 1 h at 4˚C). The beads were washed with HRB containing 1 mM EDTA (3x). The proteins were eluted with 1.5x Sample buffer (80 ul) and boiled for 10 min at 95˚C. Proteins were resolved by 7.5% SDS-PAGE, transferred to nitrocellulose, blocked with milk and probed for ADPr, GST (Proteintech, 1:2000), or His_6 (Fisher Scientific, 1:1000).

Chemical treatment with $HgCl_2$ and NH_2OH

HEK293T cells co-expressing either GFP-PARP-7 and mycX2-PARP-13.2 or GFP-PARP-10 and mycX2-PARP-13.2 were lysed and protein was quantified by Bradford assay and brought to a concentration of ~3 mg/ml. Lysates were then treated with 1% SDS to prior to lysis to prevent to inactivate enzymes. Lysates were then treated either with H_2O (control), 2 mM $HgCl_2$ in H_2O (1.5 h) in ddH2O, 0.4 M neutral NH_2OH in H_2O (15 min). Following treatment, proteins were precipitated by adding cold methanol and incubating samples at -20˚C. Following precipitation with cold methanol, proteins were centrifuged at 6,000g. The methanol was removed and protein pellets were allowed to dry for ~10 min at RT. The protein was resuspended in 1.5X sample buffer containing βME and boiled for 10 min at 95˚C. Proteins were separated by 10% SDS-PAGE, transferred to nitrocellulose, and Western blot analysis was performed to detect ADPr, GFP-PARPs, mycX2-PARP-13.2, and actin.

PARP-7 antibody validation and effects of Phthal01 on endogenous PARP-7 levels in cell culture

A549 cells or WT or KO MEFs PARP-7 (were plated at a density of 2.0 x 10^5 cell per ml in 6-well plates. The following day, the cells were treated for 4 hours with DMSO, 10 nM TCDD, 1 uM Phthal01, or co-treated with TCDD and Phthal01. Cell pellets were collected and lysed in RIPA buffer (20 mM Tris-HCl (pH 7.5), 150 mM NaCl, 1 mM EDTA, 1 mM EGTA, 1% NP-40, 1% sodium deoxycholate) supplemented with 1X protease inhibitor cocktail (Roche). Samples were sonicated at a low intensity for 2 cycles of 30 seconds on/off two times using a Bioruptor and rotated for 30 min at 4^oC. After centrifugation, the protein concentration was determined by BCA assay (Bio-Rad). 40 ug of total protein was separated by SDS-PAGE and transferred to a PVDF membrane. Membranes were incubated with in house generated anti-PARP-7 (1:1000) or anti-*B*-actin in 5% milk overnight. Membranes were stripped, blocked, and re-blotted with anti-PARP-13 (Invitrogen PA5-106389; 1:1000) or with anti-PARP-7 (Abcam 84664 lot# GR3304056-5; 1:1000).

Sample preparation for EThcD MS analysis

Samples were overall prepared as previously described[40,13]. Cell pellets were lysed in guanidinium (6 M guanidine-HCl, 50 mM TRIS, pH 8.5) by alternating vigorous vortexing and vigorous shaking of the samples, after which lysates were snap frozen in liquid nitrogen. Cell lysates were thawed at room temperature, reduced and alkylated by incubation with 5 mM TCEP and 5 mM chloroacetamide (CAA) for 30 min, followed by sonication for 15 seconds at an amplitude of 90%. Protein concentration was measured using Bradford assay (Bio-Rad). Proteins were digested for 3 hours at room temperature using Lysyl Endopeptidase (Lys-C, 1:100 w/w; Wako Chemicals). After initial digestion, samples were diluted with three volumes of 50 mM ammonium bicarbonate (ABC), after which they were digested using modified sequencing grade Trypsin (1:100 w/w; Sigma Aldrich) overnight at room temperature.

Subsequently, protease digestion was terminated by addition of trifluoroacetic acid (TFA) to a final concentration of 0.5% (v/v), and cleared from precipitates by centrifugation in a swing-out centrifuge at 4°C, for 45 min at 4,250g. Peptides were purified by reversed-phase C18 cartridges (SepPak, Waters), which were pre-activated with 5 mL ACN, and equilibrated 2X with 5 mL of 0.1% TFA. After sample loading, cartridges were washed with 3X with 10 mL of 0.1% TFA, after which peptides were eluted using 4 ml of 30% ACN in 0.1% TFA. Eluted peptides were frozen at −80°C overnight, after which they were dried to completion by lyophilization.

Lyophilized peptides were dissolved in AP buffer (50 mM TRIS pH 8.0, 50 mM NaCl, 1 mM MgCl2, and 250 µM DTT), and cleared by centrifugation in a swing-out centrifuge at room temperature, for 30 min at 4,250g. Poly-ADP-ribosylation was reduced to mono-ADP-ribosylation by incubation of samples with recombinant PARG (a kind gift from Prof. Michael O. Hottiger) at a concentration of 1:10,000 (w/w), at room temperature, overnight and with gentle sample agitation. After overnight incubation with PARG, samples were cleared from mild precipitation by centrifugation in a swing-out centrifuge at 4°C, for 60 min at 4,250g. Next, in-house prepared sepharose beads with GST-tagged Af1521 were added to the samples, in a ratio of 50 µl dry beads per 5 mg sample. Samples were incubated in a head-over-tail mixer, at 4°C for 3 h. Afterwards beads were washed twice in ice-cold AP Buffer, twice in ice-cold PBS, and twice with ice-cold MQ water. After each second washing step, tubes were changed in order to minimize non-specific carryover of contaminants. After washing, ADP-ribosylated peptides were eluted off the beads using two bead volumes of ice-cold elution buffer (0.15% TFA). The elution was performed by gentle addition of the elution buffer, gentle mixing of the beads with the buffer every 5 min, and otherwise allowing the beads to stand undisturbed on ice for 20 min. Beads were gently pelleted, and the elutions were transferred to 0.45 µm column filters (Ultrafree-MC, Millipore). Elution of the beads was repeated once, and the two elutions were combined on the 0.45 µm column filters. ADP-ribosylated peptides were then transferred through the filters by centrifugation for 1 min at 12,000g. 100 kDa cut-off filters (Vivacon 500, Sartorius) were pre-washed by surface-washing the filters with 300 µl of MQ water once, spinning 2× 400 µl of MQ water through the filters, surface-washing the filters with 300 µl of 0.15% TFA once, spinning 400 µl of 0.15% TFA through the filters, replacing the collection tubes, and spinning 400 µl of 0.15% TFA through the filters once more. Next, ADP-ribosylated peptides were transferred to the pre-washed 100 kDa cut-off filters, and centrifuged for 10 min at 8,000g.

Samples were basified by addition of ammonium hydroxide to a final concentration of 20 mM. All StageTips were prepared essentially as described previously[52] but were assembled using four layers of C18 disc material (punch-outs from 47mm C18 3M™ extraction discs, Empore). StageTips were activated using 100 µL methanol, and re-activated using 100 µl of 80% ACN in 50 mM ammonium hydroxide. StageTips were equilibrated using 2× 100 µl of 20 mM ammonium hydroxide, after which samples were loaded. The flow-through was collected at this stage (F0). Subsequently, StageTips were washed twice with 100 µl of 20 mM ammonium hydroxide, of which the first wash was collected (F0). Samples were eluted of the StageTips using 80 µl of 30% of ACN in 20 mM ammonium hydroxide (F1). Flow-through from loading of the samples were acidified to a final concentration of 1% TFA (v/v), and then processed as above except using 0.1% formic acid instead of ammonium hydroxide. All samples were vacuum dried to completion in a SpeedVac at 60 °C. Dried purified ADP-ribosylated peptides were dissolved by addition of 10 µl 0.1% formic acid, and stored at −20 °C until MS analysis.

EThcD MS data acquisition

All MS samples were measured using a Fusion Lumos Orbitrap mass spectrometer (Thermo). Samples were analyzed on 15 cm long analytical column, packed in-house using ReproSil-Pur 120 C18-AQ 1.9 µm beads (Dr. Maisch), with an internal diameter of 75 µm. On-line reversed-phase liquid chromatography to separate peptides was performed using an EASY-nLC 1200 system (Thermo). The analytical column was heated to 40°C using a column oven, and peptides were eluted from the column using a gradient of Buffer A (0.1% formic acid) and Buffer B (80% can in 0.1% formic acid). For the main samples (F1), the gradient ranged from 3% buffer B to 40% buffer B over 62 minutes, followed by a washing block of 18 minutes. For the flow-through samples (F0), the gradient ranged from 5% buffer B to 30% buffer B over 35 minutes, followed by a washing block of 15 minutes. Electrospray ionization (ESI) was achieved using a Nanospray Flex Ion Source (Thermo). Spray voltage was set to 2 kV, capillary temperature to 275°C, and RF level to 30%. For F1 samples, full scans were performed at a resolution of 60,000, with a scan range of 300 to 1,750 m/z, a maximum injection time of 60 ms, and an automatic gain control (AGC) target of 600,000 charges. Precursors were isolated with a width of 1.3 m/z, with an AGC target of 200,000 charges, and precursor fragmentation was accomplished using electron transfer disassociation with supplemental higher-collisional disassociation (EThcD) with a supplemental activation energy of 20. Precursors with charge state 3-5 were isolated for MS/MS analysis, and prioritized from charge 3 (highest) to charge 5 (lowest), using the decision tree algorithm. Selected precursors were excluded from repeated sequencing by setting a dynamic exclusion of 60 seconds. MS/MS spectra were measured in the Orbitrap, with a loop count setting of 5, a maximum precursor injection time of 120 ms, and a scan resolution of 60,000. The F0 samples were measured as described above with the following exceptions. Full scans were performed at a resolution of 120,000, with a maximum injection time of 250 ms, and MS/MS spectra were measured at a resolution of 60,000, with a maximum precursor injection time of 500 ms.

EThCD Data analysis

All raw data analysis was performed using MaxQuant software (version 1.5.3.30) supported by the Andromeda search engine[52,53] (Default MaxQuant settings were used, with the following exceptions. Methionine oxidation, N-terminal acetylation, cysteine carbamidomethylation, and ADP-ribosylation on C, D, E, H, K, R, S, T, and Y, were included as variable modifications. Up to 6 missed cleavages were allowed, and a maximum allowance of 4 variable modifications per peptide was used. Second peptide search was enabled (default), and matching between runs was enabled with a match time window of 0.7 minutes and an alignment time window of 20 minutes. Mass tolerance for precursors was set to 20 ppm in the first MS/MS search and 4.5 ppm in the main MS/MS search after mass recalibration. For fragment ion masses, a tolerance of 20 ppm was used. Modified peptides were filtered to have an Andromeda score of >40 (default), and a delta score of >20. Data was automatically filtered by posterior error probability to achieve a false discovery rate of <1% (default), at the peptide-spectrum match, the protein assignment, and the site-specific levels.

In addition to the FDR control applied by MaxQuant, the data was manually filtered using the Perseus software[54] in order to ensure proper identification and localization of ADP-ribosylation. As default MaxQuant intensity assignments to modification sites also include non-localized or poorly localized evidences, intensities were manually mapped back to the sites table based on localized PSMs only (>0.90 best-case, >0.75 for further evidences). The iceLogo web application was used for sequence motif analysis[43], and for sequence comparisons, background sequences were extracted from the same proteins and flanking the same amino acid residue type using an in-house Python script.

Supplementary Figures:

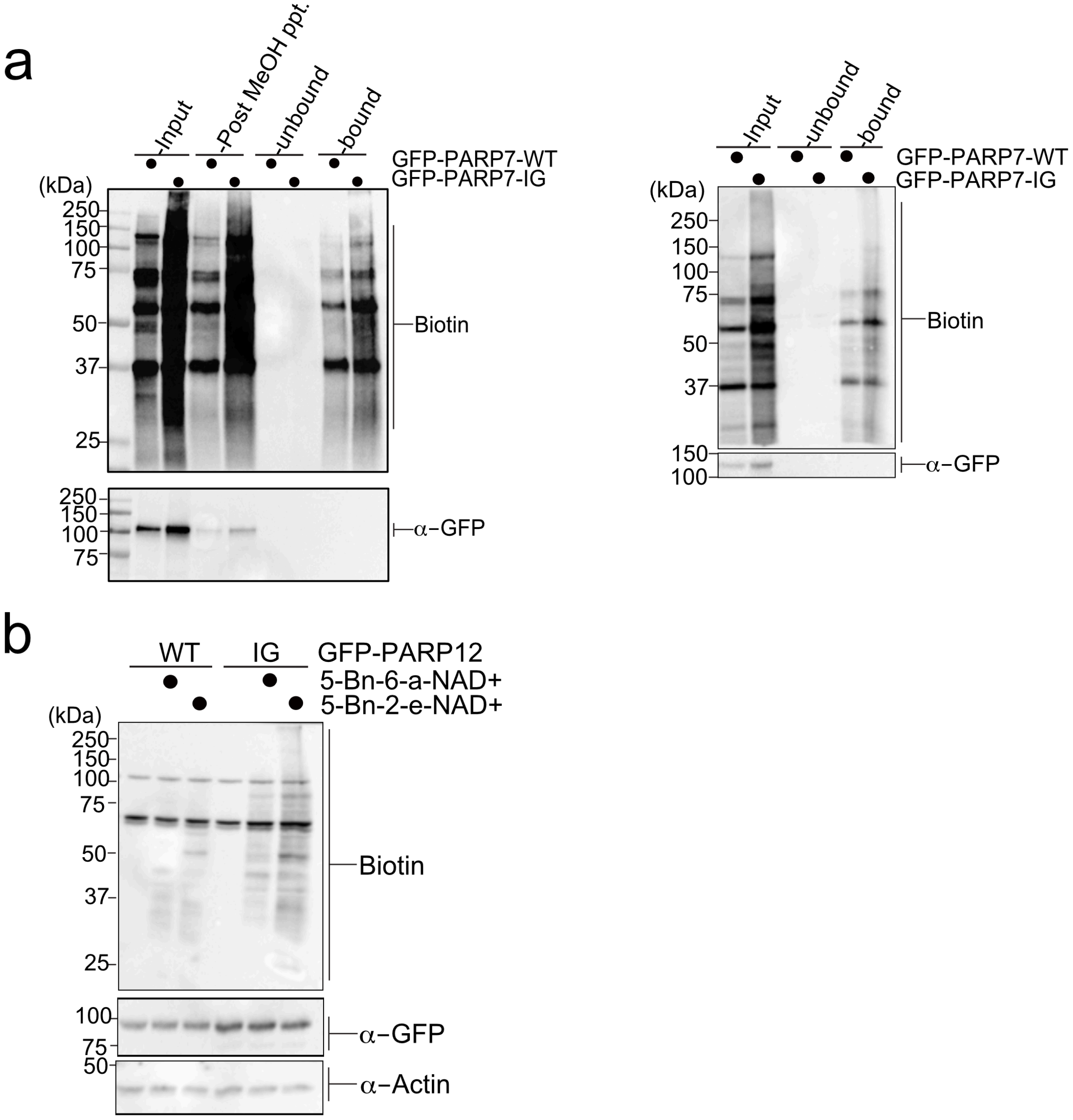

Figure Supplement 2.1. Enrichment of PARP-7 MARylation targets and labeling of PARP-12 IG targets using a chemical genetic approach.

(a) Labeling of PARP-7 MARylation targets was performed as described in Figure 2.1. Neutravidin agarose was used to enrich biotinylated proteins (i.e. MARylation targets). Proteins were resolved by SDS-PAGE and were detected by Western blot using Strep-

HRP (biotin) and an antibody against GFP. The two biological replicates collected in this study are represented here.

(b) Labeling of PARP-12 MARylation targets was performed as described in Figure 2.1. PARP-12 I660G mutant was used. Proteins were resolved by SDS-PAGE and were detected by Western blot using Strep-HRP (biotin) and an antibody against GFP. Representative figure of data collected over two biological replicates.

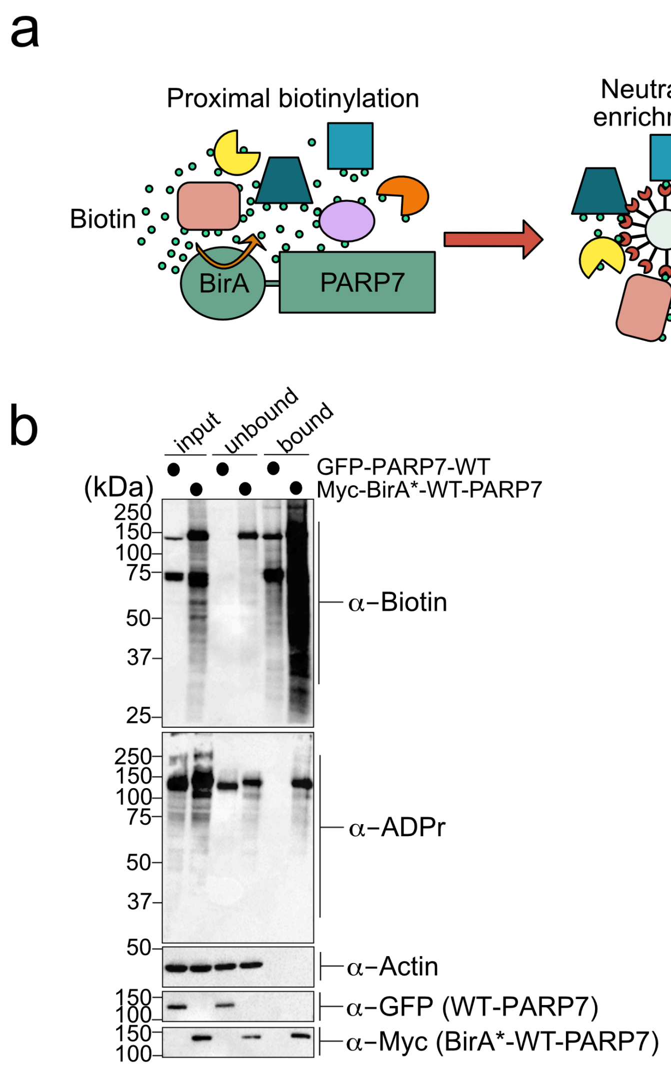

Figure Supplement 2.2. A proximity labeling approach identifies intracellular interactors of PARP-7.

(a) Schematic of proximity labeling approach (referred to as BioID) for identifying interacting proteins of PARP-7 in cells.

(b) Proximity labeling of PARP-7 interactors in cells. Myc-BirA*-WT-PARP-7 or GFP-WT-PARP-7 were expressed in HEK 293T cells (GFP-WT-PARP-7 is used as a negative control). Cells were treated with media supplemented with 50 uM biotin overnight. Neutravidin agarose was used to enrich biotinylated proteins (bound) . Proteins were resolved by SDS-PAGE and were detected by Western blot using Strep-HRP (biotin) and an antibody against GFP.

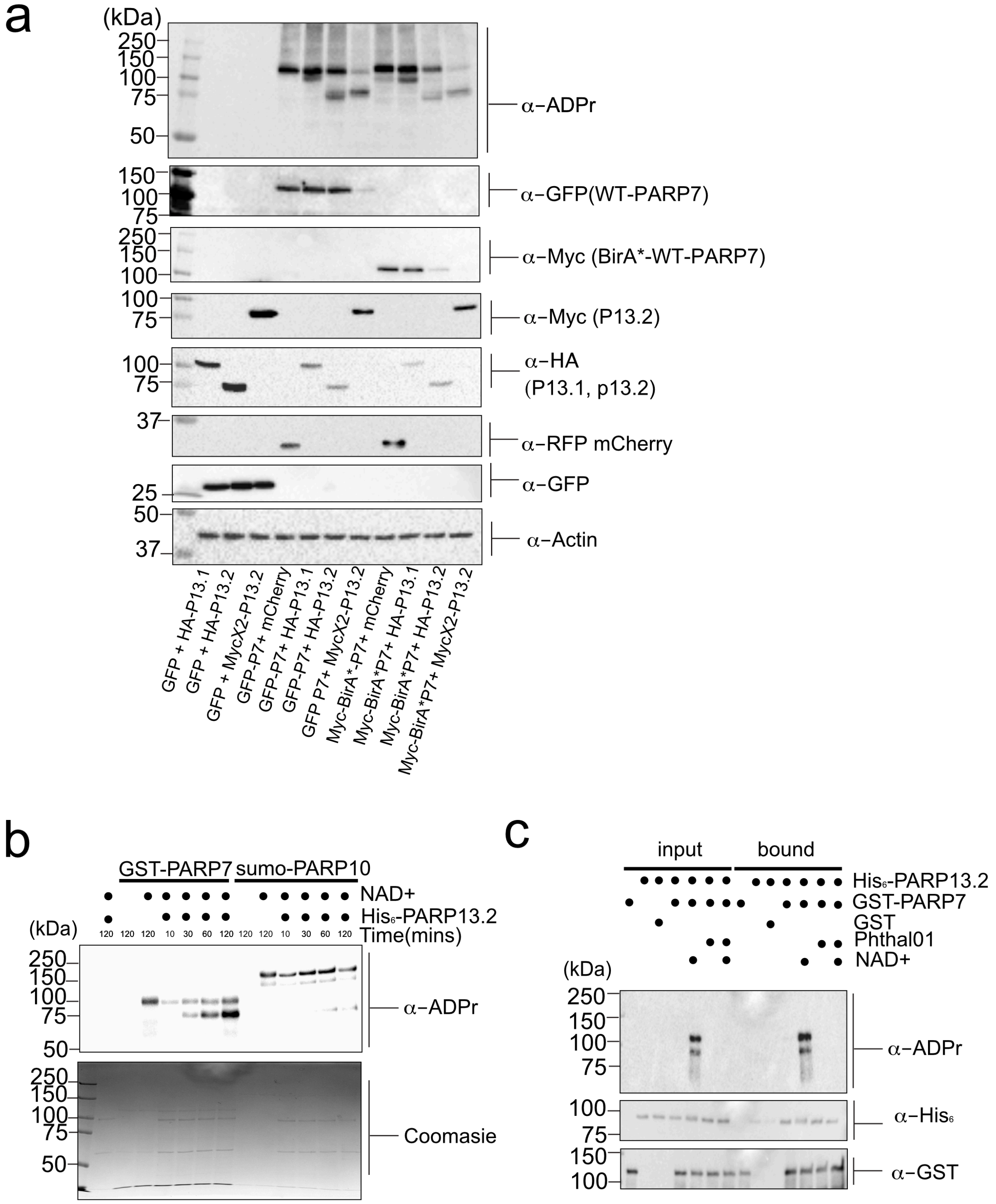
a
(kDa)
250
150
100
75
50
α−ADPr
150
100
75
α−GFP(WT-PARP7)
250
150
100
α−Myc (BirA*-WT-PARP7)
100
75
α−Myc (P13.2)
100
75
α−HA
(P13.1, p13.2)
37
α−RFP mCherry
25
α−GFP
50
37
α−Actin
GFP + HA-P13.1
GFP + HA-P13.2
GFP + MycX2-P13.2
GFP-P7+ mCherry
GFP-P7+ HA-P13.1
GFP-P7+ HA-P13.2
GFP P7+ MycX2-P13.2
Myc-BirA*-P7+ mCherry
Myc-BirA*P7+ HA-P13.1
Myc-BirA*P7+ HA-P13.2
Myc-BirA*P7+ MycX2-P13.2
b
GST-PARP7
sumo-PARP10
NAD+
His6-PARP13.2
Time(mins)
120 120 120 10 30 60 120 120 120 10 30 60 120
(kDa)
250
150
100
75
50
α−ADPr
250
150
100
75
50
Coomasie
c
input
bound
His6-PARP13.2
GST-PARP7
GST
Phthal01
NAD+
(kDa)
250
150
100
75
α−ADPr
100
75
α−His6
150
100
α−GST

Figure Supplement 2.3. Supporting figures for figure 2.3.

(a) PARP-7 MARylates PARP-13.1 and PARP-13.2 in cells. MARylation of PARP-13.1 and 13.2 by PARP-7. GFP-PARP-7 and PARP-13.1 and PARP-13.2 tagged variants were transfected in HEK 293T cells. Proteins were resolved by SDS-PAGE and were detected by Western blot using antibodies against ADPr, GFP, HA, Myc, RFP (mCherry), and actin. Representative figure of data collected over three biological replicates.

(b) PARP-7 MARylates PARP-13.2 *in vitro*. GST-PARP-7 (or His_6-SUMO-PARP-10) was incubated with His_6-SUMO-PARP-13.2 in the presence of NAD^+ (100 uM). MARylation reactions were stopped at indicted time points and proteins were resolved by SDS-PAGE and were detected by Coomassie stain and Western blot using the antibody against ADPr.

(c) The interaction between PARP-7 and PARP-13.2 is independent of PARP-7 catalytic activity. Recombinant GST-PARP-7 and His_6-SUMO-PARP-13.2 were incubated for 1 h and then subjected to GST pulldown following conditions described in the figure. Proteins were resolved by SDS-PAGE and were detected by Western blot using antibodies against ADPr, His_6, and GST.

Enzyme	IC50 (μM)
PARP-1$_{FL}$	0.021±0.004
PARP-2$_{FL}$	0.028±0.005
PARP-3$_{FL}$	0.32±0.002
PARP-4$_{brct\text{-}cat}$	0.35±0.002
PARP-5b$_{cat}$	2.52±0.2
PARP-6$_{FL}$	0.18±0.05
PARP-7$_{FL}$	0.014±0.002
PARP-8$_{FL}$	4.7±1
PARP-10$_{cat}$	0.86±0.3
PARP-11$_{FL}$	0.46±0.02
PARP-12$_{cat}$	>3
PARP-14$_{wwe\text{-}cat.}$	>10
PARP-15$_{cat}$	2.0±0.3
PARP-16$_{FL}$	4.3±1

Figure Supplement 2.4. *In vitro* IC$_{50}$ data for Phthal01 against PARP family members. Phthal01 (6-(4-(2-fluoro-5-((4-oxo-3,4-dihydrophthalazin-1-yl)methyl)benzoyl)piperazin-1-yl)nicotinonitrile) was tested against all active PARP family members using an ADP-ribosylation plate assay developed in our lab[29]. IC$_{50}$ Data represents ± SEM from at least two biological replicates.

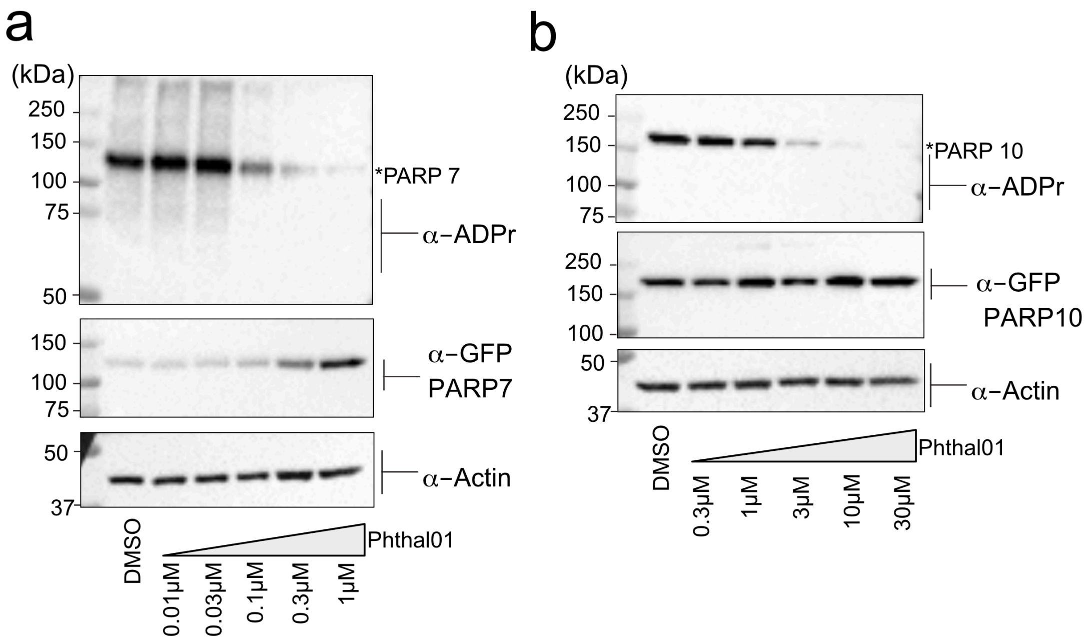

Figure Supplement 2.5. Phthal01 inhibits PARP-7-, and at much higher concentrations, PARP-10-mediated MARylation in cells.

(a) HEK 293T cells expressing GFP-PARP-7 were treated with increasing concentrations of Phthal01 for 16 h. Proteins were resolved by SDS-PAGE and were detected by Western blot using antibodies against ADPr, GFP, and actin.

(b) HEK 293T cells expressing GFP-PARP-10 were treated with increasing concentrations of Phthal01 for 16 h. Proteins were resolved by SDS-PAGE and were detected by Western blot using antibodies against ADPr, GFP, and actin.

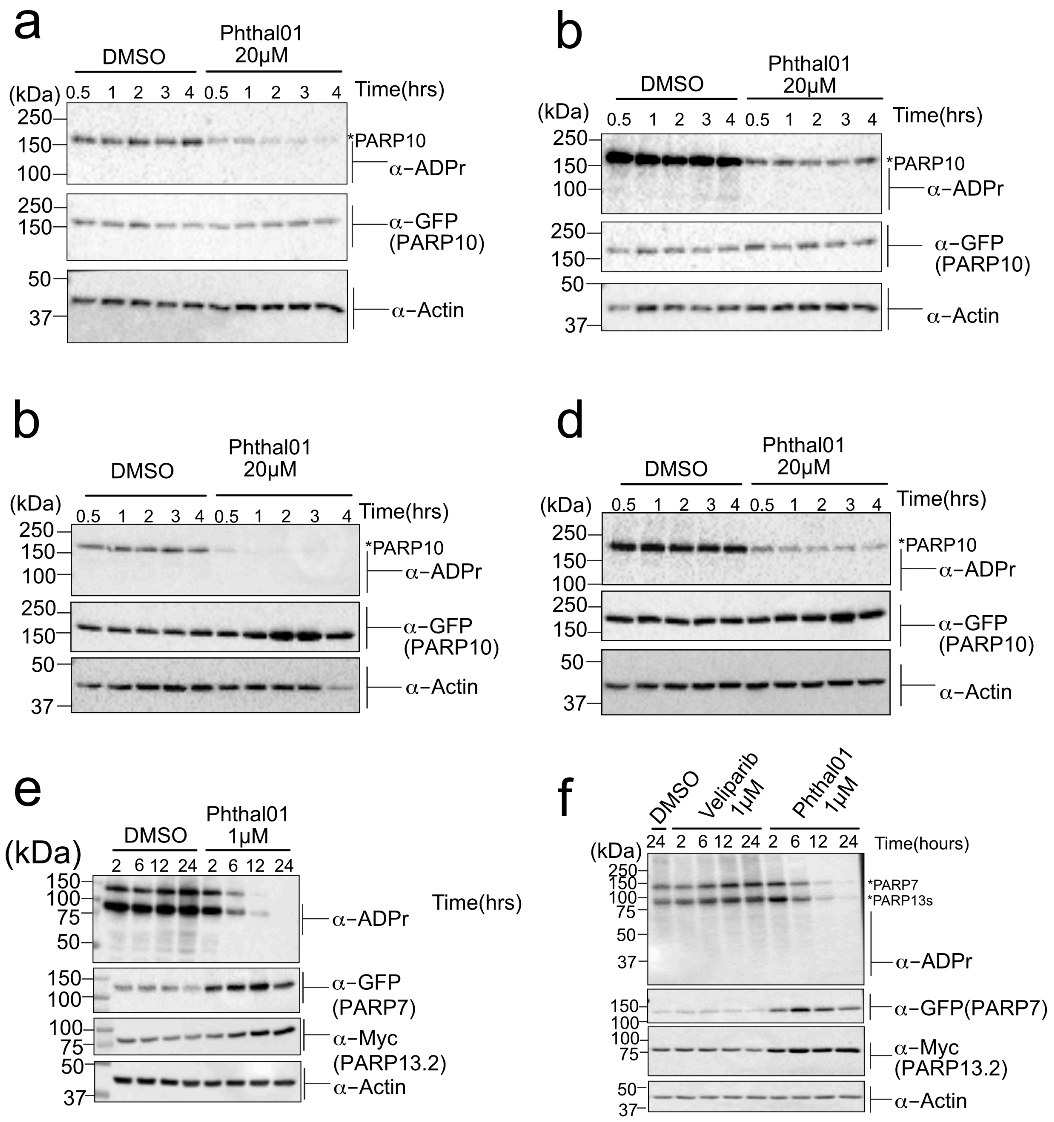

Figure Supplement 2.6. Time course repeats supporting figure 2.4F.

(a-d) Biological replicates of time course inhibition post in-cell (HEK 293T) expression of GFP-PARP-10 using Phthal01 (20 uM).

(d-f) Biological replicates of time course inhibition post in-cell (HEK 293T) expression of PARP-7 using Phthal01 (1uM). See legend of figure 2.4 D-F.

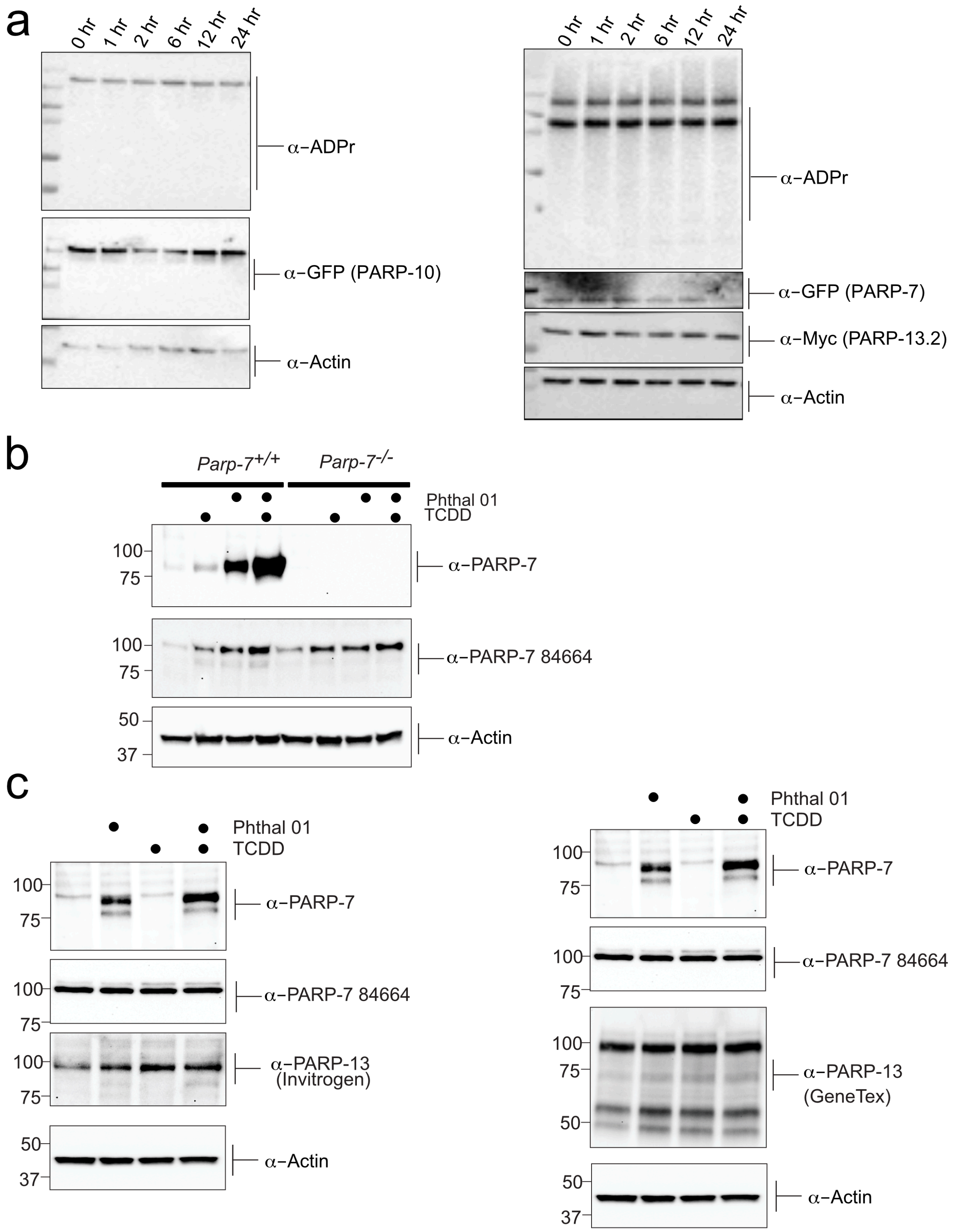

Figure Supplement 2.7. Additional supporting figures for figure 2.4.

(a) Chemical stability of ADPr modification. The chemical stability of PARP-7 and PARP-10 mediated ADPr was assessed by performing a time course post denaturation of HEK293T cellular lysates. Cells we transfected with GFP-PARP-7 and MycX2-PARP-13.2 or GFP-PARP-10, lysed, heat denatured in SDS and allowed to sit at room temperature for the indicated times. Proteins were resolved by SDS-PAGE and were detected by Western blot using antibodies against ADPr, GFP, and actin.

(b) Validation of PARP-7 (TIPARP) antibody in MEF cells (+/+) and (-/-) PARP-7 cells. Cells were treated with TCDD (2,3,7,8 -Tetrachlorodibenzo-p-dioxin) was used to induce PARP-7 and Phthal01 (24hr treatment) used to inhibit PARP-7. Proteins from the resulting lysates were resolved by SDS-PAGE and were detected by Western blot using antibodies against novel PARP-7 (TIPARP), commercially available Anti-PARP-7 antibody (ab84664), and Actin.

(c) Further investigation of endogenous PARP-7 and PARP-13 response to Phthal 01 PARP-7 inhibitor. Cells were treated with TCDD (2,3,7,8 -Tetrachlorodibenzo-p-dioxin) was used to induce PARP-7 and Phthal 01 (24hr treatment) used to inhibit PARP-7. Proteins from the resulting lysates were resolved by SDS-PAGE and were detected by Western blot using antibodies against novel PARP-7 (TIPARP), commercially available Anti-PARP-7 antibody (ab84664), Invitrogen PARP-13 (ZC3HAV1 Antibody PA5-31650), GeneTex PARP-13 antibody (ZC3HAV1 antibody [N3C2]), and Actin.

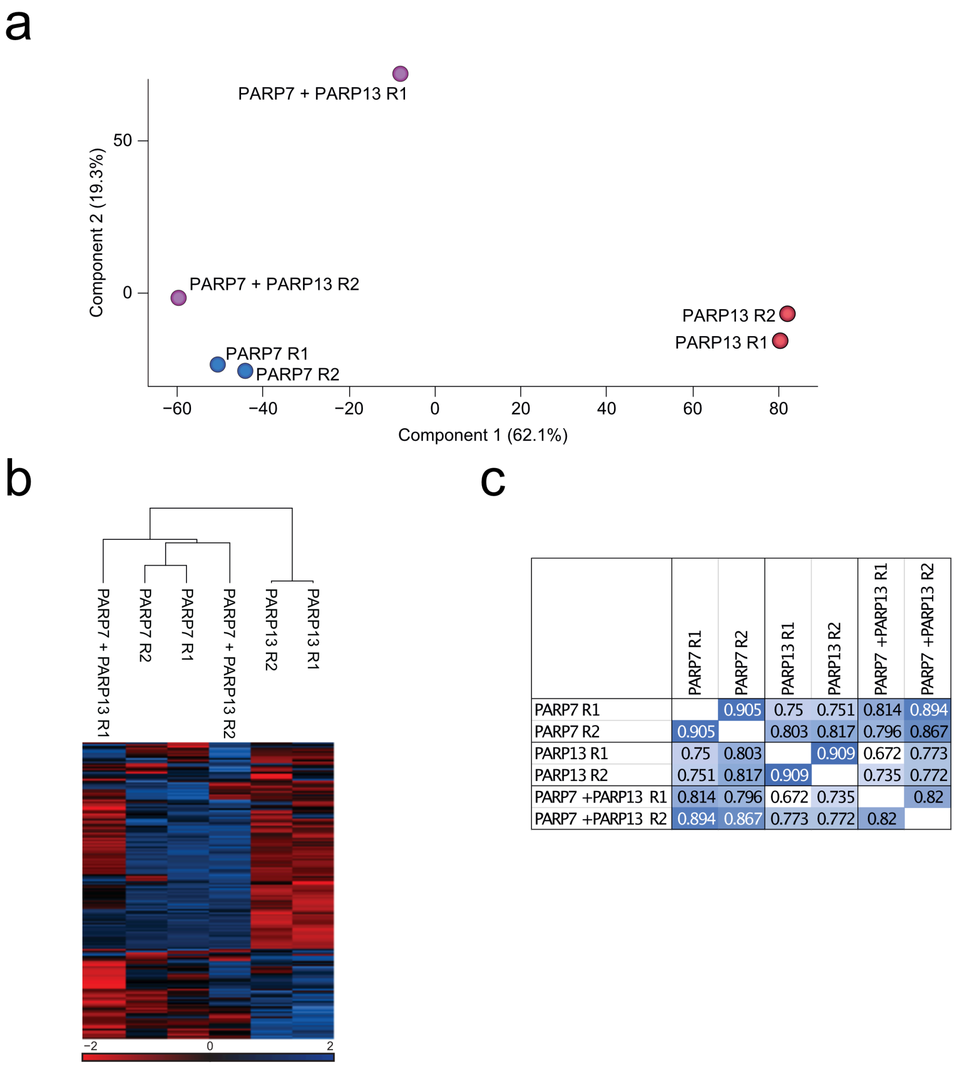

	PARP7 R1	PARP7 R2	PARP13 R1	PARP13 R2	PARP7 +PARP13 R1	PARP7 +PARP13 R2
PARP7 R1		0.905	0.75	0.751	0.814	0.894
PARP7 R2	0.905		0.803	0.817	0.796	0.867
PARP13 R1	0.75	0.803		0.909	0.672	0.773
PARP13 R2	0.751	0.817	0.909		0.735	0.772
PARP7 +PARP13 R1	0.814	0.796	0.672	0.735		0.82
PARP7 +PARP13 R2	0.894	0.867	0.773	0.772	0.82	

Figure Supplement 2.8. EThcD sample correlation data

(a) Principal component analysis (PCA) based upon unnormalized data. Blue; PARP-7 overexpressing replicates, red; PARP-13.2 overexpressing replicates, purple; PARP-7 and PARP-13.2 overexpressing replicates.

(b) Unsupervised hierarchical clustering analysis of z-scored $\log_2$-transformed intensities of ADPr sites.

(c) Pearson correlations of identified ADPr sites (localization probability >0.90).

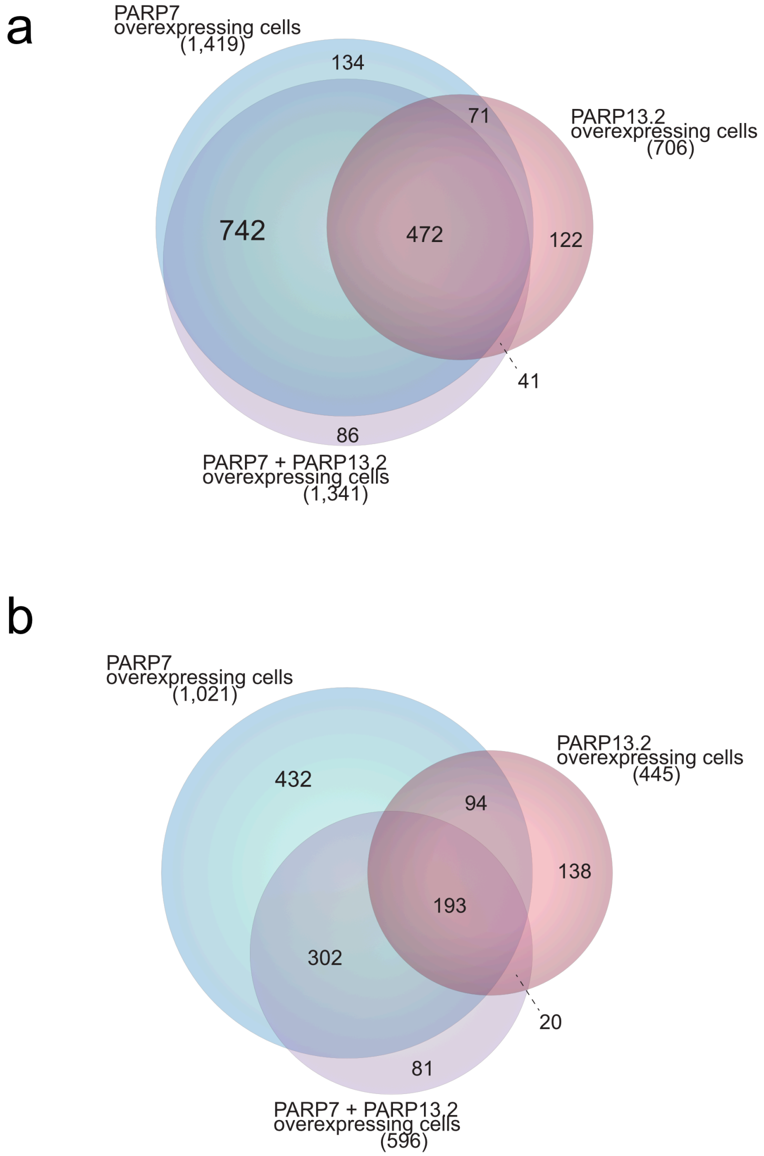

Figure Supplement 2.9. Scaled Venn diagram depicting distributions of ADP-ribosylation sites across samples.

(a) Scaled Venn diagram visualizing distribution of all identified ADP-ribosylation sites (localization probability >0.90) in GFP-PARP-7 overexpressing cells compared to PARP-13.2 overexpressing cells and PARP-7 and PARP-13.2 overexpressing cells.

(b) Scaled Venn diagram visualizing distribution of ADP-ribosylation sites (localization probability >0.90) identified in duplicate in PARP-7 overexpressing cells compared to PARP-13.2 overexpressing cells and PARP-7 and PARP-13.2 overexpressing cells.

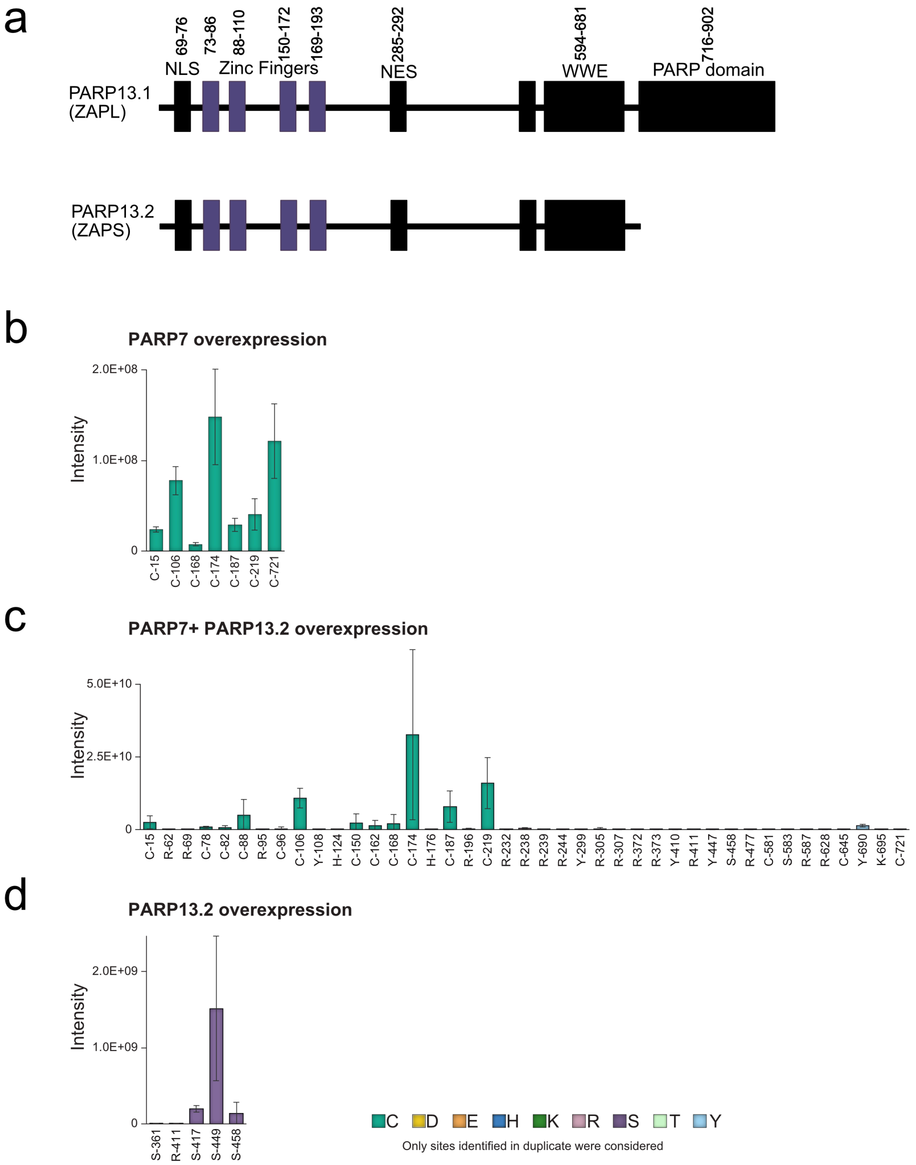

Figure Supplement 2.10. All ADPr sites on PARP-13 identified by EThcD MS

(a) Annotated domain architecture of PARP-13.1 and PARP-13.2.

(b) ADPr sites identified in duplicate on PARP-13in GFP-PARP-7 overexpressing cells.

(c) ADPr sites identified in duplicate on PARP-13 in the GFP-PARP-7 and MycX2-PARP-13.2 overexpressing cells.

(d) ADPr sites identified in duplicate on PARP-13 in the MycX2-PARP-13.2 overexpressing cells.

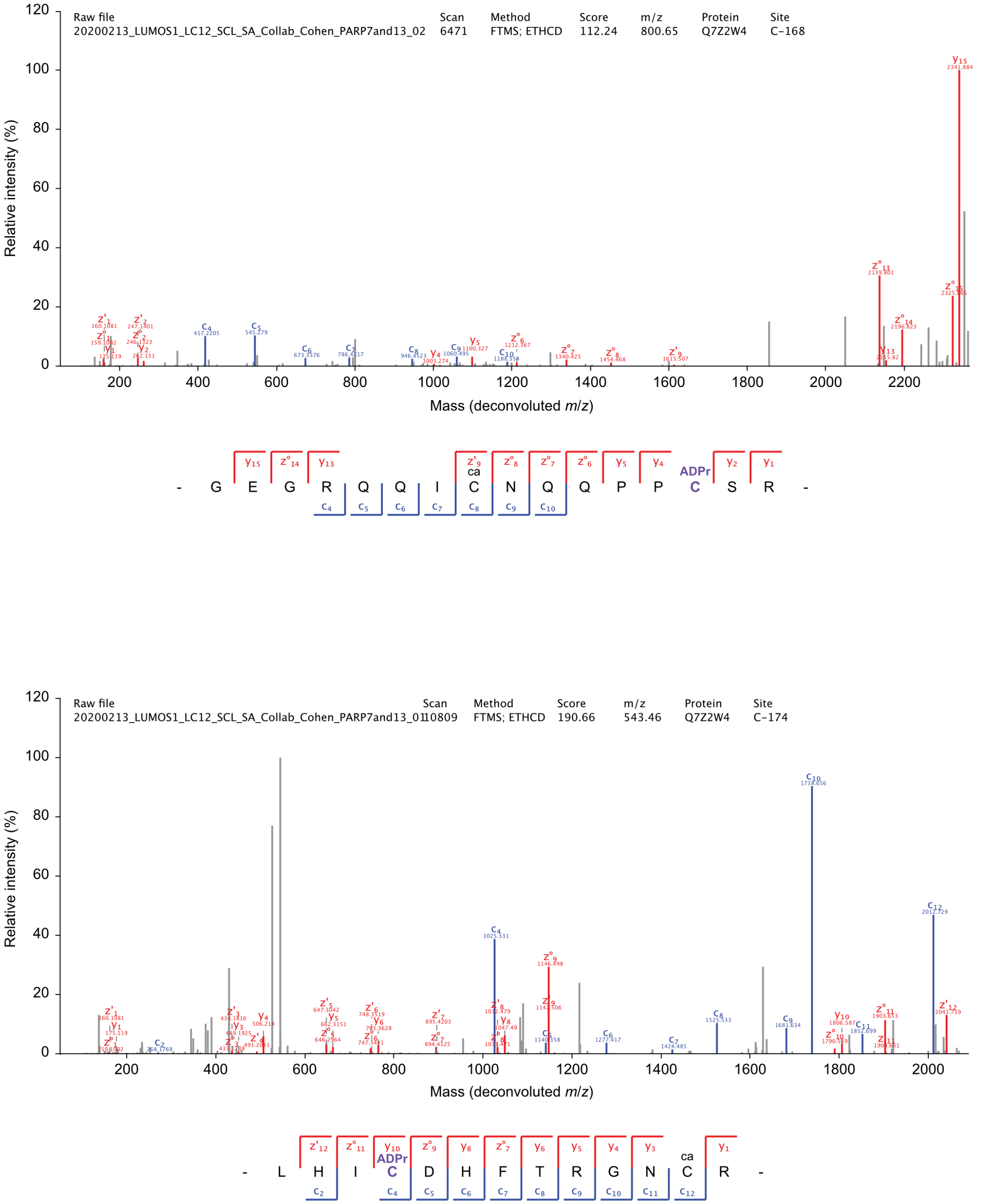

Figure Supplement 2.11. Annotated EThcD MS/MS spectra.

ADP-ribosylation of cysteine residues on PARP-13. Blue; c-ions, red; y-ions and z-ions, grey; unassigned.

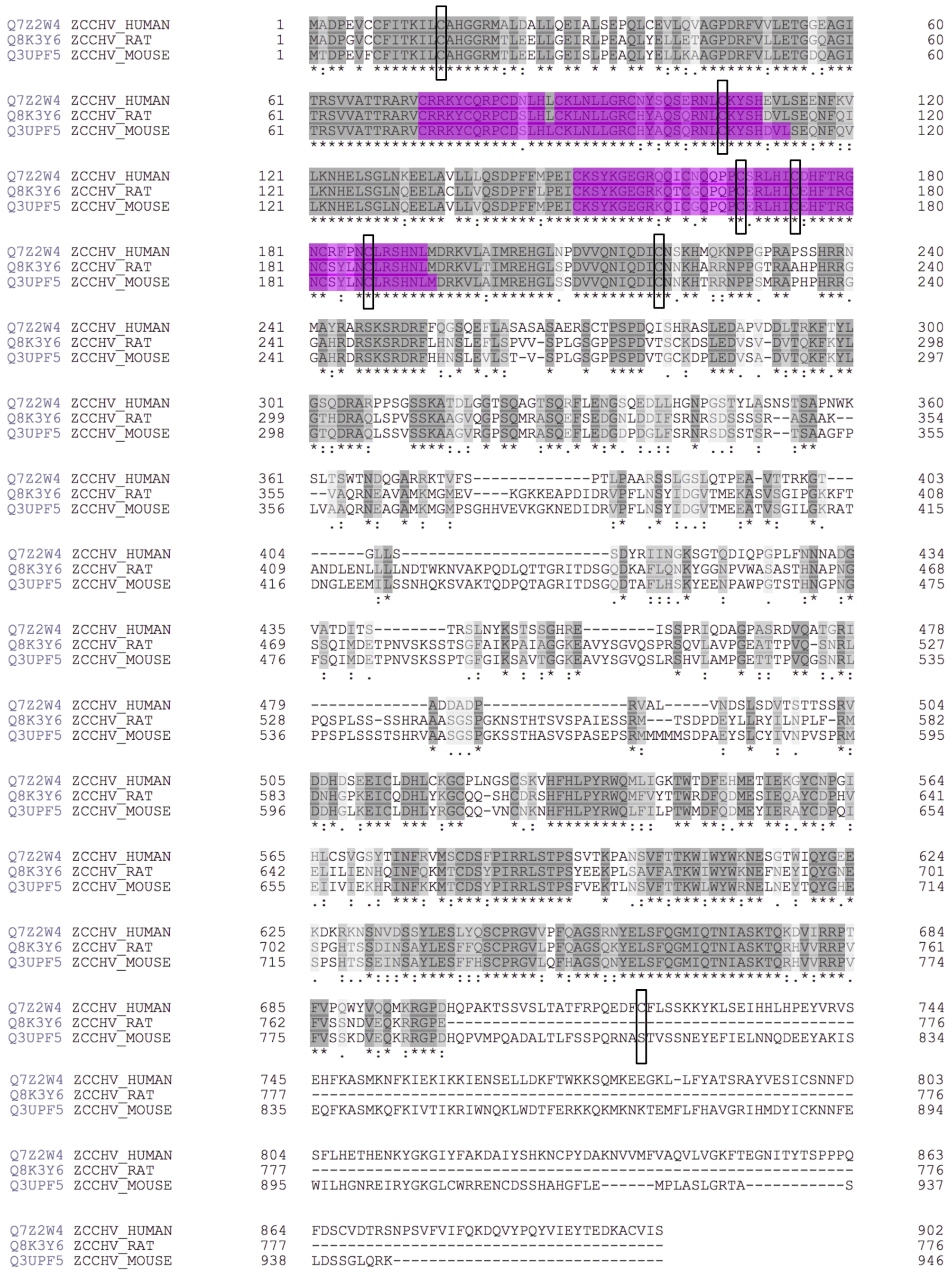

Figure Supplement 2.12. Alignment of PARP-13 human with rat and mouse with PARP-7 MARylation sites labeled.

ADPr sites identified on PARP-13 by EThcD indicated by a black box. All sites identified within the ZnF regions are conserved between species. Only one site identified, within the catalytic domain of PARP-13, C721, is not conserved between species.

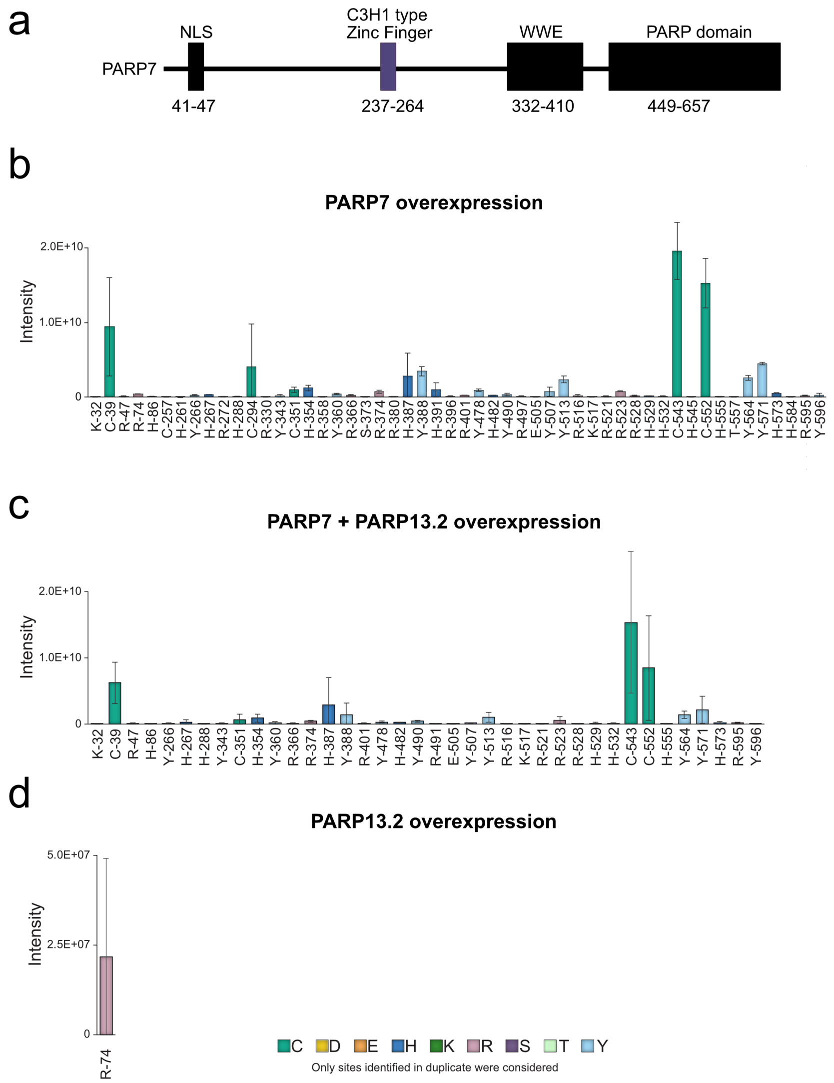

Figure Supplement 2.13. All ADPr sites identified by EThcD MS on PARP-7.

(a) Annotated domain architecture of PARP-7

(b) ADPr sites identified in duplicate on PARP-7 in the GFP-PARP-7 overexpressing cells.

(c) ADPr sites identified in duplicate on PARP-7 in the GFP-PARP-7 and MycX2-PARP-13.2 overexpressing cells

(d) ADPr sites identified in duplicate on PARP-7 in the MycX2-PARP-13.2 overexpressing cells.

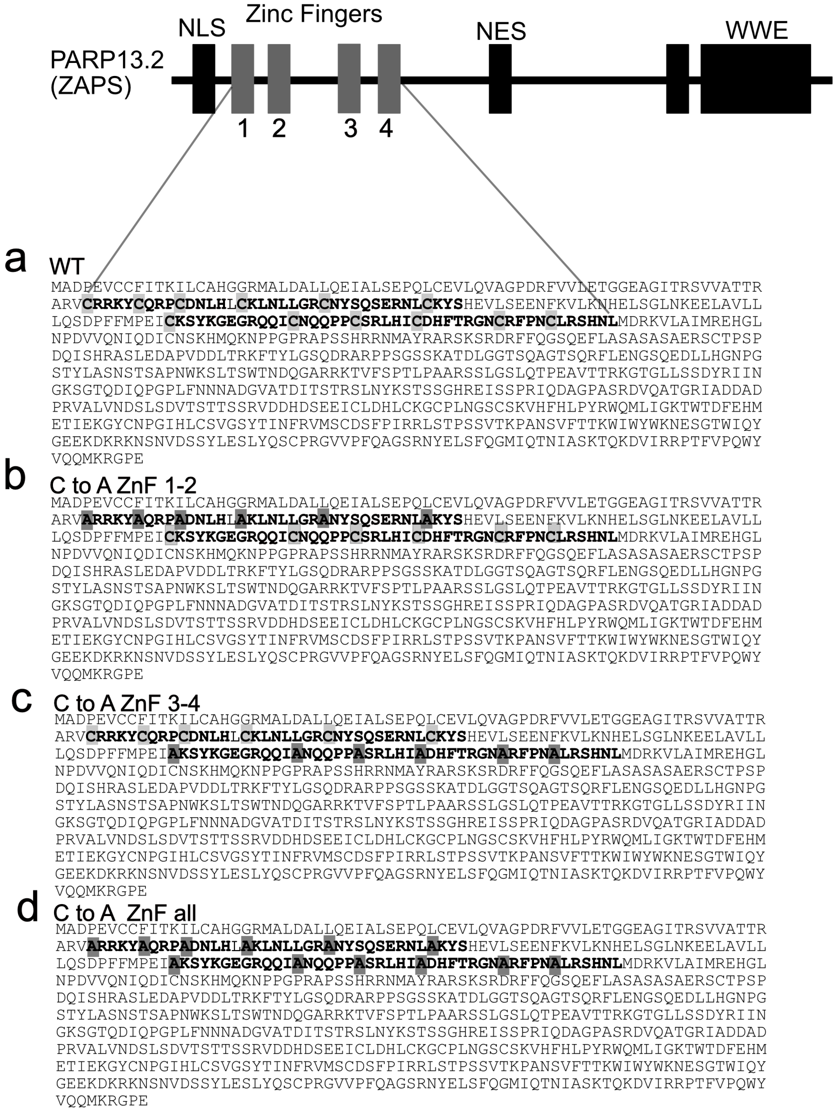

WT

MADPEVCCFITKILCAHGGRMALDALLQEIALSEPQLCEVLQVAGPDRFVVLETGGEAGITRSVVATTR
ARV**CRRKYCQRPCDNLH**L**CKLNLLGRCNYSQSERNLCKYS**HEVLSEENFKVLKNHELSGLNKEELAVLL
LQSDPFFMPEI**CKSYKGEGRQQICNQQPPCSRLHICDHFTRGNCRFPNCLRSHNL**MDRKVLAIMREHGL
NPDVVQNIQDICNSKHMQKNPPGPRAPSSHRRNMAYRARSKSRDRFFQGSQEFLASASASAERSCTPSP
DQISHRASLEDAPVDDLTRKFTYLGSQDRARPPSGSSKATDLGGTSQAGTSQRFLENGSQEDLLHGNPG
STYLASNSTSAPNWKSLTSWTNDQGARRKTVFSPTLPAARSSLGSLQTPEAVTTRKGTGLLSSDYRIIN
GKSGTQDIQPGPLFNNNADGVATDITSTRSLNYKSTSSGHREISSPRIQDAGPASRDVQATGRIADDAD
PRVALVNDSLSDVTSTTSSRVDDHDSEEICLDHLCKGCPLNGSCSKVHFHLPYRWQMLIGKTWTDFEHM
ETIEKGYCNPGIHLCSVGSYTINFRVMSCDSFPIRRLSTPSSVTKPANSVFTTKWIWYWKNESGTWIQY
GEEKDKRKNSNVDSSYLESLYQSCPRGVVPFQAGSRNYELSFQGMIQTNIASKTQKDVIRRPTFVPQWY
VQQMKRGPE

C to A ZnF 1-2

MADPEVCCFITKILCAHGGRMALDALLQEIALSEPQLCEVLQVAGPDRFVVLETGGEAGITRSVVATTR
ARV**ARRKYAQRPADNLH**L**AKLNLLGRANYSQSERNLAKYS**HEVLSEENFKVLKNHELSGLNKEELAVLL
LQSDPFFMPEI**CKSYKGEGRQQICNQQPPCSRLHICDHFTRGNCRFPNCLRSHNL**MDRKVLAIMREHGL
NPDVVQNIQDICNSKHMQKNPPGPRAPSSHRRNMAYRARSKSRDRFFQGSQEFLASASASAERSCTPSP
DQISHRASLEDAPVDDLTRKFTYLGSQDRARPPSGSSKATDLGGTSQAGTSQRFLENGSQEDLLHGNPG
STYLASNSTSAPNWKSLTSWTNDQGARRKTVFSPTLPAARSSLGSLQTPEAVTTRKGTGLLSSDYRIIN
GKSGTQDIQPGPLFNNNADGVATDITSTRSLNYKSTSSGHREISSPRIQDAGPASRDVQATGRIADDAD
PRVALVNDSLSDVTSTTSSRVDDHDSEEICLDHLCKGCPLNGSCSKVHFHLPYRWQMLIGKTWTDFEHM
ETIEKGYCNPGIHLCSVGSYTINFRVMSCDSFPIRRLSTPSSVTKPANSVFTTKWIWYWKNESGTWIQY
GEEKDKRKNSNVDSSYLESLYQSCPRGVVPFQAGSRNYELSFQGMIQTNIASKTQKDVIRRPTFVPQWY
VQQMKRGPE

C to A ZnF 3-4

MADPEVCCFITKILCAHGGRMALDALLQEIALSEPQLCEVLQVAGPDRFVVLETGGEAGITRSVVATTR
ARV**CRRKYCQRPCDNLH**L**CKLNLLGRCNYSQSERNLCKYS**HEVLSEENFKVLKNHELSGLNKEELAVLL
LQSDPFFMPEI**AKSYKGEGRQQIANQQPPASRLHIADHFTRGNARFPNALRSHNL**MDRKVLAIMREHGL
NPDVVQNIQDICNSKHMQKNPPGPRAPSSHRRNMAYRARSKSRDRFFQGSQEFLASASASAERSCTPSP
DQISHRASLEDAPVDDLTRKFTYLGSQDRARPPSGSSKATDLGGTSQAGTSQRFLENGSQEDLLHGNPG
STYLASNSTSAPNWKSLTSWTNDQGARRKTVFSPTLPAARSSLGSLQTPEAVTTRKGTGLLSSDYRIIN
GKSGTQDIQPGPLFNNNADGVATDITSTRSLNYKSTSSGHREISSPRIQDAGPASRDVQATGRIADDAD
PRVALVNDSLSDVTSTTSSRVDDHDSEEICLDHLCKGCPLNGSCSKVHFHLPYRWQMLIGKTWTDFEHM
ETIEKGYCNPGIHLCSVGSYTINFRVMSCDSFPIRRLSTPSSVTKPANSVFTTKWIWYWKNESGTWIQY
GEEKDKRKNSNVDSSYLESLYQSCPRGVVPFQAGSRNYELSFQGMIQTNIASKTQKDVIRRPTFVPQWY
VQQMKRGPE

C to A ZnF all

MADPEVCCFITKILCAHGGRMALDALLQEIALSEPQLCEVLQVAGPDRFVVLETGGEAGITRSVVATTR
ARV**ARRKYAQRPADNLH**L**AKLNLLGRANYSQSERNLAKYS**HEVLSEENFKVLKNHELSGLNKEELAVLL
LQSDPFFMPEI**AKSYKGEGRQQIANQQPPASRLHIADHFTRGNARFPNALRSHNL**MDRKVLAIMREHGL
NPDVVQNIQDICNSKHMQKNPPGPRAPSSHRRNMAYRARSKSRDRFFQGSQEFLASASASAERSCTPSP
DQISHRASLEDAPVDDLTRKFTYLGSQDRARPPSGSSKATDLGGTSQAGTSQRFLENGSQEDLLHGNPG
STYLASNSTSAPNWKSLTSWTNDQGARRKTVFSPTLPAARSSLGSLQTPEAVTTRKGTGLLSSDYRIIN
GKSGTQDIQPGPLFNNNADGVATDITSTRSLNYKSTSSGHREISSPRIQDAGPASRDVQATGRIADDAD
PRVALVNDSLSDVTSTTSSRVDDHDSEEICLDHLCKGCPLNGSCSKVHFHLPYRWQMLIGKTWTDFEHM
ETIEKGYCNPGIHLCSVGSYTINFRVMSCDSFPIRRLSTPSSVTKPANSVFTTKWIWYWKNESGTWIQY
GEEKDKRKNSNVDSSYLESLYQSCPRGVVPFQAGSRNYELSFQGMIQTNIASKTQKDVIRRPTFVPQWY
VQQMKRGPE

Figure Supplement 2.14. Sequences of CtoA PARP-13.2 mutants.

(a) Wildtype PARP-13.2.

(b) PARP-13.2 CtoA ZnF 1-2 mutant, sequence verified.

(c) PARP-13.2 CtoA ZnF 3-4 mutant, sequence verified..

(d) PARP-13.2 CtoA ZnF all mutant, sequence verified.

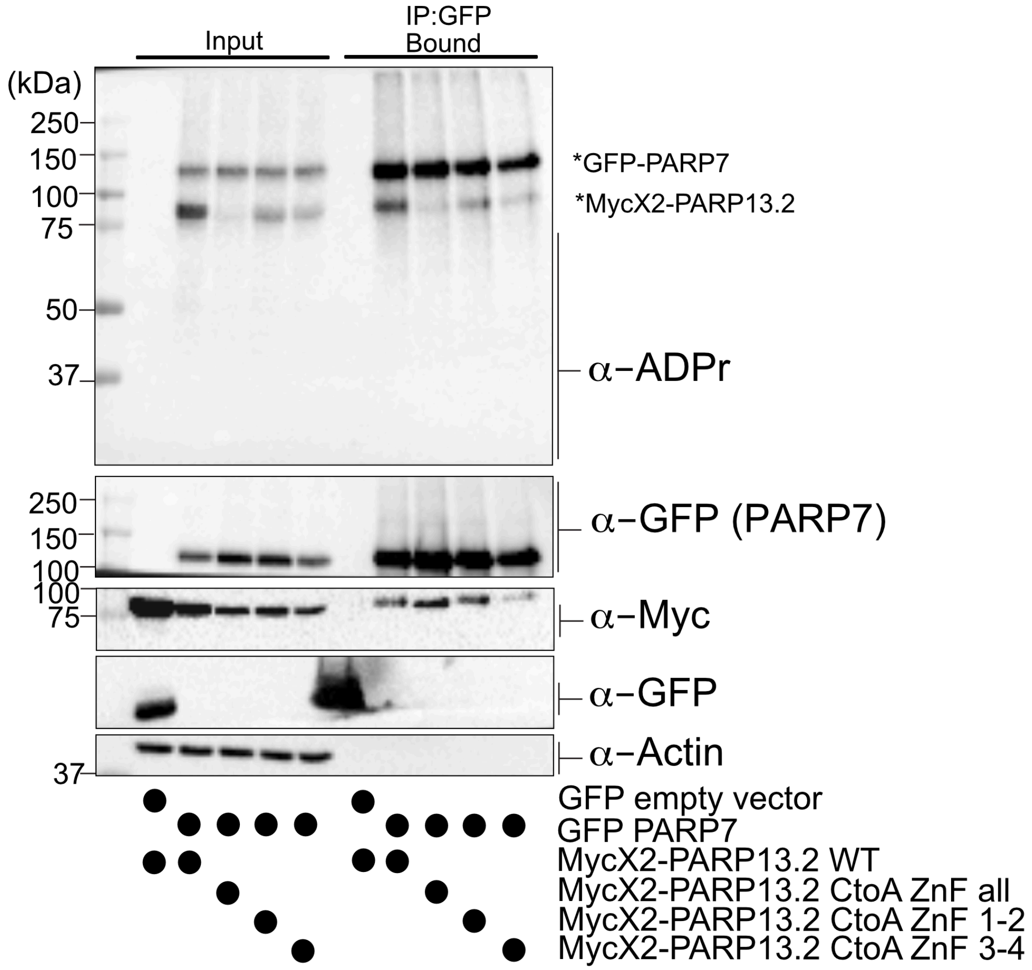

Figure Supplement 2.15. Mutation of Cys residues in the ZnF domain of PARP-13.2 do not disrupt PARP-7 binding.

MycX2 PARP-13.2 WT or ZnF domain mutants were co-expressed with GFP empty vector or GFP PARP-7 in HEK 293T cells. Proteins were resolved by SDS-PAGE and were detected by Western blot using antibodies against ADPr, GFP, Myc, and actin. GFP-PARP-7 was immunoprecipitated using GFP-nanobody magnetic beads (Chromotek). Representative figure of data collected over two biological replicates.

General Chemistry methods section:

General. ^{1}H NMR were recorded on a Bruker DPX spectrometer at 400 MHz. Chemical shifts are reported as parts per million (ppm) downfield from an internal tetramethylsilane standard or solvent references. Dichloromethane (DCM), tetrahydrofuran (THF), and Dimethylformamide (DMF) were dried using a solvent purification system manufactured by Glass Contour, Inc. (Laguna Beach, CA). Additional drying of solvents, where indicated in methods, occurred using 3Å or 4Å activated sieves. All other solvents were of ACS chemical grade (Fisher Scientific) and used without further purification unless otherwise indicated. Commercially available chemical compounds were purchased from CombiBlocks (San Diego, CA), and TCI America (Portland, OR) and were >95% pure and used without further purification. All other reagents were of ACS chemical grade (Fisher Scientific) and used as received. 5-Bn-6-a-NAD$^+$ was synthesized as previously described[18]. HPLC Methods: Gradient 10 mM tributylamine/30 mM acetic acid pH 4.4 to 100% methanol over 16 mins using c18 column.

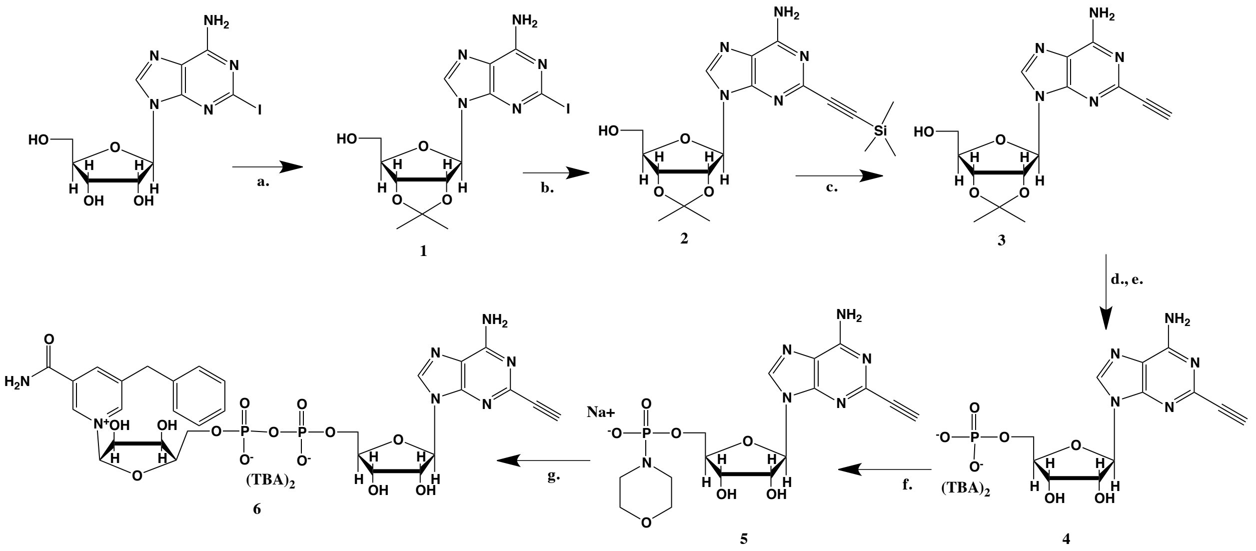

Scheme 2.1. Synthesis of 5-bn-2-ethynyl NAD$^+$. (a) p-TsOH, acetone, sodium carbonate; (b) (PPh$_3$) PdCl$_2$, CuI, TEA, TMS-acetylene; (c) 7N NH$_3$/MeOH; (d) POCl$_3$,TEA, THF, 0˚C; (e) TFA, 1:1 MeOH H2O; (f) PPh$_3$, Morpholine, 2,2-DPS, 0.2 M NaI in ACN; (g) 5-Bn-NMN, MgSO$_4$, 0.2 M MnCl$_2$ in dry formamide

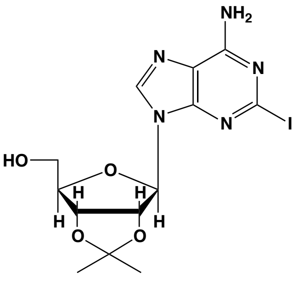

1

2-iodo-adenosine-acetonide (1). Commercially available 2-iodo-adenosine (500 mg, 1.3 mmol) was taken up into 13 ml of acetone. To this mixture, *p*-toluene sulfonic acid (3 eq., 3.9 mmol) of was added and stirred for 1 h. Consumption of the starting material was observed by TLC. The reaction was neutralized with 1 M sodium carbonate until pH = 7.0 was achieved. The product was extracted 3X with chloroform and concentrated *in* *vacuo* to yield a fine white crystalline powder. 70% yield. ^{1}H NMR (400 MHz, DMSO-d_6) δ 8.28 (d, *J* = 1.4 Hz, 1H), 7.76 (s, 2H), 6.06 (d, *J* = 2.7 Hz, 1H), 5.34 – 5.20 (m, 1H), 5.07 (t, *J* = 5.4 Hz, 1H), 4.94 (dd, *J* = 6.2, 2.8 Hz, 1H), 4.25 – 4.13 (m, 1H), 3.54 (s, 2H), 1.55 (s, 3H), 1.34 (s, 3H).

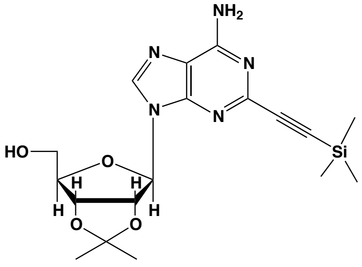

2

2-ethynyl-TMS-adenosine-acetonide (2). In a clean, oven dried round bottom flask with stir bar, **1** (342 mg, 0.78 mmol) and copper iodide (0.2 eq., 0.158 mmol) were dissolved in 5 ml dry DMF. The flask was evacuated under high vacuum and refilled with argon several times. Under argon, the flask was capped with a septum and argon was allowed to bubble through a needle through the solution for 20 min. 0.1 equivalents (55 mg, 0.16 mmol) of Bis(triphenylphosphine)palladium(II) Dichloride was added to the solution while still under argon. To the capped solution, trimethylsilylacetylene (1.5, eq., 164 µl, 1.18 mmol) of was added via syringe. To this solution, triethylamine was added (3 eq., 330 µl, 2.37 mmol) via syringe. The reaction was covered in aluminum foil and a balloon filled with argon was placed into the septum of the capped reaction and the reaction was allowed to progress, stirring overnight at RT. The reaction turned a deep brown color overnight. DMF was evaporated *in vacuo* in a water bath set to 40˚C. The residue was taken up into 25 ml ethyl acetate and remaining DMF was extracted from the organic layer with 25 ml brine (3X). The organic layer was dried over sodium sulfate, concentrated and purified via combi flash (MP A: hexanes, MP B: ethyl acetate; 0-3 min: 0-100%B, 3-18 min: 100%B). Fractions containing desired compound were pooled and concentrated to yield 191mg of product 60% yield. ^{1}H NMR (400 MHz, DMSO-d_6) δ 8.44 (s, 1H), 7.55 (s, 2H), 6.08 (d, *J* = 2.9 Hz, 1H), 5.28 (dd, *J* = 6.1, 2.9 Hz, 1H), 5.20 – 5.08 (m, 1H), 4.95 (dd, *J* = 6.1, 2.7 Hz, 1H), 4.22 (s, 1H), 3.54 (t, *J* = 5.1 Hz, 2H), 1.56 (s, 3H), 1.34 (s, 3H), 0.25 (d, *J* = 1.0 Hz, 9H).

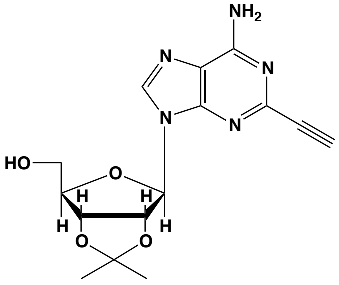

3

2-ethynyl-adenosine-acetonide (3). In a clean, dry round bottom flask, 20 ml of saturated 7N ammonia in methanol was added to **2** (200 mg, 0.5 mmol) and stirred for 1.5 h until complete trimethylsilyl deprotection was observed by TLC. The reaction was concentrated *in vacuo*. The crude residue was purified via combi flash (MP A: hexanes, MP B: ethyl acetate; 0-1 min: 0-100% B, 1-18 min: 100% B). Fractions containing desired compound were pooled and concentrated to yield 122 mg of off-white powder (74% yield). ^{1}H NMR (400 MHz, DMSO-d_6) δ 8.43 (s, 1H), 7.55 (s, 2H), 6.10 (d, *J* = 2.9 Hz, 1H), 5.30 (dd, *J* = 6.1, 3.1 Hz, 1H), 5.16 (t, *J* = 5.5 Hz, 1H), 4.96 (dd, *J* = 6.2, 2.5 Hz, 1H), 4.23 (d, *J* = 3.0 Hz, 1H), 3.55 (q, *J* = 5.0 Hz, 2H), 1.56 (s, 3H), 1.34 (s, 3H).

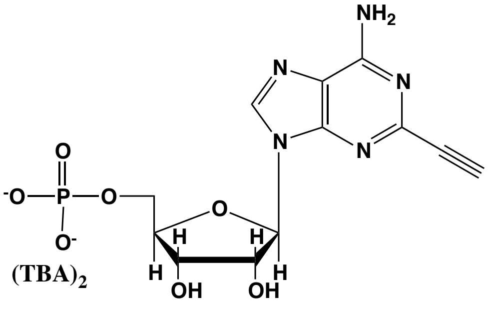

4

2-ethynyl-AMP (4). In a clean, dry round bottom flask, 5.1 ml dry THF was added to **3** (0.51 mmol, 170 mg). Triethylamine (12 eq., 858 µl, 6.1 mmol) were added to the solution and cooled to 0˚C in an ice bath. Once cooled, Phosphorous (V) oxychloride ($POCl_3$) (2 eq. , 95 µl, 1.02 mmol,) was added dropwise to the solution. Consumption of the starting material was monitored by TLC (100% ethyl acetate). To quench the reaction, 5.1 ml of H_2O was added to the solution. The solution was concentrated to dryness and co-evaporated with acetonitrile and methanol. The residue was rinsed with ether. The resulting residue was resuspended in chloroform. The desired compound, insoluble in chloroform, crashed out and the resulting TEA salt was filtered out from the mixture. Without further purification the solid was dissolved in 8.2 ml of a 1:1 mixture of H_2O and methanol. Trifluoracetic acid (65 eq., 2.0 ml, 27.0 mmol,) was added dropwise to the solution at room temperature and stirred until complete deprotection of the acetonide moiety was observed by analytical HPLC. The mixture was concentrated to a small volume (less than 2 ml) *in vacuo* and the liquid was purified on reverse phase chromatography using a Combiflash Companion system (C18Aq 5.5 g Redisep Rf; MP A: 10 mM tributylamine/30 mM acetic acid pH 4.4 (aq.), MP B: methanol; 0-1 min: 0% B, 1-12 min: 0-50% B, 12-16 min: 100% B). Fractions containing desired product were pooled and concentrated in vacuo to yield the tributylammonium (TBA) salt of the product (80 mg, 35% yield over two steps). ^{1}H NMR (400 MHz, D_2O) δ 8.67 (s, 1H), 6.14 (d, *J* = 4.9 Hz, 1H), 4.49 (t, *J* = 4.7 Hz, 1H), 4.39 (d, *J* = 3.0 Hz, 1H), 4.24 – 4.11 (m, 1H), 4.06 (s, 1H), 3.36 – 3.24 (m, 2H).

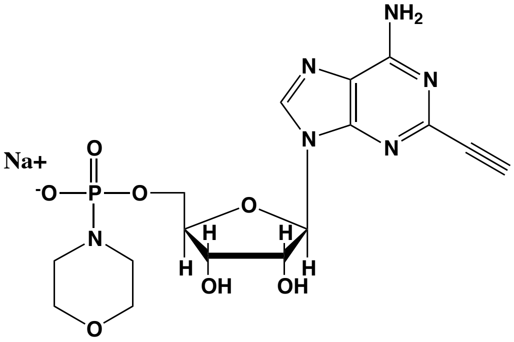

5

2-ethynyl-AMP-morpholidate (5). In a clean oven-dried round bottom flask with stir bar, **4** (80 mg, 0.144 mmol) was taken up into 2.5 mL of DMSO (dried over 3Å sieves overnight). 5 ml of dry DMF was co-evaporated 3 times *in vacuo* with the solution in a water bath set to 35˚C. After the third co-evaporation, the solution was allowed to sit under high vacuum pressure for 30 min. The solution was taken off of vacuum pressure under argon gas and capped with a septum and argon balloon. Under argon pressure and in the order listed, triphenyl phosphine (202 mg, 0.77 mmol), morpholine (108 µl, 1.24 mmol), and 2,2'-dipyridyl disulfide (170 mg, 0.77 mmol) were added to the solution. The reaction was allowed to take place for 1.5 h until consumption of the starting material was observed by HPLC. The desired compound was precipitated out in 0.2 M NaI in acetonitrile (dry) and filtered using a fine filter glass funnel. The result was an off-white powder (36 mg, 57% yield). ^{1}H NMR (400 MHz, D_2O) δ 8.45 (s, 1H), 6.04 (d, *J* =

4.8 Hz, 1H), 4.49 (t, *J* = 4.7 Hz, 1H), 4.31 (s, 1H), 3.99 (d, *J* = 12.0 Hz, 2H), 3.51 (s, 4H), 3.30 (s, 1H), 2.98 – 2.73 (m, 4H).

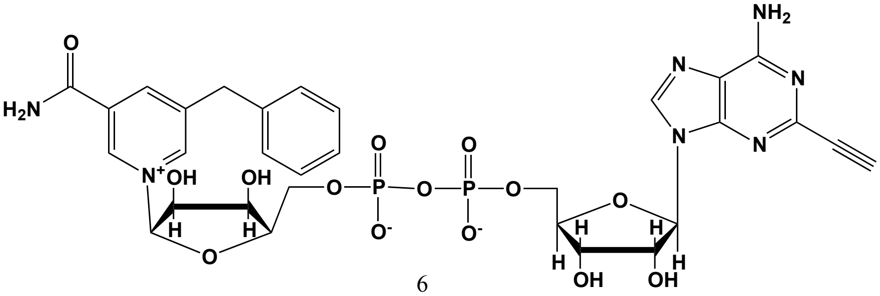

6

5-benzyl-2-ethynyl-NAD$^+$ (6). 5-benzyl-nicotinamide mononucleotide (2 eq., 29 mg, 0.068 mmol), synthesized as previously reported[18], was taken up into 2 ml dry toluene in a scintillation vile and concentrated *in vacuo* (3X) to remove excess water. 30 min under high vacuum, the solid was capped with a septum under argon pressure. **5** (15 mg, 0.034 mmol), after overnight desiccation in a chamber containing P_2O_5, was added along with $MgSO_4$ (8 mg, 0.068 mmol) to the scintillation vile containing 5-Bn-NMN under argon pressure. 500 µl of 0.2 M $MnCl_2$ in dry formamide was added to the solids via syringe and the reaction was stirred overnight under Argon balloon at room temperature. The reaction was checked by HPLC. After complete consumption of **5** was observed overnight, the reaction was diluted with 1.5 mL 10 mM tributylamine/30 mM acetic acid [pH = 4.4] and purified using HPLC. Retention time 8.5 min. The fractions containing desired compound were pooled and co-evaporated with acetonitrile (to remove excess water) and methanol to remove excess tributylamine. The resulting compound was a white powder (13 mg, 33% yield). ^{1}H NMR (400 MHz, D_2O) δ 9.16 (s, 1H), 9.00 (s, 1H), 8.87 (s, 1H), 8.60 (s, 1H), 8.52 (s, 1H), 7.29 (m, 5H), 5.98 (d, J = 5.0 Hz, 1H), 5.92 (d, J = 5.2 Hz, 1H), 4.30 - 4.24 (m, 11H), 3.53 (s, 1H).

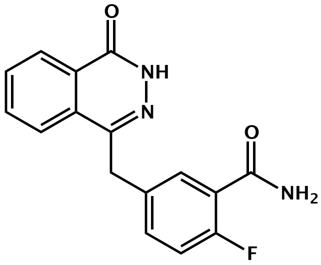

2-fluoro-5-((4-oxo-3,4-dihydrophthalazin-1-yl)methyl)benzamide: 2-fluoro-5-((4-oxo-3,4-dihydrophthalazin-1-yl)methyl)benzoic acid (50 mg, 0.17 mmol) was added to a flame dried flask and dissolved in $SOCl_2$ (20 ml) and refluxed at 80˚C for 45 min. The reaction mixture was cooled to 0˚C and then added dropwise to ice cold anhydrous NH_3/MeOH (7 N, 100 ml). White solids quickly precipitated from an orange solution accompanied by rapid heating of the reaction vessel and smoke. The reaction was left to stir over night and the product collected as a solid by vacuum filtration: 50 mg (100%).

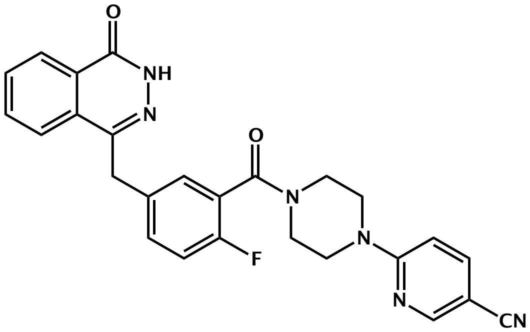

6-(4-(2-fluoro-5-((4-oxo-3,4-dihydrophthalazin-1-yl)methyl)benzoyl)piperazin-1-yl)nicotinonitrile (Phthal 01): 2-fluoro-5-((4-oxo-3,4-dihydrophthalazin-1-yl)methyl)benzoic acid (50 mg, 0.17 mmol), TBTU (60 mg, 0.19 mmol) and 6-(piperazin-1-yl)nicotinonitrile (36 mg, 0.19 mmol) were added to a flame dried flask and dissolved in anhydrous DMF/DCM (1:10) (5 mL). DIPEA (0.06 mL, 0.34 mmol) was added under argon and the reaction stirred at RT for 18 h. The product was then precipitated in water (100 mL) and collected by vacuum filtration as a cream solid: 70 mg (89%). ^{1}H NMR (400 MHz, DMSO-d_6) δ 12.60 (s, 1H), 8.51 (d, J = 2.3 Hz, 1H), 8.27 (dd, J = 7.7, 1.5 Hz, 1H), 8.01 – 7.95 (m, 1H), 7.95 – 7.87 (m, 2H), 7.87 – 7.80 (m, 1H), 7.45 (td, J = 5.5, 5.0, 2.7 Hz, 1H), 7.39 (dd, J = 6.5, 2.3 Hz, 1H), 7.25 (t, J = 9.0 Hz, 1H), 6.93 (d, J = 9.1 Hz, 1H), 4.34 (s, 2H), 3.79 – 3.69 (m, 4H), 3.61 (s, 2H). MS m/z [M-H]- for $C_{26}H_{21}FN_6O_2$: 466.7. R_t = 8.95 min.

^{1}H NMR spectra and MS:

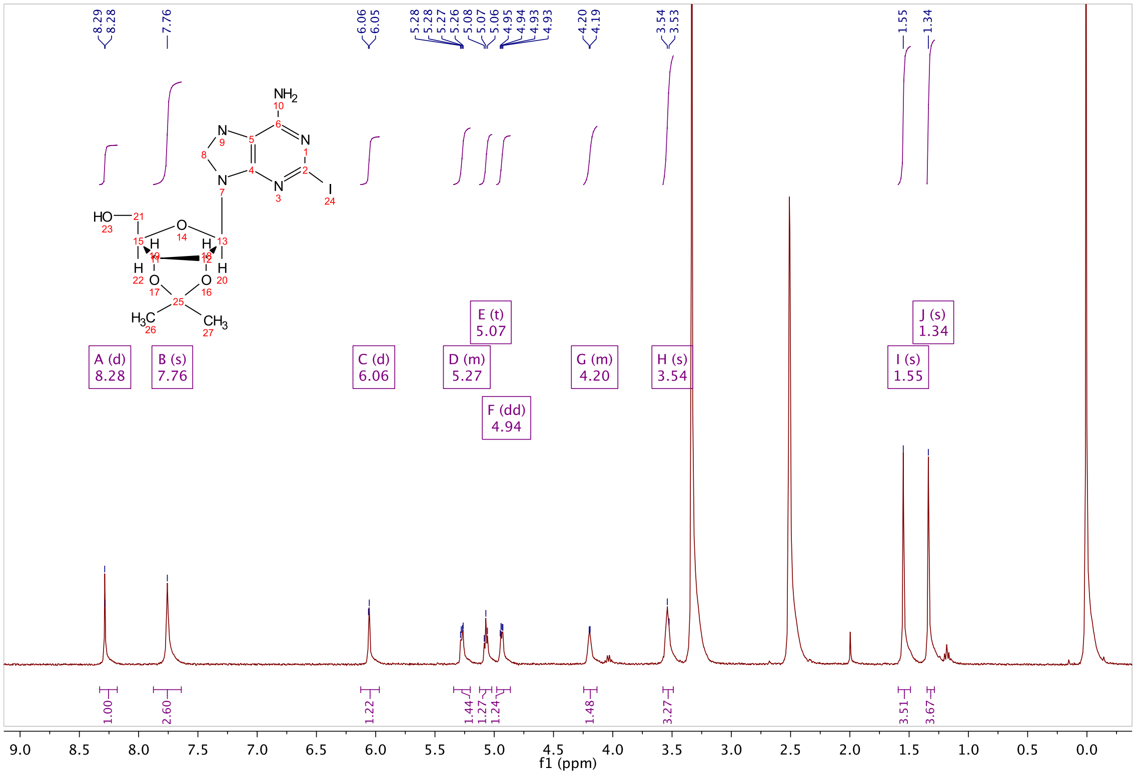

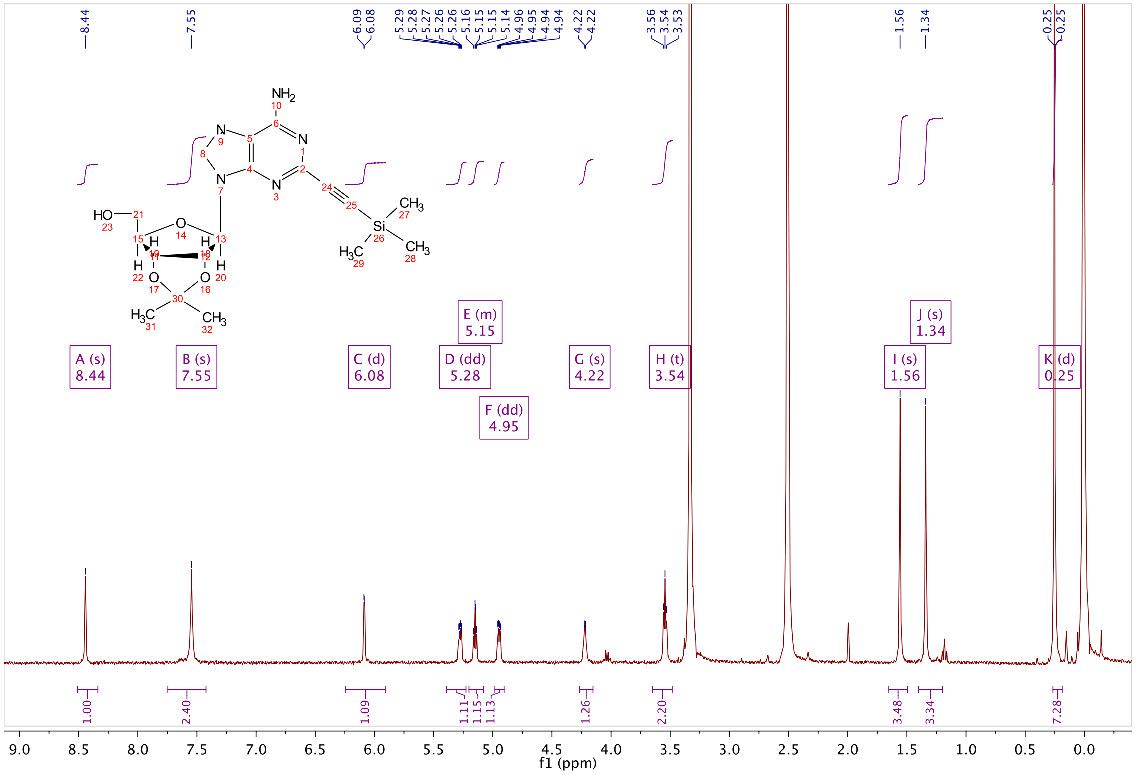
8.44
7.55
6.09
6.08
5.29
5.28
5.27
5.26
5.26
5.16
5.15
5.15
5.14
4.96
4.95
4.94
4.94
4.22
4.22
3.56
3.54
3.53
1.56
1.34
0.25
0.25
NH2
N
HO
O
H
Si
CH3
H3C
A (s) 8.44
B (s) 7.55
C (d) 6.08
D (dd) 5.28
E (m) 5.15
F (dd) 4.95
G (s) 4.22
H (t) 3.54
I (s) 1.56
J (s) 1.34
K (d) 0.25
1.00
2.40
1.09
1.11
1.15
1.13
1.26
2.20
3.48
3.34
7.28
9.0 8.5 8.0 7.5 7.0 6.5 6.0 5.5 5.0 4.5 4.0 3.5 3.0 2.5 2.0 1.5 1.0 0.5 0.0
f1 (ppm)

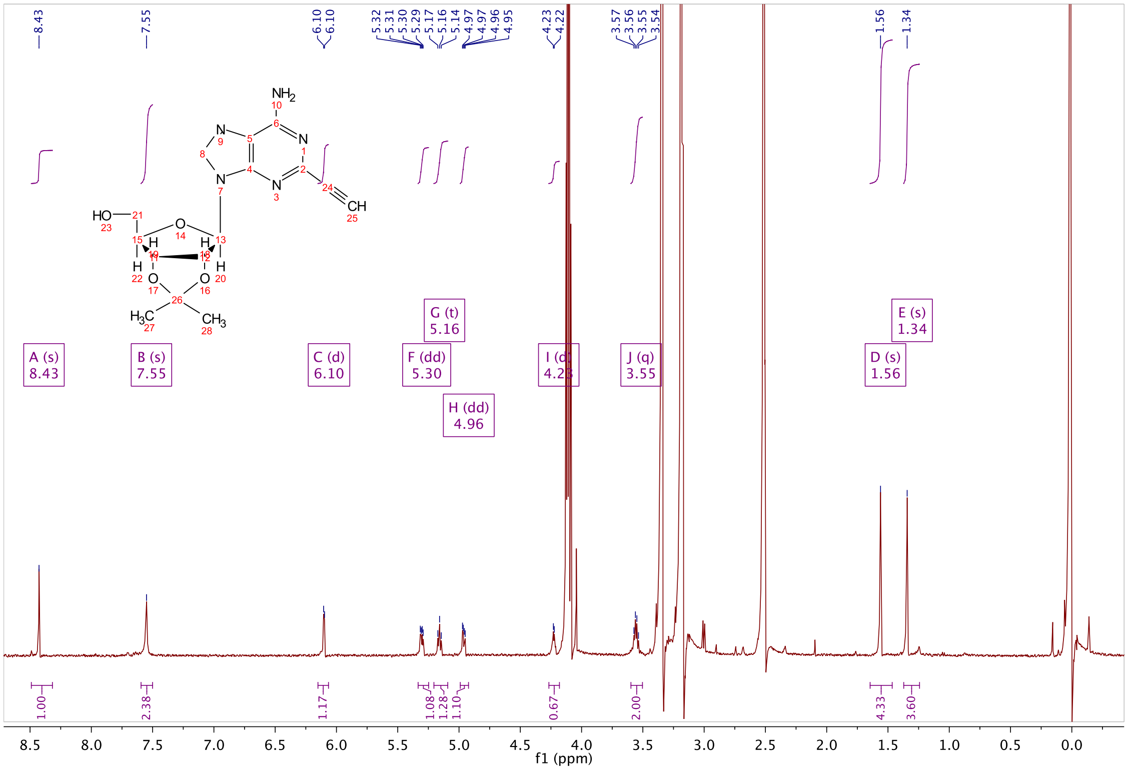
8.43
7.55
6.10
6.10
5.32
5.31
5.30
5.29
5.17
5.16
5.14
4.97
4.97
4.96
4.95
4.23
4.22
3.57
3.56
3.55
3.54
1.56
1.34
NH2
N
HO
O
H
CH
H3C
CH3
A (s) 8.43
B (s) 7.55
C (d) 6.10
F (dd) 5.30
G (t) 5.16
H (dd) 4.96
I (d 4.23
J (q) 3.55
D (s) 1.56
E (s) 1.34
1.00
2.38
1.17
1.08
1.28
1.10
0.67
2.00
4.33
3.60
8.5 8.0 7.5 7.0 6.5 6.0 5.5 5.0 4.5 4.0 3.5 3.0 2.5 2.0 1.5 1.0 0.5 0.0
f1 (ppm)

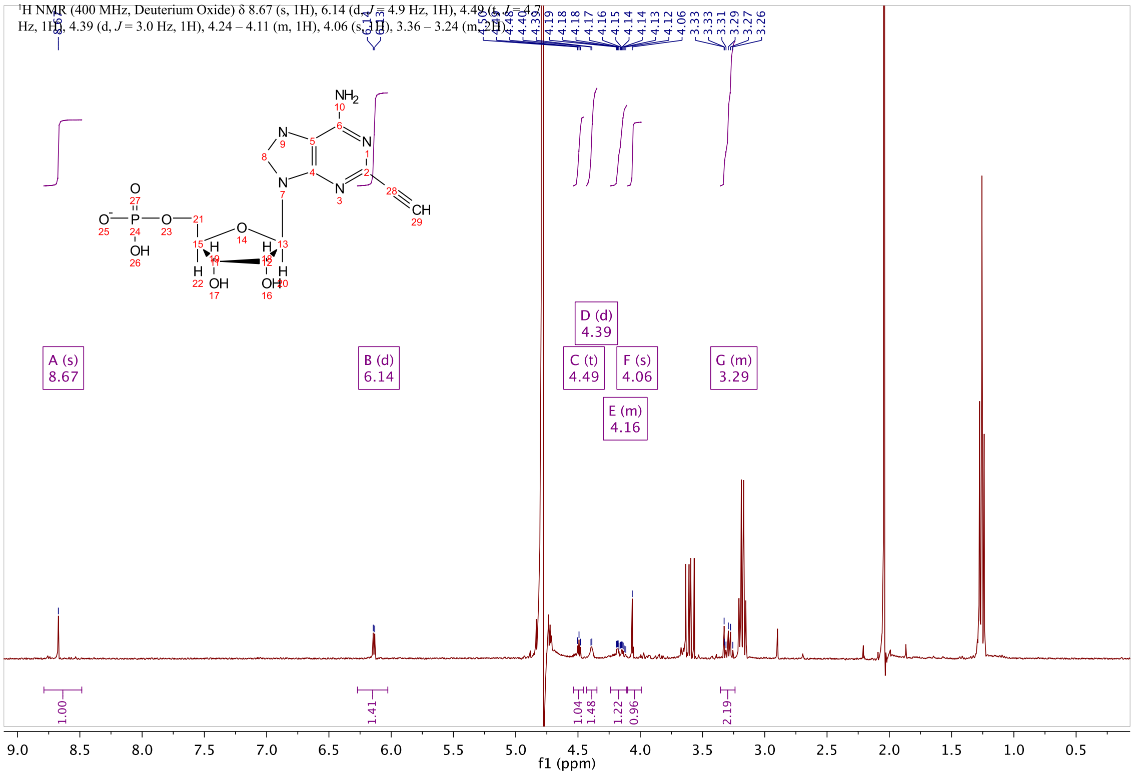

^{1}H NMR (400 MHz, Deuterium Oxide) δ 8.67 (s, 1H), 6.14 (d, J = 4.9 Hz, 1H), 4.49 (t, J = 4.7 Hz, 1H), 4.39 (d, J = 3.0 Hz, 1H), 4.24 – 4.11 (m, 1H), 4.06 (s, 1H), 3.36 – 3.24 (m, 2H).

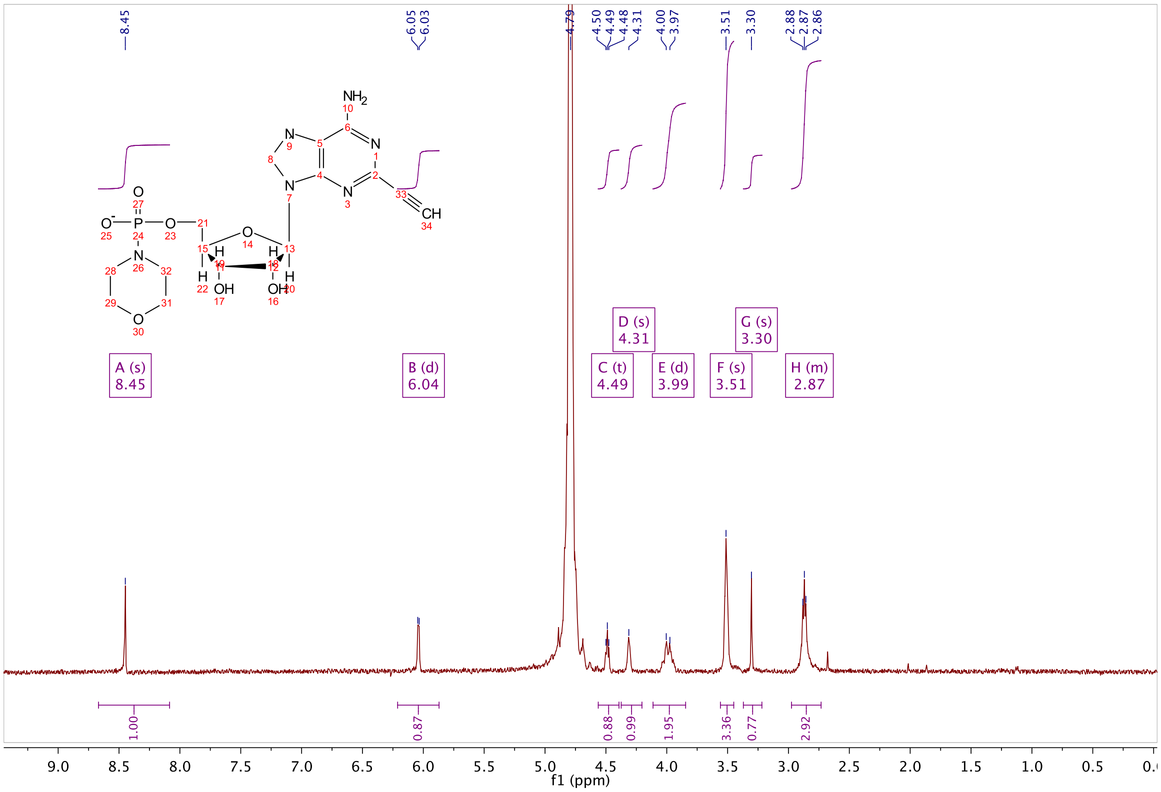

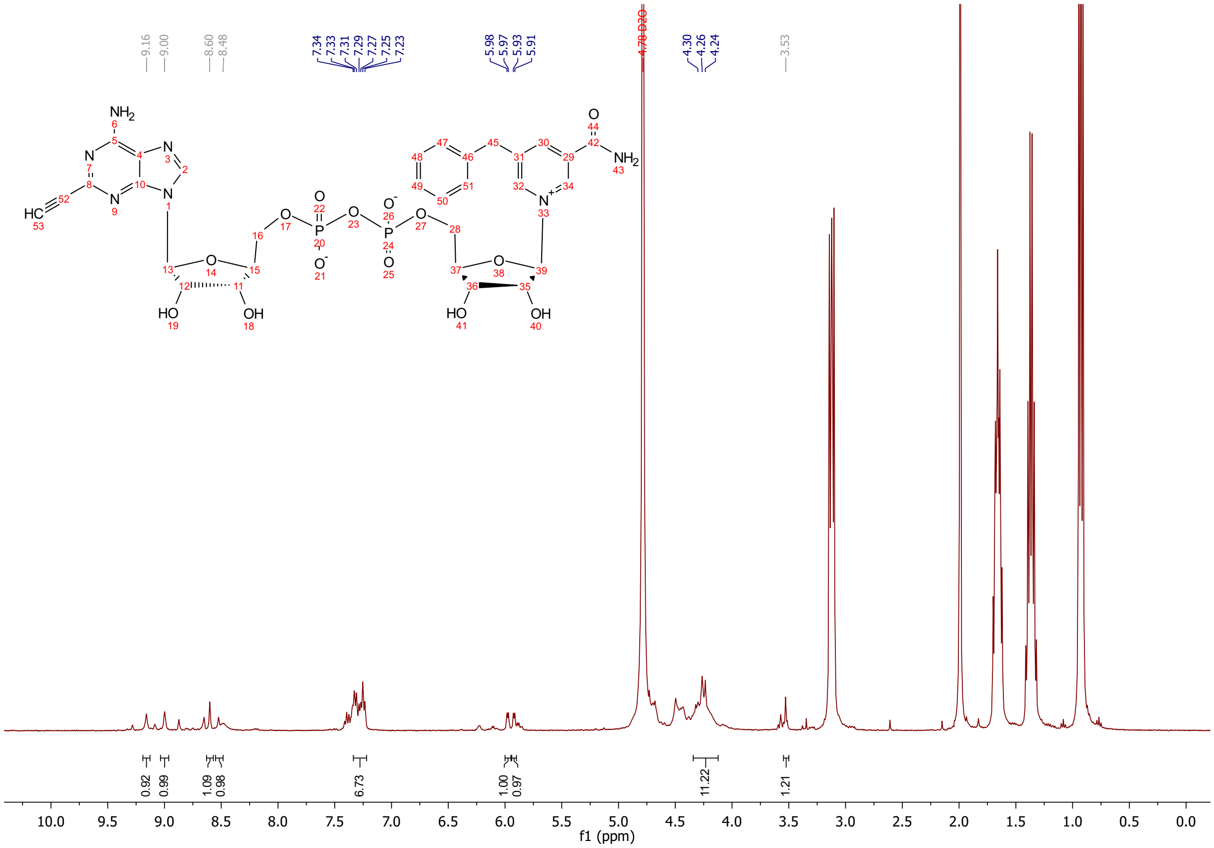

Mass spectrometry 5-bn-2e-NAD+: exact mass 776.15

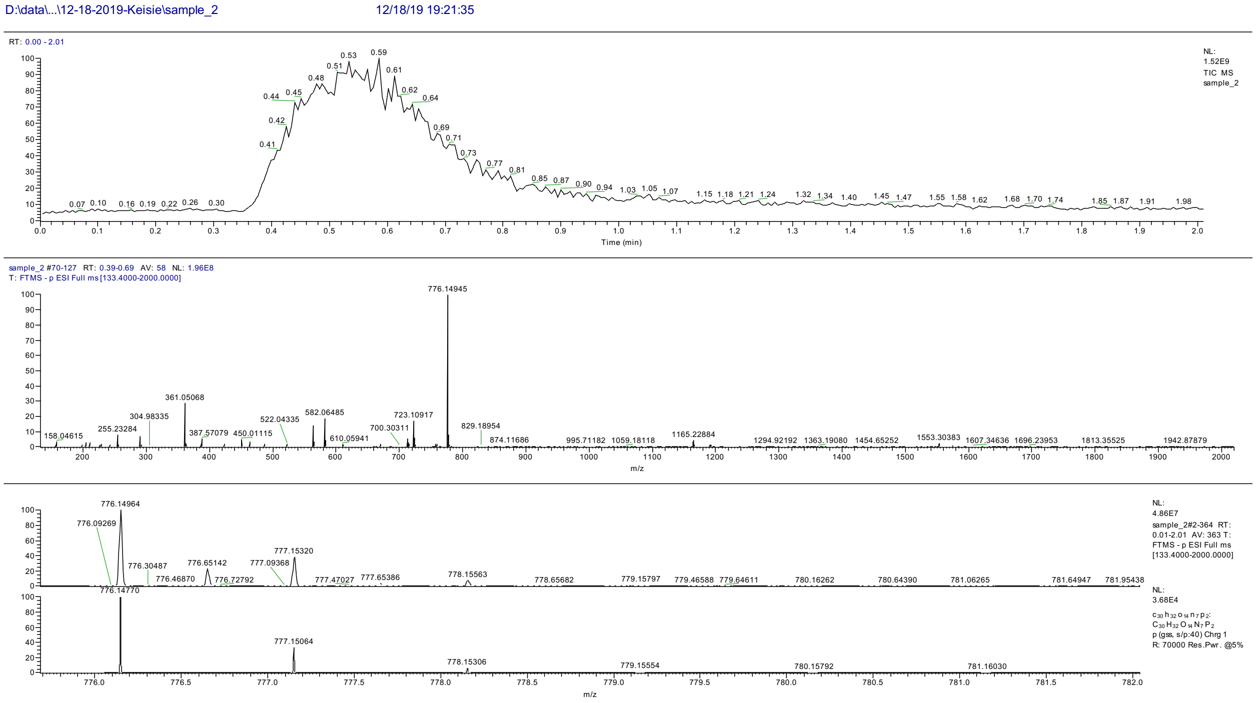

NMR Spectra: Phthal 01

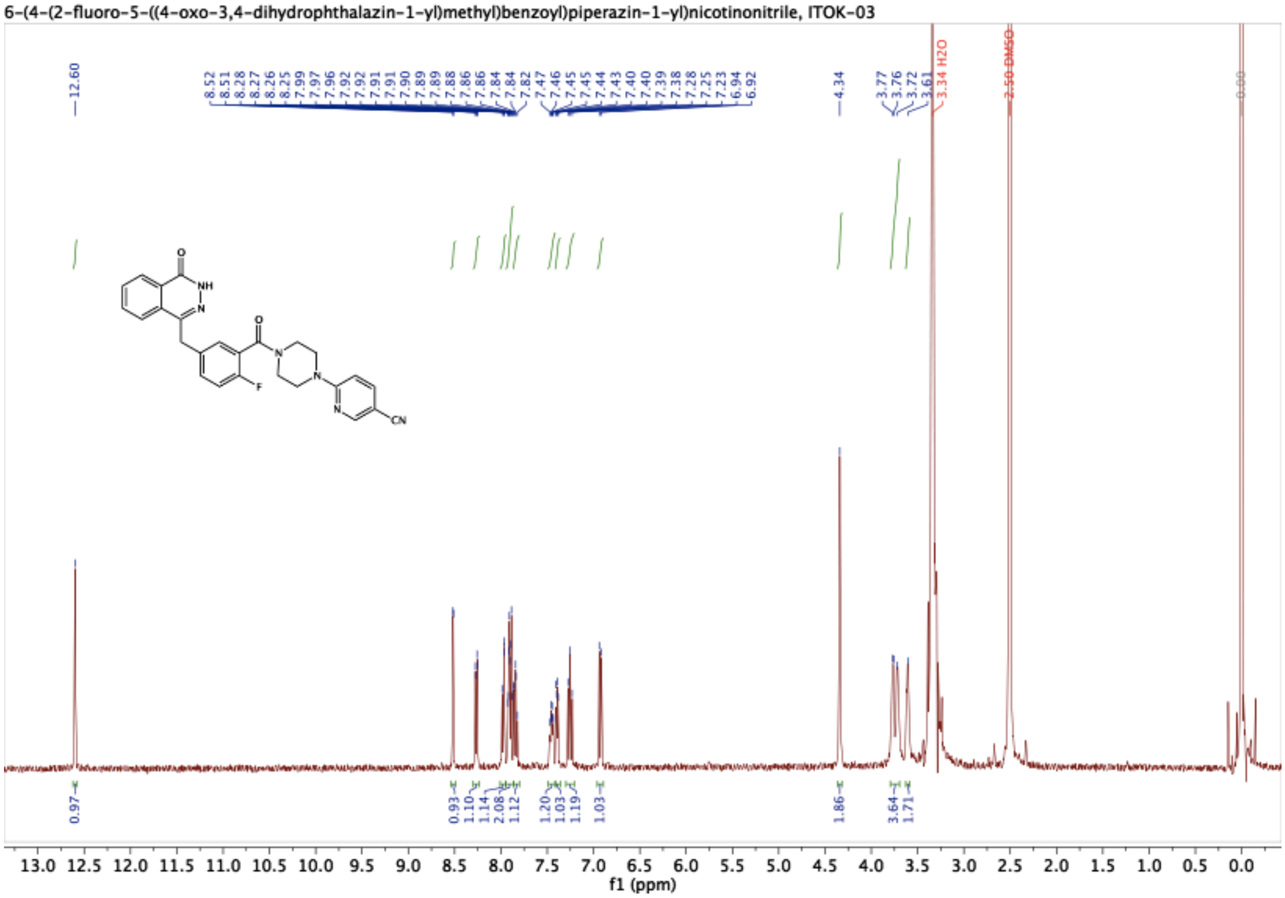
6-(4-(2-fluoro-5-((4-oxo-3,4-dihydrophthalazin-1-yl)methyl)benzoyl)piperazin-1-yl)nicotinonitrile, ITOK-03

Mass spectrometry- Phthal 01-exact mass 466.7

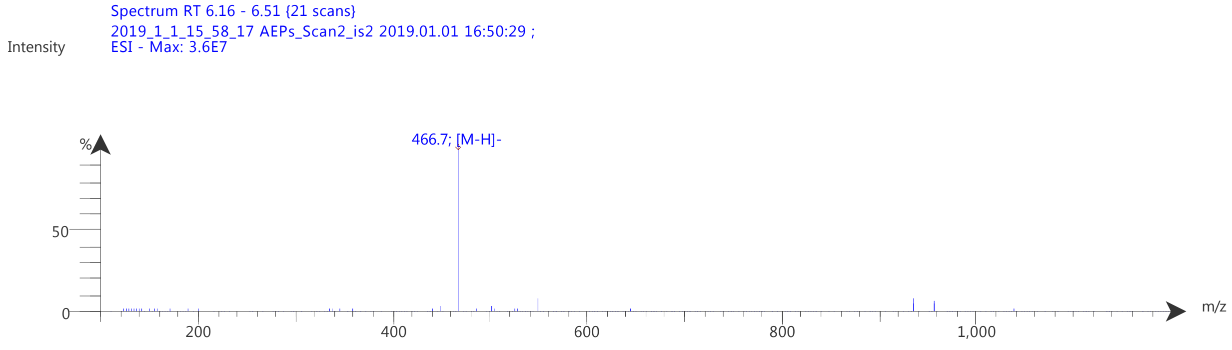

Chapter 3.

Synthesis and characterization of a PARP 7 selective inhibitor (KMR04-206)

Kelsie M. Rodriguez, Ilsa T. Kirby, Sunil Sundalam, Iain Mackley, David Hutin, Solveig Pettersen, Jason Matthews, and Michael S. Cohen

Author contributions

K.M.R. and M.S.C. designed the experiments. Most of the experiments presented were conducted by K.M.R. The initial scaffold compound (Phthal 01) and several derivatives were synthesized and characterized by I.T.K., which provided critical SAR necessary to generate KMR04-206. Additional contributions in this chapter include the synthesis of KMR04-206 precursor compounds made by S.S. and I.M. qRT-PCR data performed with KMR04-206 was generated and provided by J.M. and members of his lab: D.H. and S.P.

Acknowledgments

Materials, equipment, and qRT-PCR training were generously provided by Timothy Nice and Jacob Van Winkle to generate the data provide in Figure 3.2.

Abstract

PARP-7, a member of the PARP (Poly-ADP-ribose-polymerase) family of enzymes, catalyzes the transfer of ADP-ribose from nicotinamide adenine dinucleotide (NAD^+) to amino acids on protein targets[1]. PARP-7 has emerged as a critical regulator of innate immunity [2],[3]. Due to its role in suppressing type-I interferon signaling, we hypothesize that upregulation of PARP-7 in cancer cells prevents the immune system from recognizing cancerous cells. Inhibition of PARP-7, and subsequent production of cytokines, including IFN-β, may reduce cancer progression by allowing the immune system to better recognize and destroy cancer cells. In this chapter, progress is summarized towards a potent and selective PARP-7 inhibitor, derived from the starting scaffold: AZ12629495 (patent WO 2016/116602). Modification in a key location of the scaffold, thereby creating compound KMR04-206, established increased potency and selectivity for PARP-7. In cell and *in vitro* data show the selectivity of KMR04-206 for PARP-7 against other PARP family members. Consistent with previous findings, inhibition of PARP-7 increases PARP-7 IFN-β levels. Through fruitful collaboration with the Matthews lab, it was also observed that endogenous PARP-7 levels increase dramatically upon selective inhibition, suggesting that auto-MARylation by PARP-7 may control its stability or degradation mechanism. Additionally, PARP-7 inhibition coincides with PARP-7 knockout studies, further corroborating the role of PARP-7 in the Aryl hydrocarbon receptor (AhR) mediated response to toxicity. This body of work has facilitated a licensing agreement with a pharmaceutical company. Work on this project will be continued by other members of the lab in partnership with this company to further develop a clinical candidate.

Introduction

PARPs are a family of 17 proteins, many of which have emerged as regulators of cytokine signaling and innate immunity[2],[4],[5]. Catalytically active PARP family members can be categorized into two subfamilies based on their active site catalytic triad. HYE-PARPs (PARP-1, 2, 3, 4, 5a and 5b), contain a glutamate in the third position of the catalytic triad, which is necessary for poly-ADP-ribosylation activity (PARylation). In contrast, HY**Φ**-PARPs (PARPs-6, 7, 8, 10, 11, 12, 14, 15, and 16) contain a hydrophobic (**Φ**) amino acid in the third position of the triad. HY**Φ**-PARPs catalyze (MARylation) exclusively[6]. The third position of the catalytic triad sits at the base of the nicotinamide binding pocket[7]. Many successful PARP inhibitor scaffolds mimic the nicotinamide group of NAD^+, and occupy the same space as this endogenous PARP substrate[8],[9],[10],[11]. Our lab has previously demonstrated a strategy for exploiting the hydrophobic pocket present in HY**Φ**-PARPs to develop a PARP-11 selective inhibitor[11]. This strategy employs the use of a propynyl group on the inhibitor scaffold to occupy the hydrophobic pocket available in the HY**Φ**-PARP family members but which is absent in HYE-PARPs[11]. Using a similar strategy, we developed a PARP-7 selective inhibitor, KMR04-206.

The purpose behind design of a PARP-7 selective inhibitors is towards their use as immunomodulatory compounds for the treatment of cancer. An inhibitor of PARP-7, known as RBN-2397, is currently in a phase 1 clinical trial to assess its anti-tumor activity in patients with advanced-stage solid tumors (ClinicalTrials.gov Identifier: NCT04053673). PARP-7 is upregulated in several types of cancer including ovarian cancer and lung small cell carcinoma (NCI Genomic Data Commons Data Portal).

Knockout of PARP-7, an early interferon inducible gene, shows increased expression of the cytokine interferon-beta (IFN-β)[3]. Upregulation of PARP-7 in cancer may play a role in immune system evasion by dampening the cytokine signals that enhance the immune system's ability to recognize and clear cancerous cells. Inhibition of PARP-7, and subsequent production of cytokines, including IFN-β, may reduce cancer progression by allowing the immune system to better recognize and destroy cancer cells.

Results

Phthal01 is a potent PARP7 inhibitor which initiates aspects of the innate immune response in cells

Phthal01 (also known as ITK413B and ITOK03 in Dr. Ilsa T. Kirby's dissertation) is highly similar in structure to AZ12629495 (patent WO 2016/116602) and is a potent, low nanomolar inhibitor of multiple PARP family members. It is most potent for PARPs-1, 2, and 7. Phthal01 also exhibits some, although lesser, potency for PARP-15. The *in vitro* selectivity profile of this compound was previously established by Dr. Kirby[12].

After information on the selectivity of Phthal01 was obtained, I decided to use this compound to look at the innate immune signaling corresponding to PARP-7 inhibition. PARP-7 knockout Mouse Embryonic Fibroblasts (MEFs) elicit increased IFN-β levels in response to viral infection in comparison to wild type[3]. We therefore decided to measure IFN-β levels in response to PARP-7 inhibition. Using qRT-PCR, IFN-β levels were measured from lysates of MEF cells treated overnight with DMSO, Olaparib (1μM), or Phthal 01 (1 μM). We found that Phthal01 (which inhibits PARPs-1, 2 and 7), but not Olaparib (a PARP-1/2 selective inhibitor), leads to increased IFN-β levels **(Figure 3.1).**

While these data do not rule out the possibility of a polypharmacological effect of inhibiting multiple PARPs, they were our first indication (from data collected in our own hands) that PARP-7 may play an important role in the innate immune response. To follow up on this experiment, we decided to look at downstream signaling of the type-I interferon response by observing Stat-1 phosphorylation in response to Phthal01. We found that CT-26 cells treated with Phthal01 (1 μM), but not DMSO or Veliparib (1 μM) (a PARP-1/2 selective inhibitor) exhibited increased Stat-1 phosphorylation in a time dependent manner **(Figure 3.2)**. CT-26 cells were used in this experiment because they have endogenously high levels of ADPr, particularly at a molecular weight we originally thought could correspond to PARP-7. However, the data point to this ADPr band resulting from PARP 2, as it disappears upon veliparib inhibition **(Figure 3.2)**.

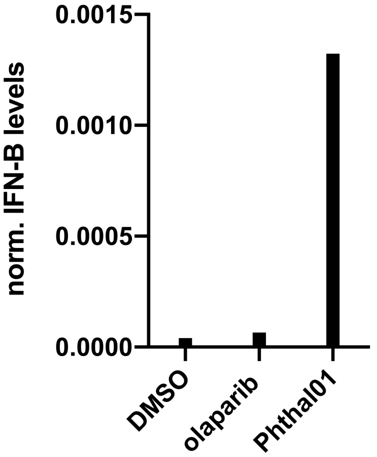

Figure 3.1. Phthal01 cellular treatment induces IFN-β levels.
Mouse embryonic fibroblasts were treated with DMSO, olaparib, or Phthal01 for 12 h. Cells were harvested IFN-β levels were determined by quantitative real-time PCR (qRT-PCR). Normalized IFN-β represent the absolute copy number of *Ifnb1* (target) divided by the absolute copy number of a housekeeping gene (Rps29).

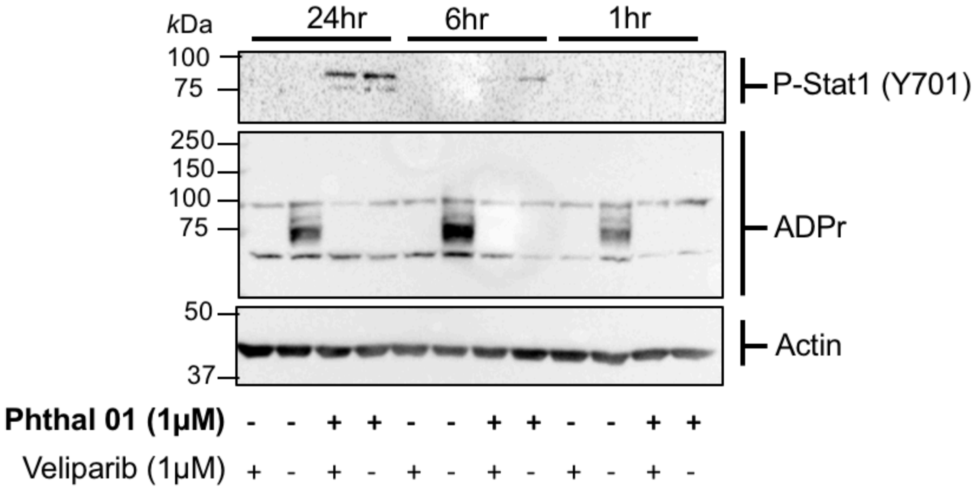

Figure 3.2. Time-dependent Stat-1 Phosphorylation in the presence of Phthal01 CT-26 cells were treated for up to 24 hours. Time points were taken at 1hr, 6hrs and 24 hrs. Phosphorylation of Stat1 increases with treatment of Phthal01 (1μM) or Phthal01 (1mM) + veliparib (1mM), but not DMSO or veliparib alone. Proteins were resolved by SDS-PAGE and were detected by Western blot using antibodies against Phospho-Stat1 (Y701) (cell signaling #9167), beta-actin (SCBT), and ADPr (cell signaling).

In vitro SAR is recapitulated in cells using analogs of Phthal01

Given the compelling evidence from both the literature and our own experiments that PARP-7 plays an important role in immune signaling, we decided to push forward to develop a PARP-7 selective inhibitor. Given its potency for PARP-7, Phthal01 served as an excellent scaffold on which to expand synthesis towards a PARP-7 selective inhibitor[12]. Structural activity relationship (SAR) assays were performed by Dr. Kirby using a 96 well-plate family-wide PARP inhibitor screening assay[11],[13]. These assays provided evidence that the nitrogen in the pyridine ring extending from the piperazine ring (highlighted in blue-grey) is essential for PARP-7 inhibition **(Figure 3.3).** Additionally, this nitrogen in the ring needs to be in the ortho- position relative to the body of the phthalazone. Furthermore, a nitrile substituent of the pyridine ring (highlighted in beige) needs to be in the para- position for the compound to maintain potency for PARP-7 **(Figure 3.3).**

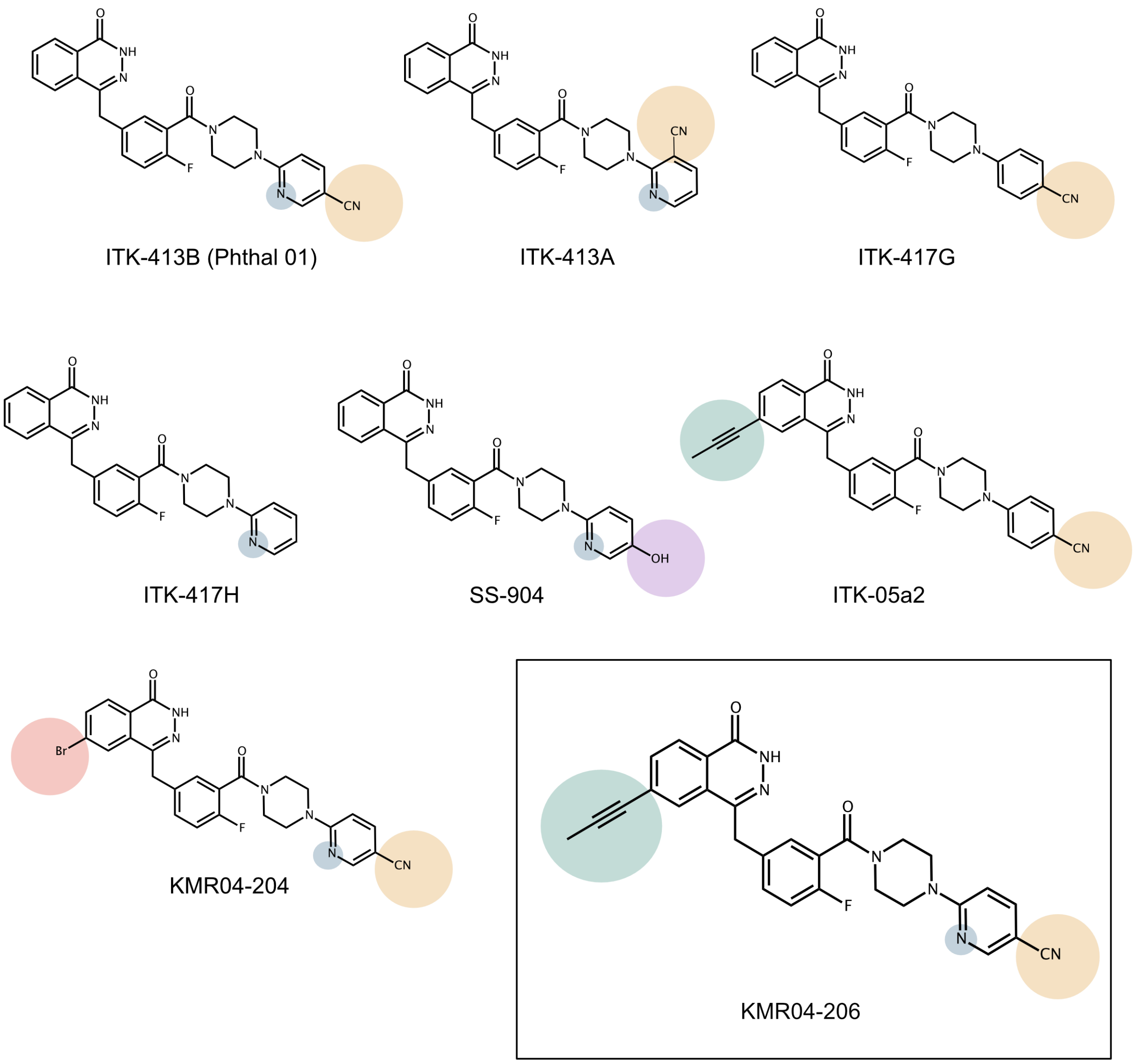
ITK-413B (Phthal 01)

ITK-413A

ITK-417G

ITK-417H

SS-904

ITK-05a2

KMR04-204

KMR04-206

Figure 3.3. Chemical structures of compounds made in this series.
Highlighted regions indicate different functional groups. Phthal01 and KMR04-206 are the most potent compounds for PARP-7. KMR04-206 is selective for PARP-7.

After the data were collected using SAR assays performed by Dr. Kirby, I next wanted to see if these results were recapitulated in cells. Based on *in vitro* data, I hypothesized that analogs of Phthal01 would lack potency in cells. However, I wanted to perform assays under cellular conditions in the hopes that we might observe differences in potencies that would provide information to guide further SAR. In order to test analogs shown in figure 3.3, HEK293T cells expressing GFP-PARP-7 were treated at a single dose, 1 μM, of the analogs overnight. The results were consistent with *in vitro* data. Compounds which showed decreased potency for PARP-7 in vitro, also were not potent in cells **(Figure 3.4).** These data provided us with key information on the locations of the scaffold which could not be modified.

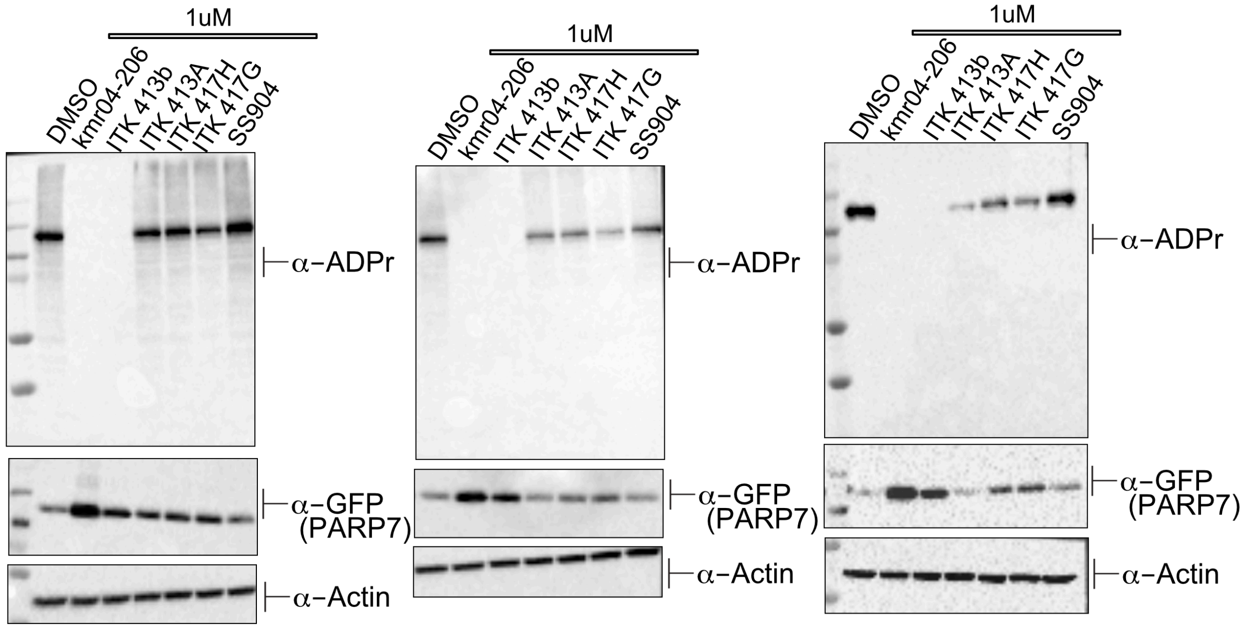

Figure 3.4 Triplicate data testing Phthal01 derived analogs against PARP7
Triplicate images of western blots depicting PARP 7 inhibition with KMR04-206 compared to other structurally related compounds at a single dose of 1 μM. Proteins

were resolved by SDS-PAGE and were detected by Western blot using antibodies against ADPr, GFP, and actin. Structures of these compounds are shown in figure 3.1.

KMR04-206 is a highly potent, selective inhibitor of PARP-7

Since Phthal01 is most potent for PARPs 1, and 2, and 7, we next decide to turn to a strategy that had proved successful in the past for modifying inhibitor potency away from PARPs 1 and 2 in order to work towards the development of a PARP-7 selective inhibitor. I synthesized a derivative of Phthal01 with a propynyl substituent present on the phthalazone ring to occupy the hydrophobic pocket present in PARP-7, an HY**Φ**-PARP **(Figure 3.3)**. I found that compound KMR04-206, which contains this defining propynyl group, confers selectivity for PARP-7 and drastically reduces potency for PARPs-1 and 2, both HYE-PARPs. The IC_{50} value of KMR04-206 for PARP-7 is 8nm in cells in comparison to an IC_{50} of 841nM for PARPs-1/2 **(Figures 3.5A, B and 3.6A, B)**. KMR04-206 was also tested in cells against mono-PARPs-8, 10, 12, and 15 **(Figures 3.5 - 3.10)**. KMR04-206 showed greater than 10 fold selectivity against all PARPs it was tested against in cells. The IC_{50} value for PARP-8 is 108nM, followed by PARP-15 (IC_{50}: 344nM), PARP-12 (IC_{50}: ~600nM), and PARP-10 (IC_{50}: ~1 μM) **(Figures 3.5 - 3.10)**.

KMR04-206, along with other closely related analogs, were tested in cells against PARP-7 at a single concentration of 1 μM. Unsurprisingly, KMR04-206 and Phthal 01 are the only compounds to inhibit PARP-7 at 1 μM **(Figure 3.4)**.

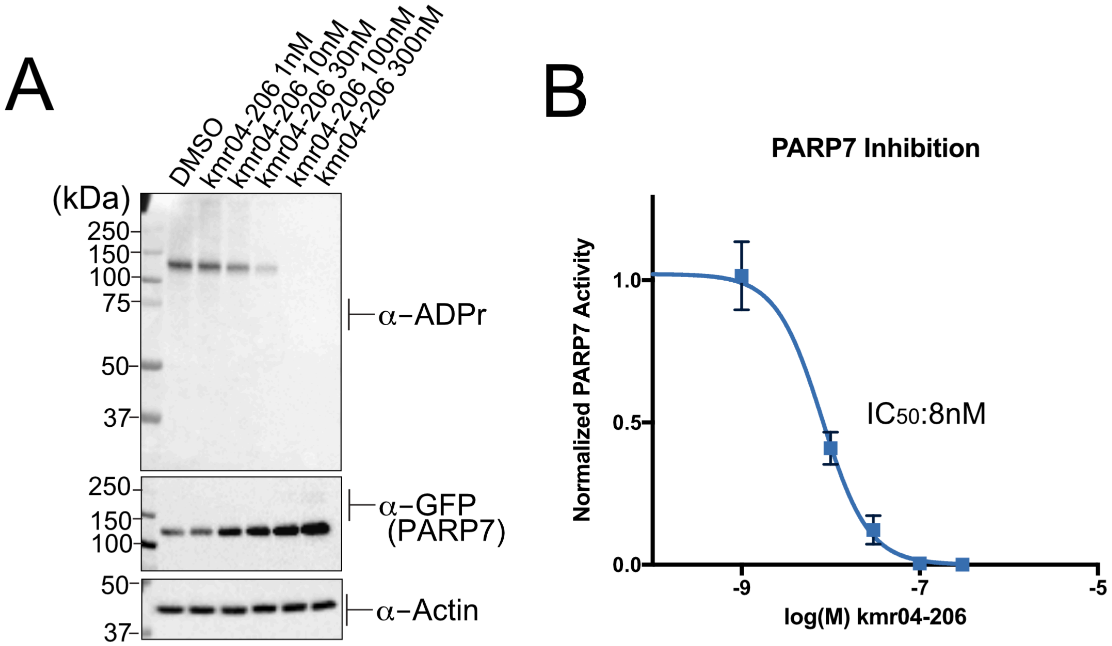

Figure 3.5. Dose response curve of kmr04-206 against PARP 7 in HEK293Tcells. **(A)** Representative image of western blot depicting PARP 7 inhibition with KMR04-206. HEK293T cells were transfected with GFP-PARP 7 and treated overnight with varying concentrations of compound added to the media. Proteins were resolved by SDS-PAGE and were detected by Western blot using antibodies against ADPr, GFP, and actin. (**B)** Blot quantification of three replicates of data. Y axis data includes PARP activity (ADPr/GFP signal) normalized to DMSO control. Non-linear fit curve produced and IC50 calculated using Prism 8.

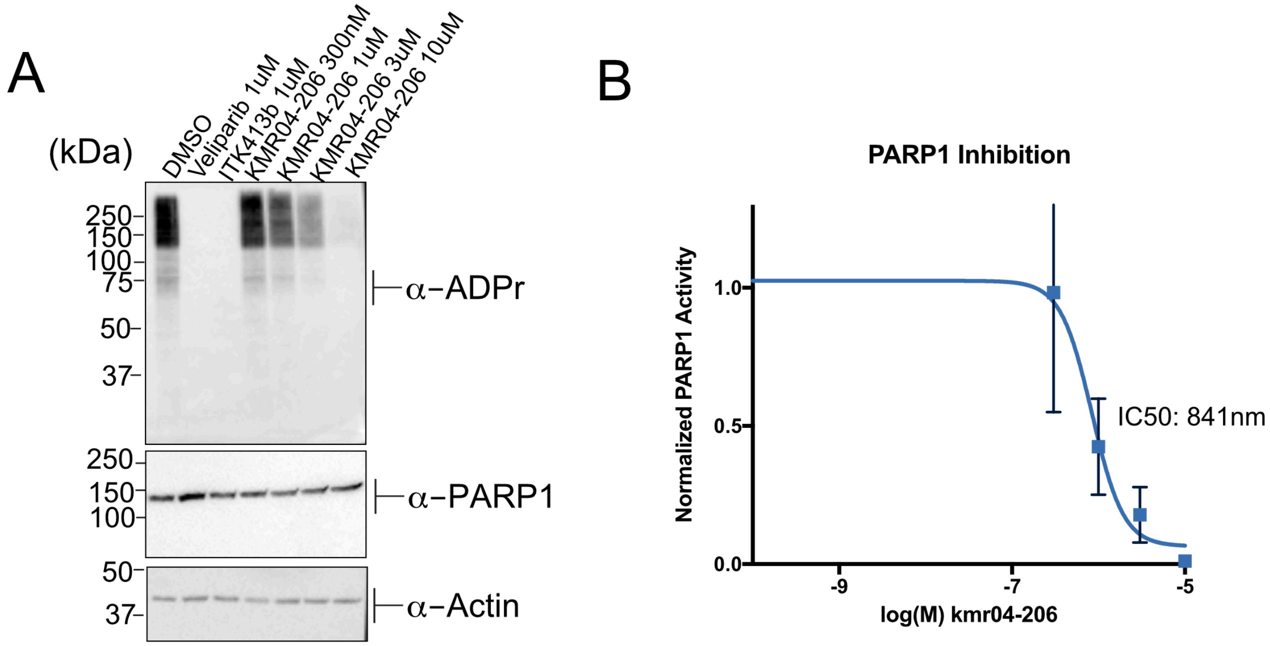

Figure 3.6. Dose response curve of kmr04-206 against PARP1 in HEK293Tcells. **(A)** Representative image of western blot depicting PARP7 inhibition with KMR04-206. HEK293T cells were and treated for 45 mins with varying concentrations of compound added to the media. PARG inhibitor was then added to the media for 15 mins to boost PARylation signal and visualize PARP1 activity. Proteins were resolved by SDS-PAGE and were detected by Western blot using antibodies against ADPr, GFP, and actin. **(B)** Blot quantification of three replicates of data. Y axis data includes PARP activity (ADPr/PARP1 signal) normalized to DMSO control. Non-linear fit curve produced and IC_{50} calculated using Prism 8.

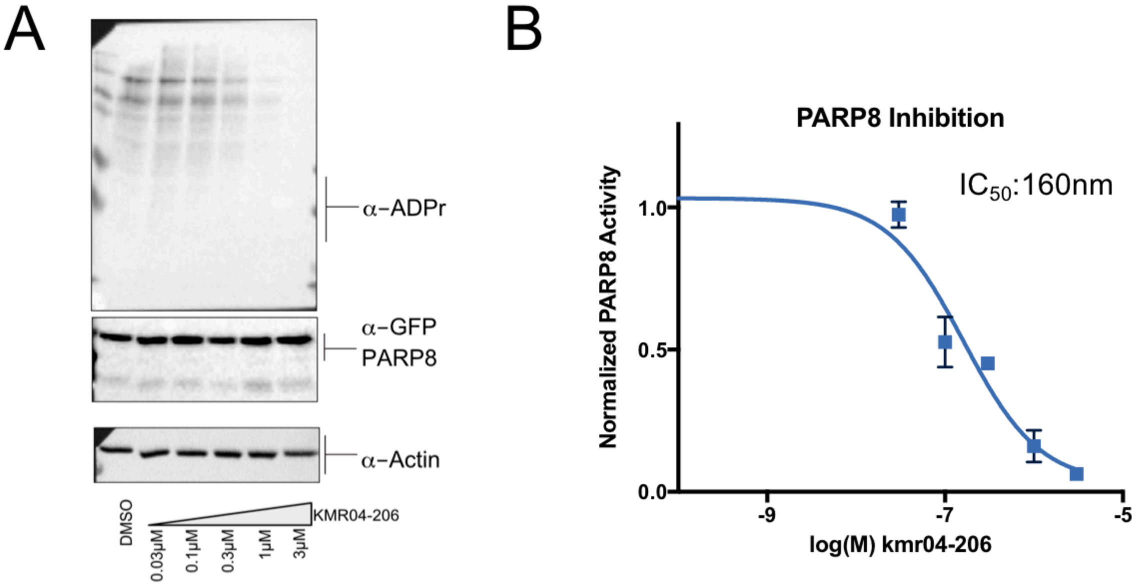

Figure 3.7. Dose response curve of kmr04-206 against PARP 8 in HEK293Tcells.

(A) Representative image of western blot depicting PARP 8 inhibition with KMR04-206. HEK293T cells were transfected with GFP-PARP 8 and treated overnight with varying concentrations of compound added to the media. PARG inhibitor, NAMPT activator, and veliparib (1 μM, to inhibit PARP) were added at the time of inhibitor treatment. Proteins were resolved by SDS-PAGE and were detected by Western blot using antibodies against ADPr, GFP, and actin.

(B) Blot quantification of three replicates of data. Y axis data includes PARP activity (ADPr/GFP signal) normalized to DMSO control. Non-linear fit curve produced and IC_{50} calculated using Prism 8.

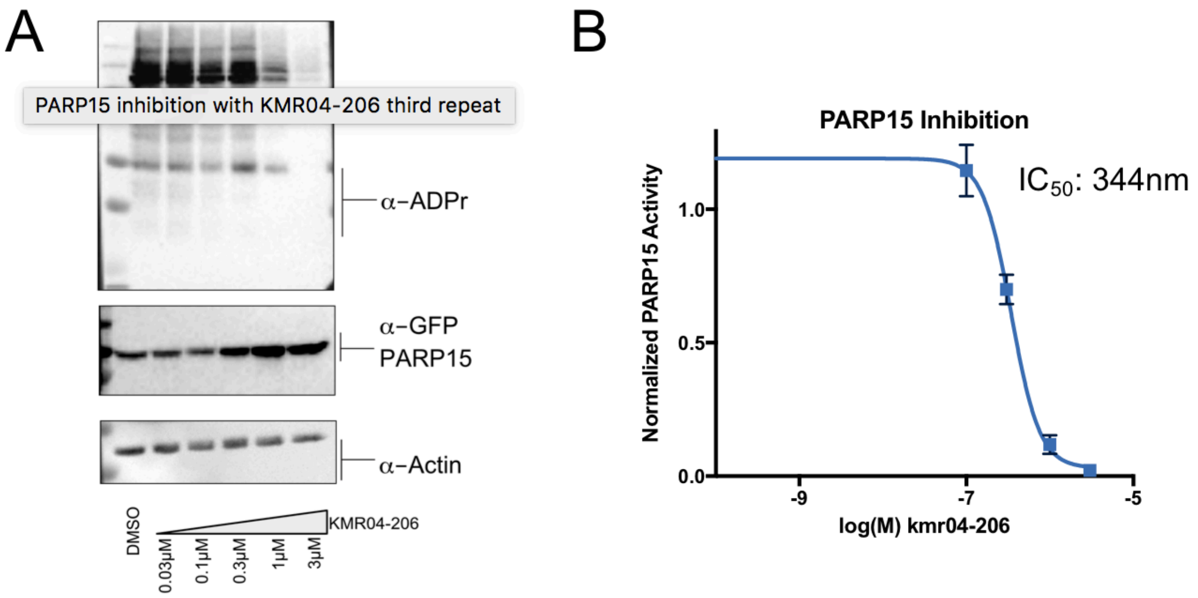

Figure 3.8. Dose response curve of kmr04-206 against PARP15 in HEK293Tcells.

(A) Representative image of western blot depicting PARP15 inhibition with KMR04-206. HEK293T cells were transfected with GFP-PARP15 and treated overnight with varying concentrations of compound added to the media. PARG inhibitor, NAMPT activator, and veliparib (1 μM, to inhibit PARP) were added at the time of inhibitor treatment. This cocktail, in combination with overexpression, allows the visualization of less active PARP family members including PARP 15. Proteins were resolved by SDS-PAGE and were detected by Western blot using antibodies against ADPr, GFP, and actin.

(B) Blot quantification of three replicates of data. Y axis data includes PARP activity (ADPr/GFP signal) normalized to DMSO control. Non-linear fit curve produced and IC_{50} calculated using Prism 8.

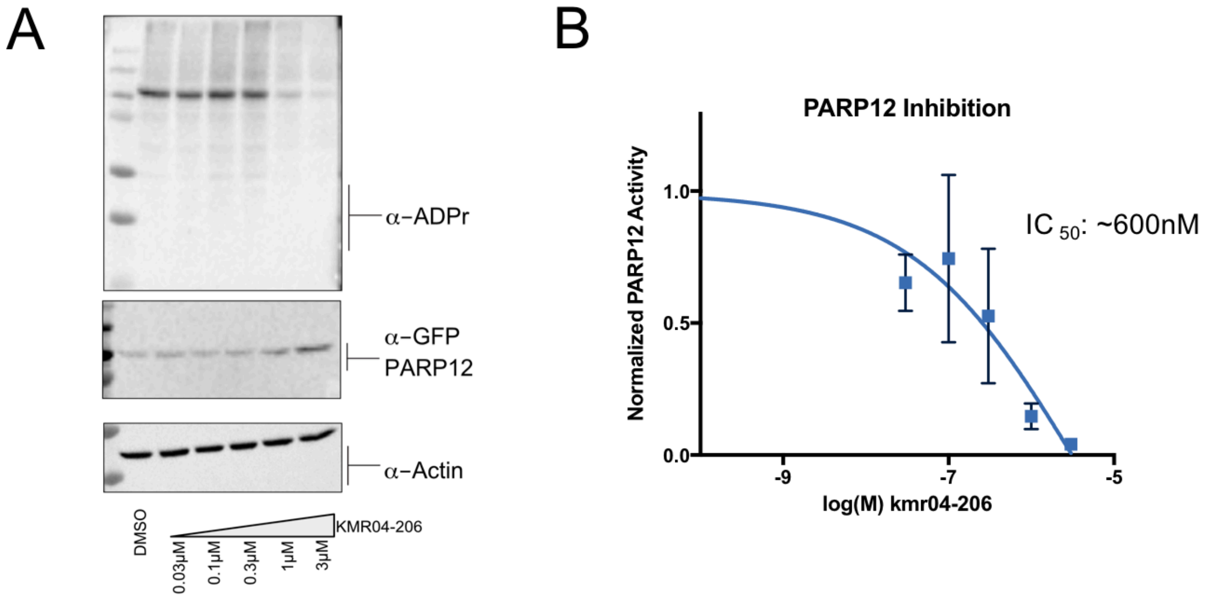

Figure 3.9. Dose response curve of kmr04-206 against PARP12 in HEK293Tcells.

A) Representative image of western blot depicting PARP12 inhibition with KMR04-206. HEK293T cells were transfected with GFP-PARP12 and treated overnight with varying concentrations of compound added to the media. PARG inhibitor, NAMPT activator, and veliparib (1 μM, to inhibit PARP) were added at the time of inhibitor treatment. Proteins were resolved by SDS-PAGE and were detected by Western blot using antibodies against ADPr, GFP, and actin.

(B) Blot quantification of three replicates of data. Y axis data includes PARP activity (ADPr/GFP signal) normalized to DMSO control. Non-linear fit curve produced using Prism 8. IC$_{50}$ could not be accurately calculated using Prism due to error and low fit to the curve. An estimate based on the curve is ~600nM.

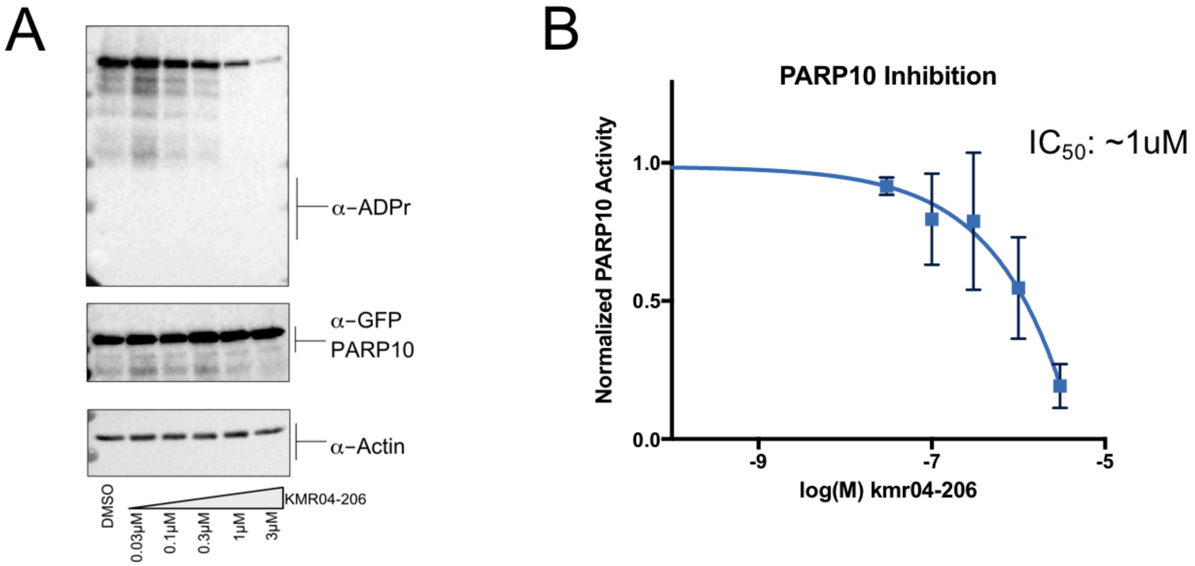

Figure 3.10. Dose response curve of kmr04-206 against PARP 10 in HEK293Tcells.

(A) Representative image of western blot depicting PARP 10 inhibition with KMR04-206. HEK293T cells were transfected with GFP-PARP 10 and treated overnight with varying concentrations of compound added to the media. PARG inhibitor, NAMPT activator, and veliparib (1 µM, to inhibit PARP) were added at the time of inhibitor treatment. Proteins were resolved by SDS-PAGE and were detected by Western blot using antibodies against ADPr, GFP, and actin.

(B) Blot quantification of three replicates of data. Y axis data includes PARP 10 activity (ADPr/GFP signal) normalized to DMSO control. Non-linear fit curve produced and IC_{50} calculated using Prism 8.

KMR04-206 is not a reversible-covalent inhibitor

After obtaining data regarding the selectivity of KMR04-206 for PARP-7, we next wanted to better understand how KMR04-206 confers selectivity. KMR04-206 contains a nitrile group extending from the pyridine ring, which is essential for its potency. Nitriles can react with cysteine residues to form thioimidate covalent moieties[14]. Several nitrile containing compounds have been developed as semi-covalent modifiers of cysteine proteases[15,16]. We therefore hypothesized that KMR04-206 may operate in a reversible-covalent manner by which the nitrile group could interact with a nearby cysteine residue with the d-loop of PARP-7 (residue C552) **(Figure 3.11A).** The d-loop is a structural region located within the active site which displays high sequence variability amongst PARP family members. To test this hypothesis, C552 was mutated to a serine residue within GFP-PARP-7. When tested in cells, GFP-PARP-7 C552S did not show decreased sensitivity to KMR04-206 in comparison to GFP-PARP-7 WT, leading us to believe that this compound does not react in a reversible-covalent manner **(Figure 3.11B)**. RBN-2397, a PARP-7 selective inhibitor currently in a Phase 1 clinical trial, was used as a control in this experiment to serve as a model of a non-covalent inhibitor of PARP-7. The results between these two compounds are similar in that they both inhibit GFP-PARP-7 WT and GFP-PARP-7 C552S **(Figure 3.11B).**

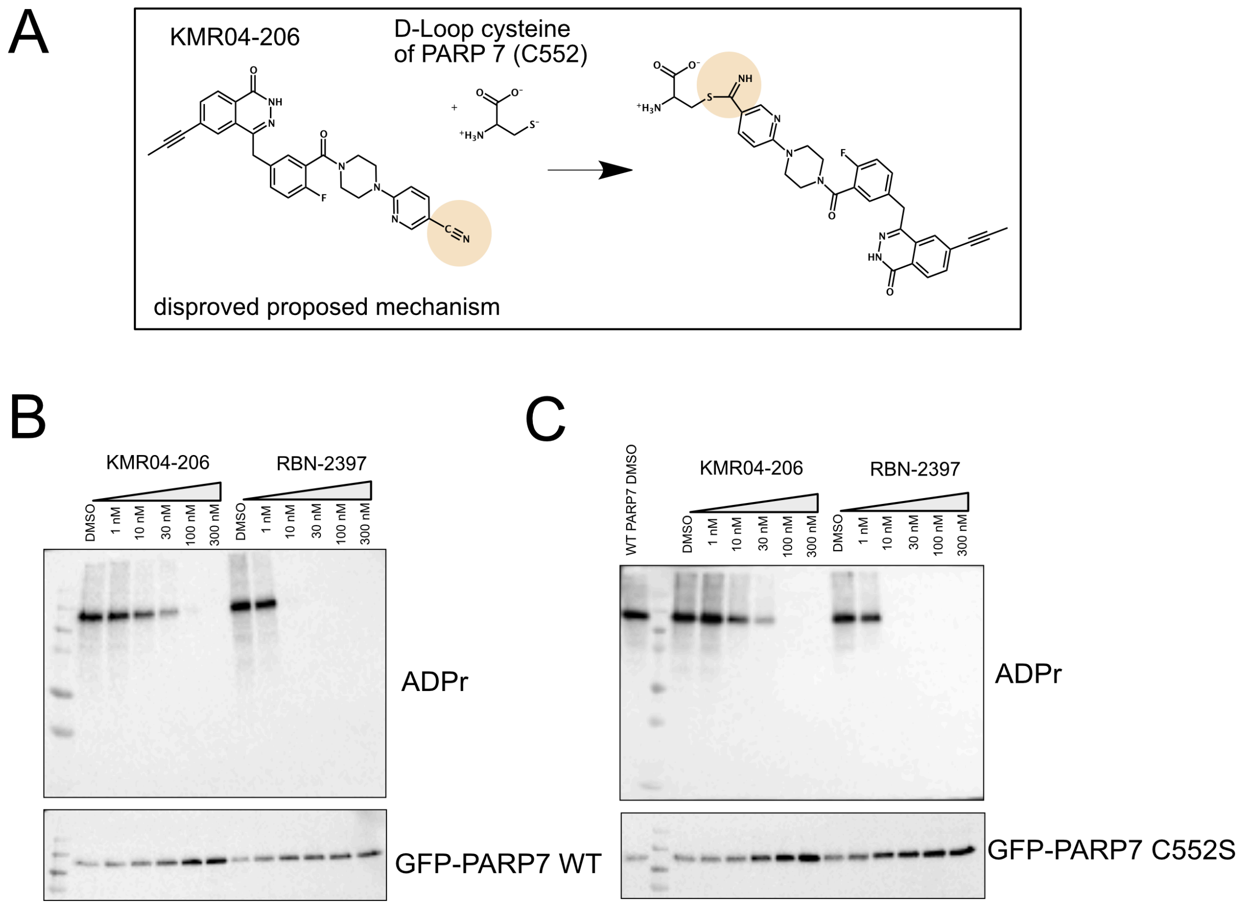

Figure 3.11. PARP7 C552S mutant shows that KMR04-206 does not inhibit in a semi-covalent mechanism

(A) Proposed mechanism for how KMR04-206 could theoretically react with C552, a residue in the D-loop of PARP7 to form a reversible-covalent bond. Nitriles can react with cysteine residue forming a thioimidate.

(B) HEK293T cells expressing either WT GFP-PARP7 were treated, DMSO, KMR04-206 (1nm-300nm) or RBN-2397 (1nm-300nm). Proteins were resolved by SDS-PAGE and were detected by Western blot using antibodies against ADPr, GFP, and actin.

Localization and protein levels of PARP-7 change in response to inhibition by KMR04-206 or RBN-2397

GFP-PARP-7 is localized in distinct small nuclear bodies. This localization has been shown to be dependent on catalytic activity through mutation of key catalytic residues including H532A[17] and I631G (data not shown). In order to test whether inhibition has similar affects as the catalytically dead mutants, I used fluorescent imaging to observe localization of GFP-PARP7 under various concentrations of inhibition. These studies were limited and will require further examination using more advance microscopy techniques and a nuclear marker to make any conclusive remarks. However, my initial observations are that a cellular change in localization of GFP-PARP-7 occurs in response to Phthal 01 treatment (data not shown), KMR04-206 treatment, or RBN-2397 **(Figure 3.12 A,B)**. Upon inhibition with KMR04-206, PARP-7 is no longer observed in distinct nuclear bodies and is distributed throughout the nucleus, with some found in larger cytoplasmic foci **(Figure 3.12 A)**. PARP-7 localization follows a similar trend of distribution upon inhibition with RBN-2397, however with this compound PARP-7 is not found in the cytoplasm, and is only distributed in the nucleus **(Figure 3.12 B)**.

In addition to changes in localization, PARP-7 protein levels are also regulated by its catalytic activity. This trend was initially observed using GFP-PARP-7 and Phthal01 **(Chapter 2: Figure Supplement 2.4)** Using a PARP-7 specific antibody generated by Matthews and colleagues, they show that treatment of MEF cells with KMR04-206 leads to stabilization of endogenous PARP-7 **(Figure 3.13).** PARP-7 knockout cells were used as a control to show the specificity of the antibody. PARP-7 was first identified as a gene induced by TCDD (2,3,7,8-tetrachlorodibenzo-p-dioxin,

dioxin), hence its other commonly used name TiPARP (TCDD-inducible poly(ADP-ribose) polymerase)[18]. While KMR04-206 substantially increases endogenous levels, co-treatment of TCDD with KMR04-206 produces even higher levels. This could possibly be because TCDD acts at the level of transcriptional activation whereas KMR04-206 likely acts to stabilize levels post-translationally. By targeting two separate pathways that both increase PARP-7 levels, a synergistic effect was observed **(Figure 3.13).**

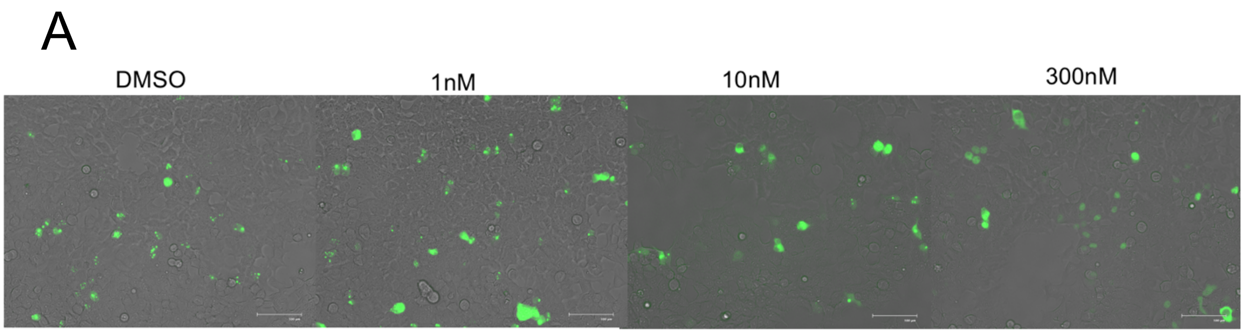

PARP7 is localized in distinct small nuclear puncta (some spread out in nucleus).

PARP7 is localized in distinct small nuclear puncta (some spread out in nucleus).

PARP7 is no longer localized in small nuclear puncta, some is in larger puncta and spread out in nucleus.

PARP7 is no longer localized in nuclear puncta. Mostly spread out in nucleus, some in the cytoplasm

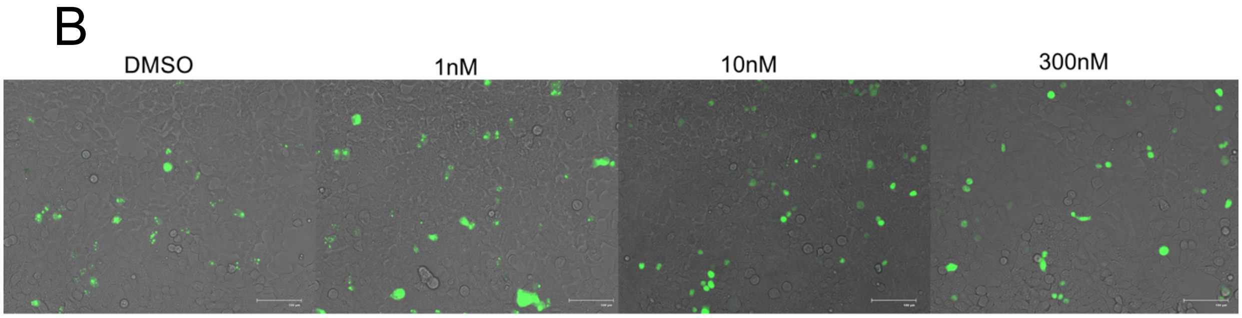

PARP7 localized in distinct SMALL nuclear puncta (some spread out in nucleus)

PARP7 localized in distinct SMALL nuclear puncta (some spread out in nucleus)

PARP7 no longer localized in puncta. Mostly spread out in nucleus.

PARP7 no longer localized in puncta. Mostly spread out in nucleus

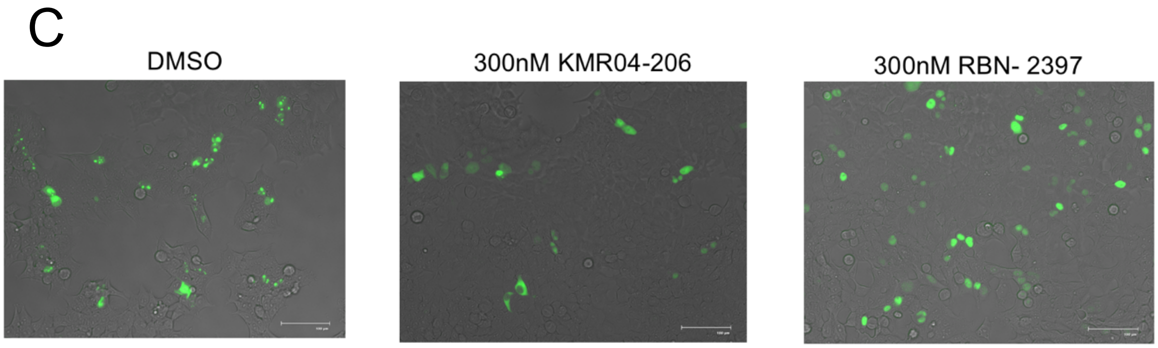

GFP-PARP7 C552S localized in distinct SMALL nuclear puncta (some spread out in nucleus)
Possibly higher overall levels of PARP7 in comp. to WT

GFP-PARP7 C552S is no longer localized in puncta. Mostly spread out in nucleus.

Some cells also show PARP7 in the cytoplasm.

GFP-PARP7 C552S is no longer localized in puncta. Mostly spread out in nucleus.

Figure 3.12. Localization of GFP- PARP 7 or GFP- PARP 7 C552S +/- inhibition

(A) Changes in localization observed when HEK293T cells expressing GFP-PARP 7 were treated overnight with KMR04-206 at concentrations ranging from 0 (DMSO)-300nM. Fluorescent images were captured using the EVOS FLoid Imaging System.

(B) Changes in localization observed when HEK293T cells expressing GFP-PARP 7 were treated overnight with RBN-2397 at concentrations ranging from 0 (DMSO)-300nM. Fluorescent images were captured using the EVOS FLoid Imaging System.

(C) Changes in localization observed when HEK293T cells expressing GFP-PARP 7 C552S mutant were treated overnight with DMSO, KMR04-206 (300nM) or RBN-2397 (300nM). Fluorescent images were captured using the EVOS FLoid Imaging System.

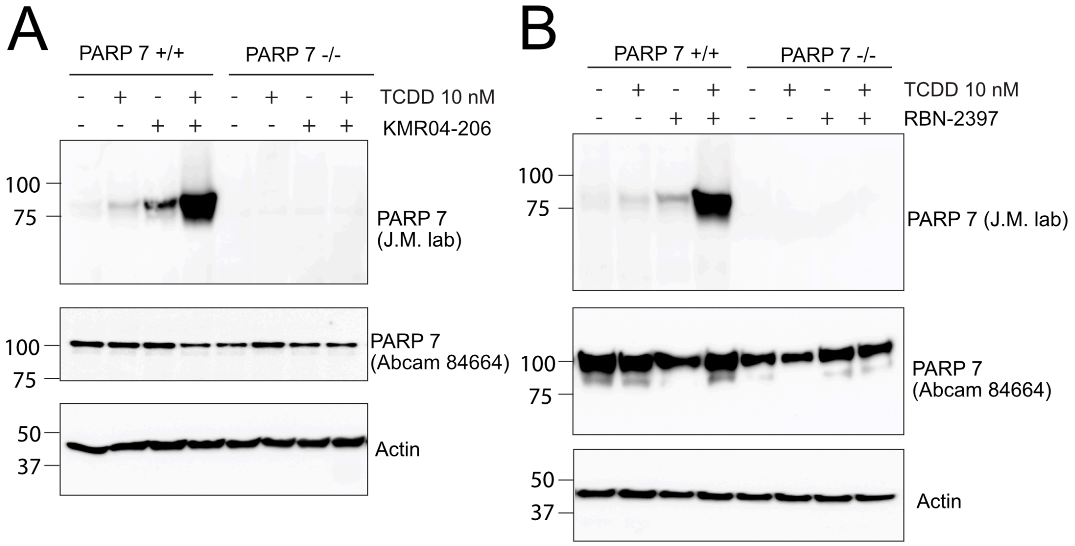

Figure 3.13. Endogenous PARP 7 levels increase in response to KMR04-206 or RBN-2397 in WT MEFs.

(A) Cells were treated with TCDD (2,3,7,8 -Tetrachlorodibenzo-p-dioxin) used to induce PARP-7 and KMR04-206 (4hr treatment) used to inhibit PARP-7. Proteins from the resulting lysates were resolved by SDS-PAGE and were detected by Western blot using antibodies against novel PARP-7 (TIPARP), commercially available Anti-PARP-7 antibody (ab84664), and Actin.

(B) Cells were treated with TCDD (2,3,7,8 -Tetrachlorodibenzo-p-dioxin) used to induce PARP-7 and RBN-2397 (4hr treatment) used to inhibit PARP-7. Proteins from the resulting lysates were resolved by SDS-PAGE and were detected by Western blot using antibodies against novel PARP-7 (TIPARP), commercially available Anti-PARP-7 antibody (ab84664), and Actin.

KMR04-206 induces increased IFN-β and CYP1A1 mRNA in MEFs

In order to test whether prior results showing increased IFN-β levels in response to Phthal 01 were due to polypharmacolgy or specific inhibition, we used qRT-PCR to look at IFN-β mRNA levels. This work, performed by Matthews and colleagues, shows that upon co-treatment with 3-pRNA, a ligand of the RNA helicase RIG-I, KMR04-206 triggers an increase in IFN-β levels in a dose dependent manner **(Figure 3.14 A)**. What can also be observed are the high levels of IFN-β in the PARP-7 catalytically inactive H532A knock-in MEFs. These data substantiate PARP-7 as a regulator of the type-I interferon innate immune response and show its role in suppressing IFN-β levels is dependent on its catalytic activity.

In addition to looking at IFN-β levels, cytochrome P450 1A1 (CYP1A1) mRNA levels were also measured **(Figure 3.14 B)**. CYP1A1 is a gene that is upregulated by the Aryl hydrocarbon receptor (AhR) as a mechanism to mediate toxicity associated with TCDD[19]. PARP-7 is transcriptionally upregulated by AhR and through a negative feedback loop, PARP-7 acts as a repressor of AhR[20]. Using a catalytic mutant of PARP-7, PARP-7 mediated inhibition of AhR has been shown to be dependent on PARP-7 catalytic activity[20]. Upon induction of PARP-7 with TCDD, KMR04-206 appears to have a similar affect as the PARP-7 catalytic mutant showing CYP1A1 mRNA is increased

(Figure 3.14 B). These data support the canonical role of PARP-7 in mediating the AhR pathway.

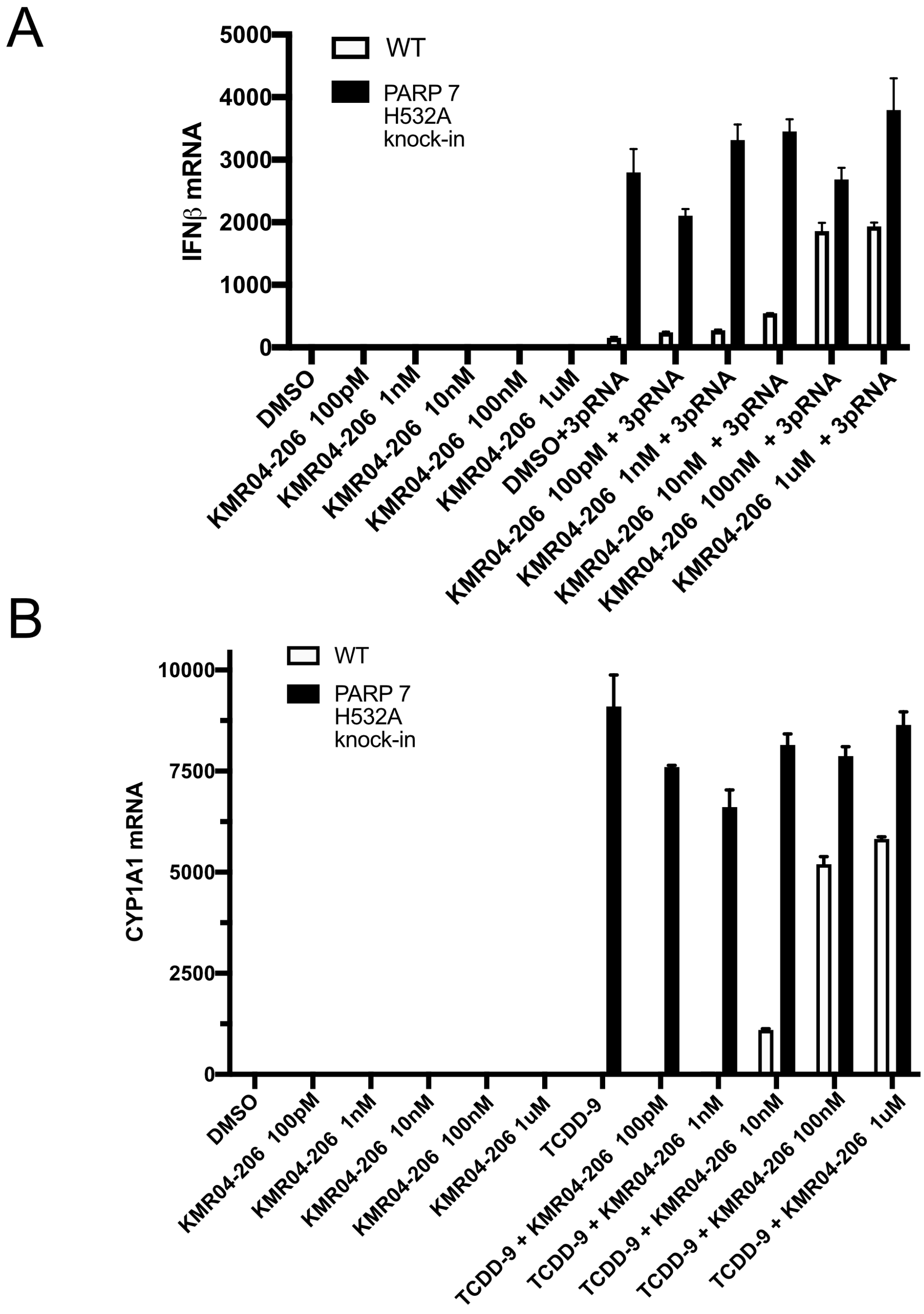

Figure 3.14. qRT-PCR of IFN-B and CYP1A1 mRNA in MEFs post inhibition of PARP 7 with KMR04-206

Data were collected using lysates of MEFs from WT mice or PARP 7 catalytically inactive H532A mutant knock-in mice.

Discussion

In this study we developed a potent PARP-7 selective inhibitor with >10 fold selectivity for PARP-7 in comparison to PARPs- 1, 2, 8, 10, 12, and 15 (all the PARP family members we were able to test in cells). The results we obtained in assays looking at the functional consequences of PARP-7 inhibition support a role for PARP-7 in the type-I interferon response. More studies need to be performed in order to better understand the context specific role of PARP-7, and KMR04-206 will be a useful tool for these studies. Moreover, KMR04-206 could serve as a useful tool for crystallization of PARP-7.

We found when PARP-7 is inhibited its levels increase and its localization changes. These results are consistent with previous studies showing PARP-7 catalytic mutants are more highly expressed compared with wildtype and no longer found in nuclear condensates[21]. Other studies show that PARP-7 is stabilized by proteasomal inhibition (MG132) resulting in higher levels and accumulation in the nucleus[22]. Moreover, PARP-7 associated nuclear condensates have been shown to recruit an E3 ubiquitin ligase HUWE1 and degrade the transcription factor HIF-1a[17]. Taken together these results support a role for PARP-7 in proteasomal degradation in nuclear condensates, which is likely dependent on its catalytic activity. KMR04-206 will serve as a useful compound to elaborate upon these studies.

The data provided in Figure 3.2 of this study show increased IFN-β mRNA levels in cells treated with Phthal 01 (a PARP-1,2, and 7 inhibitor) in the absence of additional stimulus of innate immune signaling. A slightly different result is obtained in figure 3.13 showing IFN-β mRNA levels are only increased with KMR04-206 upon co-treatment with 3-p-RNA. PARP-7 is not the only PARP to participate in the innate immune response. Recent work has highlighted the role of PARP-1 inhibitors in activating the cGAS-cGAMP-STING pathway of activation of the type-I interferon response[23,24]. It is possible that the IFN-β response in the absence of 3-pRNA, observed in figure 3.2, is a polypharmacological result of dual inhibition of PARP-1 and PARP-7, and therefore KMR04-206 does not illicit the same heightened response because it only inhibits PARP-7. Further studies are need to address this hypothesis.

Methods

Cell culture

HEK293T were grown in DMEM (Gibco) supplemented with 10% fetal bovine serum (FBS, Millipore Sigma), and glutamax (Gibco) at 37˚C and 5% CO2. CT-26 cells were grown in RPMI supplemented with 10% FBS. Mouse embryonic fibroblasts (MEFs) derived from WT or KO PARP-7 mice were cultured as previously described[3].

In cell MARylation of GFP-PARP proteins to generate inhibition curves.

HEK293T cells were seeded and grown overnight to ~60% confluency on a 6-well plate. The next morning the cells were transfected using CalPhos Mammalian Transfection kit. 1.5 µg of each plasmid (for co-transfection) were used in each well of the 6 well plate and transfection protocol according to manufacturer was followed. After 4-6 h transfection, the media was swapped with fresh warm media containing a specified dose of inhibitor (some with co-treatments to boost NAD$^+$ levels). Cells were allowed to grow overnight and typically reached ~90% confluency. The following morning, media was aspirated and cells were washed with 2 ml cold PBS/ well. All PBS was aspirated and the cell plate was frozen in the -80˚C until ready to lyse. Cell plates from -80˚C were taken out onto ice and 75 µl of LysB (50 mM HEPES pH7.4, 150 mM NaCl, 1 mM $MgCl_2$, 1% tritonX-100, 1X protease inhibitor, 1X phosphatase inhibitors, 1µM veliparib, 100 µM TCEP) added to the frozen wells of the plate. The plates were allowed to thaw for about 10 min on ice and the cells were removed from the plate by pipetting up and down in the wells to collect cell lysates. Lysates were transferred to Eppendorf tubes and centrifuged 10,000g for 5 min at 4˚C. The supernatant was transferred to a fresh tube and the protein concentration was determined by the Bradford assay (Biorad). The lysates were brought to 200 µg/60 µl and then 20 µl of 4X sample buffer was added for a final concentration of 2.5 µg/ul. The samples were boiled and 15µl (37.5 µg) of total proteins were separated by 10% SDS-PAGE. Proteins were then transferred to nitrocellulose, blocked with milk and probed for ADPr (CST) 1:1000, GFP (Chromotek, 1:1000), actin (Santa Cruz Biotechnology, 1:1000), and Myc (CST, 1:1000).

Quantitative RT-PCR (Figure 3.1 only)

RNA was isolated using Trizol (Thermo Fisher Scientific) via phase separation and DNA contamination was removed using DNase treatment. cDNA was generated with ImPromII reverse transcriptase (Promega). Quantitative PCR was performed using

PerfeCTa qPCR FastMix II (QuantaBio) and primers and probes for the following targets: Ifnb1 - Forward primer CTCCAGCTCCAAGAAAGGAC, Probe CAGGAGCTCCTGGAGCAGCTGA, Reverse primer GCCCTGTAGGTGAGGTTGAT ordered from Integrated DNA Technologies [IDT] and Rps29 (IDT assay number Mm.PT.58.21577577). The absolute copy number was determined by comparing threshold cycle (CT) values to a standard curve generated using DNA of a known copy number encoding the target sequence. Samples are graphed as the absolute copy number of the indicated target divided by the absolute copy number of a housekeeping gene (Rps29).

PARP-7 antibody validation and effects of Phthal01 on endogenous PARP-7 levels in cell culture

WT or KO PARP-7 MEFs were plated at a density of 2.0 x 10^5 cell per ml in 6-well plates. The following day, the cells were treated for 4 hours with DMSO, 10 nM TCDD, 1 μM Phthal01, or co-treated with TCDD and Phthal01. Cell pellets were collected and lysed in RIPA buffer (20 mM Tris-HCl (pH 7.5), 150 mM NaCl, 1 mM EDTA, 1 mM EGTA, 1% NP-40, 1% sodium deoxycholate) supplemented with 1X protease inhibitor cocktail (Roche). Samples were sonicated at a low intensity for 2 cycles of 30 seconds on/off two times using a Bioruptor and rotated for 30 min at 4^{o}C. After centrifugation, the protein concentration was determined by BCA assay (Bio-Rad). 40 ug of total protein was separated by SDS-PAGE and transferred to a PVDF membrane. Membranes were incubated with in house generated anti-PARP-7 (1:1000) or anti-*B*-actin in 5% milk overnight. Membranes were stripped, blocked, and re-blotted with anti-PARP-13

(Invitrogen PA5-106389; 1:1000) or with anti-PARP-7 (Abcam 84664 lot# GR3304056-5; 1:1000).

Chemistry methods:

General. ^{1}H NMR were recorded on a Bruker DPX spectrometer at 400 MHz. Chemical shifts are reported as parts per million (ppm) downfield from an internal tetramethylsilane standard or solvent references. Dichloromethane (DCM), tetrahydrofuran (THF), and Dimethylformamide (DMF) were dried using a solvent purification system manufactured by Glass Contour, Inc. (Laguna Beach, CA). Additional drying of solvents, where indicated in methods, occurred using 3Å or 4Å activated sieves. All other solvents were of ACS chemical grade (Fisher Scientific) and used without further purification unless otherwise indicated. Commercially available chemical compounds were purchased from CombiBlocks (San Diego, CA), and TCI America (Portland, OR) and were >95% pure and used without further purification. All other reagents were of ACS chemical grade (Fisher Scientific) and used as received.

Synthesis of KMR04-206

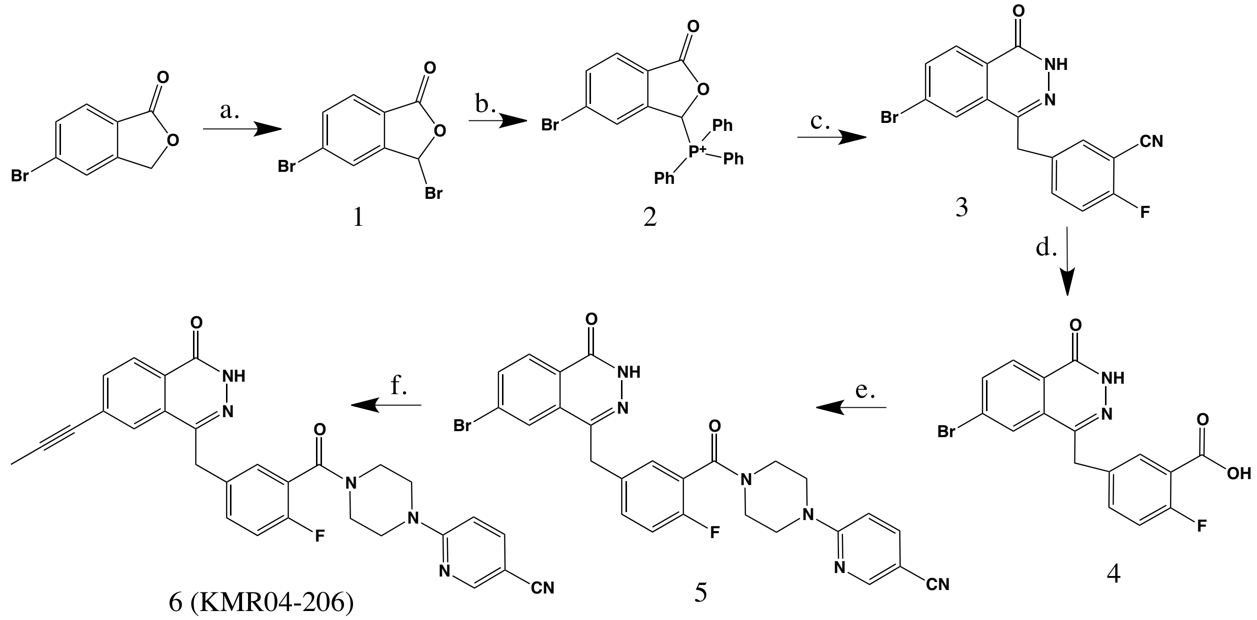

Scheme 3.1: Synthesis of KMR04-206 (a) NBS, AIBN,CCl_4 reflux; (b) PPh_3, THF reflux; (c) 1) 2-fluoro-5-formylbenzonitrile, TEA, DCM 2) Hydrazine hydrate, H_2O, EtOH, DMF reflux; (d) 1) KOH,EtOH, ddH_2O, 2) HCl; (e) 6-(piperizino)pyridine-3-carbonitrile, PPA, DIPEA, DMF; (f) tributyl (1-propynyl) tin, palladium Tetrakis, toluene reflux.

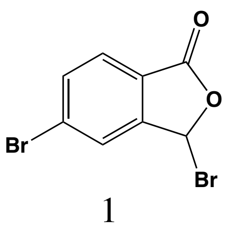

1

5-bromo-phthalide (2g, 9.44mmol) was heated to reflux in carbon tetrachloride (CCl4) with Azobisisobutyronitrile (160mg, 0.944 mmol) and N-Bromosuccinimide, (1.9g, 10.7 mmol) for 4 hours until reaction was completed. The reaction was then filtered and the filtrate was concentrated. The crude mixture was then purified via column purification using combiflash ISCO purification system using a mobile phase gradient from 0 to 30% ethyl acetate in hexanes. 2.35g of **compound 1** was obtained (86% yield). ^{1}H NMR (400 MHz, CDCl3) δ 7.84 – 7.71 (m, 3H), 7.34 (s, 1H).

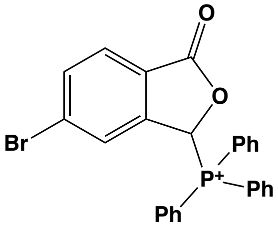

2

Under dry conditions, in a clean, oven dried flask, **compound 1** (white solid) (2g, 6.9mmol) was heated slightly (50˚C) under vacuum pressure with dry triphenyl phosphine (1.81g, 6.9mmol) for 30 mins. Triphenyl phosphine and compound 1 were both dried over P2O5 overnight prior to starting the reaction. To the dry starting materials, dry THF was added and the reaction was allowed to stir under reflux overnight. A white precipitate formed quickly after reaction started. The white precipitate, **compound 2**, was filtered out and dried under vacuum. (2.6g, 80% yield) ^{1}H NMR (400 MHz, $CDCl_3$) δ 10.29 (s, 1H), 7.88 (ddd, *J* = 19.4, 15.0, 9.1 Hz, 8H), 7.70 (td, *J* = 7.9, 3.7 Hz, 7H), 7.60 (d, *J* = 8.2 Hz, 2H), 7.25 (s, 1H).

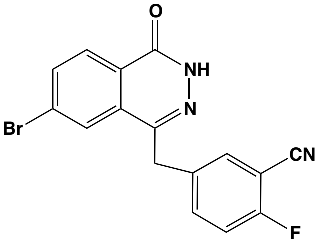

3

Compound 2 (0.475 g, 1.0mmol) and 2-fluoro-5-formylbenzonitrile (.180 g, 1.2 mmol) were dissolved DCM (4.0 mL), to this was added triethylamine (0.18 mL, 1.3 mmol) and the reaction was stirred overnight. The reaction mixture was quenched with water (5 mL), extracted with DCM (2 x 10 mL), the organic layer was dried over MgSO4, filtered and evaporated the solvent to yield a pale white solid (0.335 g, 98%). ^{1}H NMR (400 MHz, DMSO) δ 8.22 (d, *J* = 1.7 Hz, 1H), 8.17 (d, *J* = 8.5 Hz, 1H), 8.02 (dd, *J* = 8.5, 1.8 Hz, 1H), 7.90 (dd, *J* = 6.2, 2.2 Hz, 1H), 7.73 (ddd, *J* = 7.9, 5.3, 2.3 Hz, 1H), 7.48 (t, *J* = 9.1 Hz, 1H), 4.38 (s, 2H).

To the crude were added water (2.5 mL), EtOH (2.5 mL) and DMF (0.25 mL). Refluxed the mixture and added Hydrazine hydrate (0.3 mL, 9.7 mmol) and left to reflux overnight. The reaction was cooled and the precipitate was collected by filtration, washed with EtOH (5 mL) and dried under high vacuum to afford **compound 3** as a white solid (0.2 g, 60%) ^{1}H NMR (400 MHz, DMSO) δ 8.22 (d, J = 1.7 Hz, 1H), 8.17 (d, J = 8.5 Hz, 1H), 8.02 (dd, J = 8.5, 1.8 Hz, 1H), 7.90 (dd, J = 6.2, 2.2 Hz, 1H), 7.73 (ddd, J = 7.9, 5.3, 2.3 Hz, 1H), 7.48 (t, J = 9.1 Hz, 1H), 4.38 (s, 2H).

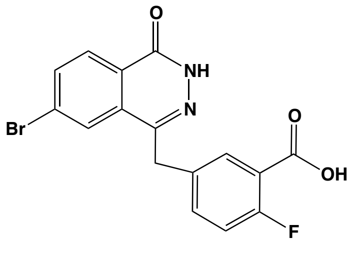

4

Compound 3 (0.20 g , 0.57mmol) and potassium hydroxide (0.323g, 5.75 mmol) were added to ethanol (2 mL) and water (7 mL) and heated at 100° C for 4.5 hours. The ethanol was evaporated off and the aqueous was extracted with ethyl acetate (2 x 5mL).

The aqueous was then acidified to pH=1 with conc. HCl to form a precipitate which was sonicated, filtered, washed with water and dried under high vacuum to afford a beige solid (0.2 g, 94 % yield). ^{1}H NMR (400 MHz, DMSO) δ 12.68 (s, 1H), 8.27 – 8.07 (m, 2H), 7.99 (d, *J* = 8.5 Hz, 1H), 7.86 – 7.71 (m, 1H), 7.62 – 7.48 (m, 1H), 7.24 (t, *J* = 9.6 Hz, 1H), 4.35 (d, *J* = 8.2 Hz, 2H).

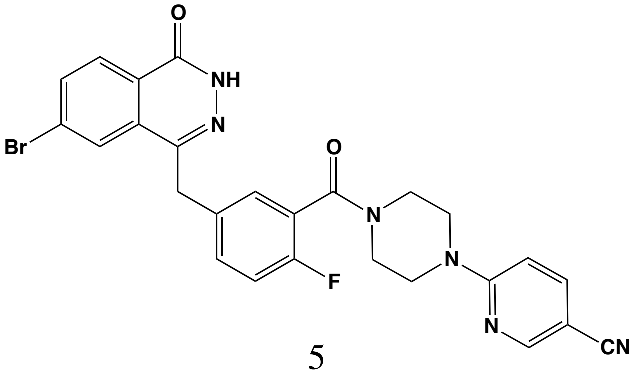

5

Compound 4 (100 mg, 0.266mmol) and 6-(piperizino)pyridine-3-carbonitrile (50mg, 0.266mmol) were dissolved in 700uL DMF in a small scintillation vile. 1-propane phosphoric acid cyclic anhydride (338uL, 0.532mmol) and DIPEA (140uL, 0.798mmol) were added via syringe and the reaction was stirred until complete conversion of the starting material was observed (2.5hours). The reaction was monitored via TLC using 5% MeOH in DCM with 1-2drops glacial acetic acid (to separate the starting material acid from product). The reaction was then dissolved in ethyl acetate (5mL) and washed with saturated NaCO3, ddH2O, and brine. The organic layer was then concentrated to yield 102mg of **compound 5 (KMR04-204)** (70% yield) ^{1}H NMR (400 MHz, DMSO) δ 12.69 (s, 1H), 8.50 (d, *J* = 2.4 Hz, 1H), 8.16 (dd, *J* = 5.2, 3.3 Hz, 2H), 7.94 (ddd, *J* = 45.0, 8.8, 2.1 Hz, 2H), 7.41 (dd, *J* = 8.5, 4.4 Hz, 2H), 7.26 (t, *J* = 8.9 Hz, 1H), 6.91 (d, *J* = 9.1 Hz, 1H), 4.34 (s, 2H), 3.74 (d, *J* = 10.3 Hz, 4H), 3.61 (s, 2H).

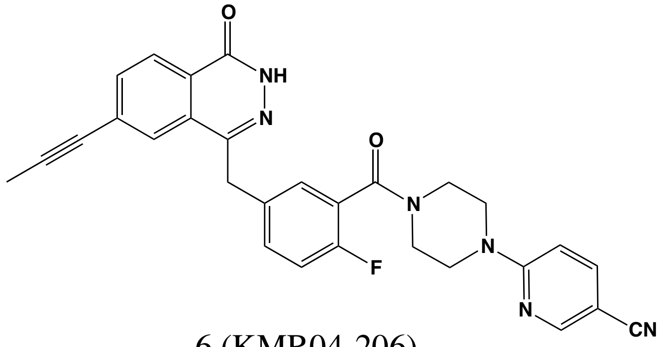

6 (KMR04-206)

In a clean, oven dried 15mL round bottom flask, **Compound 5** (50mg, 0.092mmol) was co-evaporated with dry toluene (5mL) and allowed to sit under high vacuum for 20 mins. Dry toluene (1mL) was added and argon was bubbled through the solution for 10 mins. Under argon pressure, Palladium Tetrakis (10.4mg, 0.009mmol) and Tributyl (1-propynyl) tin (30.4uL, 0.1mmol) were added and the reaction was refluxed under argon pressure for 3 hours until reaction had reached completion. The crude reaction was purified via dry loading method (1g silica) on a 4g silica manual column. The column was initially washed with 100% ethyl acetate to elute excess triphenyl phosphine, followed by 5%MeOH in ethyl acetate to separate impurities and elute desired compound. Fractions containing desired compound were pooled and concentrated to yield 22mg of **compound 6 (KMR04-206)** (47% yield). 1H NMR (400 MHz, DMSO) δ 12.61 (s, 1H), 8.49 (s, 1H), 8.18 (d, J = 8.2 Hz, 1H), 7.89 (d, J = 18.6 Hz, 2H), 7.82 – 7.63 (m, 3H), 7.40 (s, 2H), 7.25 (d, J = 8.5 Hz, 1H), 6.90 (d, J = 9.2 Hz, 1H), 4.32 (s, 2H), 4.12 (s, 2H), 3.84 – 3.55 (m, 8H).

References

1. Gupte, R., Liu, Z. & Kraus, W. L. Parps and adp-ribosylation: Recent advances linking molecular functions to biological outcomes. *Genes Dev.* **31**, 101–126 (2017).
2. Fehr, A. R. *et al.* The impact of PARPs and ADP-ribosylation on inflammation and host-pathogen interactions. *Genes Dev.* **34**, 341–359 (2020).
3. Yamada, T. *et al.* Constitutive aryl hydrocarbon receptor signaling constrains type I interferon–mediated antiviral innate defense. *Nat. Immunol.* **17**, 687 (2016).
4. Kunze, F. A. & Hottiger, M. O. Regulating Immunity via ADP-Ribosylation: Therapeutic Implications and Beyond. *Trends Immunol.* **40**, 159–173 (2019).
5. Daugherty, M. D., Young, J. M., Kerns, J. A. & Malik, H. S. Rapid Evolution of PARP Genes Suggests a Broad Role for ADP-Ribosylation in Host-Virus Conflicts. *PLoS Genet.* **10**, (2014).
6. Vyas, S., Chesarone-Cataldo, M., Todorova, T., Huang, Y.-H. & Chang, P. A systematic analysis of the PARP protein family identifies new functions critical for cell physiology. *Nat. Commun.* **4**, 1–13 (2013).
7. Wahlberg, E. *et al.* Family-wide chemical profiling and structural analysis of PARP and tankyrase inhibitors. *Nat. Biotechnol.* **30**, 283–288 (2012).
8. Donawho, C. K. *et al.* ABT-888, an Orally Active Poly(ADP-Ribose) Polymerase Inhibitor that Potentiates DNA-Damaging Agents in Preclinical Tumor Models. *Clin. Cancer Res.* **13**, 2728 LP – 2737 (2007).
9. Kristeleit, R. *et al.* A Phase I–II Study of the Oral PARP Inhibitor Rucaparib in Patients with Germline BRCA1/2-Mutated Ovarian

Carcinoma or Other Solid Tumors. *Clin. Cancer Res.* **23**, 4095 LP – 4106 (2017).

10. Huang, S.-M. A. *et al.* Tankyrase inhibition stabilizes axin and antagonizes Wnt signalling. *Nature* **461**, 614–620 (2009).
11. Kirby, I. T. *et al.* A Potent and Selective PARP11 Inhibitor Suggests Coupling between Cellular Localization and Catalytic Activity. *Cell Chem. Biol.* **25**, 1547-1553.e12 (2018).
12. Rodriguez, K. M. *et al.* Chemical genetics and proteome-wide site mapping reveal cysteine MARylation by PARP-7 on immune-relevant protein targets. *Elife* **10**, e60480 (2021).
13. Kirby, I. T., Morgan, R. K. & Cohen, M. S. A Simple, Sensitive, and Generalizable Plate Assay for Screening PARP Inhibitors. *Methods Mol. Biol.* **1813**, 245–252 (2018).
14. Berteotti, A. *et al.* Predicting the reactivity of nitrile-carrying compounds with cysteine: a combined computational and experimental study. *ACS Med. Chem. Lett.* **5**, 501–505 (2014).
15. Frizler, M., Stirnberg, M., Sisay, M. T. & Gütschow, M. Development of nitrile-based peptidic inhibitors of cysteine cathepsins. *Curr. Top. Med. Chem.* **10**, 294–322 (2010).
16. Frizler, M., Lohr, F., Furtmann, N., Kläs, J. & Gütschow, M. Structural optimization of azadipeptide nitriles strongly increases association rates and allows the development of selective cathepsin inhibitors. *J. Med. Chem.* **54**, 396–400 (2011).
17. Zhang, L., Cao, J., Dong, L. & Lin, H. TiPARP forms nuclear condensates to degrade HIF-1α and suppress tumorigenesis. *Proc. Natl. Acad. Sci. U. S. A.* **117**,

13447–13456 (2020).

18. Ma, Q., Baldwin, K. T., Renzelli, A. J., McDaniel, A. & Dong, L. TCDD-inducible poly(ADP-ribose) polymerase: a novel response to 2,3,7,8-tetrachlorodibenzo-p-dioxin. *Biochem. Biophys. Res. Commun.* **289**, 499–506 (2001).
19. Diani-Moore, S. *et al.* Identification of the aryl hydrocarbon receptor target gene TiPARP as a mediator of suppression of hepatic gluconeogenesis by 2,3,7,8-tetrachlorodibenzo-p-dioxin and of nicotinamide as a corrective agent for this effect. *J. Biol. Chem.* **285**, 38801–38810 (2010).
20. MacPherson, L. *et al.* 2,3,7,8-Tetrachlorodibenzo-p-dioxin poly(ADP-ribose) polymerase (TiPARP, ARTD14) is a mono-ADP-ribosyltransferase and repressor of aryl hydrocarbon receptor transactivation. *Nucleic Acids Res.* **41**, 1604–1621 (2013).
21. Gomez, A. *et al.* Characterization of TCDD-inducible poly-ADP-ribose polymerase (TIPARP/ARTD14) catalytic activity. *Biochem. J.* **475**, 3827–3846 (2018).
22. Lu, A. Z. *et al.* Enabling drug discovery for the PARP protein family through the detection of mono-ADP-ribosylation. *Biochem. Pharmacol.* **167**, 97–106 (2019).
23. Ding, L. *et al.* PARP Inhibition Elicits STING-Dependent Antitumor Immunity in Brca1-Deficient Ovarian Cancer. *Cell Rep.* **25**, 2972-2980.e5 (2018).
24. Chabanon, R. M. *et al.* PARP inhibition enhances tumor cell-intrinsic immunity in ERCC1-deficient non-small cell lung cancer. *J. Clin. Invest.* **129**, 1211–1228 (2019).

^{1}H-NMR spectra

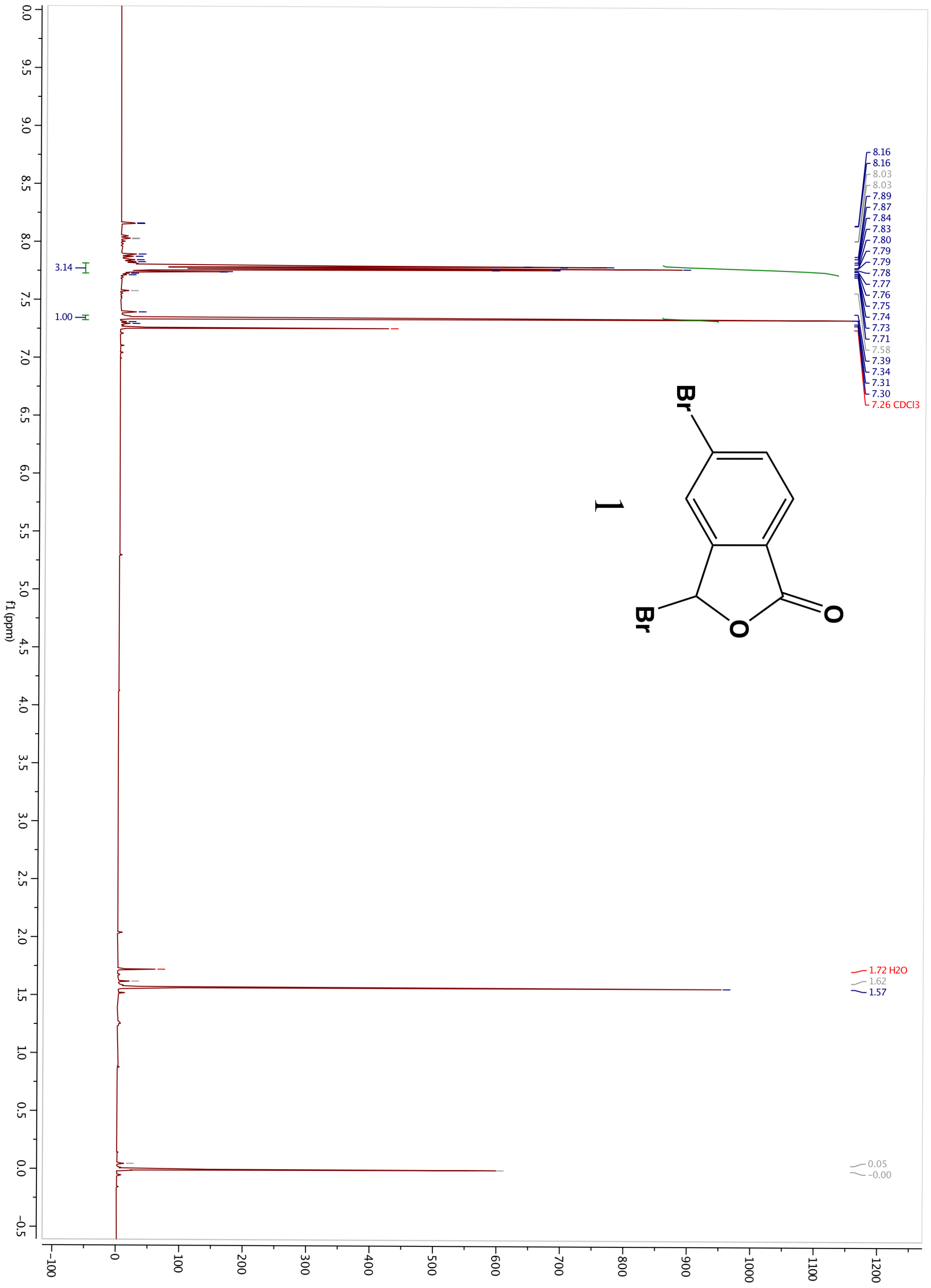

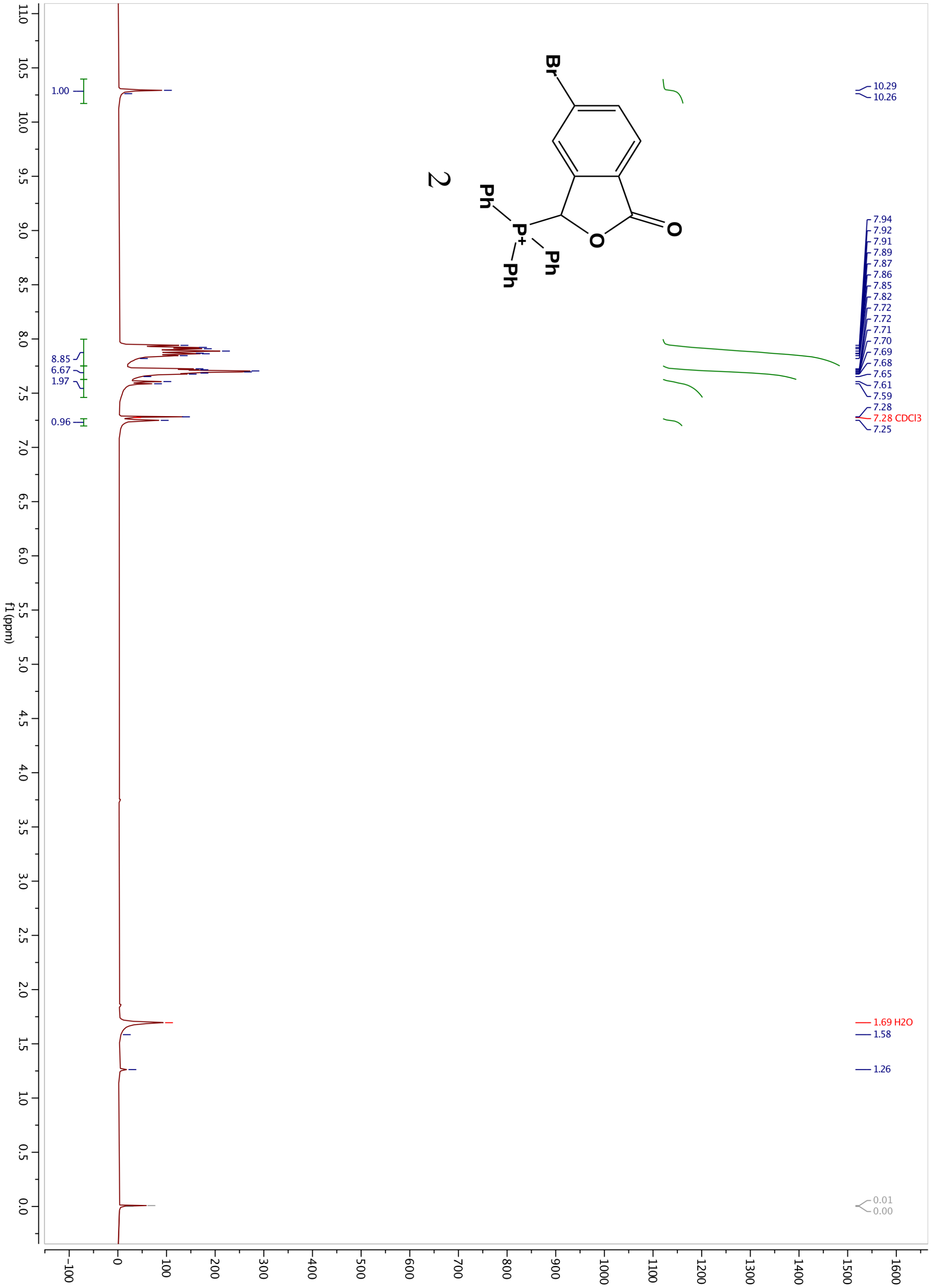2
Br
O
O
P+
Ph
Ph
Ph
10.29
10.26
7.94
7.92
7.91
7.89
7.87
7.86
7.85
7.82
7.72
7.72
7.71
7.70
7.69
7.68
7.65
7.61
7.59
7.28
7.28 CDCl3
7.25
1.69 H2O
1.58
1.26
0.01
0.00
1.00
8.85
6.67
1.97
0.96
f1 (ppm)
11.0
10.5
10.0
9.5
9.0
8.5
8.0
7.5
7.0
6.5
6.0
5.5
5.0
4.5
4.0
3.5
3.0
2.5
2.0
1.5
1.0
0.5
0.0
-100
0
100
200
300
400
500
600
700
800
900
1000
1100
1200
1300
1400
1500
1600

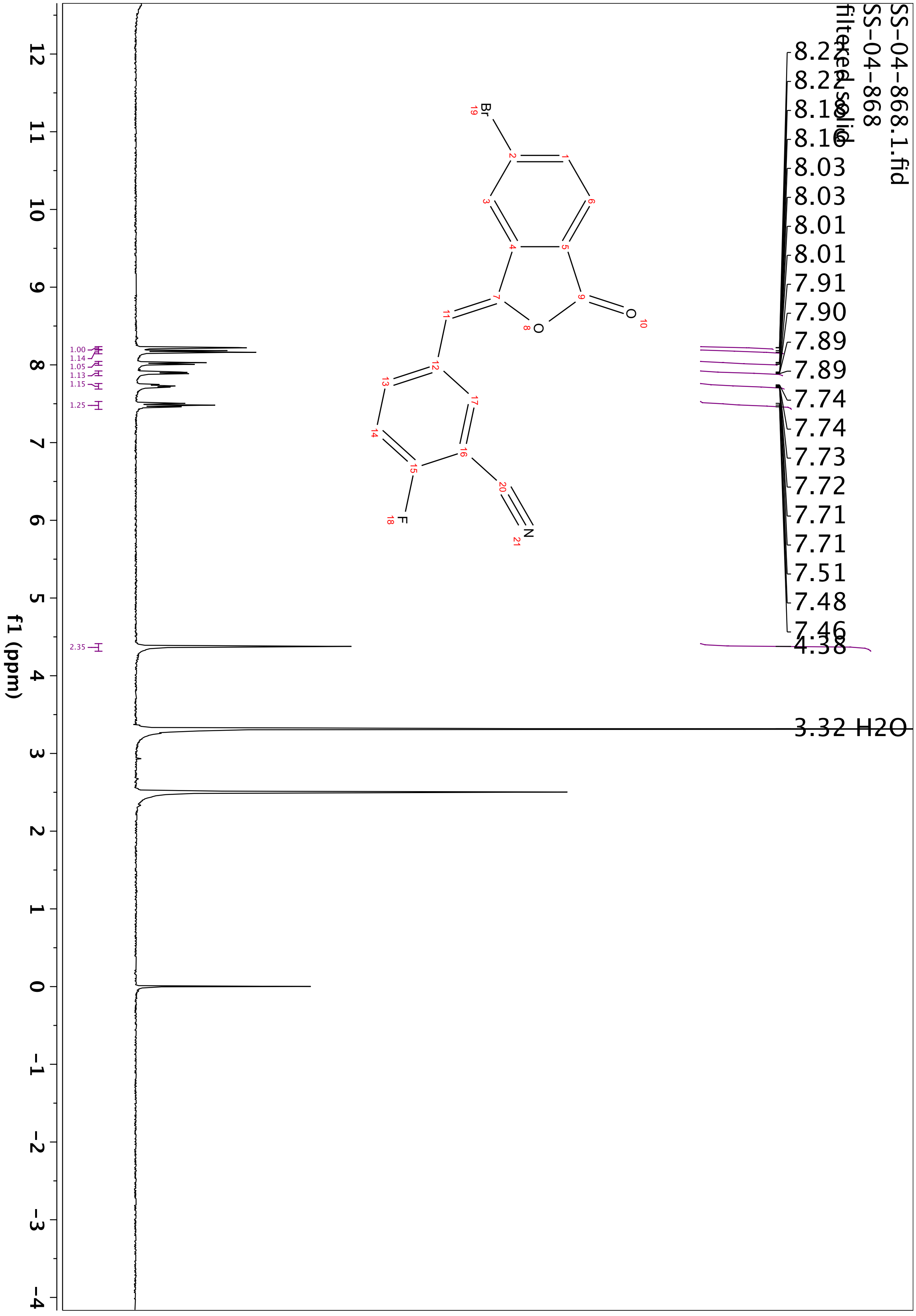
SS-04-868.1.fid
SS-04-868
filtered solid
8.21
8.21
8.16
8.16
8.03
8.03
8.01
8.01
7.91
7.90
7.89
7.89
7.74
7.74
7.73
7.72
7.71
7.71
7.51
7.48
7.46
4.38
3.32 H2O
Br
O
O
F
N
1.00
1.14
1.05
1.13
1.15
1.25
2.35
12
11
10
9
8
7
6
5
4
3
2
1
0
-1
-2
-3
-4
f1 (ppm)

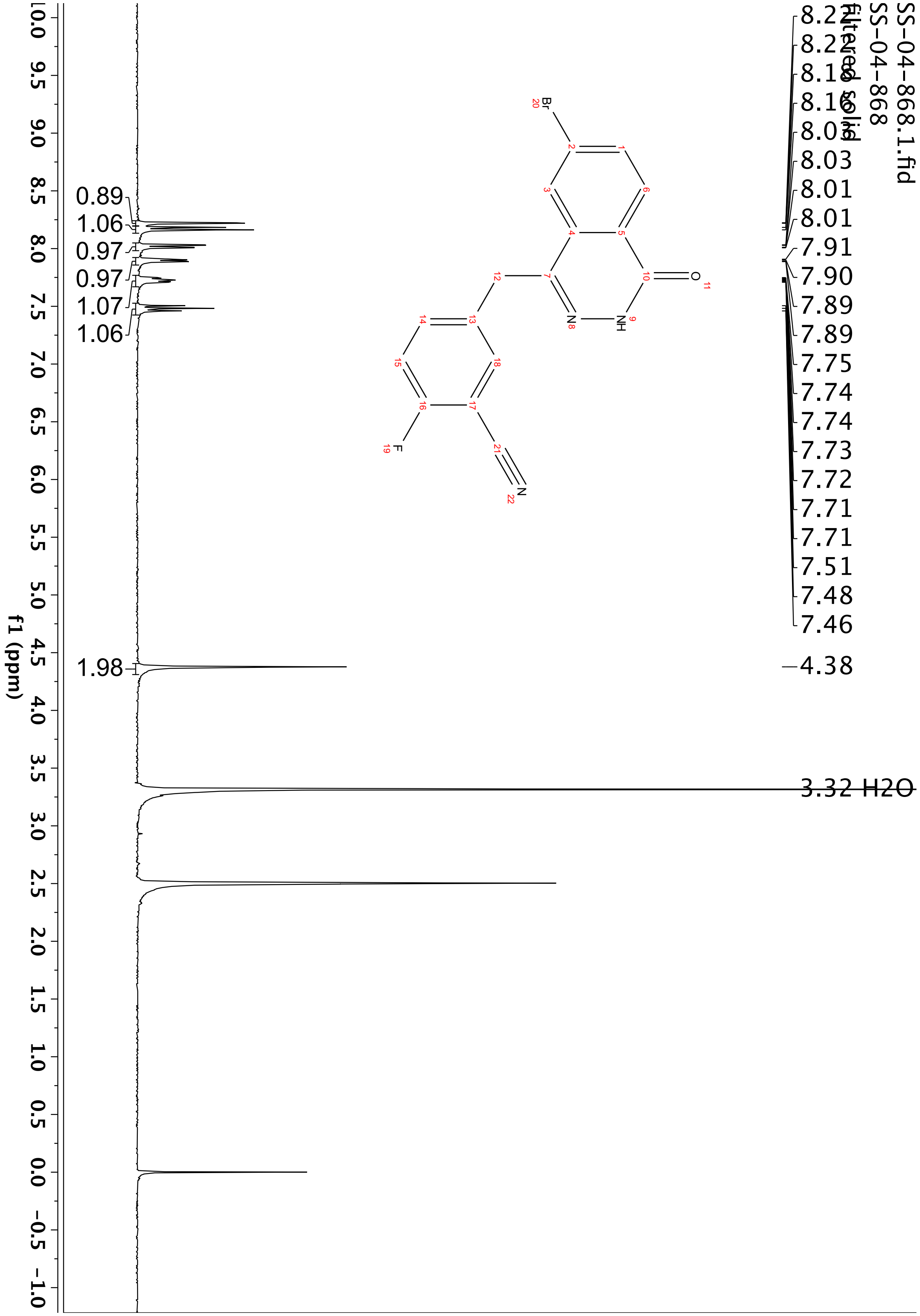
SS−04−868.1.fid
SS−04−868
filtered solid
8.22
8.22
8.18
8.16
8.03
8.03
8.01
8.01
7.91
7.90
7.89
7.89
7.75
7.74
7.74
7.73
7.72
7.71
7.71
7.51
7.48
7.46
4.38
3.32 H2O
0.89
1.06
0.97
0.97
1.07
1.06
1.98
Br
20
1
2
3
4
5
6
7
NH
9
N
8
10
O
11
12
13
14
15
16
17
18
F
19
21
N
22
10.0
9.5
9.0
8.5
8.0
7.5
7.0
6.5
6.0
5.5
5.0
4.5
4.0
3.5
3.0
2.5
2.0
1.5
1.0
0.5
0.0
−0.5
−1.0
f1 (ppm)

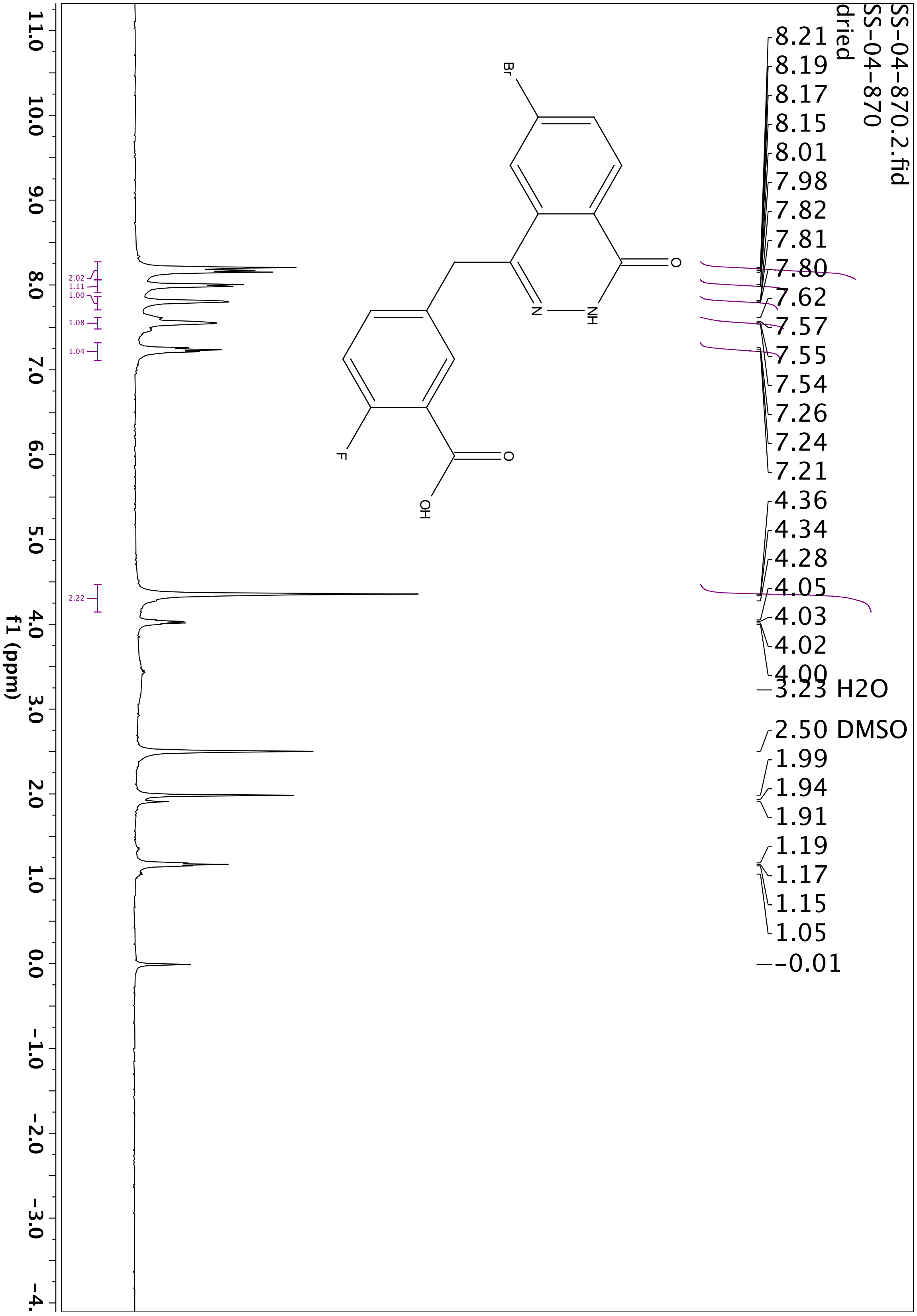
SS-04-870.2.fid
SS-04-870
dried
8.21
8.19
8.17
8.15
8.01
7.98
7.82
7.81
7.80
7.62
7.57
7.55
7.54
7.26
7.24
7.21
4.36
4.34
4.28
4.05
4.03
4.02
4.00
3.23 H2O
2.50 DMSO
1.99
1.94
1.91
1.19
1.17
1.15
1.05
-0.01
Br
O
NH
N
F
O
OH
2.02
1.11
1.00
1.08
1.04
2.22
11.0
10.0
9.0
8.0
7.0
6.0
5.0
4.0
3.0
2.0
1.0
0.0
-1.0
-2.0
-3.0
-4.
f1 (ppm)

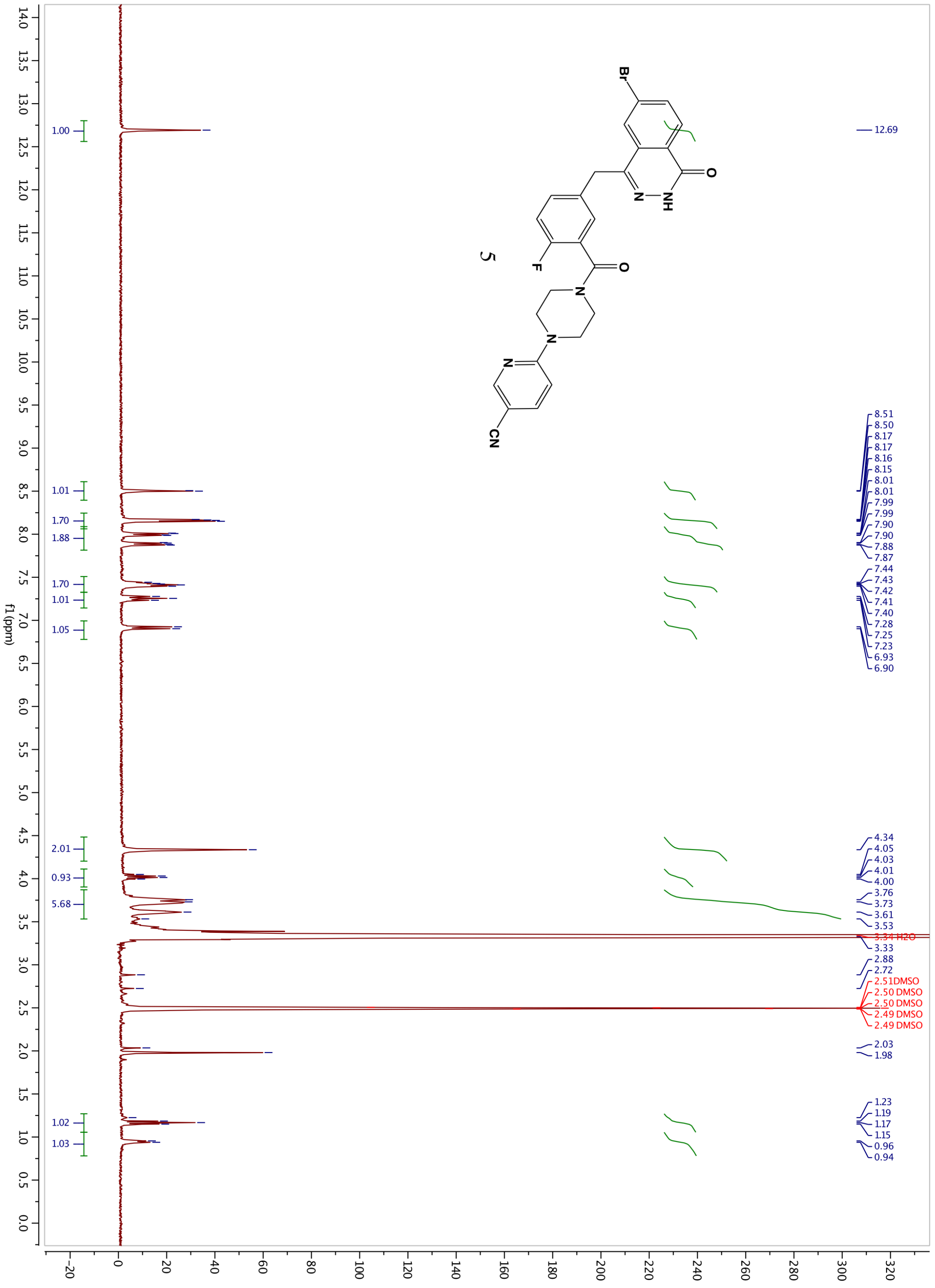

5
Br
O
NH
N
O
F
N
N
N
CN
12.69
8.51
8.50
8.17
8.17
8.16
8.15
8.01
8.01
7.99
7.99
7.90
7.90
7.88
7.87
7.44
7.43
7.42
7.41
7.40
7.28
7.25
7.23
6.93
6.90
4.34
4.05
4.03
4.01
4.00
3.76
3.73
3.61
3.53
3.34 H2O
3.33
2.88
2.72
2.51 DMSO
2.50 DMSO
2.50 DMSO
2.49 DMSO
2.49 DMSO
2.03
1.98
1.23
1.19
1.17
1.15
0.96
0.94
1.00
1.01
1.70
1.88
1.70
1.01
1.05
2.01
0.93
5.68
1.02
1.03
f1 (ppm)

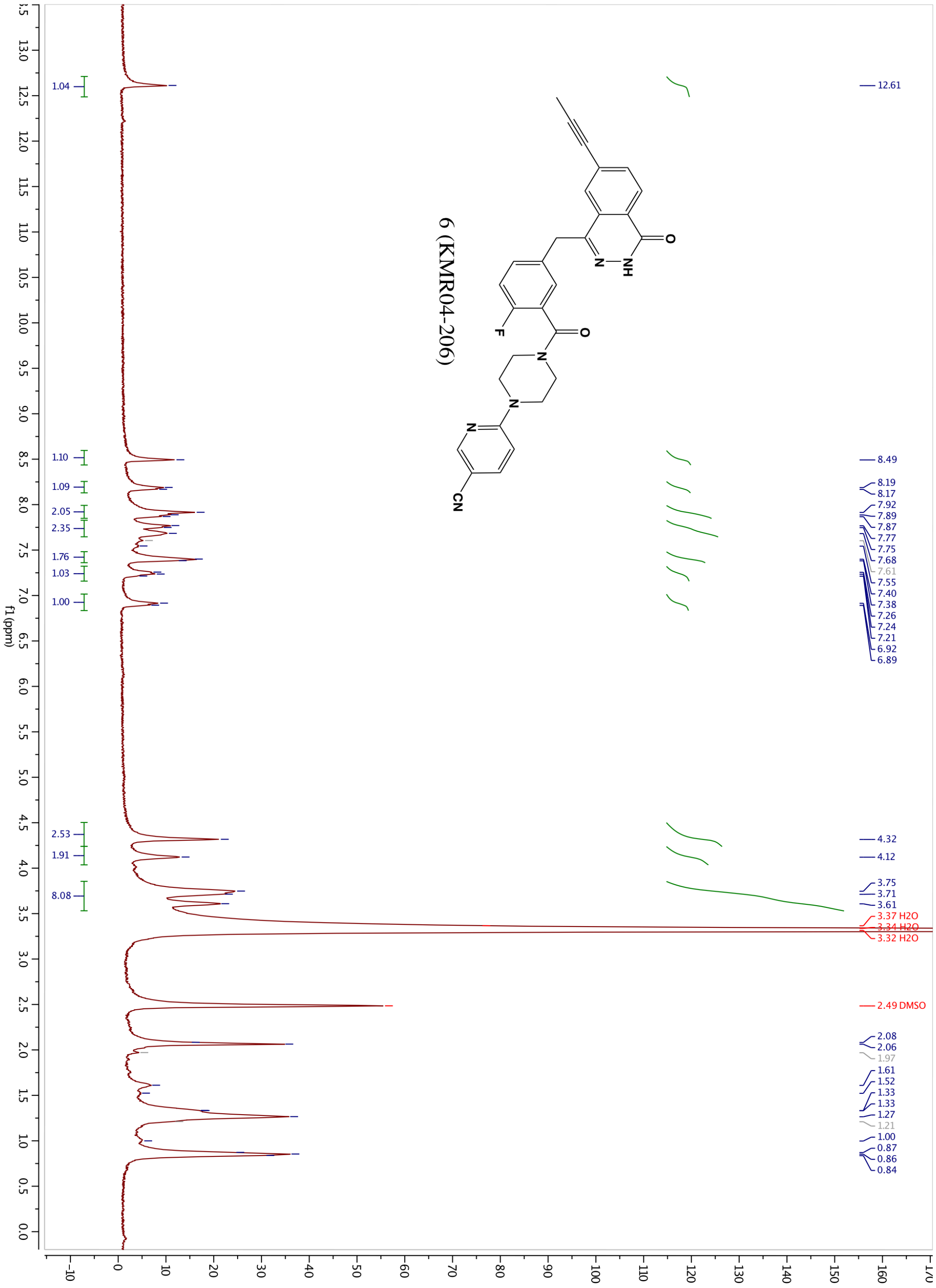
6 (KMR04-206)

O
NH
N
O
N
F
N
N
CN
f1 (ppm)
12.61
8.49
8.19
8.17
7.92
7.89
7.87
7.77
7.75
7.68
7.61
7.55
7.40
7.38
7.26
7.24
7.21
6.92
6.89
4.32
4.12
3.75
3.71
3.61
3.37 H2O
3.34 H2O
3.32 H2O
2.49 DMSO
2.08
2.06
1.97
1.61
1.52
1.33
1.33
1.27
1.21
1.00
0.87
0.86
0.84
1.04
1.10
1.09
2.05
2.35
1.76
1.03
1.00
2.53
1.91
8.08

Chapter 4.

Brief chapter: NAD$^+$ based chemical probes for identifying protein binding partners of ADP-ribose

Contributions from Sunil Sundalam, Ph.D.: synthesis of 8-azido and 2-azido NAD$^+$ used in this study.

Abstract/ Introduction

ADP ribosylation (ADPr) is a dynamic post-translational modification essential for a variety of cellular processes. Cellular “writers” of ADPr, known as Poly (ADP-ribose) polymerases(PARPs), transfer ADPr to target proteins from nicotinamide adenine dinucleotide (NAD^+). Subsequently, there are several ADPr-hydrolases, or “erasers”, known to remove ADPr, including: MacroD1/D2, ARH1/3, TARG1, PARG, and DarGs[1]. Our lab has shown that knockdown of the known “erasers” is not enough to sufficiently prevent removal of ADPr on PARP-10 (unpublished data not shown). This result leads us to believe there may be additional “erasers” of ADPr that have not yet been discovered. Furthermore, work from our lab and others have shown ADPr-linkages for which there are no known ADPr-hydrolases, including cysteine ADPr [1]. Through synthesis of well-designed chemical probes, *in vitro* experiments, and mass spectrometry proteomics we hope to capture and identify novel “readers” and “erasers” of ADPr. This goal will be accomplished through synthesis of photo-reactive chemical probes.

While several tools have been developed and used to identify ADP-ribosylated (PARylated and MARylated) proteins, no such tool exists to identify ADP-ribose binding partners. The goal of this project, which will continue beyond this chapter by current and future lab members, is to identify interacting proteins of ADPr. This work will provide hypothesis generating information about the cellular interactions amongst ‘readers’ ‘writers’ and ‘erasers’ of ADPr.

In this chapter, a number of NAD^+ probes, some with photo-reactive groups were designed and synthesized with modifications to the adenosine ring. These analogs provided key information showing how placement of modifications to the adenosine ring of NAD$^+$ are tolerated by PARPs to transfer ADPr. We used PARP10 as a model protein because it robustly labels itself and other proteins *in vitro*. We learned that small substituents in the C2 and C8- positions of adenosine ring are the best substrates for PARP10. Through synthesis of C2 and C8-azido-NAD$^+$ derivatives, we were able to successfully crosslink ADPr auto-modified his-PARP10 catalytic domain (His$_6$-PARP10$_{cat)}$ to proteins in cell lysates.

Rational design of photoreactive NAD$^+$ analogs to crosslink and identify binding partners of modified ADPr

To rationally design an NAD$^+$ based chemical probe that can be used to identify ADPr binding partners, there were two critical points to consider: 1) The probe needs to be used as a substrate by PARPs onto a target protein as a modified ADPr photoaffinity tag (mADPr), and 2) The mADPr must be able to bind readers with high enough affinity to allow abundant photo-crosslinking of ‘readers’ and ‘erasers’ **(Figure 4.1).** To aid in this second aspect of design, the crystal structure of a known eraser of ADPr, MacroD2, bound to ADPr was considered (**Figure 4.2**)[5]. The macro domain proteins have a conserved fold that allows binding to ADPr. Within this fold, it appears that only one hydrogen bond is made in the N6 position of the adenosine ring. We thought that it might be possible that macro domain binding may not be disrupted at this position as long as this hydrogen bond is maintained. Additionally, it appears that the 8-position of the adenosine ring is exposed to solvent, and therefore may be amenable to modification. The 2-position appears to be buried in a pocket, suggesting that a macro domain ‘reader’ may have difficulty recognizing substituents in this position. However, if binding does occur, there will be nearby amino acid residues available to react with mADPr during photo-crosslinking.

Taken together these rationale inspired the synthesis of NAD^+ derivatives with substituents in the C2, C8, and N6 position of the adenosine ring to be tested by PARP family members.

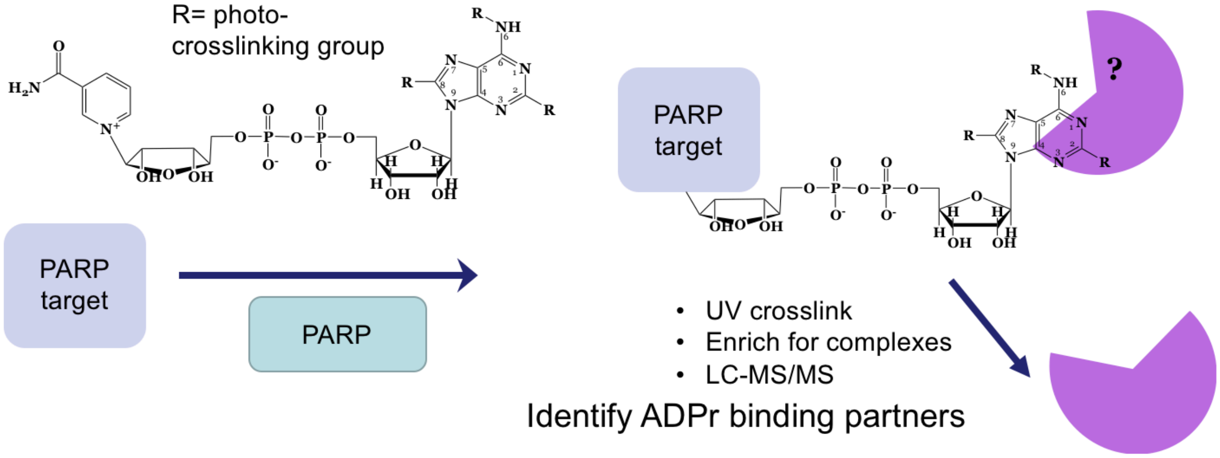

Figure 4.1. Schematic of approach for identifying ADP-ribose binding proteins via photo-reactive crosslinking

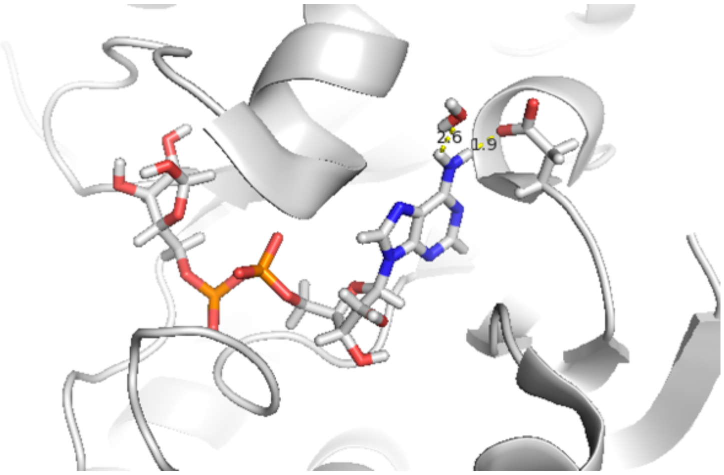

Figure 4.2: crystal structure of MacroD2 bound to ADP-ribose. A hydrogen bond is made at the N6-position of the adenosine ring, at 1.9A with an Asp residue. The other labeled contact is water. The 8-position is solvent exposed and the 2-position is buried.

Results

Assessment of NAD$^+$ analog transfer of ADPr by PARP10 to SRPK2

Initially two straightforward molecules were synthesized with photo-crosslinking units in the N6 position of the adenosine ring. Modification of the N6-position with a propynyl substituent minimally disrupts PARP activity[2]. Based on this, two photo-reactive NAD$^+$ derivatives with modification in the N6-position were synthesized; a diazirine derivative and a benzophenone derivative (6-BP-NAD+ and 6-DA-NAD$^+$) **(Scheme 4.1, Figure 4.3).** Once the analogs were synthesized, ADPr assays were performed using His$_6$-PARP10$_{cat}$ to MARylate a substrate known as serine/arginine-rich protein-specific kinase 2 (SRPK2). SRPK2 has served as an excellent "dummy substrate" as it is robustly labeled *in vitro* and thus serves as a measurement to assess ADPribosylation[6]. Results of ADPr assays were visualized using two methods: 1) ADPr was measured using an aminooxy-TAMRA (AO-TAMRA) probe developed by our lab to measure ADPribosylation [7] and 2) western blot analysis using an anti-ADPr reagent. The ADPr (MAR and PAR) recognition portion of the anti-ADPr reagent is a macrodomain protein (Af1521) which is fused to a rabbit Fc tag[8]. In addition to assessing ADP-ribosylation, this anti-ADPr reagent served as a useful tool to assess the binding efficiency of a 'reading' domain to the mADPr. ADP-ribosylation of SRPK2 by His_6-$PARP10_{cat}$ using N6-DA-NAD^+ is approximately 10% as efficient as native NAD^+, at the same concentration (100μM) **(Figure 4.4).** ADP-ribosylation with N6-BP-NAD+ is an even worse substrate (~5%).

Next, three NAD^+ derivatives, synthesized for previous projects (8-s-butyne NAD+, 2-alkyne NAD+ and 6-alkyne NAD^+) as well as two others that were commercially available (6-biotin NAD^+ and 8-bromo NAD^+) were tested to assess transfer efficiency by His_6-$PARP10_{cat}$ **(Figure 4.4a)**. Although these derivatives are not photo crosslinking compounds, they were used to provide insight into the length and location of where modifications could be made around the ring. 8-bromo NAD^+ showed robust ADPr of SRPK2, appearing to have an even higher transfer efficiency by His_6-$PARP10_{cat}$ than NAD^+, the endogenous substrate **(Figure 4.4b,c).** 8-s-butyne NAD^+ showed extremely poor ADPr, indicating that only a small modification in the C8 position is tolerated **(Figure 4.4b,c).** 2-alkyne NAD^+ appeared to be more efficient than other analogs, particularly when looking at in gel fluorescence using the AO-TAMRA probe. A western blot using the anti-ADPr reagent showed a relative decrease in signal when compared to AO-TAMRA, indicating that the reading motif on the antibody may have difficulty recognizing ADPr with the 2-alkyne modification. However, the robust transfer by His_6-$PARP10_{cat}$ indicated that the 2-position may be a viable location for derivation.

(**Figure 4.4**). Through these preliminary studies, we gained insight in to the type of substituents that can be accommodated on the adenosine ring.

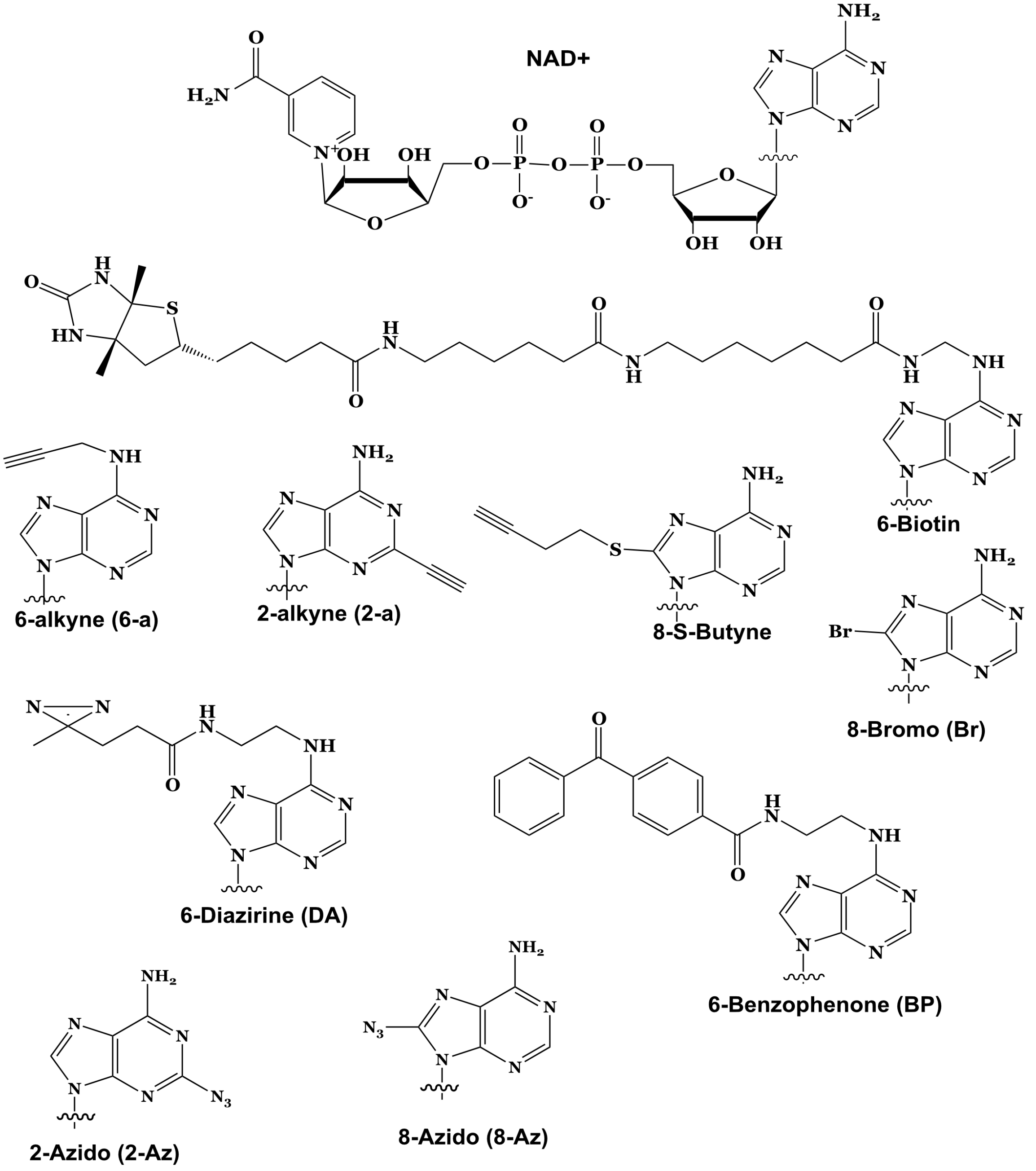

Figure 4.3 Chemical structure of adenosine ring-modified NAD+ analogs used in this study.

All but 8-Br and 6-biotin NAD+ were synthesized by our lab. 6-DA, 6-BP, 2-Az, and 8-az have photo-crosslinking groups, the others were used as comparison compounds to obtain data on positions amenable to modification.

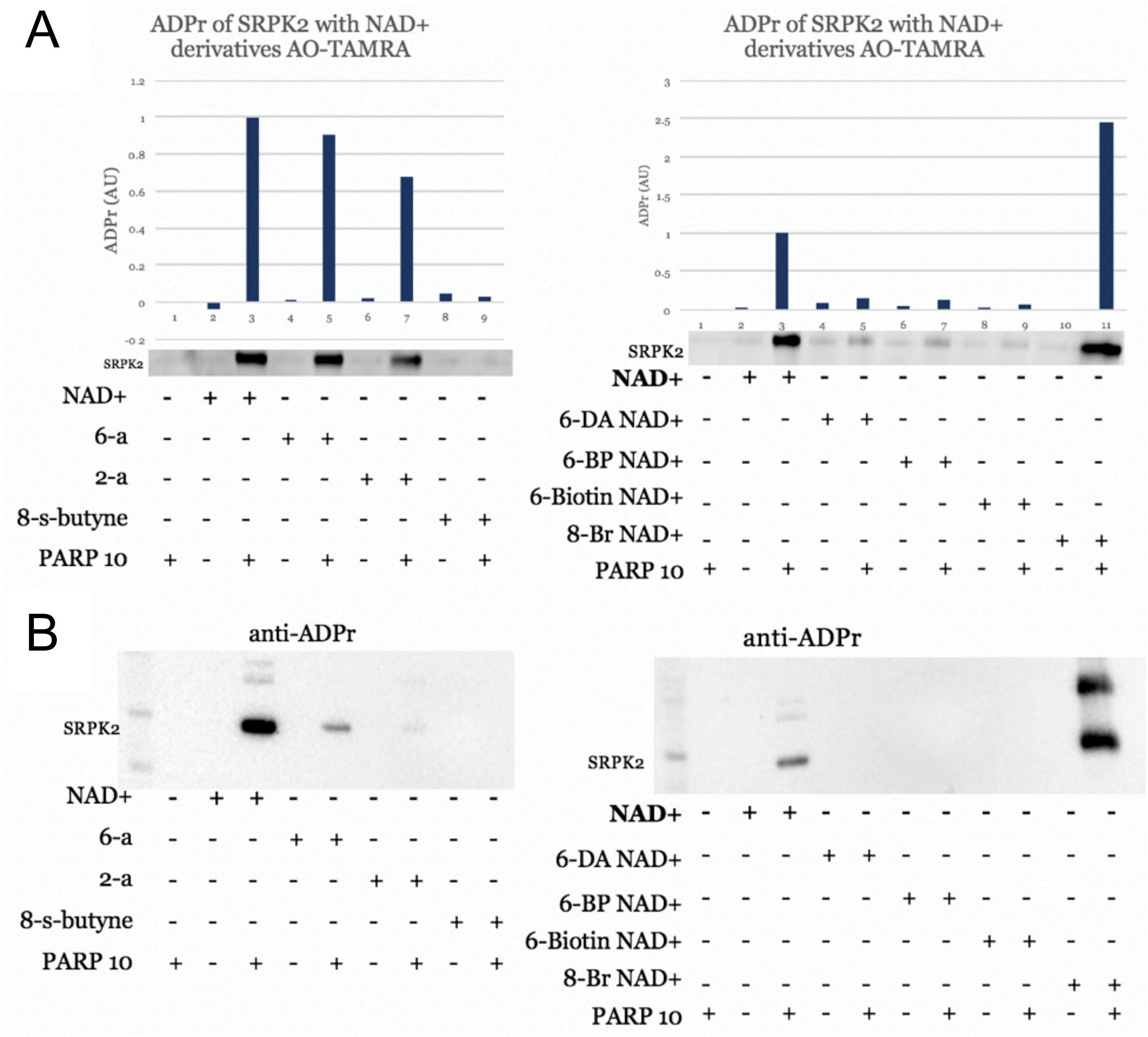

Figure 4.4. Data collected using PARP10$_{cat}$ to transfer mMAR onto SRPK2 from NAD+ derivatives.

(A) AO-TAMRA probe and in gel fluorescence detection was used to visualize mMAR. For each derivative used, a control sample without PARP10 was used to assess non-specific labeling. Background was quantified using a lane 1, a sample without NAD+

present. ADPr (AU) is background subtracted and divided by the total abundance of protein from a coomasie total protein stain (not pictured) then normalized to the ADPr signal of NAD+ at an incubation time of 120 mins. Below quantification, the imaged gel is present with band at the molecular weight of SRPK2

(B) Western blot using anti-ADPr reagent, from separate ADPr experiments using the same conditions as described in figure 4.4A.

mADPr from 2-az-NAD$^+$ can be photo-crosslinked to recombinant proteins and proteins from a cellular lysate

With a better understanding of the limitations of large substituents placed in the N6 and C8 positions of the adenosine ring, we next decided to turn our attention to small substituents in the C2 and C8 positions of the ring. Placement of azido groups within the C2 and C8 positions of adenosine ring of NAD$^+$ have been shown to act as aryl-azides and crosslink to protein at a wavelength of 254nm.[9],[10],[11]. These NAD$^+$ molecules were synthesized by Dr. Sunil Sundalam according to previously reported synthetic methods[11]. They were then tested to see how well they were transferred by PARPs and subsequently crosslinked to proteins from a lysate. We found that both 8-Az-NAD$^+$ and 2-Az-NAD$^+$ were well tolerated by His$_6$-PARP10$_{cat}$ and could be transferred via auto-modification or modification of SRPK2; However, only 2-Az-NAD$^+$ was successfully crosslinked to recombinant proteins present in the solution (Af1521 and SRPK2) **(Figure 4.5, Figure 4.6).**

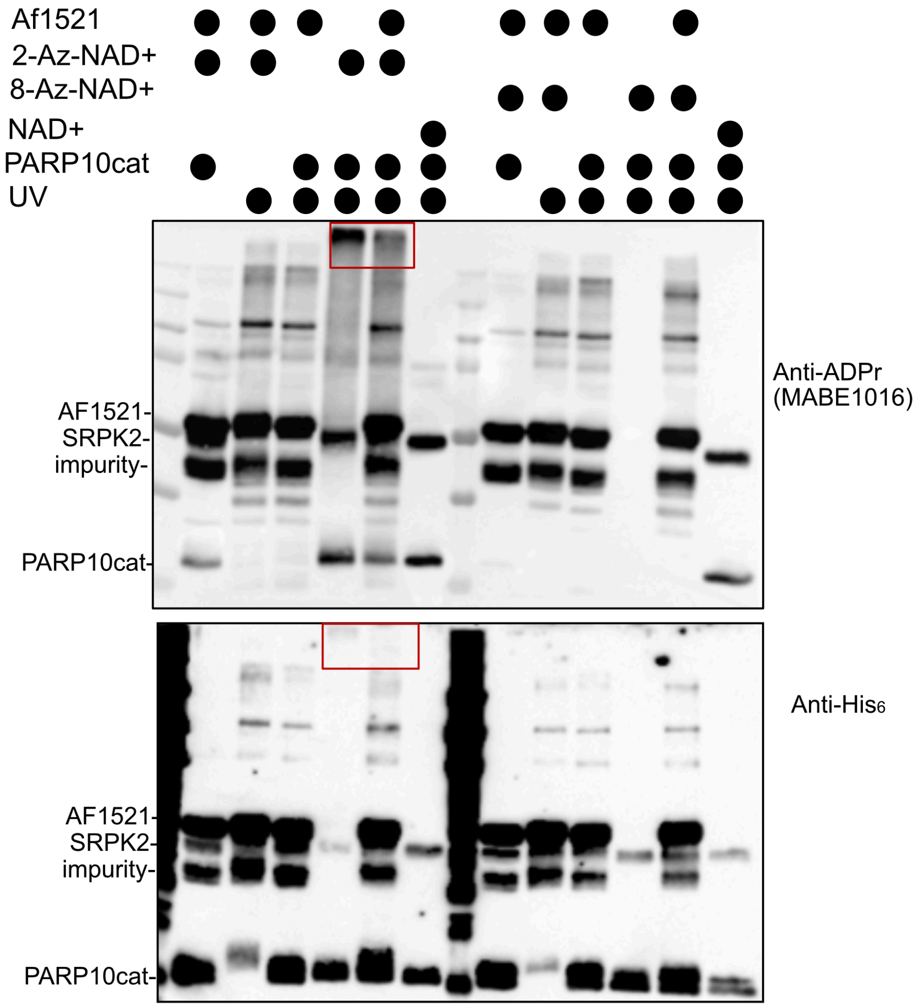

Figure 4.5. 2-Az-NAD+ is successfully transferred by His-PARP10$_{cat}$ and crosslinks recombinant proteins.
8-Az-NAD+ is transferred but does not crosslink. The red box indicates crosslinked high molecular weight protein conjugates.

We next wanted to know if 2-Az-NAD$^+$ could be used to photo-crosslink proteins in cellular lysates. To address this question, we first used 2-Az-NAD$^+$ to automodify His$_6$PARP10$_{cat}$ and incubated the mADPr- His$_6$PARP10$_{cat}$ with a cellular lysate. Photo-crosslinking was performed and high-molecular weight covelent-mADPr- His$_6$PARP10$_{cat}$ complexes were observed via western blot against His$_6$ **(Figure 4.6c)**. This exciting result shows potential for this strategy to be used to identify ADPr binders from a cellular lysate.

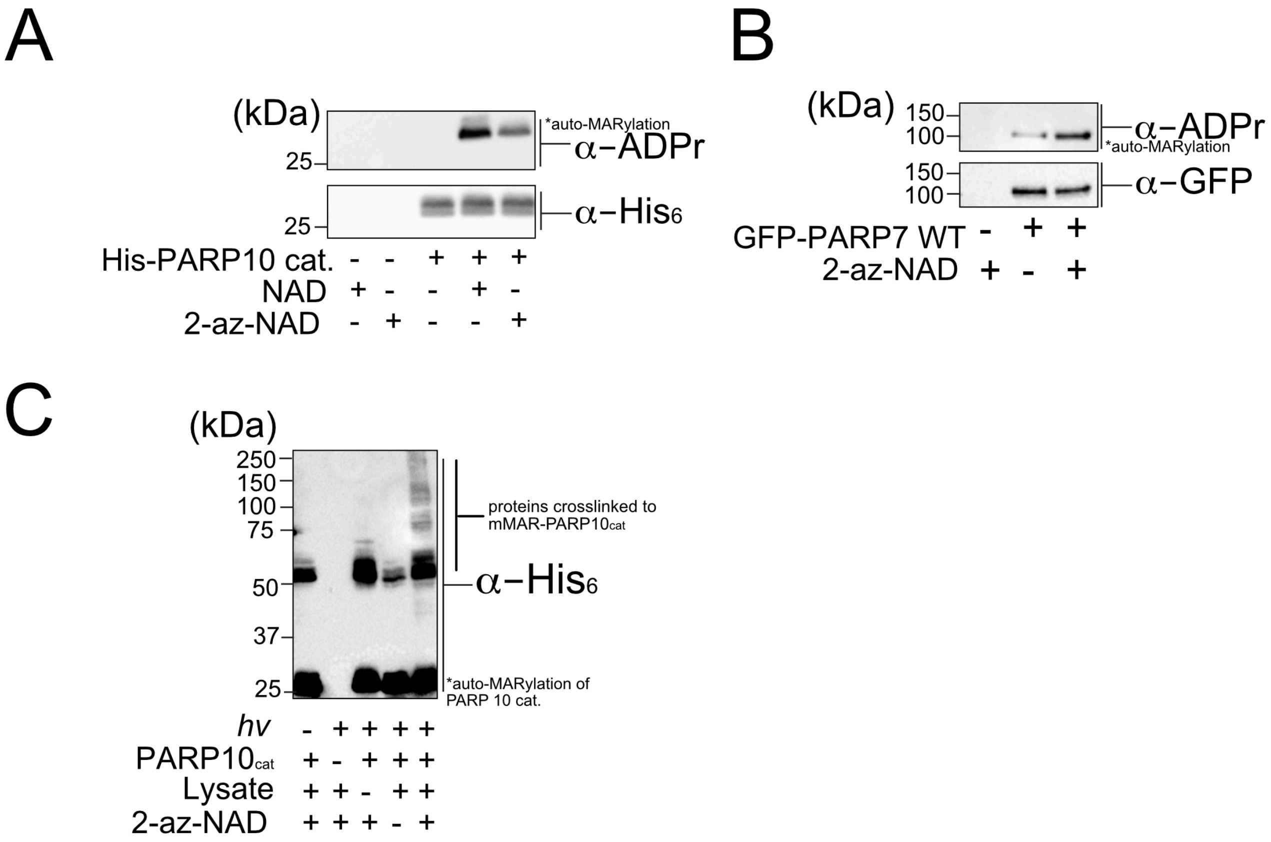

Figure 4.6. Auto-MARylated PARP10$_{cat}$ generated using 2-az-NAD$^+$ can be transferred and crosslinked to proteins via azido-modified MAR.

(**A**) His$_6$-PARP10$_{cat}$ is auto-MARylated using 2-az-NAD$^+$ (200 μM) as a substrate.

(B) GFP-PARP7 is auto-MARylated using 2-az-NAD$^+$ (200 μM) as a substrate.

(C) His$_6$-PARP10$_{cat}$ was auto-MARylated using 2-az-NAD$^+$ (200 μM) as a substrate. We purified MAR*-modified His$_6$-PARP10$_{cat}$ using nickel-NTA beads. We then incubated beads containing MAR*-His$_6$-PARP10$_{cat}$ with HEK 293T cell lysates and photo-crosslinked with 265 nm light or left untreated for 1 min on ice. Proteins were detected by Western blot using an anti-ADPr antibody, or an anti-His$_6$ antibody. The band ~50 kDa is a cross-contaminating band.

Future Directions

At the time when this project started to yield successful results, the other project I was working on, the chemical genetics project described in chapter 2, also took off with successful results. I was unable to work on both projects simultaneously, and decided to put my efforts towards the chemical genetics project to identify PARP-7 targets. I had always hoped I would be able to pick this project back up, but PARP-7 kept holding my attention. I hope this project provides a good jumping off point for other lab members to continue this work.

The most logical future direction of this project is to use methods described in **Figure 4.6c** to identify proteins via tandem mass spectrometry. Extending from this, it would be very interesting to see if this method could be used in partnership with chemical genetics by creating a bumped-photo-crosslinking analog. In this way mADPr could be added to targets from an individual PARP family member and binding partners could be identified.

Methods

Expression and purification of PARP10$_{cat}$ and SRPK2.

PARP10$_{cat}$ and SRPK2 were expressed in the Escherichia coli BL21 pRARE2 strain (EMD Millipore). Cells were first cultured in LB media overnight at 225 rpm and 37°C in an Excella® E24 Incubator (New Brunswick Scientific). One liter of TB media (12 g Bacto Tryptone (BD Biosciences), 24 g Bacto Yeast Extract (BD Biosciences), 0.4% glycerol, 17 mM KH_2PO_4, 72 mM $KHPO_4$, 50 μg/ml kanamycin, 34 μg/ml chloramphenicol) was inoculated with the starting culture and grown to OD_{600} = 0.8 – 1.0 at 225 rpm and 37°C. The temperature was reduced to 16°C and expression was induced by adding isopropyl β-d- thiogalactoside (IPTG) to 0.4 mM. After incubation at 16°C for 18 – 24 h, cells were harvested by centrifugation at 6,000 g for 10 min. The cell pellet was resuspended in lysis buffer (100 mM HEPES, pH 7.5, 0.5 mM tris(2-carboxyethyl)phosphine hydrochloride (TCEP•HCl, Thermo Scientific Pierce), 500 mM NaCl, 10 mM imidazole, 10% glycerol, 1 mM benzamidine, 1 mM phenylmethylsulfonyl fluoride (PMSF), 8.3 mg/L DNAse I (Roche)) at 4°C, subjected to cell lysis using a Sonifier 450 (Branson) at 4°C, and the resulting lysate was clarified by centrifugation at 12,000 g for 30 min at 4°C. Lysates were incubated with pre-washed Ni-NTA agarose resin (50% slurry, Qiagen) with end- over-end rotation at 4°C for 1 h. Following extensive washing with buffer B1+25 (20 mM HEPES, pH 7.5, 0.5 mM TCEP•HCl, 1 mM PMSF, 1 mM benzamidine, 500 mM NaCl, 25 mM imidazole) protein was eluted in buffer B1+200 (20 mM HEPES, pH 7.5, 0.5 mM TCEP•HCl, 500 mM NaCl, 200 mM imidazole) for PARP10$_{cat}$ and B1+100 (20 mM HEPES, pH 7.5, 0.5 mM TCEP•HCl, 500 mM NaCl, 100 mM imidazole) for SRPK2. Fractions containing desired protein were collected and dialyzed to 50 mM Tris-HCl, pH 7.5, 0.1 mM EDTA, 1 mM β-Me, 0.4 M NaCl at 4°C. Protein concentrations were determined by Bradford assay with BSA standards and purity was assessed by PageBlue staining (Pierce) after SDS-polyacrylamide gel electrophoresis (SDS-PAGE). ≥ 90% purity was achieved for PARP10$_{cat}$ and ≥ 50% purity was achieved for SRPK2.

PARP10$_{cat}$ ADPr of SRPK2 with NAD+ analogs

Recombinantly expressed PARP10 catalytic domain (5μM) was suspended in reaction buffer (50mM HEPES pH7.5, 100mM NaCl, 12mM MgCl2) with 100μM NAD+ analog or with reaction buffer as a control to a final volume of 20μL reaction mixture. The ADP-ribosylation reaction was allowed to proceed for 90 mins, shaking at 30˚C. For AO-TAMRA labeling, a 3X mixture of AO-TAMRA (3x: 450mM Acetate pH5, 1.5M NaCl, 300uM AO-TAMRA, 30mM PDA catalyst) was added and incubated at RT for 60 mins. 4X sample buffer was added and samples were resolved via SDS-PAGE. The gel was them imaged using a biorad imager with rhodamine setting.

Photo-crosslinking of PARP10$_{cat}$ to cellular lysate components using 2-N$_3$-NAD+

Recombinantly expressed PARP10 catalytic domain (5μM) was suspended in reaction buffer (50mM HEPES pH7.5, 100mM NaCl, 12mM MgCl2) with 100μM 2-N$_3$-NAD+ or with reaction buffer as a control to a final volume of 20μL reaction mixture. The ADP-ribosylation reaction was allowed to proceed for 90 mins, shaking at 30˚C. During this time, 200μL Ni-NTA resin was washed 2X with 500μL ddH2O, followed by 500μL dilution buffer (1X PBS, 113 NaCl. 1% NP-40, 1X Roche protease inhibitor). After two washes the resin was suspended in 500µL dilution buffer. 100µL of the bead slurry was then added to each ADP-ribosylation reaction mixture. 400µL dilution buffer was then added to each mixture. The solutions were rotated at RT for 1 hour. After rotation the solutions were centrifuged on a tabletop centrifuge and resin mixtures were washed 3X with PBS. After aspiration of PBS wash, 60µL of cellular lysate at a concentration of 2µg/µL was added to the resin. The samples were then placed on a shaker for 5 mins at room temperature. The solution from each sample was then pipetted into a well of a 96 well plate. The UV (-) sample was place in the opposing corner to the rest of the samples on the plate. A piece of carboard with a hole was used to cover the entire plate, except for the 4 samples receiving light. A Newport light source set to 1000W (Arc Lamp Housing, model: 66921, Oriel instruments power source model: OPS-A1000) was used to photo-crosslink samples on the plate, on ice for 1min. 20µL of 4X sample buffer+ 5% BME was added to each sample on the plate. The solutions were then transferred to Eppendorf tubes and boiled for 10 mins. 20µL of each sample was then loaded onto a 10% gel and ran for 60 mins at 200V. The blot was then probed for his-tagged proteins and ponceau stained for total protein.

Lysate details: 6-wells of HEK293 cells from a 6-well plate were grown to 90% confluency. The cells were then trypsinized off the plate, spun down at 1000 RPM, washed 2X with cold PBS, and resuspended in 500µL of lysis buffer (25mM HEPES pH 7.4, NaCl 50mM, 5mM MgCl2, 1% NP-40, and 1X Roche Protease inhibitor).

Chemistry methods:

General. ^{1}H NMR were recorded on a Bruker DPX spectrometer at 400 MHz. Chemical shifts are reported as parts per million (ppm) downfield from an internal tetramethylsilane standard or solvent references. Dichloromethane (DCM), tetrahydrofuran (THF), and Dimethylformamide (DMF) were dried using a solvent purification system manufactured by Glass Contour, Inc. (Laguna Beach, CA). Additional drying of solvents, where indicated in methods, occurred using 3Å or 4Å activated sieves. All other solvents were of ACS chemical grade (Fisher Scientific) and used without further purification unless otherwise indicated. Commercially available chemical compounds were purchased from CombiBlocks (San Diego, CA), and TCI America (Portland, OR) and were >95% pure and used without further purification. All other reagents were of ACS chemical grade (Fisher Scientific) and used as received. HPLC Methods: Gradient 10 mM tributylamine/30 mM acetic acid pH 4.4 to 100% methanol over 16 mins using c18 column.

Synthesis of NAD+ analogs

6-a-NAD+ was synthesized as previously reported[2].

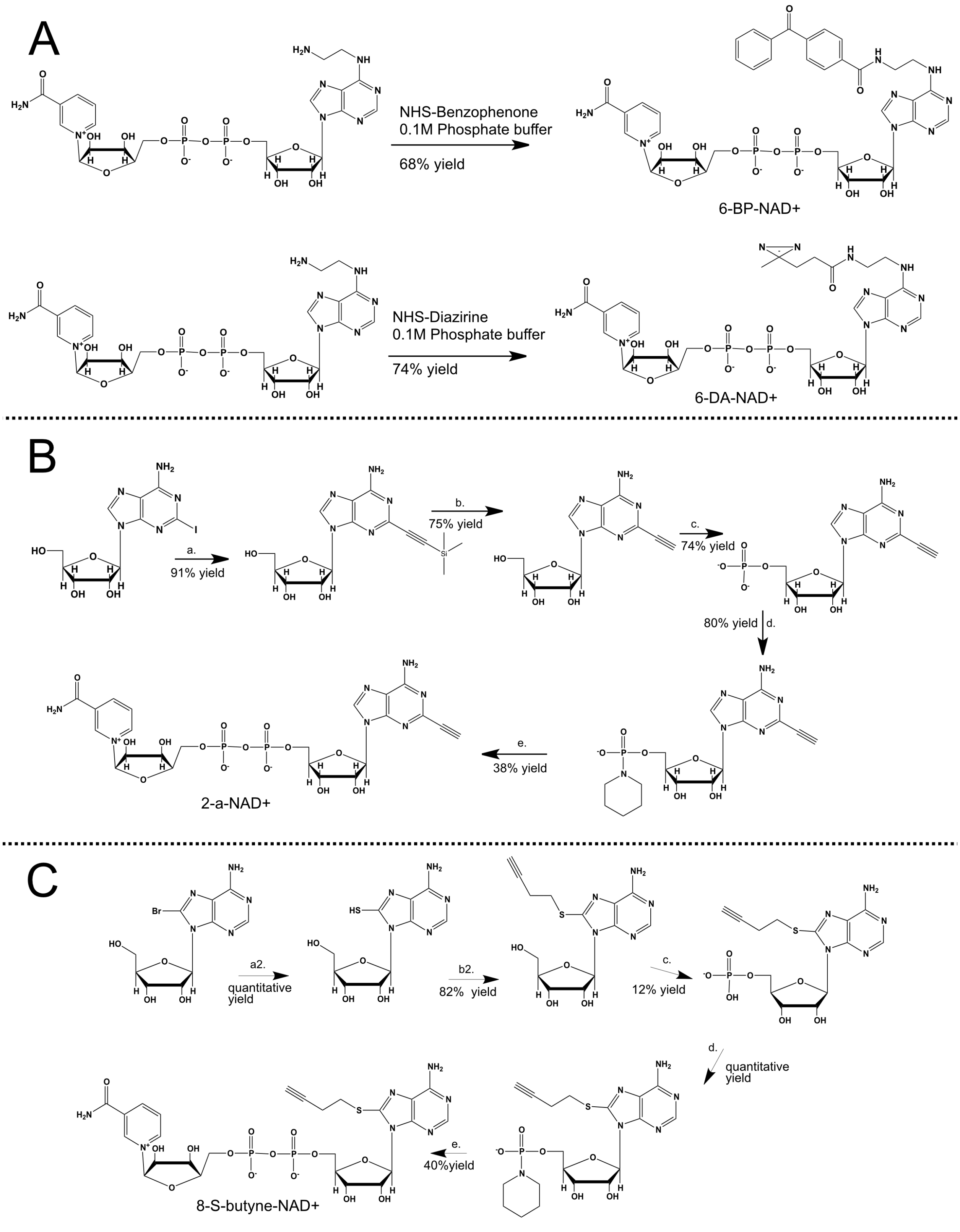
A
NHS-Benzophenone
0.1M Phosphate buffer
68% yield
6-BP-NAD+
NHS-Diazirine
0.1M Phosphate buffer
74% yield
6-DA-NAD+
B
a.
91% yield
b.
75% yield
c.
74% yield
80% yield d.
e.
38% yield
2-a-NAD+
C
a2.
quantitative yield
b2.
82% yield
c.
12% yield
d.
quantitative yield
e.
40%yield
8-S-butyne-NAD+

Scheme 4.1 A-C. Synthesis of NAD+ analogs: 6-Diazerine-NAD+, 6-benzophenone-NAD+, 2-a-NAD+ and 8-S-butyne NAD+.

(A) 6-Diazerine-NAD+ and 6-benzophenone-NAD+ synthesis using commercially available NHS-photocrosslinkers and 6-AE-NAD+ in 0.1M phosphate buffer

(B) 2-a-NAD+ synthesis **a)** Trimethylsilyl acetylene, (PPh3)2PdCl2, CuI, Et3N (TEA) **b)** 7N NH3/MeOH **c)** TMP, POCl3, 6-Me-Nicotinamide, H20 0˚C **d)** PPH3, morpholine, 2,2 DPS, 0.2M NaI **e)** B-NMN, MgSO4, 0.2M MnCl2 in dry formamide

(C) 8-S-butyne NAD+ synthesis **a2.)** NaSH, DMF, H20, 100˚C **b2.)** 4-Bromo-1-butyne, DMF 60˚C **c)** TMP, POCl3, 6-Me-Nicotinamide, H20 0˚C **d)** PPH3, morpholine, 2,2 DPS, 0.2M NaI **e)** B-NMN, MgSO4, 0.2M MnCl2 in dry formamide

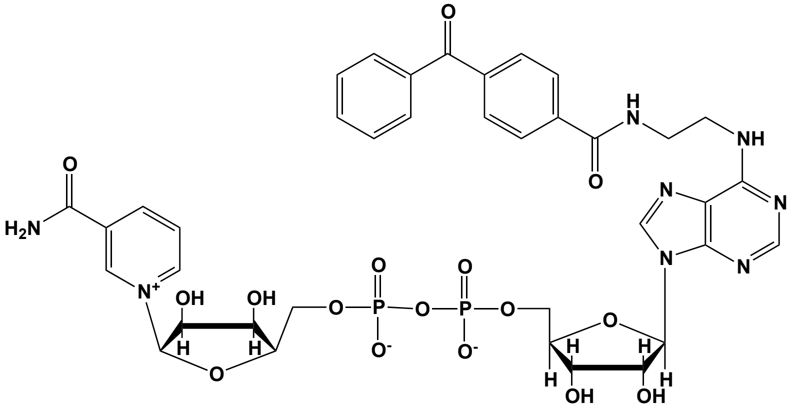

6-BP-NAD+

Synthesis of 6-Benzophenone-NAD+. In a clean scintillation vial, 3.5mg (0.005 mmol) 6-EA-NAD+ (BIOLOG life science institute Cat. No.: N 013) was dissolved in 750uL 0.1M phosphate buffer (prepared according to a Cold Spring Harbor Protocol recipe). To solubilize, 200uL of DMSO was added when cloudiness was observed. To this solution 2mg (0.006 mmol) NHS-benzophenone (4-Benzoylbenzoic acid N-succinimidyl ester: Sigma-Aldrich cat. number 775924) was added. The reaction was allowed to stir for 1 hour. The resulting solution was purified via reverse phase HPLC. RT 12.5 mins. 3.06 mg product was obtained (68% yield) ^{1}H NMR (400 MHz, D_2O) δ 9.22 (s, 1H), 9.06 (s, 1H), 8.70 (s, 1H), 8.31 (s, 2H), 8.00 (s, 1H), 7.76 – 7.39 (m, 6H), 5.95 (s, 1H), 5.87 (s, 1H), 4.48 – 4.35 (m, 2H), 4.24 (s, 1H), 4.10 (s, 2H), 3.64 (s, 1H).

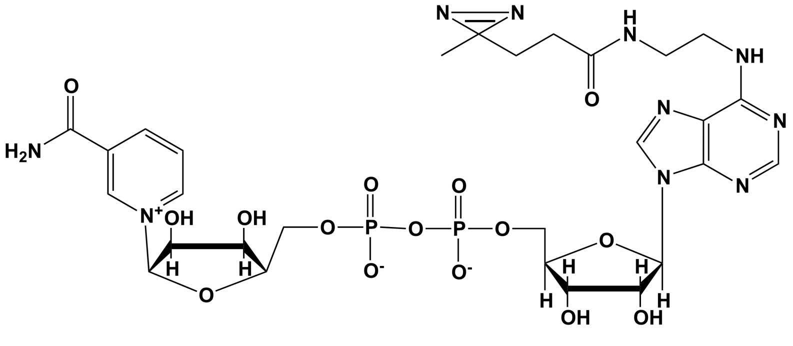

6-DA-NAD+

6-Diazirine-NAD+. In a clean scintillation vial, 3.5mg (0.005 mmol) 6-EA-NAD+ (BIOLOG life science institute Cat. No.: N 013) was dissolved in 750uL 0.1M phosphate buffer (prepared according to a Cold Spring Harbor Protocol recipe). To this solution 2mg (0.006 mmol) NHS-diazirine (thermo-fisher scientific cat. number: 26167) was added. The reaction was allowed to stir for 1 hour. The resulting solution was purified via reverse phase HPLC. 2.97 mg product was obtained (73% yield). ^{1}H NMR (400 MHz, D_2O) δ 9.37 (s, 1H), 9.20 (d, *J* = 6.6 Hz, 1H), 8.87 (d, *J* = 21.5 Hz, 1H), 8.41 (s, 1H), 8.22 (s, 2H), 6.10 (s, 1H), 6.06 (s, 1H), 4.38 (s, 3H), 4.24 (s, 3H), 3.82 (s, 2H), 3.55 (d, *J* = 5.6 Hz, 2H).

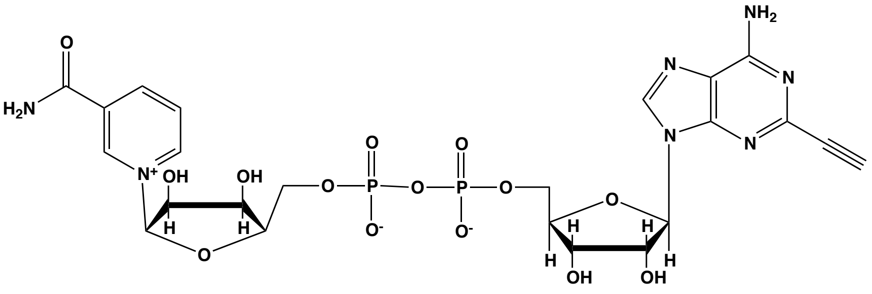

2-alkyne-NAD+

2-alkyne-NAD+ was synthesized as previously reported in chapter 2, with the exception of the last step which combined 2-ethynyl-AMP-morpholidate with β-NMN. 2-ethynyl-AMP-morpholidate (19.5mg, 0.42mmol), after overnight desiccation in a chamber containing P_2O_5, was added along with β-NMN (15.5mg, 0.05 mmol), $MgSO_4$ (10 mg, 0.08 mmol) to a scintillation vile. 300 µl of 0.2 M $MnCl_2$ in dry formamide was added to the solids via syringe and the reaction was stirred overnight under Argon balloon at room temperature. The reaction was checked by HPLC. After complete consumption of 2-ethynyl-AMP-morpholidate was observed overnight, the reaction was diluted with 1.5 mL 10 mM tributylamine/30 mM acetic acid [pH = 4.4] and purified using HPLC. Retention time 9 min. The fractions containing desired compound were pooled and co-evaporated with acetonitrile (to remove excess water) and methanol to remove excess tributylamine. The resulting compound was a sticky residue (due to excess tributylamine) which was dissolved in water to yield 200uL of an 8mM solution (38% yield). ^{1}H NMR (400 MHz, D_2O) δ 9.24 (s, 1H), 8.98 (d, *J* = 6.3 Hz, 1H), 8.82 (d, *J* = 8.1 Hz, 1H), 8.43 (s, 1H), 8.22 – 8.06 (m, 1H), 5.90 (dd, *J* = 14.1, 5.6 Hz, 2H), 4.48 – 4.43 (m, 1H), 4.40 (s, 1H), 4.39 – 4.29 (m, 2H), 4.24 – 4.07 (m, 3H), 3.45 (s, 1H).

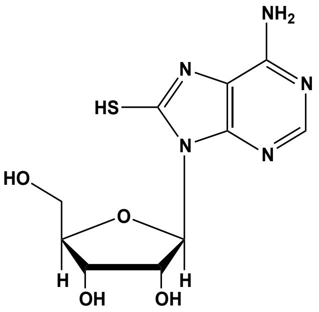

8-SH-adenosine

8-SH-adenosine. NaSH (10 eq) was added to a solution of 8-bromoadenosine (0.5 g, 1.44 mmol) in DMF (7 mL). The mixture was warmed to 100°C and a few drops of water were added to improve solubility. The mixture was stirred at 100°C overnight. The solvent was evaporated under high vacuum and the residue was co-evaporated repeatedly with MeOH, until the residue turned into a solid. The residue was dissolved in water and neutralized with NaOH. The product was concentrated and obtained as a yellowish powder (quantitative yield). ^{1}H NMR (400 MHz, D_2O) δ 7.93 (s, 1H), 7.87 (s, 3H), 6.56 (d, *J* = 7.5 Hz, 1H), 5.00 (dd, *J* = 7.5, 5.4 Hz, 1H), 4.40 (dd, *J* = 5.4, 2.1 Hz, 1H), 4.23 (q, *J* = 2.3 Hz, 1H), 3.94 – 3.73 (m, 2H).

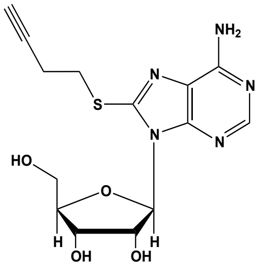

8-S-butyne-adenosine

8-S-butyne-adenosine. A suspension of 8-SH-adenosine (200 mg, 0.669 mmol) was dissolved in dry DMF (4 mL) and 4-Bromo-1-butyne (97mg, 1.1 eq) was added. The solution was stirred under argon at 60°C. The solution was concentrated and the yellow residue was coevaporated repeatedly with MeOH, until the residue turned into a yellow solid. (90% yield). ^{1}H NMR (400 MHz, DMSO) δ 8.06 (s, 1H), 7.35 (s, 2H), 5.74 (d, *J* = 6.9 Hz, 1H), 5.67 (dd, *J* = 8.9, 3.7 Hz, 1H), 5.44 (d, *J* = 6.5 Hz, 1H), 5.23 (d, *J* = 4.5 Hz, 1H), 4.98 (q, *J* = 6.3 Hz, 1H), 4.23 – 4.08 (m, 1H), 3.97 (d, *J* = 2.4 Hz, 1H), 3.67 (dt, *J* = 12.2, 3.7 Hz, 1H), 3.52 (ddd, *J* = 13.3, 9.5, 4.7 Hz, 1H), 3.02 – 2.93 (m, 1H), 2.70 (td, *J* = 7.1, 2.8 Hz, 2H).

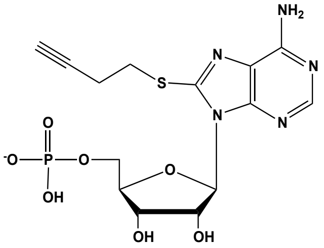

8-S-butyne-AMP

8-S-butyne-AMP. In a clean, dry round bottom flask, 5.1 ml dry THF was added to 8-S-butyne-adenosine (500 mg, 1.64 mmol) was heated under vacuum at 60°C for 30 min and suspended in dry trimethyl phosphate (5.5 ml) the mixture was heated at 50 °C for

15 min with gradual clearing, 6-me-nicotiamide was added under argon pressure. The mixture was cooled to 0°C with an ice bath and POCl3 (457 µl, 4.91 mmol) was added dropwise. The mixture was stirred at 0°C until HPLC analysis revealed consumption of the starting material. The mixture was precipitated in cold ether (150 ml) in an ice bath. The residue was dissolved in ice cold H2O (6 ml) and stirred for 10 min. The reaction was immediately neutralized with 6N NaOH. The mixture was concentrated to a small volume (less than 2 ml) *in vacuo* and the liquid was purified on reverse phase chromatography using a Combiflash Companion system (C18Aq 5.5 g Redisep Rf; MP A: 10 mM tributylamine/30 mM acetic acid pH 4.4 (aq.), MP B: methanol; 0-1 min: 0% B, 1-12 min: 0-50% B, 12-16 min: 100% B). Fractions containing desired product were pooled and concentrated in vacuo to yield the tributylammonium (TBA) salt of the product (12% yield). ^{1}H NMR (400 MHz, DMSO) δ 8.06 (s, 1H), 7.18 (s, 2H), 5.77 (dd, *J* = 23.0, 6.3 Hz, 1H), 5.35 (s, 1H), 5.25 – 5.08 (m, 1H), 4.18 (s, 2H), 3.95 (s, 4H).

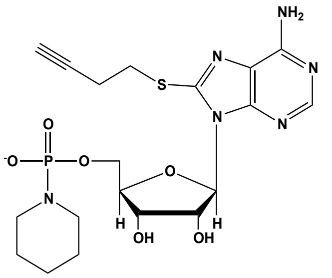

8-S-butyne-AMP-morpholidate

8-S-butyne-AMP-morpholidate. 8-S-butyne-AMP (34 mg, 0.055 mmol) was dissolved in anhydrous DMSO (250uL) and coevaporated with anhydrous DMF (3 x 2 ml). The resulting residue was redissolved in additional anhydrous DMSO (200 uL) and the following were added in sequence: PPh3 (77 mg, 0.29 mmol), morpholine (41uL, 0.473 mmol), and 2,2′-dipyridyldisulfide (Aldrithiol) (64.8 mg, 0.29 mmol). The resulting yellow solution was stirred at room temp. under argon for 90 min until HPLC analysis revealed consumption of starting material. To the reaction 0.2 M NaI in dry acetonitrile (20 ml) was added dropwise to form a white precipitate (ppt) (left overnight to ppt further). The mixture was filtered using a fine filter and the ppt was washed with EtOAc (2 x 5 ml) or until the yellow color was removed. The ppt was redissolved in MeOH and concentrated in vacuo to yield the sodium salt of the product as a white solid (quantitative yield) which was used in subsequent coupling without further purification. ^{1}H NMR (400 MHz, D_2O) δ 8.76 (s, 1H), 6.68 (s, 1H), 6.09 (s, 1H), 5.47 (s, 2H), 4.06 (d, *J* = 33.3 Hz, 2H), 3.82 (s, 2H), 2.67 (s, 2H).

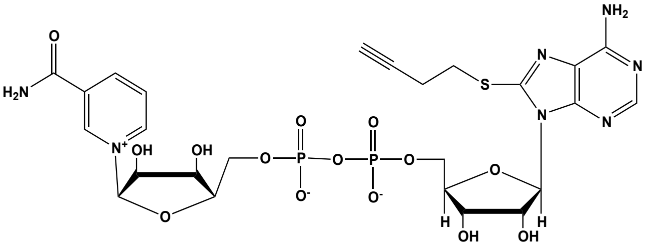

8-S-butyne NAD+, TBA salt

8-S-butyne NAD+. 8-S-butyne-AMP-morpholidate (70mg, 0.13mmol), after overnight desiccation in a chamber containing P_2O_5, was added along with β-NMN (49 mg, 0.15 mmol), $MgSO_4$ (35.6 mg, 0.29 mmol) to a scintillation vile. 1mL of 0.2 M $MnCl_2$ in dry formamide was added to the solids via syringe and the reaction was stirred overnight under Argon balloon at room temperature. The reaction was checked by HPLC. After complete consumption of 8-S-butyne-AMP-morpholidate was observed overnight, the reaction was diluted with 1.5 mL 10 mM tributylamine/30 mM acetic acid [pH = 4.4] and purified using HPLC. Retention time 10 min. The fractions containing desired compound were pooled and co-evaporated with acetonitrile (to remove excess water) and methanol to remove excess tributylamine. The resulting compound was a sticky residue (due to excess tributylamine) which was dissolved in water to yield 200uL of an 8mM solution (yield unknown due to contamination of sieves from NaI ACN solution in the starting material). ^{1}H NMR (400 MHz, D_2O) δ 9.21 (s, 1H), 9.06 (d, *J* = 6.2 Hz, 1H), 8.73 (d, *J* = 8.1 Hz, 1H), 8.17 – 8.10 (m, 1H), 8.06 (s, 1H), 6.08 (d, *J* = 2.8 Hz, 1H), 5.90 (d, *J* = 4.9 Hz, 1H), 5.56 – 5.46 (m, 1H), 5.21 – 5.09 (m, 1H), 4.41 – 4.10 (m, 9H), 3.43 (dt, *J* = 13.0, 6.3 Hz, 1H), 3.34 – 3.20 (m, 2H), 2.60 (s, 3H), 2.33 (s, 1H).

References

1. Rack, J. G. M., Palazzo, L. & Ahel, I. (ADP-ribosyl)hydrolases: Structure, function, and biology. *Genes Dev.* **34**, 263–284 (2020).
2. Carter-O’Connell, I., Jin, H., Morgan, R. K., David, L. L. & Cohen, M. S. Engineering the substrate specificity of ADP-ribosyltransferases for identifying direct protein targets. *J. Am. Chem. Soc.* **136**, 5201–5204 (2014).
3. Carter-O’Connell, I. *et al.* Identifying Family-Member-Specific Targets of Mono-ARTDs by Using a Chemical Genetics Approach. *Cell Rep.* 1–11 (2015). doi:10.1016/j.celrep.2015.12.045
4. Zhang, J. Vitamins and Coenzymes Part J. *Methods Enzymol.* **280**, 255–265 (1997).
5. Rosenthal, F. *et al.* Macrodomain-containing proteins are new mono-ADP-ribosylhydrolases. *Nat. Struct. Mol. Biol.* **20**, 502–7 (2013).
6. Kirby, I. T., Morgan, R. K. & Cohen, M. S. A Simple, Sensitive, and Generalizable Plate Assay for Screening PARP Inhibitors. *Methods Mol. Biol.* **1813**, 245–252 (2018).
7. Morgan, R. K. & Cohen, M. S. A Clickable Aminooxy Probe for Monitoring Cellular ADP-Ribosylation. *ACS Chem. Biol.* **10**, 1778–1784 (2015).
8. Gibson, B. A., Conrad, L. B., Huang, D. & Kraus, W. L. Generation and Characterization of Recombinant Antibody-like ADP-Ribose Binding Proteins. *Biochemistry* **56**, 6305–6316 (2017).
9. Mahajan, S., Manetsch, R., Merkler, D. J. & Stevens, S. M. Synthesis and evaluation of a novel adenosine-ribose probe for global-scale profiling of

nucleoside and nucleotide-binding proteins. *PLoS One* **10**, 1–17 (2015).

10. Trabbic, C. J., Zhang, F., Walseth, T. F. & Slama, J. T. Nicotinic acid adenine dinucleotide phosphate analogues substituted on the nicotinic acid and adenine ribosides. Effects on receptormediated Ca^{2+} release. *J. Med. Chem.* **58**, 3593–3610 (2015).
11. Ramsinghani, S. *et al.* Syntheses of photoactive analogues of adenosine diphosphate (hydroxymethyl)pyrrolidinediol and photoaffinity labeling of poly(ADP-ribose) glycohydrolase. *Biochemistry* **37**, 7801–7812 (1998).

H_1-NMRs

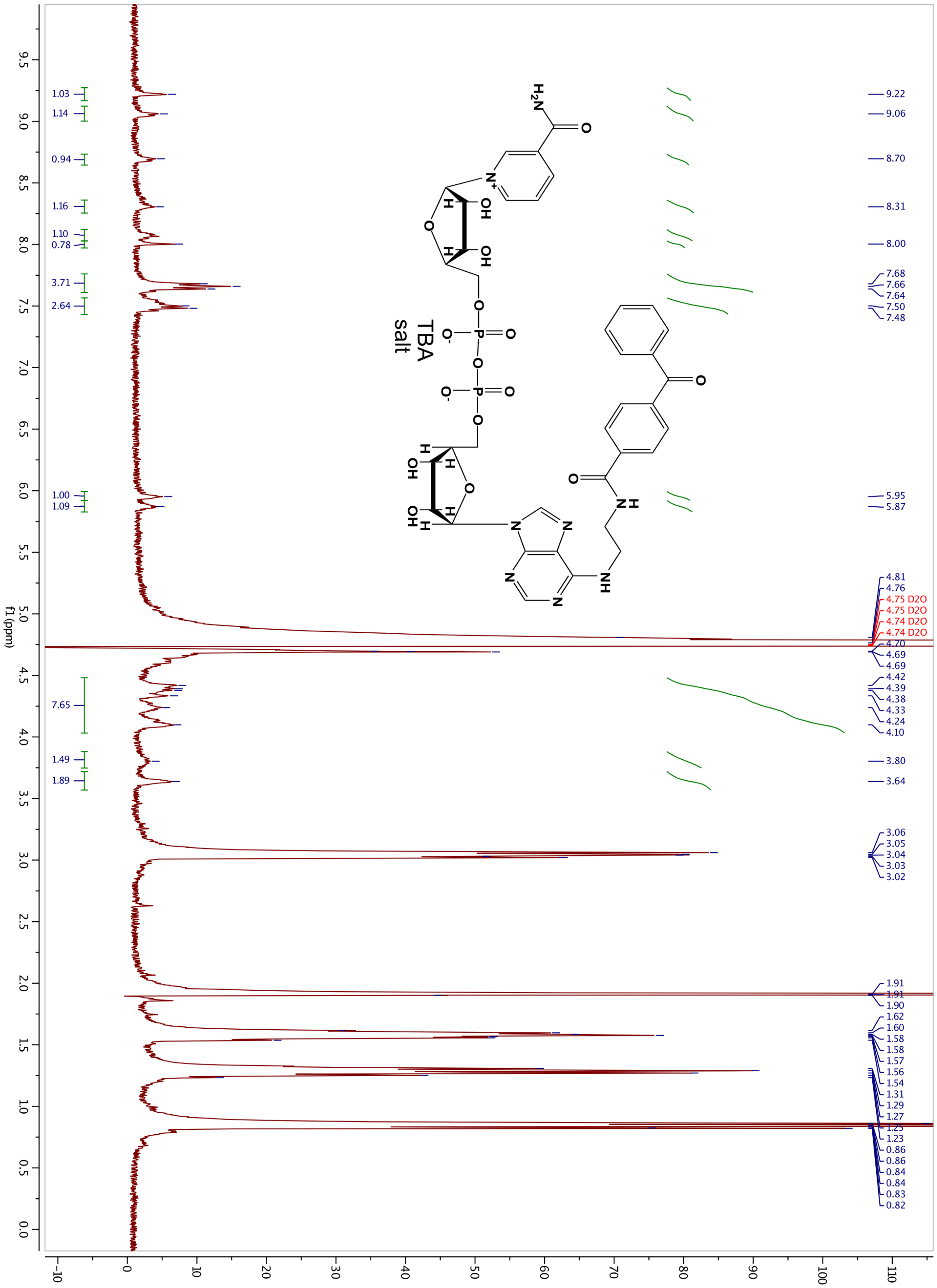

9.5
9.0
8.5
8.0
7.5
7.0
6.5
6.0
5.5
5.0
4.5
4.0
3.5
3.0
2.5
2.0
1.5
1.0
0.5
0.0
f1 (ppm)
-10
0
10
20
30
40
50
60
70
80
90
100
110
1.03
1.14
0.94
1.16
1.10
0.78
3.71
2.64
1.00
1.09
7.65
1.49
1.89
9.22
9.06
8.70
8.31
8.00
7.68
7.66
7.64
7.50
7.48
5.95
5.87
4.81
4.76
4.75 D2O
4.75 D2O
4.74 D2O
4.74 D2O
4.70
4.69
4.69
4.42
4.39
4.38
4.33
4.24
4.10
3.80
3.64
3.06
3.05
3.04
3.03
3.02
1.91
1.91
1.90
1.62
1.60
1.58
1.58
1.57
1.56
1.54
1.31
1.29
1.27
1.25
1.23
0.86
0.86
0.84
0.84
0.83
0.82
TBA
salt

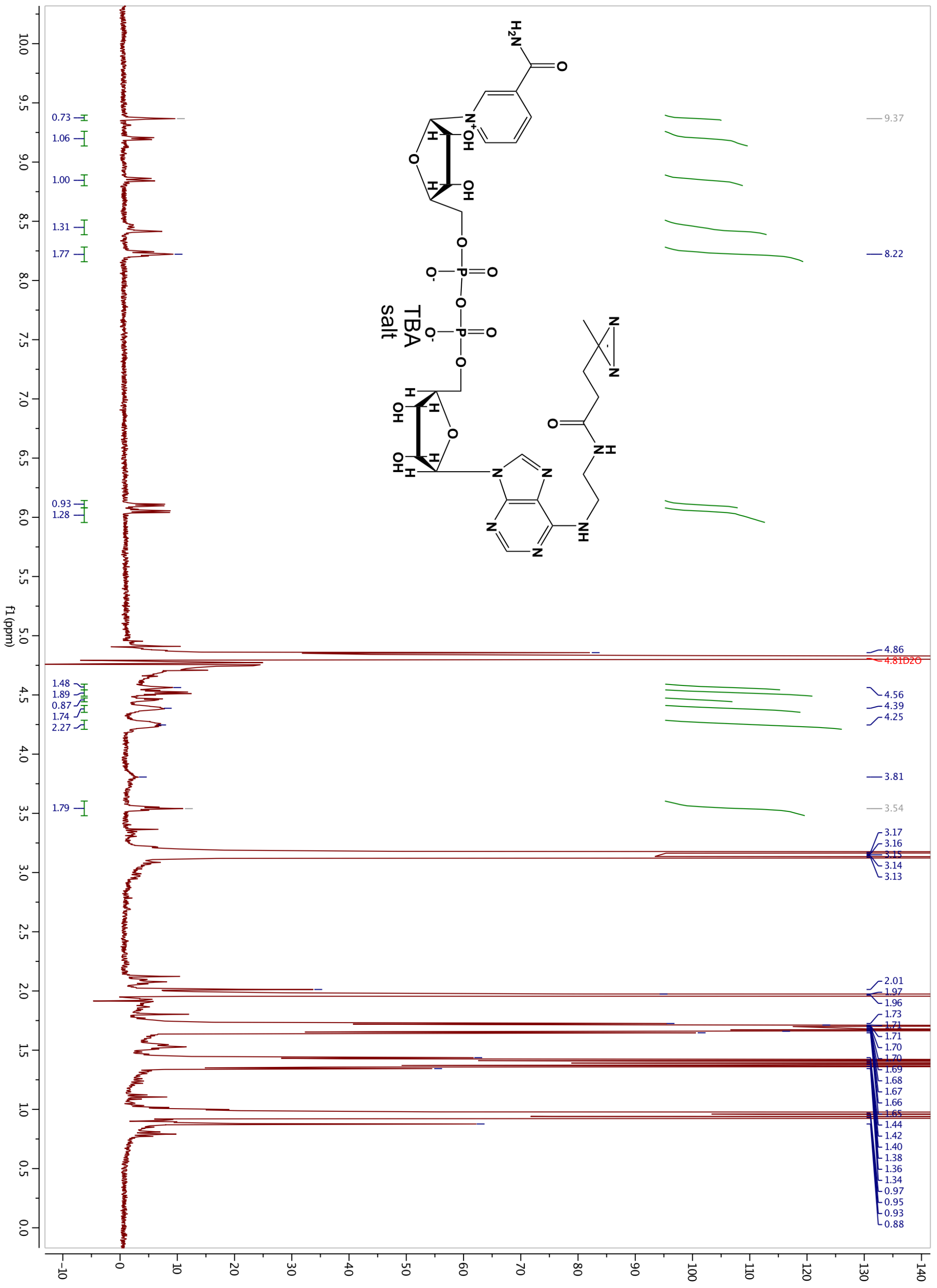
TBA
salt
H2N
O
N+
OH
OH
O
H
H
O-
P
O
N
NH
HN
f1 (ppm)
10.0
9.5
9.0
8.5
8.0
7.5
7.0
6.5
6.0
5.5
5.0
4.5
4.0
3.5
3.0
2.5
2.0
1.5
1.0
0.5
0.0
-10
0
10
20
30
40
50
60
70
80
90
100
110
120
130
140
0.73
1.06
1.00
1.31
1.77
0.93
1.28
1.48
1.89
0.87
1.74
2.27
1.79
9.37
8.22
4.86
4.81D2O
4.56
4.39
4.25
3.81
3.54
3.17
3.16
3.15
3.14
3.13
2.01
1.97
1.96
1.73
1.72
1.71
1.70
1.70
1.69
1.68
1.67
1.66
1.65
1.44
1.42
1.40
1.38
1.36
1.34
0.97
0.95
0.93
0.88

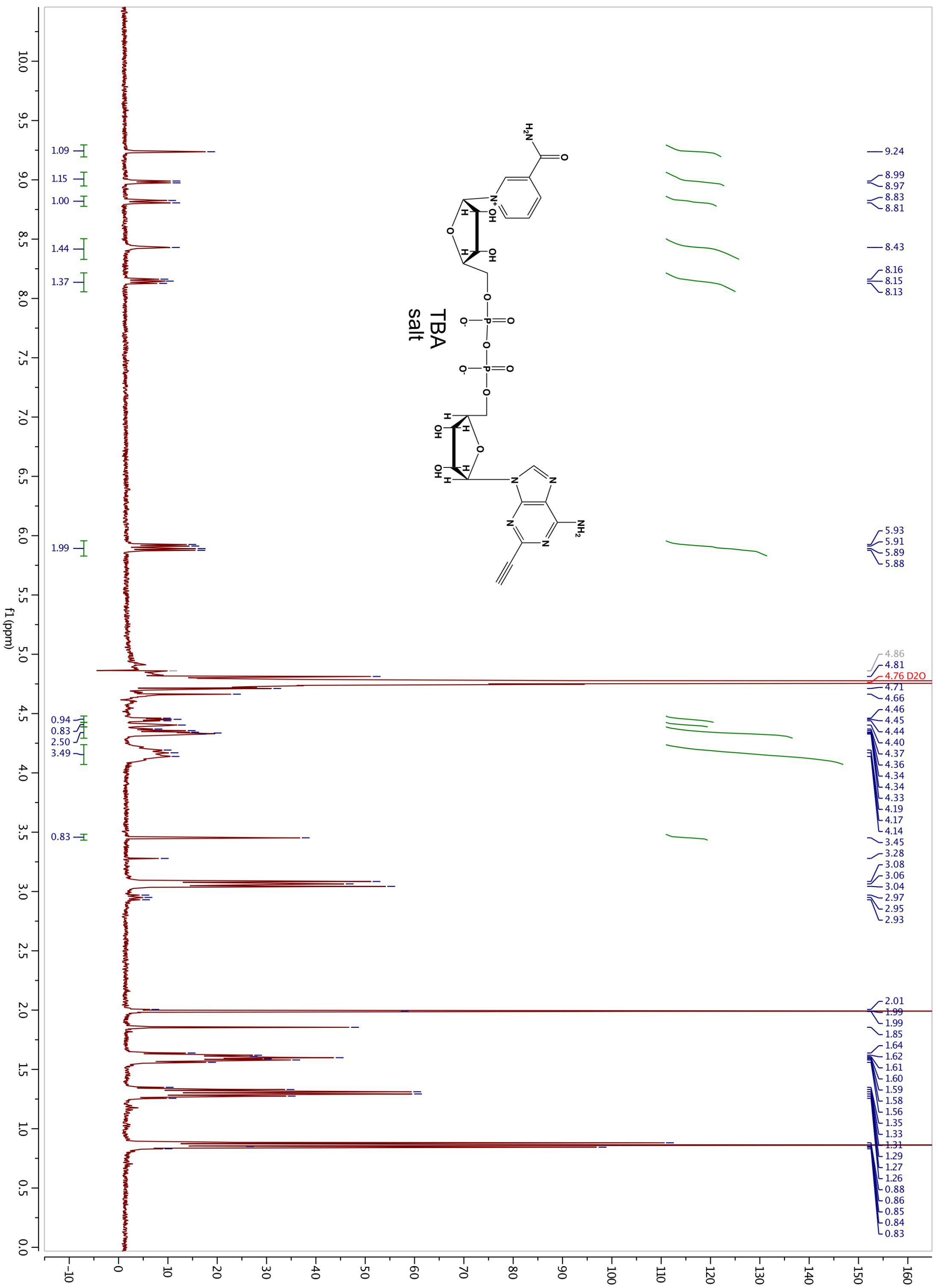
TBA salt
f1 (ppm)
1.09
1.15
1.00
1.44
1.37
1.99
0.94
0.83
2.50
3.49
0.83
9.24
8.99
8.97
8.83
8.81
8.43
8.16
8.15
8.13
5.93
5.91
5.89
5.88
4.86
4.81
4.76 D2O
4.71
4.66
4.46
4.45
4.44
4.40
4.37
4.36
4.34
4.34
4.33
4.19
4.17
4.14
3.45
3.28
3.08
3.06
3.04
2.97
2.95
2.93
2.01
1.99
1.99
1.85
1.64
1.62
1.61
1.60
1.59
1.58
1.56
1.35
1.33
1.31
1.29
1.27
1.26
0.88
0.86
0.85
0.84
0.83

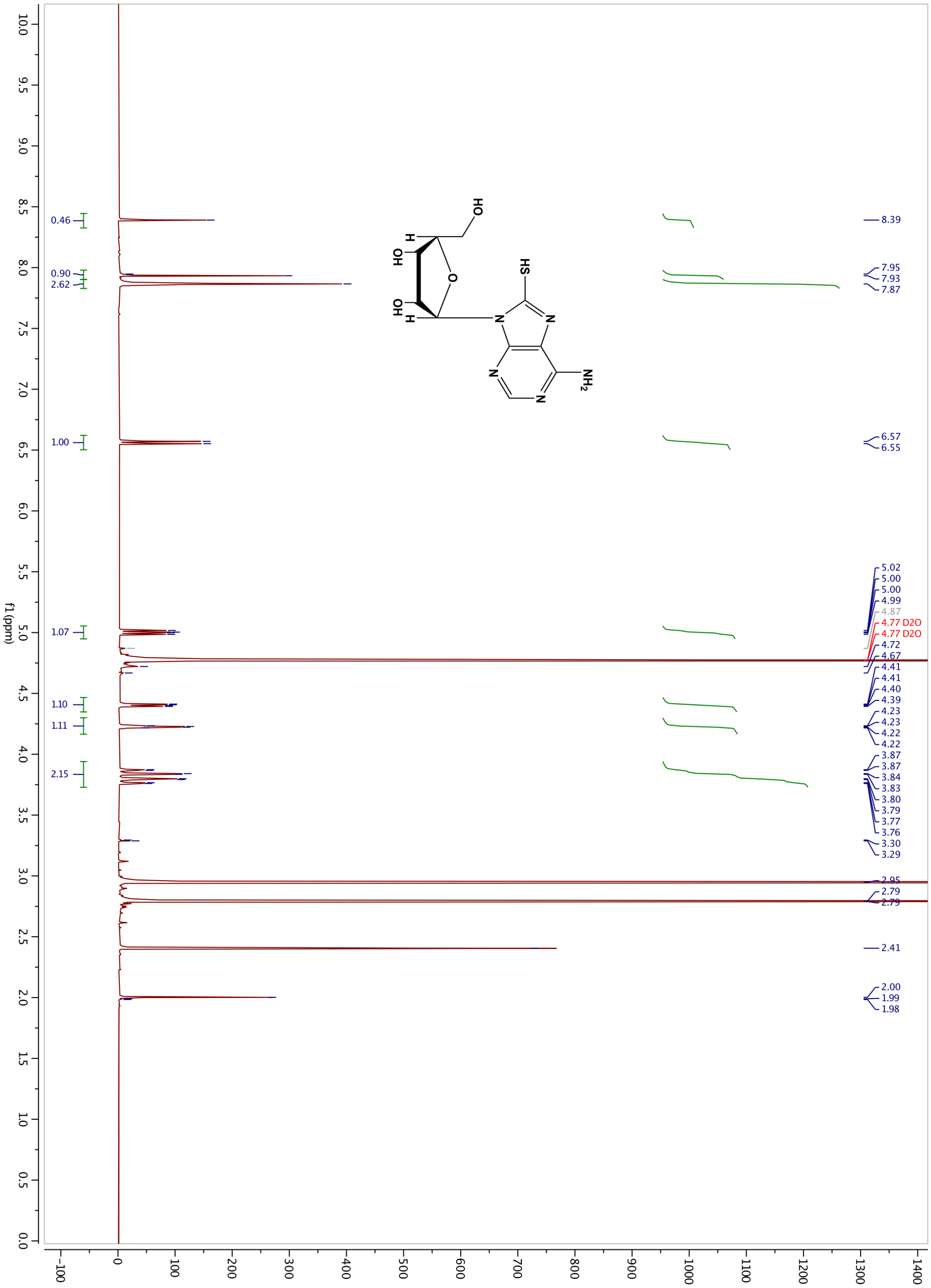
f1 (ppm)
10.0
9.5
9.0
8.5
8.0
7.5
7.0
6.5
6.0
5.5
5.0
4.5
4.0
3.5
3.0
2.5
2.0
1.5
1.0
0.5
0.0
-100
0
100
200
300
400
500
600
700
800
900
1000
1100
1200
1300
1400
0.46
0.90
2.62
1.00
1.07
1.10
1.11
2.15
8.39
7.95
7.93
7.87
6.57
6.55
5.02
5.00
5.00
4.99
4.87
4.77 D2O
4.77 D2O
4.72
4.67
4.41
4.41
4.40
4.39
4.23
4.23
4.22
4.22
3.87
3.87
3.84
3.83
3.80
3.79
3.77
3.76
3.30
3.29
2.95
2.79
2.79
2.41
2.00
1.99
1.98
HO
H
HO
O
HO
H
SH
N
N
N
N
NH2

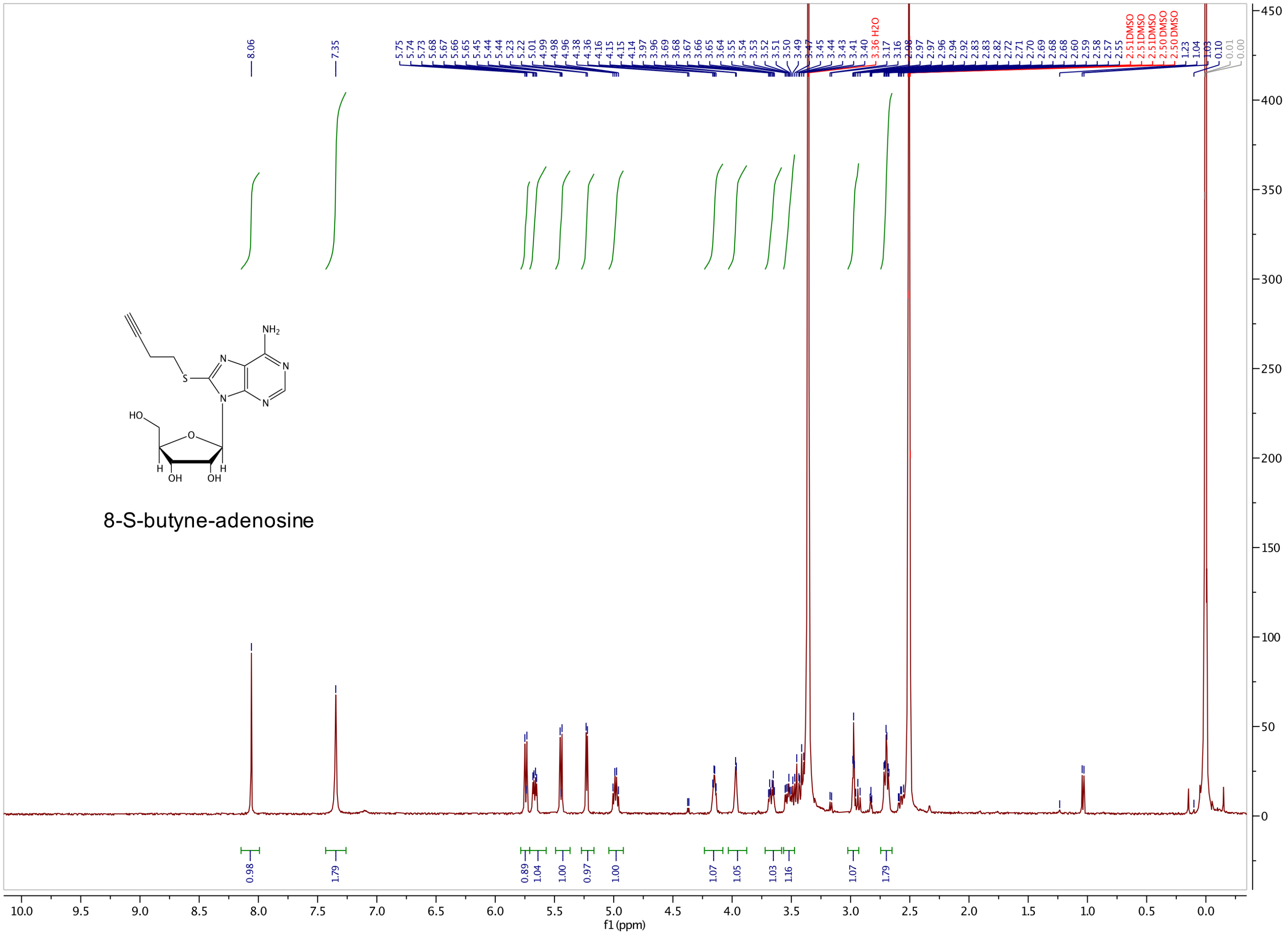8-S-butyne-adenosine
NH2
N
N
N
N
S
O
HO
H
H
OH
OH
8.06
7.35
5.75
5.74
5.73
5.68
5.67
5.66
5.65
5.45
5.44
5.44
5.23
5.22
5.01
4.99
4.98
4.96
4.38
4.36
4.16
4.15
4.15
4.14
3.97
3.96
3.69
3.68
3.67
3.66
3.65
3.64
3.55
3.54
3.53
3.52
3.51
3.50
3.49
3.47
3.45
3.44
3.43
3.41
3.40
3.36 H2O
3.17
3.16
2.98
2.97
2.97
2.96
2.94
2.92
2.83
2.83
2.82
2.72
2.71
2.70
2.69
2.68
2.68
2.60
2.59
2.58
2.57
2.55
2.51DMSO
2.51DMSO
2.51DMSO
2.50 DMSO
2.50 DMSO
1.23
1.04
1.03
0.10
0.01
0.00
0.98
1.79
0.89
1.04
1.00
0.97
1.00
1.07
1.05
1.03
1.16
1.07
1.79
10.0
9.5
9.0
8.5
8.0
7.5
7.0
6.5
6.0
5.5
5.0
4.5
4.0
3.5
3.0
2.5
2.0
1.5
1.0
0.5
0.0
f1 (ppm)
450
400
350
300
250
200
150
100
50
0

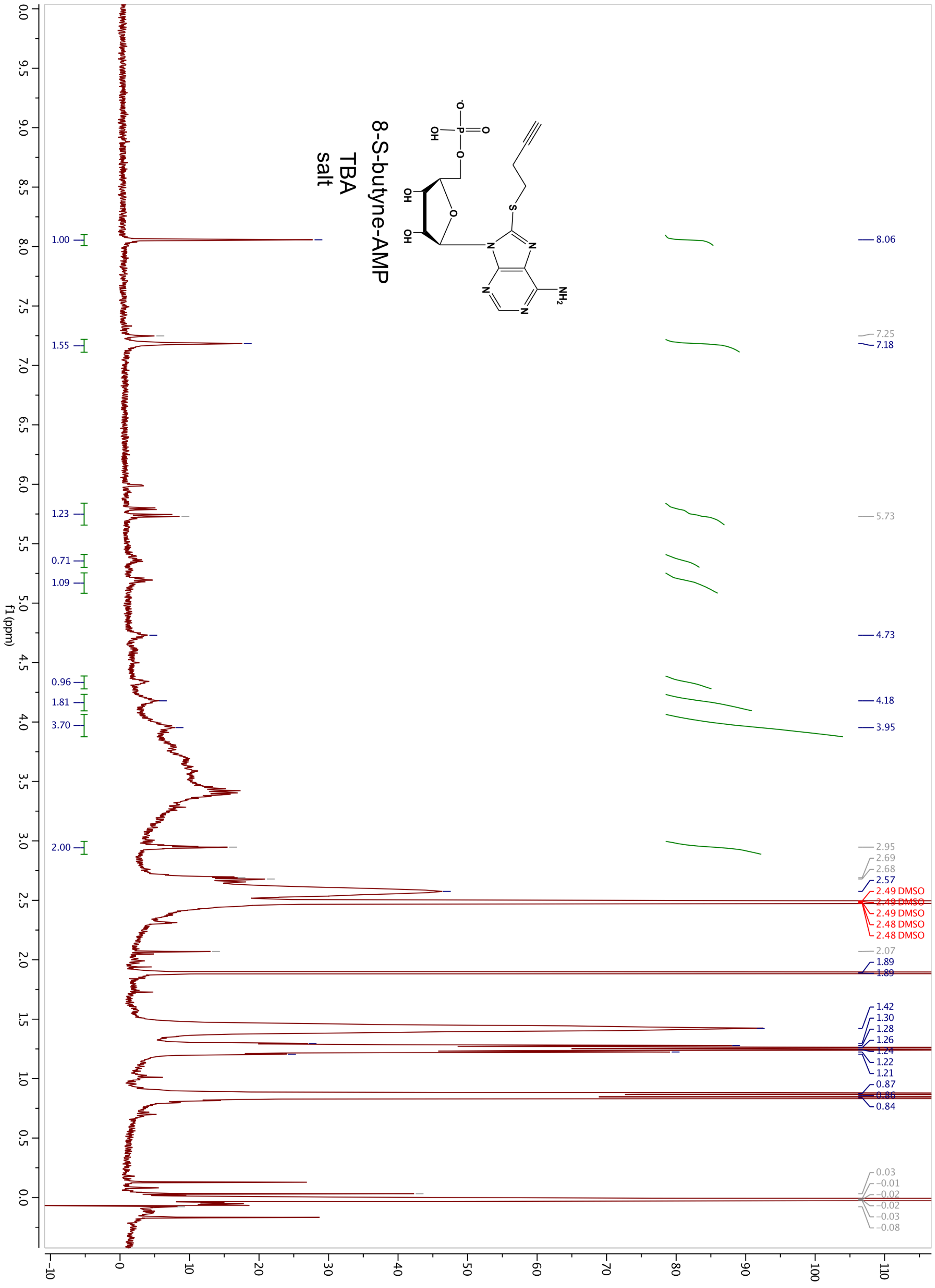
8-S-butyne-AMP
TBA
salt
NH2
N
S
O
OH
HO
P
O-
1.00
1.55
1.23
0.71
1.09
0.96
1.81
3.70
2.00
8.06
7.25
7.18
5.73
4.73
4.18
3.95
2.95
2.69
2.68
2.57
2.49 DMSO
2.49 DMSO
2.49 DMSO
2.48 DMSO
2.48 DMSO
2.07
1.89
1.89
1.42
1.30
1.28
1.26
1.24
1.22
1.21
0.87
0.86
0.84
0.03
-0.01
-0.02
-0.02
-0.03
-0.08
f1 (ppm)
10.0
9.5
9.0
8.5
8.0
7.5
7.0
6.5
6.0
5.5
5.0
4.5
4.0
3.5
3.0
2.5
2.0
1.5
1.0
0.5
0.0
-10
0
10
20
30
40
50
60
70
80
90
100
110

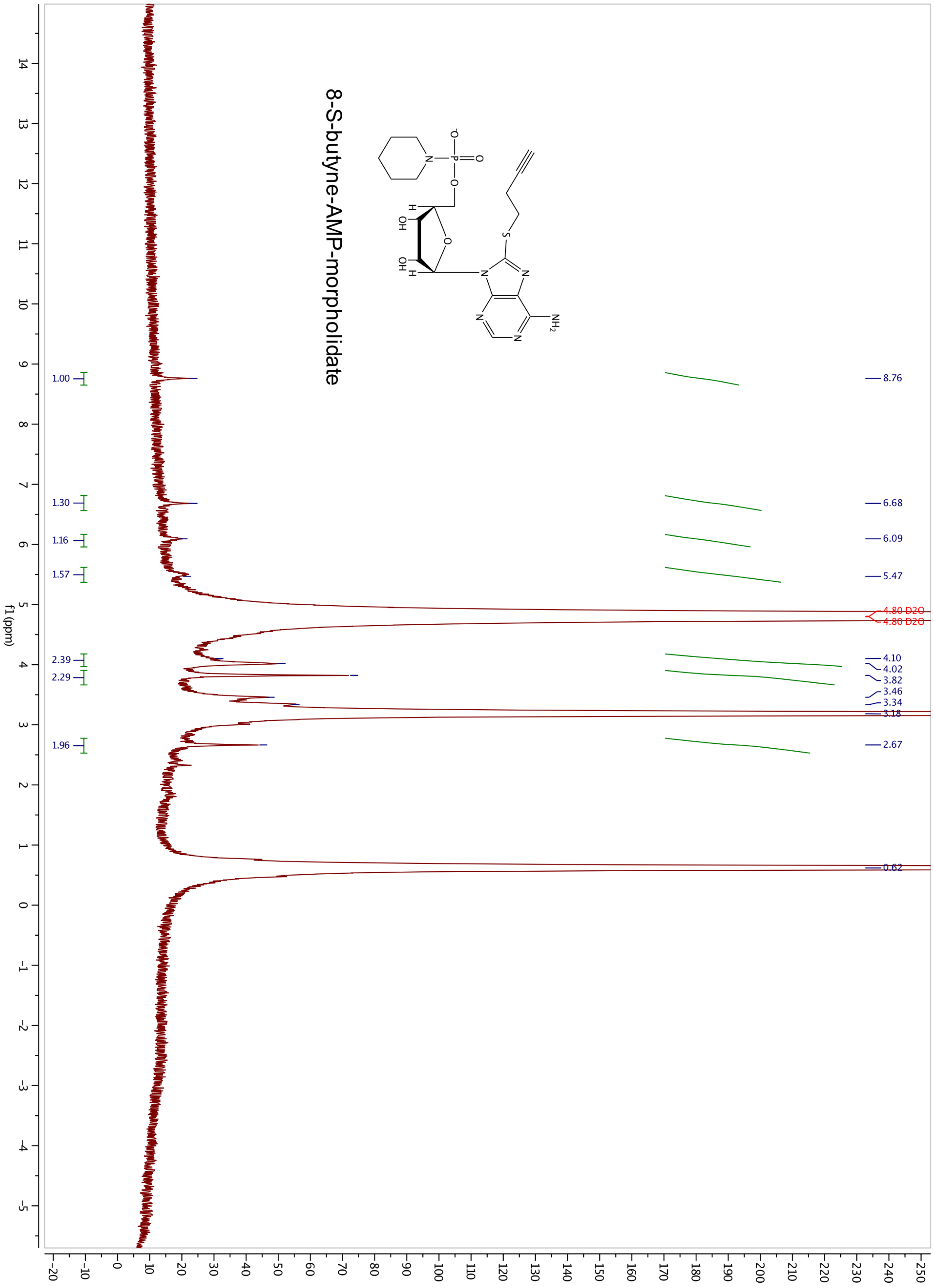
8-S-butyne-AMP-morpholidate
NH2
N
S
O
P
OH
H
8.76
6.68
6.09
5.47
4.80 D2O
4.80 D2O
4.10
4.02
3.82
3.46
3.34
3.18
2.67
0.62
1.00
1.30
1.16
1.57
2.39
2.29
1.96
f1 (ppm)
14
13
12
11
10
9
8
7
6
5
4
3
2
1
0
-1
-2
-3
-4
-5
-20
-10
0
10
20
30
40
50
60
70
80
90
100
110
120
130
140
150
160
170
180
190
200
210
220
230
240
250

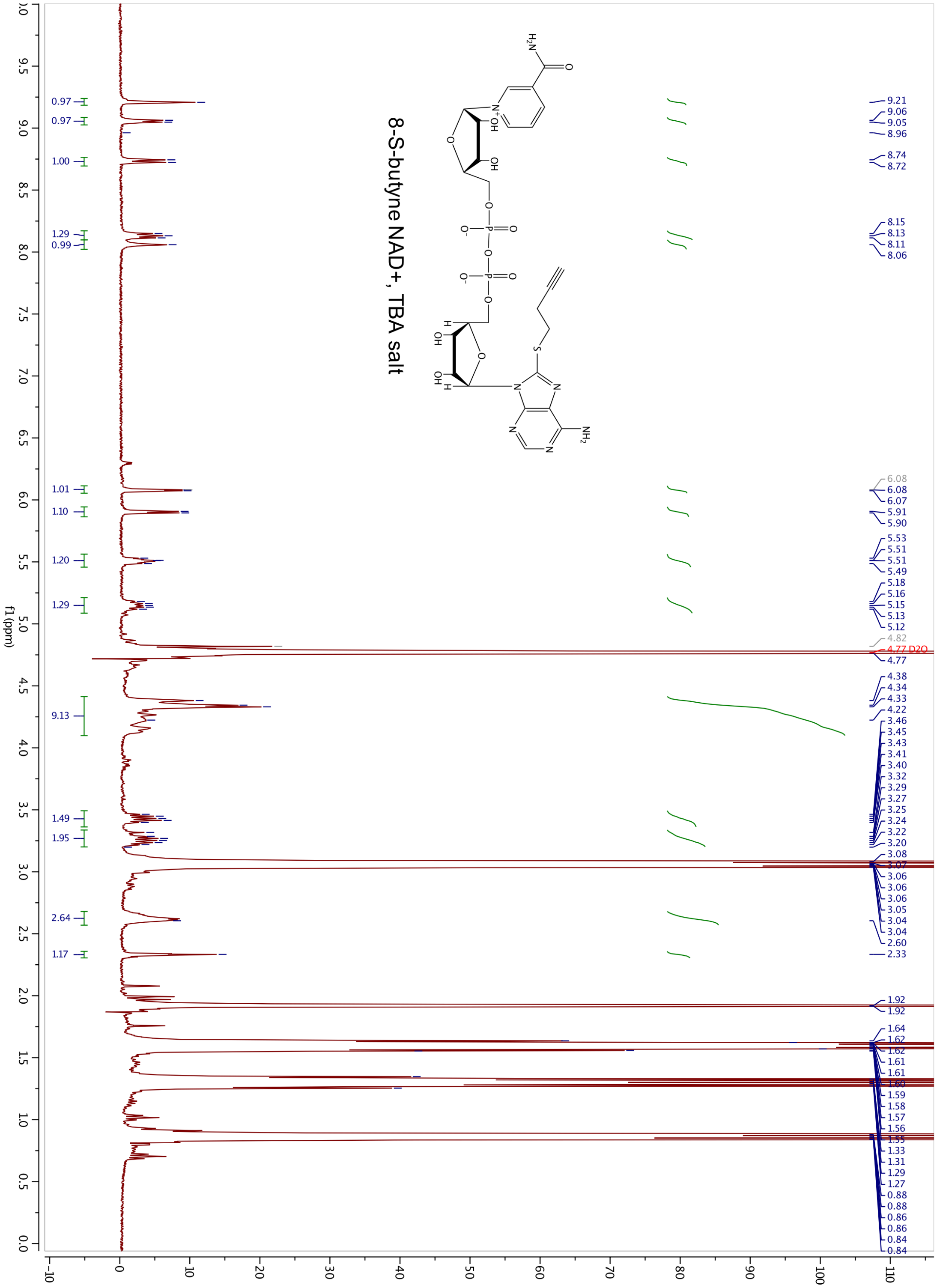

8-S-butyne NAD+, TBA salt
f1 (ppm)
0.97
0.97
1.00
1.29
0.99
1.01
1.10
1.20
1.29
9.13
1.49
1.95
2.64
1.17
9.21
9.06
9.05
8.96
8.74
8.72
8.15
8.13
8.11
8.06
6.08
6.08
6.07
5.91
5.90
5.53
5.51
5.51
5.49
5.18
5.16
5.15
5.13
5.12
4.82
4.77 D2O
4.77
4.38
4.34
4.33
4.22
3.46
3.45
3.43
3.41
3.40
3.32
3.29
3.27
3.25
3.24
3.22
3.20
3.08
3.07
3.06
3.06
3.06
3.05
3.04
3.04
2.60
2.33
1.92
1.92
1.64
1.62
1.62
1.61
1.61
1.60
1.59
1.58
1.57
1.56
1.55
1.33
1.31
1.29
1.27
0.88
0.88
0.86
0.86
0.84
0.84

Chapter 5.

Concluding remarks

The poly(ADP-ribose) polymerase (PARP) family of enzymes regulate diverse cellular roles through catalysis of ADP-ribosylation (ADPr) from nicotinamide adenine dinucleotide (NAD^+). PARPs have rapidly evolved to regulate host-pathogen interactions. Several PARPs including PARPs-1,7,9,13,12,14, and 15 have been shown to regulate immune signaling. Additionally, several PARP family members are upregulated in certain types of cancers, and some have been shown to play critical roles in cancer progression. While genetic manipulation has provided useful and important information, a major limitation in the field is discerning the cellular role of individual PARP family members. The development and use of novel chemical tools can allow us to address this limitation and provide answers to specific biological questions.

In chapter 1, I provided a review of the chemical genetic methodologies that have been developed to identify PARP targets. In this chapter, key findings that have been facilitated by chemical genetics were summarized using figure 1.4. Below I provide the same figure but highlight my contributions to our understanding of PARP biology which are outlined in this dissertation.

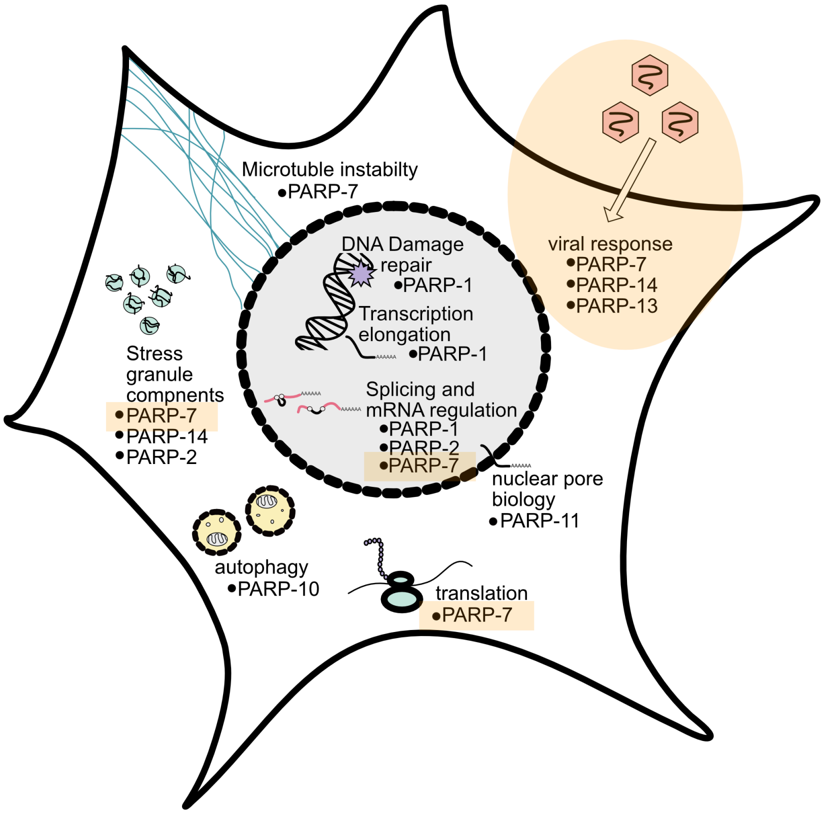

Figure 5.1 Figure 1.4. with the work from this dissertation highlighted. Highlighted in peach are my contributions. PARP-7 targets identified through my work show roles in viral response, translation, splicing, and cell stress. Future projects will focus on further elucidation of the direct role of PARP-7 in these processes, particularly in viral response.

In Chapter 2, I expanded upon an existing chemical genetic method, developed by the Cohen lab for identifying specific targets of individual PARP family members. This was accomplished through synthesis of a novel NAD+ analog capable of being used by an analog sensitized version of PARP-7. This approach was partnered with BioID and proteome wide-site mapping to identify numerous PARP-7 targets, many of which support a role for PARP-7 in the innate immune system. I identified PARP-13 as a robustly modified target of PARP-7 and showed that PARP13 is primarily modified on cysteine residues within its zinc finger residues.

In Chapter 3, I synthesized and characterized a PARP-7 selective inhibitor (KMR04-206). I showed that this inhibitor is potent and has at least 10-fold selectivity for PARP-7 in comparison to other PARP family members in cells. Additionally, through collaborative efforts, we showed that KMR04-206 elicits a dose dependent increase in type-I interferon signaling upon co-treatment with a cellular activator of the innate immune system. Below is a proposed mechanism by which PARP-7 may operate through PARP-13 to affect IFN-β levels and innate immune signaling. Both PARP13 and PARP 7 are known effectors of IFN-β production. PARP-13 stimulates the interferon response in response to viral infection via activation of the RNA helicase RIG-I. PARP-13 interacts with RIG-I and stimulates its oligomerization and ATPase activity, leading to interferon induction. This interaction is dependent on the ZnF domains of PARP-13, hence Cys MARylation of PARP-13 by PARP-7 could potentially disrupt the interaction between PARP-13 and RIG-I. Future studies will focus on understanding how PARP-7-mediated Cys MARylation of PARP-13 regulate their antiviral and immune regulatory roles **(Figure 5.2).** The next steps towards validation of this model are to assess the functional role of MARylation of PARP13 by PARP7 and test whether RIG-I interaction with PARP13 is affected by PARP-7 mediated MARylation. KMR04-206 will serve as a useful inhibitor in these studies.

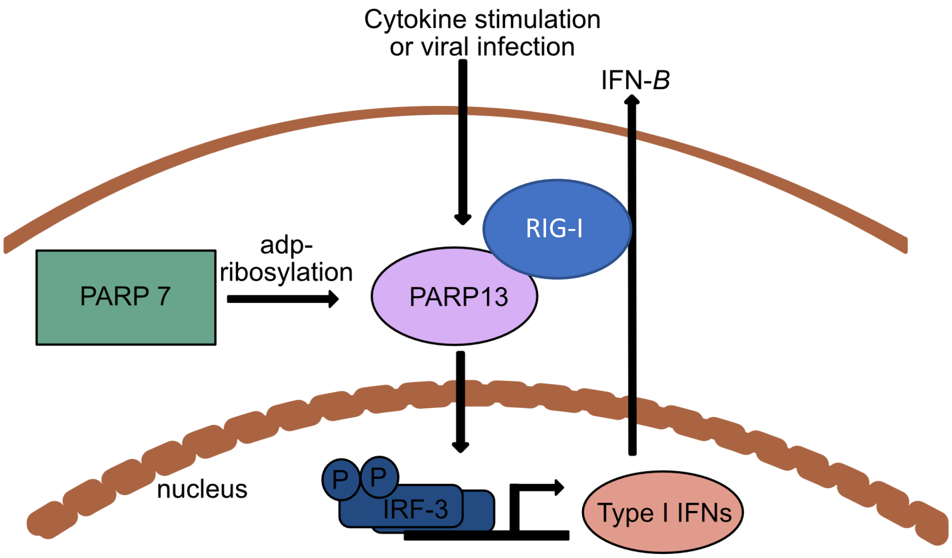

Figure 5.2 Proposed model of PARP-7-PARP-13 antiviral role and innate immune signaling.

In Chapter 4, I synthesized and characterized NAD+ probes for the identification of ADP-ribose binding partners. Of the probes synthesized toward this effort, 2-Az-NAD+ was distinguished as a lead compound, capable of being transferred by PARPs and photo-crosslinked to proteins from a cellular lysate.

The chemical tools and the work outlined in this dissertation furthered our understanding of ADP-ribosylation and the PARP family, particularly in regard to PARP-7 biology. The research detailed in chapters 2 and 3 will provide critical information towards the further development of a PARP-7 inhibitor to eventually serve as a chemical therapeutic.

Appendix I.

Additional experiments supporting Chapter 2.

After submission of chapter 2 to eLife, we spent significant time attempting to address the question of whether or not ADPr of PARP-13 by PARP-7 affects binding to RNA. We used an experiment from the paper entitled “RNA-binding protein isoforms ZAP-S and ZAP-L have distinct antiviral and immune resolution functions” by Schwerk/ Soveg et al. In this paper, they developed a biotinylated RNA probe of Interferon Lambda 3 (IFNL3) and show that PARP-13 binds this probe via mass spec analysis.

We adapted their protocol and created the same IFNL3-biotinlyated RNA probe to pulldown PARP-13 from cells and also used purified proteins. We used western blot analysis to observe the amount of PARP-13 bound to the probe (-/+) MARylation by PARP-7. We saw minimal changes of PARP13 binding to IFNL3 RNA when PARP7 is expressed or inhibited. Additionally we saw similar unsubstantial results with recombinant PARP13.2 binding (+/-) ADP-ribosylation **(Figure A1).**

Moreover, in Chapter 2, we observed interesting effects of ADPr by PARP7 on protein stability of both PARP-7 and PARP-13.2. We collaborated with Jason Matthew’s lab to further characterize the protein levels of endogenous proteins using a novel PARP-7 specific antibody recently developed by their lab. Their data show that both endogenous PARP7 levels are increased with PARP-7 is inhibited by Pthal01, but we do not see much of a change on the PARP-13 levels. The endogenous PARP-7 levels may be too low in this context to observe a significant change on the PARP-13 levels. When the two proteins are co-expressed we do see a significant increase in PARP13.2 levels upon inhibition of PARP7, a phenomenon that we have not observed for other proteins co-expressed, such as GFP or mCherry **(Figure A2).**

We sought to further investigate this phenomenon by inhibiting protein synthesis using cycloheximide and observing degradation of PARP7 and PARP13.2 in the presence of PARP7 inhibition. If proteins are stabilized with the compound then that may suggest that ADPr regulates proteasomal degradation. We expressed GFP-PARP7 and mycX2-PARP13.2 in cells, we then used cycloheximide to inhibit protein synthesis and treated the cells with DMSO, Phthal01 to inhibit PARP7, or veliparib to inhibit PARP1. We performed a time course of treatment to look at how protein stability is influenced by ADPr. In one of the experimental replicates (replicate 1), it appeared that PARP-7 and PARP-13 were both stabilized by Phthal01 in comparison to the control DMSO and veliparib, however in the second biological replicate, this result did not hold true (replicate 2, **Figure A3**).

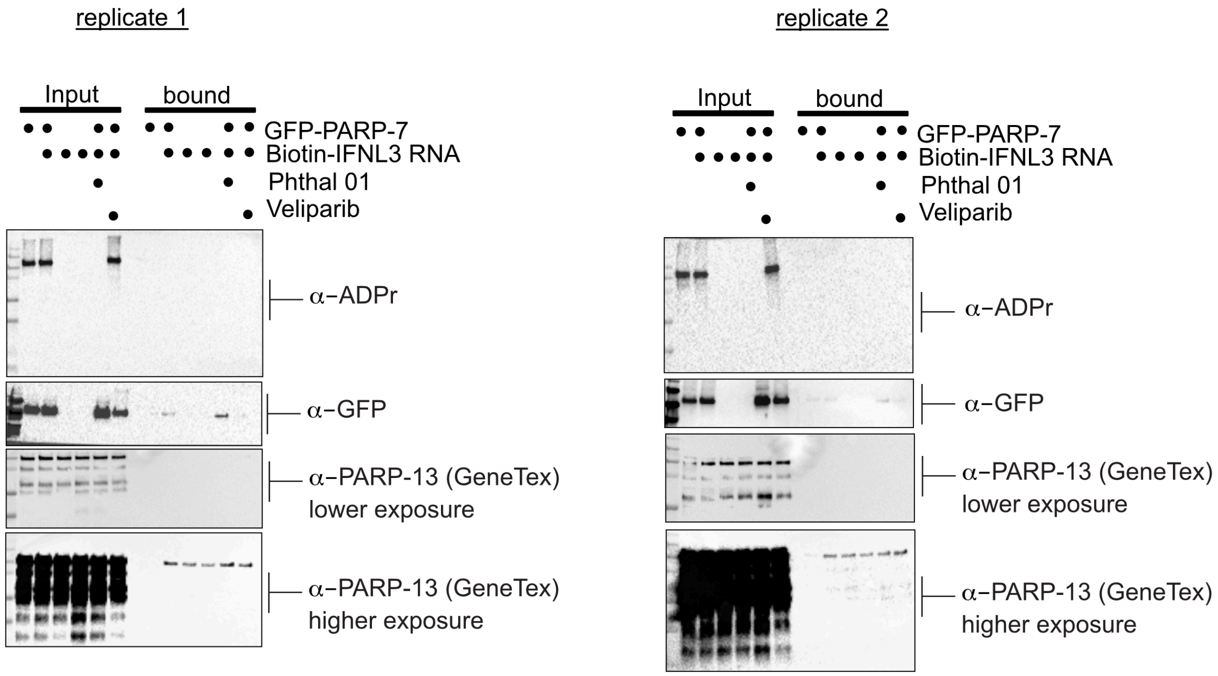

Figure A1. Biotin-IFNL3 RNA pulldown to look at endogenous PARP-13 binding in the presence and absence of PARP-7 mediated inhibition.

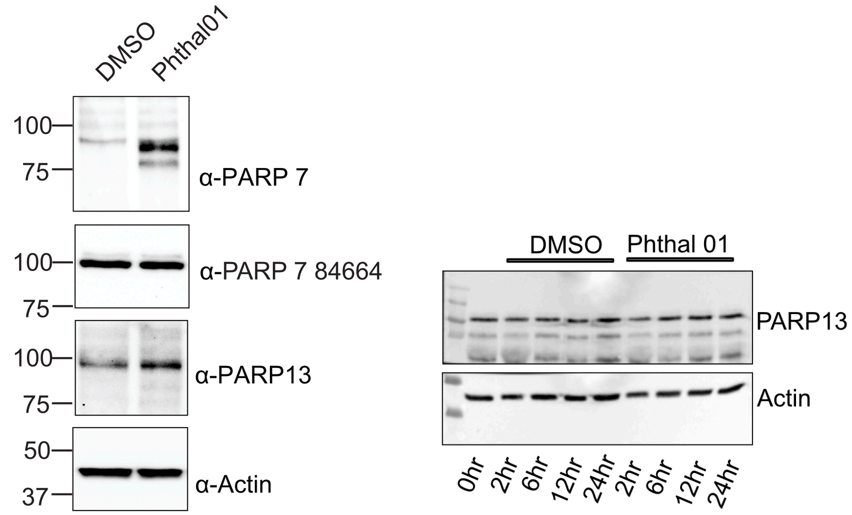

Figure A2. Endogenous protein levels of PARP13 do not change much in response to Phthal01 inhibition.

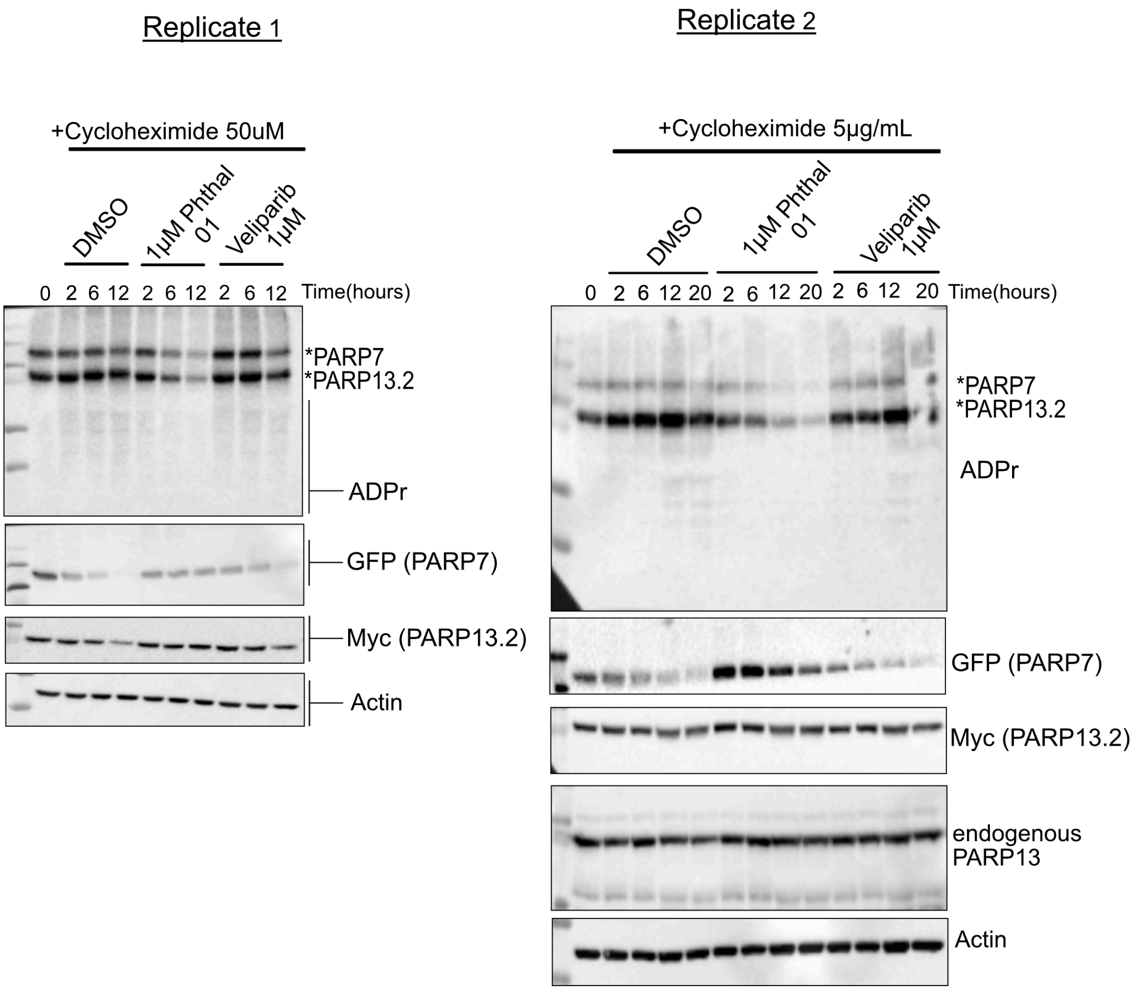

Figure A3. Cycloheximide (protein synthesis inhibitor) co-treatment with PARP inhibitors to observe protein stabilization.